



University of HUDDERSFIELD

University of Huddersfield Repository

Sahare, Shrawasti Ganesh

Inverse Design of Functional Surfaces for Prescribed Simple and Complex Flow Characteristics

Original Citation

Sahare, Shrawasti Ganesh (2020) Inverse Design of Functional Surfaces for Prescribed Simple and Complex Flow Characteristics. Doctoral thesis, University of Huddersfield.

This version is available at <https://eprints.hud.ac.uk/id/eprint/35259/>

The University Repository is a digital collection of the research output of the University, available on Open Access. Copyright and Moral Rights for the items on this site are retained by the individual author and/or other copyright owners. Users may access full items free of charge; copies of full text items generally can be reproduced, displayed or performed and given to third parties in any format or medium for personal research or study, educational or not-for-profit purposes without prior permission or charge, provided:

- The authors, title and full bibliographic details is credited in any copy;
- A hyperlink and/or URL is included for the original metadata page; and
- The content is not changed in any way.

For more information, including our policy and submission procedure, please contact the Repository Team at: E.mailbox@hud.ac.uk.

<http://eprints.hud.ac.uk/>

INVERSE DESIGN OF FUNCTIONAL SURFACES FOR PRESCRIBED SIMPLE AND COMPLEX FLOW CHARACTERISTICS

SHRAWASTI GANESH SAHARE

A thesis submitted to the University of Huddersfield in partial fulfilment of the
requirements for the degree of the Doctor of Philosophy

July 2020

ABSTRACT

In recent years, bio-inspired designs have gained industrial popularity as innovation drivers. Optimum process and design generate greater value such as low fuel cost, low operating cost, low carbon emissions etc. Bio-inspired functional surfaces can be key solutions to unlock these value potentials. The functional surfaces can be employed to generate desired flow characteristics resulting in optimum design and process performance. The functional surfaces can provide optimised solutions by better flow control within flow handling systems. One of the major advantages of bio-inspired functional surfaces is its geometrical simplicity and the resultant major flow effects that might be produced. These flow effects, although produced at immediate local vicinity within the geometry, can potentially bring global flow behaviour change. Stacked discs within multistage continuous resistance trim, an integral part of globe type control valve, can be envisaged as functional surface. Local flow effects in trim geometrical features vicinity can potentially be precursor to global undesirable effects such as cavitation, noise, vibration etc. Functional surface design thus become imperative for globe type control valve efficient performance.

In this thesis, advanced numerical and computational techniques have been employed. Mesoscopic approach is adopted to compute simple flow characteristics while continuum approach is adopted to compute complex flow characteristics. Furthermore, results computed are integrated into a framework. The framework principally links flow features to geometrical features for inverse design process.

The thesis focuses on quantitative and qualitative geometrical effects on flow behaviour by analysing developed equations. Modal analysis of design space computes governing flow features and resulting flow sensing locations. Flow features and their corresponding mathematical contribution within inverse design process is further analysed. As a result, optimised modal selection criterion is developed for considered cases. Consequently, inverse design environment for functional surfaces containing simple discontinuous geometry structure is developed for identified subspace. Furthermore, inverse design framework for functional surfaces containing simple discontinuous geometry structure is developed for multistage continuous resistance trim.

DECLARATION

- (a) The author of this thesis (including any appendices and/or schedules to this thesis) owns any copyright in it (the “Copyright”) and he has given The University of Huddersfield the right to use such Copyright for any administrative, promotional, educational and/or teaching purposes.

- (b) Copies of this thesis, either in full or in extracts, may be made only in accordance with the regulations of the University Library. Details of these regulations may be obtained from the Librarian. This page must form part of any such copies made.

- (c) The ownership of any patents, designs, trademarks and any and all other intellectual property rights except for the Copyright (the “Intellectual Property Rights”) and any reproductions of copyright works, for example graphs and tables (“Reproductions”), which may be described in this thesis, may not be owned by the author and may be owned by third parties. Such Intellectual Property Rights and Reproductions cannot and must not be made available for use without the prior written permission of the owner(s) of the relevant Intellectual Property Rights and/or Reproductions.

ACKNOWLEDGEMENTS

First and foremost, I would like to thank my parents, Mr. Ganesh Sahare and Mrs. Lata Sahare, for giving unconditional support during PhD. Their support has been a source of motivation and pushed to undertake this quality research study. Without my parent's support, this achievement would not have been possible.

I would like to express my gratitude to Prof. Rakesh Mishra for offering this PhD opportunity and guidance. I would also acknowledge Dr. Krzysztof Kubiak for his generous help during my initial PhD days. Furthermore, I would like to thank Dr. Paul Baker and Dr Taimoor Asim for insightful discussions. Finally, I would like to express gratitude to Dr. Dharminder Singh for his support and providing subject level expertise.

I would like to acknowledge Chaudhari Family, Kawade Family and Prakash Sahare Family for continuous support to my family in my absence. I like to acknowledge their unconditional moral, emotional and financial support throughout the growing years.

I also acknowledge support of my colleagues in EEERG at University of Huddersfield. Sree Nirjhor Kaystha, Dr. Noukhez Ahmed, Yusuf Airede and Dr. Isuru Sendanayake Achchige thank you for making this journey fun and insightful.

Shrawasti Sahare

January 2020

Huddersfield, UK

CONTENTS

ABSTRACT	II
DECLARATION	III
ACKNOWLEDGEMENTS	IV
CONTENTS	V
LIST OF FIGURES	VIII
LIST OF TABLES	X
NOMENCLATURE	XI
CHAPTER 1 INTRODUCTION	1
1.1. Functional Surfaces	2
1.2. Control Valve	5
1.3. Motivation	8
1.4. Organisation of the Thesis	9
CHAPTER 2 LITERATURE REVIEW	11
2.1. Functional surface flow characterisation	12
2.2. Control valve flow characterisation	20
2.3. Inverse Design Methodologies	23
2.4. Summary	26
2.5. Research Aims	27
2.6. Research Objectives	28
CHAPTER 3 NUMERICAL MODELLING APPLIED TO FUNCTIONAL SURFACES AND SEVERE SERVICE CONTROL VALVE	29
3.1. Numerical simulations by Lattice Boltzmann method	30
3.2. Computational Fluid Dynamics (CFD) Model for Severe Service Control Valve Trim	35

CONTENTS

3.3. Proper Orthogonal Decomposition (POD)	38
3.4. Gappy Proper Orthogonal Decomposition	40
3.5. Gappy POD based Inverse Design	41
3.6. Summary	46
CHAPTER 4 INVERSE DESIGN OF FUNCTIONAL SURFACES CONTAINING SIMPLE DISCONTINUOUS GEOMETRY STRUCTURE FOR PRESCRIBED SIMPLE FLOW CHARACTERISTICS	47
4.1. Introduction	48
4.2. Inverse Design	66
4.2.1. Inverse design sensitivity	67
4.2.2. Control points based inverse design	69
4.2.3. Surface shear based inverse design	76
4.3. Innovative Low Fidelity based Functional Surface Inverse Design Environment (LFF-SIDE)	83
4.3.1. High fidelity module	86
4.3.2. Snapshot Ensemble	86
4.3.3. Optimizer	87
4.3.4. Low fidelity module/Geometry Generator	87
4.3.5. Advantages of LFF-SIDE	87
4.3.6. Limitations of LFF-SIDE	87
4.4. Summary	88
CHAPTER 5 INVERSE DESIGN OF FUNCTIONAL SURFACES CONTAINING SIMPLE DISCONTINUOUS GEOMETRY STRUCTURE FOR PRESCRIBED COMPLEX FLOW CHARACTERISTICS	89
5.1. Introduction	90
5.2. Qualitative and quantitative description	94
5.2.1. Influence on Cv1	94
5.2.2. Influence on Cv2	98

CONTENTS

5.2.3.	Influence on Cv3	100
5.2.4.	Influence on Cv4	103
5.2.5.	Influence on Cv5	106
5.3.	Modal analysis and sparsity investigation	108
5.3.1.	Sparse Trim Ensemble	113
5.4.	Original trim inverse design investigation	121
5.5.	Novel Low Fidelity based Trim Design Framework (LF-TDF)	130
5.5.1.	High fidelity module	131
5.5.2.	Snapshot Ensemble	132
5.5.3.	Modal Optimisation	132
5.5.4.	Optimizer	136
5.5.5.	Low fidelity module/Geometry Generator	136
5.5.6.	LF-TDF Advantages	136
5.5.7.	LF-TDF Limitations	137
5.6.	Summary	137
CHAPTER 6	CONCLUSIONS	138
6.1.	Research Problem Synopsis	139
6.2.	Research Aims and Major Achievements	140
6.3.	Thesis Conclusions	142
6.4.	Thesis Contribution	146
6.5.	Recommendations for Future Work	147
REFERENCES		150
APPENDICES		162
A-1.	Lattice Boltzmann Code	162
A-2.	Gappy Proper Orthogonal Decomposition Code	184
LIST OF PUBLICATIONS		186

LIST OF FIGURES

FIGURE 4.1: (A) FLOW DOMAIN XY VIEW (B) DISCONTINUOUS GEOMETRY STRUCTURE PARAMETERS	48
FIGURE 4.2: CONTROL POINTS COMPUTATION FLOW CHART	50
FIGURE 4.3: CONTROL POINT A SPATIAL DISTRIBUTION (A) H=1; SX=4 (B) H=1; SX=7 (C) H=1; SX=10 (D) H=2; SX=4 (E) H=2; SX=7 (F) H=2; SX=10 (G) H=3; SX=4 (H) H=3; SX=7 (I) H=3; SX=10	52
FIGURE 4.4: CONTROL POINT B SPATIAL DISTRIBUTION (A) H=1; SX=4 (B) H=1; SX=7 (C) H=1; SX=10 (D) H=2; SX=4 (E) H=2; SX=7 (F) H=2; SX=10 (G) H=3; SX=4 (H) H=3; SX=7 (I) H=3; SX=10	54
FIGURE 4.5: CONTROL POINT C SPATIAL DISTRIBUTION (A) H=1; SX=4 (B) H=1; SX=7 (C) H=1; SX=10 (D) H=2; SX=4 (E) H=2; SX=7 (F) H=2; SX=10 (G) H=3; SX=4 (H) H=3; SX=7 (I) H=3; SX=10	56
FIGURE 4.6: MODES FOR CONTROL POINT A (A) MODE1, (B) MODE 2, (C) MODE 3, (D) MODE 4, (E) MODE 5, (F) MODE 6 AND (G) MODE 7	58
FIGURE 4.7: EIGENVALUE SPECTRUM FOR POD MODES OF CONTROL POINT A	58
FIGURE 4.8: MODES FOR CONTROL POINT B (A) MODE1, (B) MODE 2, (C) MODE 3, (D) MODE 4, (E) MODE 5 AND (F) MODE 6	61
FIGURE 4.9: EIGENVALUE SPECTRUM FOR POD MODES OF CONTROL POINT B	61
FIGURE 4.10: MODES FOR CONTROL POINT C (A) MODE1, (B) MODE 2, (C) MODE 3, (D) MODE 4, (E) MODE 5 AND (F) MODE 6	64
FIGURE 4.11: EIGENVALUE SPECTRUM FOR POD MODES OF CONTROL POINT C	64
FIGURE 4.12: GEOMETRICAL PARAMETER CORRELATION AT DIFFERENT CONTROL POINTS	68
FIGURE 4.13: GEOMETRICAL PARAMETER CORRELATION FOR CONTROL POINTS DISTRIBUTION	70
FIGURE 4.14: (A) GAPPY INNER PRODUCT $(\Phi_I, \Phi_J)_N$ (B) GAPPY INNER PRODUCT $(G, \Phi_I)_N$ (C) MODAL COEFFICIENT FOR $H/SX=0.42$; (D) GAPPY INNER PRODUCT $(\Phi_I, \Phi_J)_N$ (E) GAPPY INNER PRODUCT $(G, \Phi_I)_N$ (F) MODAL COEFFICIENTS FOR $H/SX=0.3$	72
FIGURE 4.15: (A) GAPPY INNER PRODUCT $(\Phi_I, \Phi_J)_N$ (B) GAPPY INNER PRODUCT $(G, \Phi_I)_N$ (C) MODAL COEFFICIENT FOR $H/SX=0.5$;	72
FIGURE 4.16: (A) GAPPY INNER PRODUCT $(\Phi_I, \Phi_J)_N$ (B) GAPPY INNER PRODUCT $(G, \Phi_I)_N$ (C) MODAL COEFFICIENT FOR $H/SX=0.28$; (D) GAPPY INNER PRODUCT $(\Phi_I, \Phi_J)_N$ (E) GAPPY INNER PRODUCT $(G, \Phi_I)_N$ (F) MODAL COEFFICIENTS FOR $H/SX=0.2$	73
FIGURE 4.17: (A) GAPPY INNER PRODUCT $(\Phi_I, \Phi_J)_N$ (B) GAPPY INNER PRODUCT $(G, \Phi_I)_N$ (C) MODAL COEFFICIENT FOR $H/SX=0.25$	73
FIGURE 4.18: (A) GAPPY INNER PRODUCT $(\Phi_I, \Phi_J)_N$ (B) GAPPY INNER PRODUCT $(G, \Phi_I)_N$ (C) MODAL COEFFICIENT FOR $H/SX=0.14$; (D) GAPPY INNER PRODUCT $(\Phi_I, \Phi_J)_N$ (E) GAPPY INNER PRODUCT $(G, \Phi_I)_N$ (F) MODAL COEFFICIENT FOR $H/SX=0.1$	74

LIST OF FIGURES

FIGURE 4.19: (A) GAPPY INNER PRODUCT (Φ_I, Φ_J)N (B) GAPPY INNER PRODUCT (G, Φ_I)N (C) MODAL COEFFICIENT FOR $H/SX=0.75$ -----	74
FIGURE 4.20: GEOMETRICAL PARAMETER CORRELATION FOR FRICTION FACTOR DISTRIBUTION -----	77
FIGURE 4.21: (A) GAPPY INNER PRODUCT (Φ_I, Φ_J)N (B) GAPPY INNER PRODUCT (G, Φ_I)N (C) MODAL COEFFICIENT FOR $H/SX=0.42$; (D) GAPPY INNER PRODUCT (Φ_I, Φ_J)N (E) GAPPY INNER PRODUCT (G, Φ_I)N (F) MODAL COEFFICIENTS FOR $H/SX=0.50$ -----	79
FIGURE 4.22: (A) GAPPY INNER PRODUCT (Φ_I, Φ_J)N (B) GAPPY INNER PRODUCT (G, Φ_I)N (C) MODAL COEFFICIENT FOR $H/SX=0.28$; (D) GAPPY INNER PRODUCT (Φ_I, Φ_J)N (E) GAPPY INNER PRODUCT (G, Φ_I)N (F) MODAL COEFFICIENTS FOR $H/SX=0.20$; (G) GAPPY INNER PRODUCT (Φ_I, Φ_J)N (H) GAPPY INNER PRODUCT (G, Φ_I)N (I) MODAL COEFFICIENT FOR $H/SX=0.75$ -----	79
FIGURE 4.23: (A) GAPPY INNER PRODUCT (Φ_I, Φ_J)N (B) GAPPY INNER PRODUCT (G, Φ_I)N (C) MODAL COEFFICIENT FOR $H/SX=0.25$; (D) GAPPY INNER PRODUCT (Φ_I, Φ_J)N (E) GAPPY INNER PRODUCT (G, Φ_I)N (F) MODAL COEFFICIENTS FOR $H/SX=0.30$ -----	80
FIGURE 4.24: (A) GAPPY INNER PRODUCT (Φ_I, Φ_J)N (B) GAPPY INNER PRODUCT (G, Φ_I)N -----	81
FIGURE 4.25: (A) GAPPY INNER PRODUCT (Φ_I, Φ_J)N (B) GAPPY INNER PRODUCT (G, Φ_I)N -----	81
FIGURE 4.26: LFF-SIDE ARCHITECTURE -----	85

LIST OF TABLES

TABLE 4.1: DESIGN POINTS	49
TABLE 4.2: CONTROL POINT A MODES MAXIMA AND MINIMA	59
TABLE 4.3: CONTROL POINT B MODES MAXIMA AND MINIMA.....	62
TABLE 4.4: CONTROL POINT C MODES MAXIMA AND MINIMA.....	65
TABLE 4.5: COMPUTATION MODES.....	70
TABLE 4.6: ORIGINAL ENSEMBLE BASED MODAL VARIATIONS.....	75
TABLE 4.7: NEW ENSEMBLE BASED MODAL VARIATIONS	76
TABLE 4.8: COMPUTATIONAL MODES	78
TABLE 4.9: ORIGINAL ENSEMBLE BASED MODAL VARIATIONS.....	82
TABLE 4.10: NEW ENSEMBLE BASED MODAL VARIATIONS	82

NOMENCLATURE

$C_{V_{\text{Control-Valve}}}$	Control valve flow coefficient
$C_{V_{\text{Trim}}}$	Trim flow coefficient
Q_{Trim}	Trim flow rate
ΔP_{Trim}	Overall/global pressure drop
$f = f(\vec{x}, \vec{v}, t)$	Particle density function
\vec{x}	Position
\vec{v}	Velocity
t	Time
ξ	Macroscopic (average) particle velocity
$f^{(0)}$	Maxwellian equilibrium distribution
τ	Single relaxation time
\vec{e}_i	Discreet velocity
ρ	Macroscopic mass density
U	Macroscopic velocity
w_i	Weighting factor
X	X direction (streamwise)
Z	Z direction (Cross-streamwise)
Y	Y direction (Wall normal)
dx	Spacing
dt	Time step
$\frac{u}{U_{\text{max}}}$	$\frac{\text{velocity}}{\text{Centreline velocity}}$
g	Augmented snapshot vector
Φ	Eigenfunction
K	Kernel
g^*	Hermitian of g
U^i	Computed solution
R	Auto-correlation matrix
λ_i	i th eigenvalue
\tilde{g}	Approximated representation of field g

α_i, b	POD coefficients
E	Approximation error
$M_{ij} = (\Phi^i, \Phi^j)$	Elements in Hermitian matrix
n	Support space
$M_{ij} = (\Phi^i, \Phi^j)_n$	Hermitian matrix over support space n
m	Considered flow characteristics
h	Discontinuous structure height
S_x	Discontinuous structure intermittent spacing
R	Cylinder radius
D	Row cylinder centre diameter
a, b & c	Velocity functional form control points
f	Local friction factor
τ_w	Wall shear stress
μ	Viscosity
$\frac{1}{2}\rho u^2$	Local kinetic energy density
\bar{u}	Mean velocity profile
lu	Lattice units
y	Wall normal distance
δ	Half channel height
U_{\max}	Maximum centreline velocity
$\frac{\bar{u}}{U_{\max}}$	Actual non-dimensional velocity
$\frac{\widehat{\bar{u}}}{U_{\max}}$	Functional form expressed non-dimensional velocity
Σ	Data summation
J	Gappy cost function
V^*	Target distribution
V	Achieved distribution
R_n	n th row cylinder radius

$\frac{D_n}{2}$	nth radial cylindrical elements row position from trim disc centre
Cv_n	nth row local flow capacity
P_i	ith power coefficient of design parameter
Ψ^T	Modal matrix transpose
E_i	ith iteration energy
E_0	Exact energy
Cv_{Disc}	Disc flow capacity
POD	Proper Orthogonal Decomposition
BGK	Bhatnagar Gross Krook

CHAPTER 1

INTRODUCTION

Bio-inspired designs have been the industrial innovation drivers. Optimum process and design generate greater value such as low fuel cost, low operating cost, low carbon emission etc. Bio-inspired functional surfaces can be one of the solutions to generate these values. These functional surfaces can be employed to generate desired flow characteristics resulting in optimum design and process performance. This chapter provides introductory discussion on current bio-inspired surfaces employed in various engineering application and its way forward in fluid dynamics. Chapter also introduces globe type valve, a flow handling system, and its multistage continuous resistance trim. Chapter connects functional surfaces with multistage continuous resistance trim and cites research motivation. Chapters ends by summarizing research motivation for this study.

1.1. Functional Surfaces

Numerous solutions are developed within nature to solve various problems. By combining physico-chemical properties of material with aligned micro and nanostructures, a well sophisticated solutions are found for such problems. Solutions to the problems of friction, wettability and reflectivity are well inspired from sharks, pangolins, snakes, lotus leaves, springtails, dessert beetles, moth eyes and butterfly wings. The following paragraphs give comprehensive review on functional surfaces that each of these organisms deploy to perform certain function.

Many drag reducing organisms have been studied over the course of time. Literature records drag reducing mechanisms were investigated and explained for barracuda [1], tuna [2], penguin [3] etc. Among marine animals, surface features present on the shark's skin have been studied extensively. The features consist of small scale parallel riblets (Figure 1.1a & 1.1b) aligned in the flow direction [4,5]. The scales range from 100-200 μm while the riblets have a height of 20-30 μm [6]. Such features allow shark or dolphins to swim at higher speeds than their physiological condition could allow.

The skin of soil-burrowing animals like beetles and pangolin must offer effective resistance against abrasive wear and friction. It is for this function that the body of pangolin is covered with keratin scales with a size of each scale about 25mm \times 40 mm (Figure 1.1c & 1.1d). Previous research conducted showed that scaled surface's abrasive wear is a function of riblets orientation with respect to sliding direction of abrasive particles, relative sliding velocity and abrasive particle size [7]. As per particle size, they can roll between the riblets ("Rolling effect") or can be guided along the direction of riblets ("Guiding effect") [7].

For reptiles like snakes, the fundamental requirements for their movement are increase in abrasive resistance as well as frictional anisotropy and adhesion reduction [8]. In particular, frictional anisotropy should be maintained for enhanced forward motion until the skin is shed. An extensive research conducted by Klein and Gorb [9] showed that snake skin consists of flexible inner layers and inflexible outer surface. In another research, it was also observed that the reptile's ventral side consists of elongated hexagonal scales which contains micro fibre structures (Figure 1.1 e-f). The direction and the shape of these textures induces high frictional anisotropy [10].

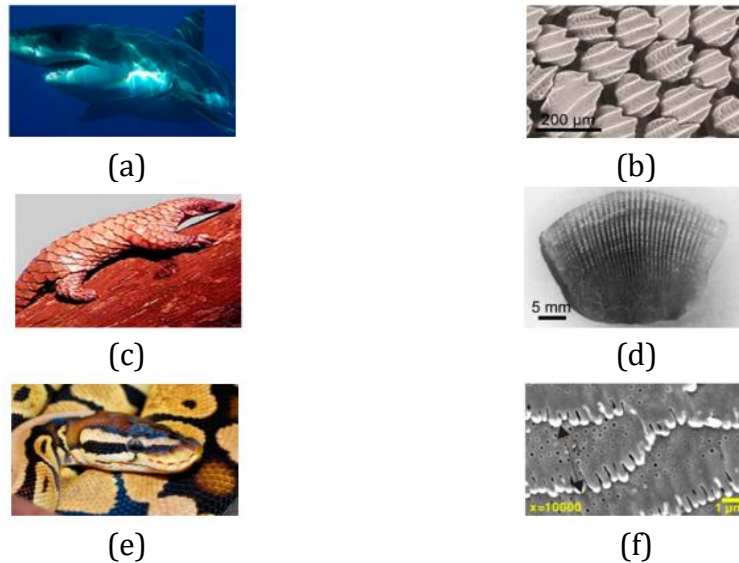


Figure 1.1: Examples of drag & wear reducing surfaces in nature (a-b) shark's skin; (c-d) Pangolin *Manis tricuspis* (e-f) Python's skin
Adapted from Kunz *et al.* [17]

Plants like lotus leaf (Figure 1.2 a-c) has developed superhydrophobic surfaces by combining surface profiles with hydrophobic materials. These are structured surface profiles that are formed by the combination of roughness on nanoscale and waviness on microscale. Such a heavy investment to generate complex structures has a particular aim of keeping surface clean and dry. The surface of Namib Desert beetle (Figure 1.2 d-f) is another example which combines hydrophilic and hydrophobic regions. Being a desert beetle, hydrophilic peaks facilitates water condensation from fog and the pathway for water droplets to roll towards the beetle's mouthparts are provided by superhydrophobic troughs.

Nature also has examples on antireflective functional surfaces. The moth eye antireflective surface consists of fine array of parabolic shape nipples which are at a distance of 200 nm from each other and are 250 nm in height (Figure 1.3 a-c). These nipples are touching each other at the base and completely prevent reflectance for normally incident light [11]. This significantly reduces the eye glare of the moths which consequently make them less visible to the predators. This happens due to gradation of refractive index by nipple arrays which consequently reduces the reflectance [12]. Glass wing butterfly's wings also has camouflage motivated antireflective functional surface. The wing surface has high aspect ratio nanopillars which are arranged irregularly with random height and width (Figure 1.3 d-f) [13]. Such random distribution of nanopillars

results in low reflectance transparent wings which makes it difficult for predatory birds to track during flight.

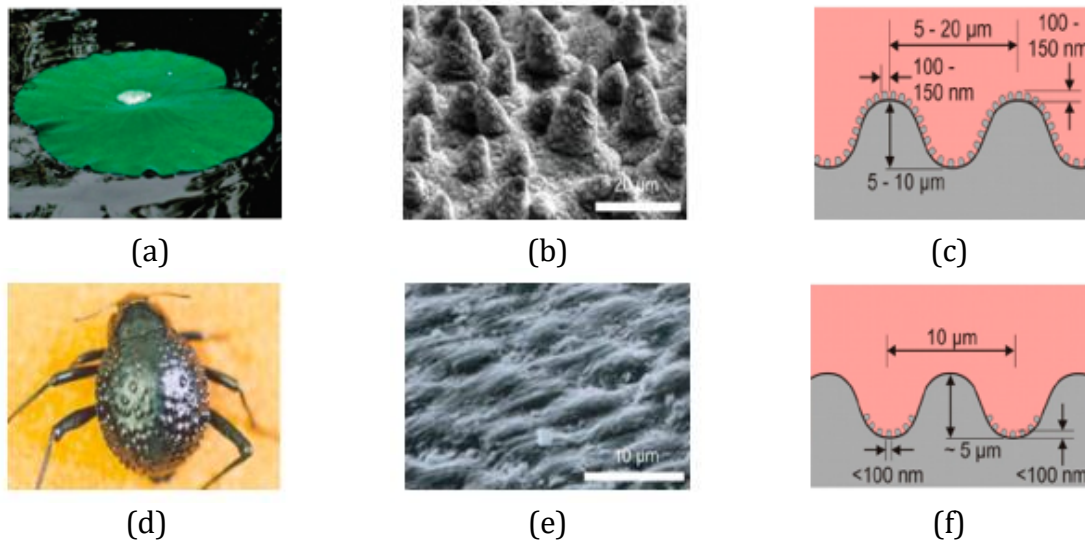


Figure 1.2: Examples of wettability functional surfaces in nature (a-c) Lotus leaf; (d-f) Namib Desert Beetle
Adapted from Kunz *et al.* [17]

Selective light reflection, diffraction and absorption can produce structural colours over the surface. This is aptly demonstrated by Morpho butterflies (Figure 1.4 a-c). The structures present on the wings are characterized by longitudinal ridges spanned by cross ribs [14]. Through wavelength interference, these structures selectively cancel out wavelengths of certain colours. The mechanism of cancelling out certain wavelengths depends on the structure and interspatial distance between diffracting layers [15]. The Brazilian weevil beetle appears iridescent due to 3D photonic crystals present on its surface. The surface of beetle consists of cylindrically shaped building blocks and air gaps. These building blocks are arranged in diamond lattice symmetry with 450 nm lattice constant [16]. Such surface structural arrangement is transparent for all wavelengths except 500-550 nm which makes the beetle appear iridescent.

INTRODUCTION

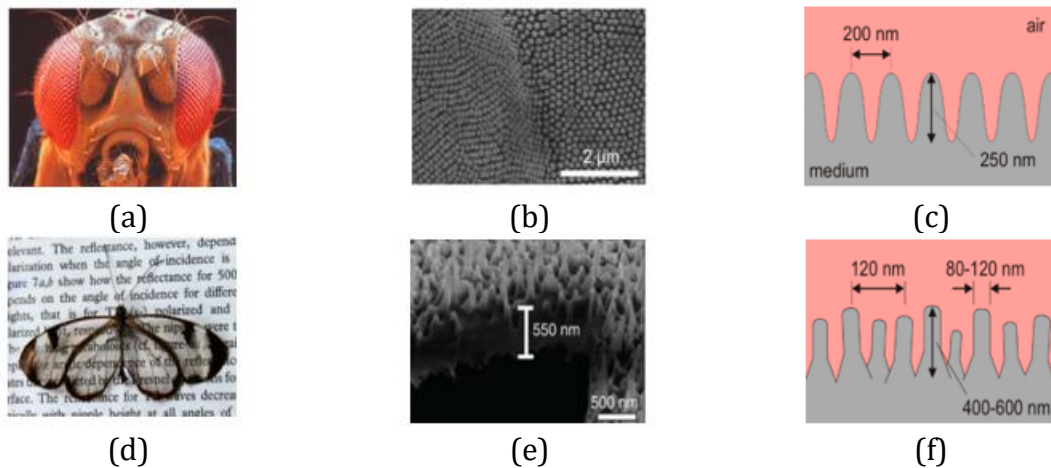


Figure 1.3: Examples of antireflective functional surfaces in nature (a-c) moth eye; (d-f) glass wing butterfly
Adapted from *Kunz et al.* [17]

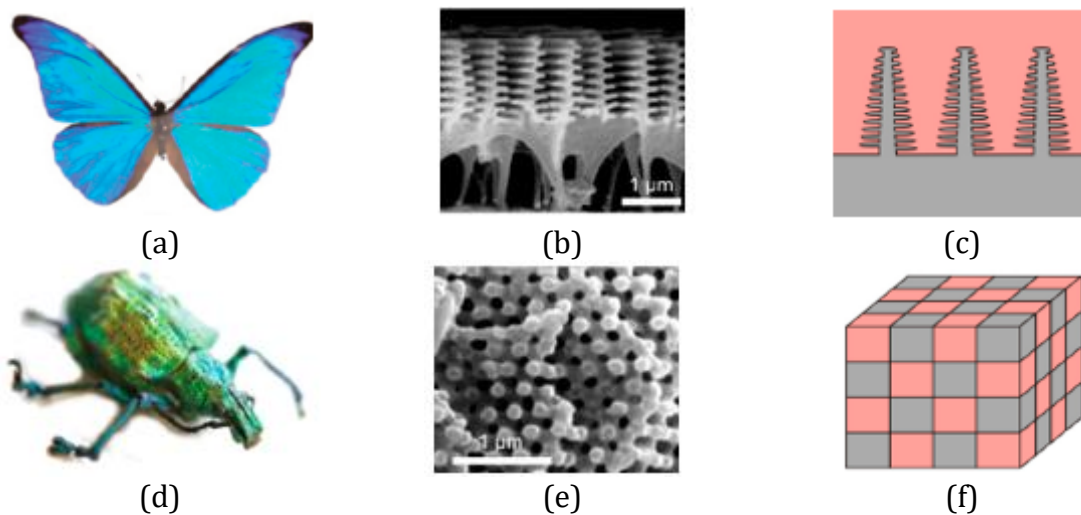


Figure 1.4: Examples of structural colors functional surfaces in nature (a-c) Morpho butterfly; (d-f) Brazilian weevil beetle
Adapted from *Kunz et al.* [17]

1.2. Control Valve

Control valve forms an integral part of process control industry. By controlling flow parameters such as pressure drop, flow rate etc. the flow conditions are controlled. Much of this flow process control is incorporated by installed valve gates that opens and closes at different Valve Opening Positions (VOP). The changes in flow conditions are sensed by installed sensors that signals actuators against predetermined set point. Thus, an optimum flow process control can be obtained by effectively controlling the VOPs.

INTRODUCTION

A typical industrial valve consists of different parts. Figure 1.5 shows control valve structure with easy to identify main parts. Figure shows the main valve body, the trim and the seat. The flow enters the valve body through inlet and exits via outlet. Trim forms the complicated structure within valve components and has primary function for fluid flow control. The controlling application of trim depends on the environment it is operating. Typical severe service application includes fluid pressure drop in steps to avoid cavitation and high pressure drops across valve [18].

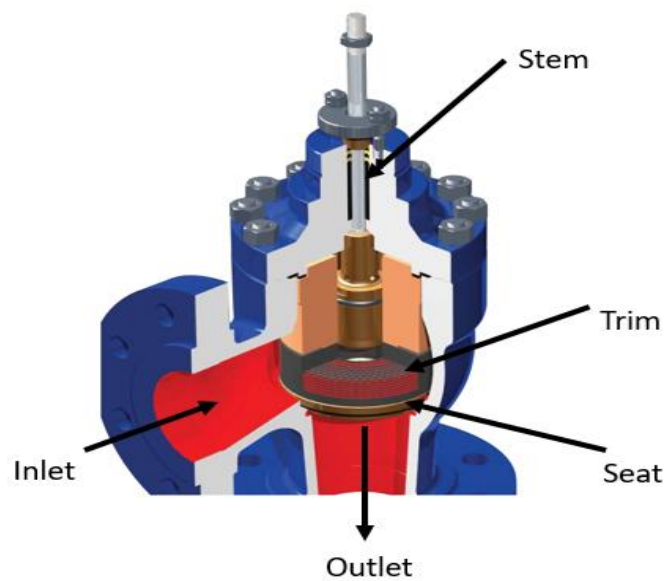


Figure 1.5: Control valve components [18]

Figure 1.6 shows trim example that is typically used in severe service application. It can be seen that the trim is divided into different discs that are stacked/layered over each other. Each individual trim disc consists of small cylinder that are protruding from the bottom surface. The protruding cylinder are arranged in staggered form. It can be seen when fluid passes through trim, the protruding cylindrical elements offer flow resistance thus modifying flow behaviour. In short, individual discs within trim acts as functional surfaces with cylindrical elements.

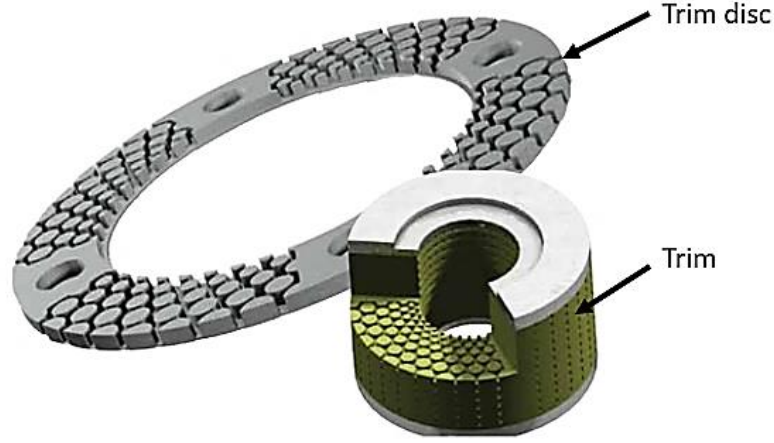


Figure 1.6: Trim considered in this study [18]

As previously mentioned, the environment in which trim operates is of high importance. This is referred to the erosive and corrosive fluid that valve typically encounters. The forces demanded by valve actuator is predominantly dictated by trim design. Following are some of the factors that to be considered while choosing valve trim:

- Service life of trim depending on erosive or corrosive fluid nature.
- Specific operating conditions i.e. constant trim service, severe temperature etc.
- Trim serviceability.
- Cavitation problem or noise generation during valve operations.
- Requirements for valve actuators.
- Flow characteristics for understanding and controlling valve gain.

Control valve flow coefficient ($Cv_{\text{Control-Valve}}$) is the primary parameter that governs control valve design. Control valve flow coefficient depends on the trim flow coefficient as shown [19]:

$$\frac{1}{Cv_{\text{Control-Valve}}^2} \propto \frac{1}{Cv_{\text{Trim}}^2} \quad 1.1$$

$$Cv_{\text{Trim}} \propto \frac{Q_{\text{Trim}}}{\sqrt{\Delta P_{\text{Trim}}}} \quad 1.2$$

Cv_{Trim} is trim flow coefficient. Q_{Trim} and ΔP_{Trim} are trim flow rate(m^3/hr) and overall/global pressure drop (kPa) respectively. Thus, Cv can be seen to embed global

flow information. The above equations are used in sizing equations determining multi-stage control valve designing [20].

1.3. Motivation

Bio-inspired designs can provide optimised solutions. The designs can be implemented for better flow control within engineering systems. One of the major advantages of bio-inspired design is its geometrical simplicity and the resultant major flow effects that might be produced from it. These flow effects, although produced at immediate local vicinity within the geometry, can potentially bring global flow behaviour change such as cavitation, noise, vibration etc.

It can be seen that although control valve design follows well established top-down design approach where performance evaluator equation (eq. 1.2) is coupled with sizing equations [20]. However, this approach fails to undertake local flow effects into design consideration. The top-down design approach can severely affect global performance which is a function of local phenomenon. Local flow effects can potentially be precursor to global undesirable effects such as cavitation, noise, vibration etc. It thus becomes imperative for local flow effect inclusion within design procedure. The bottom-up design approach computes local geometrical features for prescribed local flowfield. Such approach not only takes local insight into design consideration but also leaves wider room for customised product design. Furthermore, recent control valve research suggests three dimensional flowfield existence. However, traditional top-down design approach does not take flow three dimensionality for design considerations.

Motivated by this thought, the research focus on inverse design methodology of bio-inspired functional surfaces for prescribed flow behaviour. In short, bottom-up design procedure is applied for prescribed flow properties within flow handling system. Furthermore, functional surface design methodology devised in this research can potentially be implemented into wider adaptive flow control scheme.

1.4. Organisation of the Thesis

Chapter 1: The chapter discusses comprehensive and introductory review on functional surfaces. The chapter dwells into various type of mechanisms that are employed within nature to find solutions to the problems of friction, wettability and reflectivity. It outlines the examples from animal kingdom that deploy solutions to achieve functions of greater swimming efficiency, less wear, greater reflectivity etc. Chapter further explores functional surface implementation into flow handling systems. Efficacy of top-down design idea is challenged while exploring bottom-up design for better flow handling system efficiency. Chapter closes with research motivation for this study.

Chapter 2: The chapter elaborates previous work that has been carried out in functional surface influence on flow characteristics. It cites previous literature on surface roughness, riblets, macro and micro surface elements etc. Chapter discusses literature work on bio inspired designs and its application within engineering industry. Furthermore, recent development within flow handling system is discussed. The discussion focuses on industrial control valve and related research development for flow control that has been taken place. Literature on control valve trim design is explored. The chapter closes by outlining aims and objectives for the study.

Chapter 3: This chapter explains three methodologies that are employed for this study. The first two are the numerical techniques that are predominantly used in data generation for different design conditions. The first of these techniques is based on mesoscopic approach while the second is based on continuum approach. The chapter informs about the boundary conditions, fluid properties, and geometrical designs etc. that are considered for numerical solution. The third adopted methodology outlines an algorithmic process that is extensively deployed within thesis.

Chapter 4: Detailed discussions are carried out in this chapter that provide qualitative and quantitative description of the simple flow contained within two parallel plates. Chapter outlines the functional form of obtained velocity profile. Furthermore, this functional form is leveraged to carry out inverse design sensitivity. Detail mathematical process is explored for inverse design along with modal effects. Chapter ends by

proposing an environment for functional surface inverse design contained within subspace derived from arbitrary design space.

Chapter 5: Chapter introduces inverse design methodology for prescribed local flow capacity of control valve trim. Chapter establishes relationship of local flow capacity with trim local cylinder geometrical parameter. This aids in qualitative description of local geometry influence on the local flow coefficient. Furthermore, chapter explores sparsity effect on the snapshot ensemble and establishes the efficacy of Gappy POD for this snapshot ensemble. Chapter ends with the proposed inverse design framework for control valve trim.

Chapter 6: The chapter summarise and outlines the results obtained during the research. Furthermore, it outlines the knowledge contribution of the thesis. Additionally, it also defines recommendation on future research of this field.

CHAPTER 2

LITERATURE REVIEW

Further to introducing functional surfaces and multistage continuous resistance trim, this chapter develops relevant literature review detailing existing knowledge gaps. A varied resource has been critically cited that details better understanding of the flow behaviour for functional surfaces. Extensive literature review has been carried out detailing current flow behaviour understanding within multistage continuous resistance trim. This assisted in defining scope for this current work.

2.1. Functional surface flow characterisation

Research into wall roughness effect on near-wall flow characteristics span over eight decades. The seminal work done by Colebrook and Moody [21, 22] is still of practical importance for engineering applications. The Moody diagram, that represents friction factor as a function of Reynolds number for different non-dimensional roughness heights, has three different flow regimes. First, hydraulically smooth regime in which wall shear stress is entirely due to the viscosity of fluid. Second, transitionally rough regime where wall shear stress arises from viscous and pressure drag exerted on roughness elements. Third, fully rough regime in which wall shear stress is completely due to pressure drag on the roughness elements.

Recent research focused on exploring riblets, bio-inspired small structure on the surface, for drag reduction. Bechert *et al.* [23] carried an extensive investigation on the optimal size of riblet for drag reduction. A 10% drag reduction was observed for an optimal riblet spacing to height ratio $s/h=2$ and at viscous scaled spacing $s^+=17$. Lee & Lee [24] conducted PIV experiments and measured flow field. An increase in drag was reported for riblet spacing $s^+ >30$ during their investigation. Vortex accommodation inside riblet valley was cited as possible reason for drag increase. This settling actively increased vortices interaction with surface consequently increasing surface skin friction (Choi *et al.* [25]; Goldstein *et al.* [26]). On the contrary, for $0 < s^+ < 30$, vortices are larger in diameter than the riblet spacing. This results in most of the vortices staying above the riblets and touching only the tips. A reduction in drag was observed for such a case. However, drag reduction was observed for $0 < s^+ < 30$ possibly due to vortices staying above the riblets and only touching their tips. However, information gathered in this study was not further implemented for riblet design.

Bandyopadhyay *et al* [27] studied shark skin behaviour in controlling and delaying flow transition. The study modelled how shark and dolphin skin effectively control transitional vorticity by the application of spatiotemporal phase reset mechanism. Study found spatiotemporal analysis of control to be instructive. Additionally, it also found, for control purposes, part of low Reynolds number wall-turbulence to be systemically deterministic. Finally, the study revealed same adaptation mechanism of shark and dolphin to their respective fluid environments.

In a study conducted by Wen *et al* [28], hydrodynamic function of biologically accurate 3D rigid denticles embedded in flexible membrane were tested against smooth control at relevant Strouhal and Reynolds numbers. This study varies from the investigations conducted by Oeffner & Lauder [29], in which hydrodynamic performance comparison under static condition was limited between skin with denticles and skin with denticles sanded off. However, the true need is to investigate flow around denticles under dynamic propulsive conditions. Geometrical features of denticles, as shown in figure 2.1, extracted for this study conducted by Wen *et al* [28] were: Denticle Length (DL), Denticle Width (DW), spacing between mid and side denticle ridges (RS), Denticle Height (DH), denticle Base Width (BW), denticle Base Length (BL), height of the mid-ridge (RHM) and height of the side-ridge (RHS). 3D printed shark skin was found to have increased swimming speed with reduced energy consumption in comparison to its counterpart, under certain motion protocols. The increased swimming speed was attributed to the observed leading-edge vortex generated by the printed shark skin.

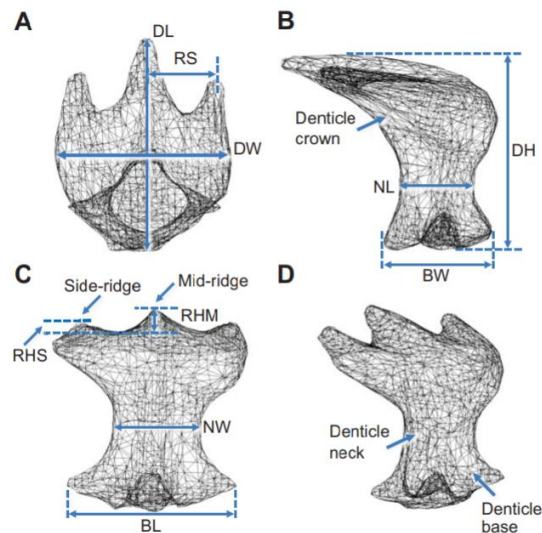


Figure 2.1 Geometrical features of a shark skin denticle

In another study conducted by Wen *et al* [30], effect of denticle pattern and spacing on the hydrodynamic performance of shark skin was measured. Geometrical features extracted from the real shark skin for this study were: denticle spacings and their arrangement patterns. Figure 2.2 shows Scanning Electron Microscope (SEM) images of the arrays as visible from different viewpoints. Performance of 3D printed flexible membrane with three different types of denticle patterns and spacing were compared

over 3D printed smooth surface control. These membranes were then subjected to both static and dynamic test conditions. At low speeds static test, a drag reduction was observed for pattern denticles compared to smooth control but an increase was revealed for speeds above 25 cm/s. However, for dynamic test, at a heave frequency of 1Hz and amplitude of ± 1 cm, a significant increase in speed was recorded for staggered-overlap pattern compared to smooth control. It was noted that only staggered-overlapped pattern provided an advantage over the smooth controlled surface and other two patterns. Useful results were presented in this study and further investigation to be carried for integrating these results for denticle shark skin design for targeted hydrodynamic performance.

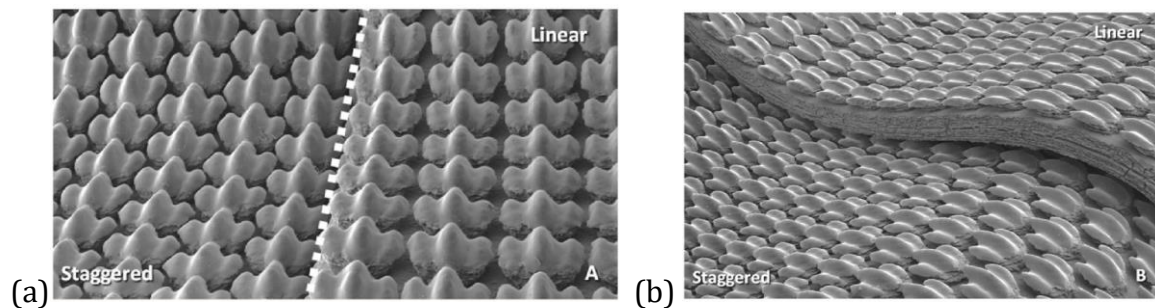


Figure 2.2 SEM images of fabricated synthetic shark skin membranes. Staggered and linear arrays as visible (a) from above (b) and from side

Investigations were carried out on riblets that were arranged oblique to the flow direction. (Schwarz van Manen [31]; Schneider and Dinkelacker [32]; Hage *et al.* [33], Hage *et al.* [34]). The results are summarized as follows: (1) Drag reduction performance remained nearly unchanged for yaw angle between 10° - 15° . (2) For yaw angle between 20° - 35° , a zero drag reduction was observed. (3) Skin friction value grew with an increase in yaw angle. (4) Highest skin friction value was observed at 90° yaw angle. The values also depended on both viscous scaled riblet height and spacing. Dinkelacker *et al.* [35] observed following riblet patterns on shark skin: (1) A convergence of riblets was observed near so-called pit organs (Fig. 2.3(a)). A divergence of riblets was observed upstream of pores of the lateral-line organ (Fig.2.3(b)). Motivated by this observation, Koeltzsch *et al.* [36] conducted hot-wire measurements for flow over converging diverging riblet patterns (herringbone pattern) embedded on the surface of turbulent pipe flow. The study revealed a considerable difference between streamwise velocity

fluctuations and time-averaged mean velocity. Over converging riblet section, the mean velocity decreased while velocity fluctuations increased. An opposite was observed for the diverging riblet section. By embedding small scale herringbone riblet arrangement on pipe wall, a large-scale counter rotating streamwise vortices were observed disrupted the naturally occurring coherent motions within pipeline. By applying herringbone riblet surfaces many potential boundary layer control applications can be envisaged and hence a framework needs to be devised that integrates flow structure information into herringbone pattern design for targeted velocity flowfield.

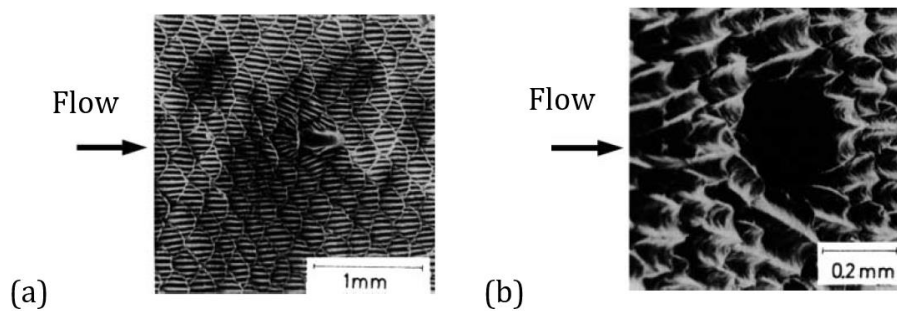


Figure 2.3 (a) Convergent riblet pattern upstream of pit organ (b) Divergent riblet pattern upstream of pores of the lateral-line organ
Flow: left to right

Schoppa & Hussain [37] conducted direct numerical study and demonstrated that by imposing large scale counter rotating streamwise vortices a drastic reduction in turbulent skin friction drag can be achieved. Schoppa & Hussain [38] investigated these riblets induced vortices and further suggested that these riblet surfaces modified near-wall cycle of quasi streamwise vortices and streaks. Although weak, these vortices can yet disrupt near-wall cycle to produce almost 20% skin friction drag reduction. A way needs to be found out to integrate flow information for riblet design.

A parametric study was conducted by Monty *et al.* [39] looking into the effects of converging-diverging yaw angle, viscous scaled riblet height and streamwise development length over the rough surface on higher order statistics. In this study, different viscous scaled riblet dimensions were obtained by varying free stream velocity. 10° and 30° angles were two tested angles. Riblet angle change influenced spanwise variation strength. As angle decreased, so did the strength of spanwise variation in boundary layer. Furthermore, 10° riblet angle observed closest surface spanwise variation. Viscous scaled riblet height (h^+) influence was also observed. It was seen that

with an increase in h^+ , the strength of three dimensionality imposed by the surface roughness increased. This increase was noted in mean velocity profile and turbulent intensity, producing more pronounced boundary layer variation. Furthermore, variation in mean spanwise velocity was observed to increase with h^+ . Additionally, the study documented effect of streamwise fetch for 10° yaw angle with h^+ value varying between 18 and 19. Spanwise mean velocity variation and turbulent intensity was observed to be diminishing with decrease in streamwise fetch. The study, however, was not extended to converging diverging surface design to achieve prescribed velocity flowfield.

Harun *et al.* [40] conducted experimental investigation in which herringbone pattern was implemented on NACA 0026 airfoil as shown in figure 2.4 detail C & D. Hotwire measurements were used to collect turbulence quantities. Drag and flow characteristics were then derived from the measurement along with some higher order turbulent statistics. Herringbone pattern tested had a dimensions of height $h = 1$ mm, spacing $s = 1$ mm. Converging and diverging patterns offered approximately similar skin friction coefficient. However, zero-degree riblet pattern and smooth surface flow offered higher skin friction value of 30% and 70% respectively. Maximum turbulent intensities for converging diverging riblets were observed to be exhibited near the wall. The study overall concluded that converging diverging riblets caused boundary layer to thicken with pronounced turbulence intensity profile peaks. The study can further be extended to airfoil herringbone pattern design for targeted drag characteristics.

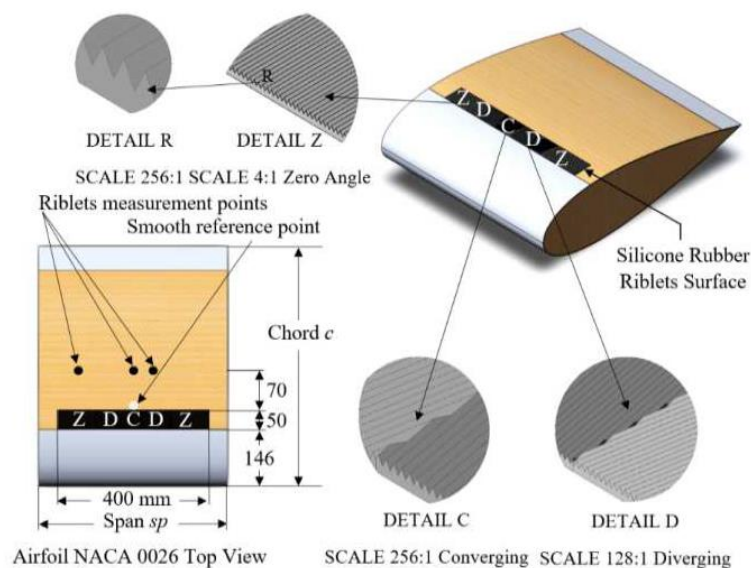


Figure 2.4 Application of Riblet of various dimensions on NACA 0026 airfoil

Flow transition is characterised by Tollmien-Schlichting (TS) wave instability. Herbert [41] observed turbulence transition when TS wave instability amplitude exceeded critical amplitude. Cossu & Brandt [42] conducted numerical study and observed that introducing certain amplitude streaks stabilized TS waves and delayed transition. Fransson *et al.* [43-46] experimentally verified this by generating streaks through cylinder shaped roughness elements. The study can further be extended for cylinder shaped roughness element design for prescribed flow streaks characteristics. Fransson & Talamelli [41] further extended this work by generating stronger streaks with the help of miniature vortex generators. The study can further be extended for miniature vortex generator design for prescribed stronger streaks characteristics.

In another research, functional surface was further exploited to alter heat transfer characteristics. This is predominantly achieved by controlling flow over the surface. Elyyan [47] conducted direct numerical and large-eddy simulations and investigated dimpled fin pitch effect on heat transfer enhancement. The geometry adopted in the study shown in figure 2.5. It was established that in low Reynolds number region, larger fin pitch exhibited higher heat transfer augmentation compared to smaller fin pitch. However, in turbulent region no substantial difference was spotted between the two geometries performances. A correlation was also observed between volume weighted time averaged coherent vorticity with Nusselt number. In a similar study, a minimum effect of dimple imprint diameter on the flow was observed. However, a perforation was introduced inside the dimple and a profound change was found in heat transfer properties. It was observed that perforation in dimple cavity redirected the flow from cavity towards protrusion side of the fin. More mixing was encouraged in the wake of protrusion which aided in heat transfer enhancement. By doing so, the recirculating flow formed inside dimple was reduced. Additionally, this led to more flow being directed towards dimple cavity with an enhancement in vorticity production. Overall, 12-50% increase in heat transfer was recorded at a cost of up to 60% increase in friction expenditure. Another high-fidelity transient calculation was performed on a novel split-dimple interrupted fin structure. Such structure actively disrupted the passively formed thermal boundary layer. Flow impingement and separated shear layer induced by split-dimple surface were identified as contributing factors towards heat transfer enhancement. Although this also led to increase in flow pressure loss, the overall split-dimple fin had 60-175% increase in heat transfer with 4-8 time the friction loss. However,

study lacked framework integrating flowfield information to design dimpled fins for prescribed heat transfer characteristics.

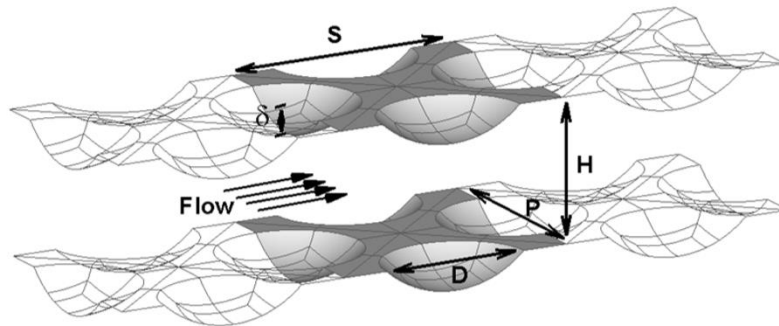


Figure 2.5 Dimpled channel geometry. Channel height (H); Dimple diameter (D); Dimple depth (δ); Dimple pitch (S & P)

Critical Heat Flux (CHF) is a phenomenon that takes place when a vapour layer [48,49] starts to develop in between solid surface and liquid, drastically limiting heat transfer. Previous studies on CHF enhancement focused on surface and fluid property modification [50, 51,52]. The studies pointed out at surface wettability, roughness and porosity as an important factor affecting CHF. Hypothetical explanations were given for these factors such as liquid macrolayers [53,54], hydrodynamic instabilities [55,56] and vapour recoil [57,58,59]. Although these studies were informative, they lacked clear understanding of surface texture effect on CHF. For instance, recent experimental data challenges the existence of the macrolayer, thus questioning empirical macrolayer theory [58]. In another example, hydrodynamic instability formulation of CHF [59] does not account for surface effects present due to roughness. Other parametric studies carried out suggested a monotonic increase in CHF value with surface texture density [60,61,62]. After recent experiments [65-67], surface wetting has been found to be a factor that enhanced CHF. Although the findings were consistent they lacked in a physical mechanism detailing role of liquid imbibition during boiling crisis. In an article published by Varanasi *et al.* [63] an attempt was made to explain this obscure mechanism governing CHF enhancement maxima of industrial boiler with surface texturing. They employed micropillars and nanograss as shown in figure 2.6 for CHF enhancement. It was found that for partially wetting subtract, both micropillars and nanopillars enhanced CHF by small value while decrease in surface-level liquid-solid contact angle. This enhanced gravity induced rewetting of dry spot which was large when only micropillars were employed. A decrease

in micro-texture level liquid-solid contact angle was recorded in the presence of nanopillars on the top of micropillars.

However, no further attempts have been made towards proposing designing micropillar based surface textures framework for prescribed CHF characteristics.

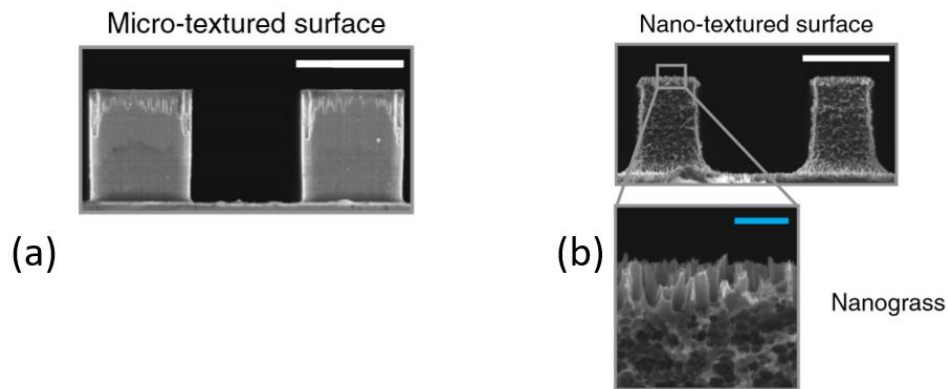


Figure 2.6 Textured surfaces adopted in CHF study (a) Micro pillars (b) Micro pillars covered with nanograss

A direct velocity measurement was taken by Rothstein *et al.* [64] of the flow past drag reducing ultrahydrophobic surfaces. The microridges itched were 20 to 30 μm wide and spaced at 20 to 120 μm apart. An experimental flow cell was used to measure velocity profile across microchannel through microparticle image Velocimetry ($\mu\text{-PIV}$). $\mu\text{-PIV}$ was used to take velocity measurements microridges and air-water interface. A slip velocity greater than 60% of the average velocity were observed along air-water interface while no-slip condition was maintained along microridges. From such observation a direct correlation was concluded between increase in pressure drop reduction and increase in slip velocity along air-water shear free interface. An increase in pressure drop reduction was observed as microridge spacing increased and channel depth decreased. However, study concluded without proposing ultrahydrophobic surface designing framework for prescribed drag characteristics.

Krogstad & Antonia [65] analysed surface roughness effect on turbulent boundary layer. Two distinct surfaces containing two- and three-dimensional surface features respectively were used for analysis. The two surfaces were observed to produce same downward shift of mean velocity profile. The only flow related distinction was observed in higher order flow turbulence statistics. However, the study lacked a framework linking higher order flow turbulence statistics to inverse design surface features. Techhie *et al.*

[66] led a study to investigate effect of wire mesh and sand grain roughness on flow characteristics of open channel flow. Investigation revealed regular wire sand roughness to enhance turbulence characteristics more than sand grain roughness. However, research concluded without using generated turbulence characteristics to inverse design roughness over the surface. Bakken *et al.* [67] compared effects of square bars and perforated plates roughness on the outer layer of the velocity profile. A shift was observed in the velocity profile compared to the plane channel flow. However, this shifted velocity information was not utilised to inverse design surface features. Shah *et al.* [68] investigated two- and three-dimensional roughness on boundary layer. It was found that wire mesh effect confined to buffer region while rib roughness effects extended to the entire boundary layer. However, these flow effects were not utilized to inverse design surface elements. Bond *et al.* Volino *et al.* [69] compared effects of regular 2D and 3D roughness on the turbulence. It was concluded that 3D roughness generated large scale motions of the order of roughness height while due to width of 2D roughness elements generated much larger scales of motions. However, the flow structures generated at different scales were not utilized to inverse design 2D and 3D roughness elements.

2.2. Control valve flow characterisation

Asim *et al.* [70] studied local geometrical effect on globe type valve trim flow capacity. Trim local geometrical features dictated local flow area arrangement that further impacted pressure drop regulation. Investigation started by pressure drop computation within baseline trim. Highest pressure drop was recorded across third row cylinders while lowest across fifth row cylinders. Additionally, pressure drop considerably increased from row one to two while eventually decreasing in subsequent row. This behaviour was attributed to flow area increase and subsequent less resistance when moved from row one cylinders to row five. Further modified trims numerical analysis revealed flow capacity increase with flow area. However, this linear trend was only limited to VOP range from 20-80%. Investigation revealed that trim flow capacity increases with flow area but to a critical limit. Study continued into recovering trim inherent opening characteristics with careful flow area manipulation.

Green *et al.* [71] conducted experimental and numerical study for better understanding complex flow features with globe type control valve. Multi-stage continuous-resistance

trim was used within control valve operating under pressure conditions ranging 2-5bar. Investigation revealed control valve and trim flow coefficients to be flow rate independent. A simplified numerical investigation by Green et al. [72] was carried out on only quarter trim disc and computed trim flow coefficient. A 25% deviation was noted between experimental and numerical values. This deviation was attributed to the trim modelling simplification that was considered, although highly three-dimensional flow presence within valve.

Klas *et al.* [73] numerical study confirmed valve flow three dimensionality. The study investigated failure of 2D numerical modelling based on backflow within the valve section before entering trim. Asim *et al.* [74], Asim *et al.* [75] and Antonio *et al.* [76] studied 3D local flow behaviour within control valve using numerical approach. Although previous studies suggested flow coefficient independence of installed multi-stage continuous-resistance trim and control valve from flow rate, this numerical study revealed solo dependence on valve opening conditions [74]. Asim *et al.* [75] undertook critical local flow analysis and found significant flow field variations within trim. Investigation revealed that local static pressure in the area between cylinders (flow paths) may drop below vapour pressure subjecting trim to cavitation. Antonio *et al.* [76] also reported flow non-uniformity in trim radial direction. Furthermore, this complex flow behaviour was also observed in different trim discs. The included studies although provided detailed local flowfield view within trim, no further attempt was made to embed local flowfield information within control valve design process.

Wang *et al.* [77] computed detailed flow structures within bell-shaped control valves during numerical investigations. The study revealed control valve flow bifurcation into two separate flow regimes. These regimes were found to be significantly affected by control valve pressure and opening positions. Coanda effect was reported as the primary reason for flow behaviour change. Study gave qualitative local flow behaviour analysis however lacked quantification. Furthermore, the local flow information was not implemented for control valve design. Qiu *et al.* [78] numerically investigated internal cavitation behaviour as a function of control valve spindle speed. Study revealed decreased cavitation with an increase in spindle speed. The decrease was attributed to an increased mass flow rate through valve. Although useful information, research lacked its further exploitation for better operational and design control.

Local geometrical features were seen to alter local flow behaviour within multi-stage continuous-resistance trim. Charlton *et al.* [79], manufactured and conducted parametric study for ridged, arced, wavy and tear-drop shaped concept flow path designs. The configurations were numerically analysed and were shown to greatly influence trim performance. The influence was found to be exerted by increased flow path area that generally increased trim flow coefficient and vice versa. However, no major improvement was observed for tear-drop shaped flow path in comparison to like-to-like designs. Furthermore, investigation outcome was not embedded within trim design for improvement.

Lisowski & Filo [80] characterised hydrodynamic behaviour for different valve spool geometries. Characterisation was carried out numerically for Reynolds number in range of 300-2500. Investigation revealed global impact by local flowfield manipulation. Valve operating range increased by 40% due to triangular opening designs. The 2 notches design modification altered and reduced spool radial forces by 102%. However, this design modification knowledge has not been integrated within existing control valve design practices.

Kong *et al.* [81] analysed control valve hydrodynamic characteristics by internal flowfield decomposition. Flow rates ranging 20-250 l/min were investigated using Proper Orthogonal Decomposition (POD). The study reconstructed valve local flowfield using 10 energy modes with 5% accuracy. These 10 modes represented dominant flow structures with total energy contain of 99.53%. Investigation presented important findings. However, these findings were not utilized further for control valve design.

Failure mode is defined as the way an equipment can potentially fail. Dominant failure modes within a control valve could be related to operational speed, localised leakage, vibration etc. Cavitation induced erosion is a potential danger to the service life of the control valve. Cavitation is defined as the phenomenon of vapour bubble formation when the fluid pressure falls below the vapour pressure. The collapse of bubble can result in unbearable noise and vibration [82] that can lead to equipment failure. However, the most prominent effect of the cavitation bubble collapse near control valve solid wall can lead to localised internal erosion [83,84] as shown in figure 2.7[85] for control valve stem.

Early non-detection of the degree of erosion damage can severely compromise control valve structural integrity, eventually leading to the failure.



Figure 2.7 Cavitation induced damage to the control valve guide plug [85]

2.3. Inverse Design Methodologies

Traditional inverse design methodologies are mostly developed for airfoil design with a focus on optimisation. Lighthill [86] proposed a pioneering work for 2D aerodynamic design using conformal mapping. MacFadden [87] further extended this work to compressible flows. Hicks and Hanne [88] attempted to solve airfoil design problem. The study solved the problem as constrained optimisation that evaluated derivative sensitivity by introducing finite difference method. This further introduced gradient based methods for constrained aerodynamic design. Jameson [89] computed gradient information using adjoint approach. Legresley & Alonso [90], however, used computational cost-effective Proper Orthogonal Decomposition (POD) technique for airfoil design optimisation.

Gappy POD was developed by Everson and Sirovich [91] as an extension of basic POD method to handle incomplete data sets. Everson et al. successfully applied this method for human face image reconstruction from partial data set. Wilcox *et al.* [92] applied Gappy POD to reconstruct missing aerodynamic data and for inverse design problem. For missing aerodynamic data, a steady state pressure solution around NACA 0012 airfoil at a freestream Mach number of 0.8 was considered. 26 snapshots were collected at different angles of attack ranging from 0 degree to 1.25 degree uniformly spaced at an interval of 0.05 deg. Around 1/3rd of the pressure data was randomly discarded from this snapshot database to make it incomplete. Missing data was iteratively obtained using

Gappy POD. Iterative process was stopped after 50 iterations. Error between original and repaired data kept on decreasing with iterations. Furthermore, spatial frequency flow structures and amount of missing data present in snapshots influenced convergence. Conclusion was drawn that more energetic a POD mode, faster is its rate of convergence. Eigenvalue spectrum observed that two modes capturing 90.65% energy required only two convergence iterations while subsequent two modes capturing 7.7% and 1.4% of energy required 31 and 50 convergence iterations, respectively. This trend was attributed to the fact that higher modes correspond to higher spatial frequency. Gappy POD was further applied to obtain optimal airfoil shape producing a given target pressure distribution. The target pressure distribution specified was that for Korn airfoil. 63 different airfoil snapshots were obtained by perturbing RAE 2822 airfoil as shown in figure 2.8. At zero angle of attack and 0.5 freestream Mach number, CFD based flow solution ensemble was computed for each airfoil. It was observed that as number of modes increased, Gappy POD yielded predicted shape and its corresponding pressure distribution closer to the exact solutions with an increase in number of modes.

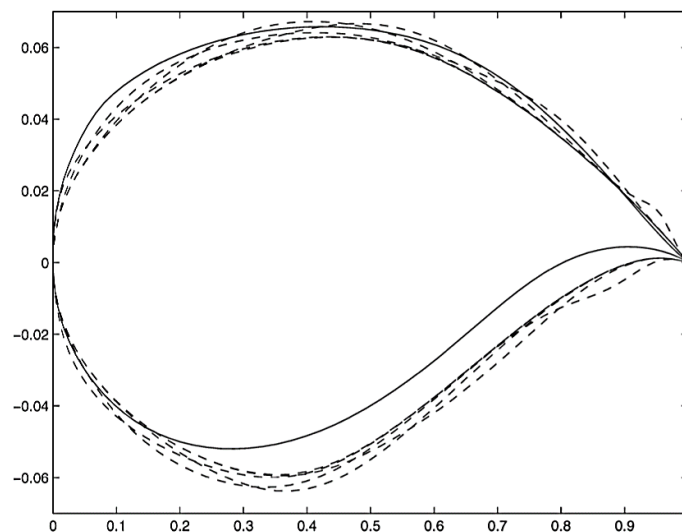


Figure 2.8 Parametrised airfoil based on RAE 2822 and the Korn airfoil used in inverse design process

Zhang *et al.* [93] carried Gappy POD based centrifugal pump impeller inverse design. A target blade load distribution was specified and corresponding objective blade shape was computed. Initial blade shape was parameterized and geometry variations were obtained by control point perturbation. A snapshot ensemble containing perturbed geometries

and corresponding flow solutions was developed. The blade shape parameters data missing in the vector of objective blade. POD basis was subsequently computed from the flow ensemble and were used to repair missing snapshot data. Study introduced iterative correction method for convergence improvement. Snapshot ensemble was renewed at every iteration by simulating inner flow of renewed blade and replenishing it to the ensemble. Inverse design was computed in 2D and 3D space. For 2D pressure was observed to be converge to objective pressure within two iterations. Furthermore, error between objective and computed blade shape was observed to be limited to 4%. A deviation of around 3.5% and 5.0% for pump head and efficiency respectively was observed. For 3D, head and efficiency were observed to be limited within 6% and 3.5% respectively. However, Gappy POD based inverse design process have not been applied for control valve design.

Murray & Lawrence [94] applied Gappy POD methodology for subsonic cavity flow PIV data. The missing field vectors within PIV data were estimated by repeated iterative procedure. POD modes of the obtained were updated during each iteration until a stipulated convergence criterion. Effect of number of modes on to the obtained results were observed. In a similar attempt, Xu & Tsering-xiao [95] applied Gappy POD to reconstruct temperature field data in Tibet. Study compared two data reconstruction methodologies and found Gappy POD to outperform the other when missing spatial data amount is not severe. Carlberg & Stephan [96] applied Gappy POD to reconstruct archaeology data. The data focused on Roman housing on the sites of Pompeii and Herculaneum. Housing characteristics were reconstructed and studied using Gappy POD. Wilcox [97] applied Gappy POD to handle unsteady flow reconstruction problem. The method was also extended to formulate effective sensor placement strategy utilizing condition number criterion for limited flow measurement data. The study showed effective flow reconstruction accuracy using dominant POD flow modes and limited number of sensors. Raben *et al.* [98] modified Gappy POD by developing locally adaptive criterion to compute optimum number of modes for reconstruction process. The study showed that newly developed adaptive Gappy POD data reconstruction method provides higher accuracy and robustness. Saini *et al.* [99] developed and evaluated Gappy POD for noisy PIV data obtained from gas turbine combustors. Median filter outlier detection technique was used along with Gappy POD to test reconstruction effectiveness. It was

found that medium filter when coupled with Gappy POD produces an effective method for filling missing PIV data of gas turbine combustor flows.

As discussed previously, literature records two traditional Aerodynamic Shape Optimization (ASO) approaches: local and global methods. Local method is most common method in ASO framework [100,101,102] and utilizes design space local gradient for search direction in design space. Convergence during optimisation process is achieved while local gradient value through design space becomes very small. However, within global optimisation algorithms the candidate solutions that are scattered in design space, cooperate to locate global optimum solution. To determine global optimum solution among candidate pool, objective function is evaluated on each candidate solution. This decreases computational efficiency of global search algorithm. However, global search algorithms have a primary advantage of not converging over local optimum which is a possibility in local search algorithm.

Gappy POD approach for inverse design is fast and efficient compared to traditional optimisation approaches. This is predominantly due to bypassing gradient evaluation that is typically encountered within traditional optimisation approaches. Furthermore, gradient sensitivity becomes an important issue in traditional optimisation approach. Moreover, traditional optimisation approaches are computationally inefficient to adopt for complex engineering optimisation problems. Gappy POD surpasses these limitations by being computationally efficient and easily adoptable framework. It further facilitates integrating computational and experimental data into design process.

2.4. Summary

The presented literature review highlighted some of the functional surface flow characterisation. The functional surface review described the experimental and numerical work that has been carried out. Most of these functional surfaces were found to be bio-inspired, producing certain flow effects. Surface made out of riblets were observed to perform specific function of drag reduction while surface containing dimples and protrusions modified heat transfer characteristics. Small scale herringbone riblets were observed to heavily disrupt 3D boundary layer by producing counter-clockwise

vortices. Surface texture within industrial boilers were observed to play important role in modifying Critical Heat Flux characteristics.

Furthermore, the review also presented current standing in the research of multistage continuous resistance trim. Review discussed flow behaviour understanding within trim using numerical and experimental techniques. Primarily, flow behaviour was observed to be three dimensions within the trim. Consequently, it can be envisaged that local flow capacity for individual trim discs varies. Review focused on local geometrical effect on trim local flow capacities. Review also discussed modal analysis as applied to the control valve hydrodynamic characteristics.

Moreover, review on inverse design methodologies was conducted. Specifically, the review focused on Gappy POD as applied to various problems. Review discussed Gappy POD origin along with its diverse applications applied to aerodynamics, hydrodynamics, Geospatial and archaeology. Limitations of current Aerodynamic Shape Optimization approaches were highlighted along with Gappy POD advantages. Based on literature review, a limited research can be seen to have carried out to inverse design functional surfaces for prescribed simple local flow characteristics. As established in chapter 1, multistage continuous resistance trim individual disc can be treated as individual functional surfaces. Based on literature review conducted, it can be seen that no study was published outlining trim inverse design for prescribed trim complex local flow characteristics.

2.5. Research Aims

The specific research aims formulated for this research study are described in this section, whereas the detailed objectives are discussed after carrying out the literature review. The research aims of the current study are:

1. Establishing inverse design environment for functional surfaces containing simple discontinuous geometry structure for prescribed simple flow characteristics.
2. Developing inverse design framework for functional surfaces containing simple discontinuous geometry structure for prescribed complex flow characteristics.

2.6. Research Objectives

Based on the literature review and the research aims, following research objectives have been identified:

- Developing functional form of velocity field with qualitative and quantitative control points spatial description for various design changes.
- Identifying governing flow structures and flow sensing positions for functional surface.
- Investigating Gappy POD sensitivity for prescribed control point or friction factor distribution and identifying particular number of modes operated functional surface design subspace.
- Developing regression-based model relating local flow capacity with local geometrical features for qualitative and quantitative description.
- Identifying governing flow structures and flow sensing positions for multistage continuous resistance trim.
- Investigating trim ensemble sparsity and developing novel optimised modal selection criteria.

The next chapter presents the details of the numerical solver used in the present study in order to achieve the above objectives.

CHAPTER 3

NUMERICAL MODELLING APPLIED TO FUNCTIONAL SURFACES AND SEVERE SERVICE CONTROL VALVE

This chapter outlines the methodologies that are employed in investigation. Chapter is divided into three sections: Lattice Boltzmann Method (LBM), Computational Fluid Dynamics (CFD) and Gappy Proper Orthogonal Decomposition (POD). The first two methodologies are numerical methods that are predominantly employed for data generation of an engineering system. Gappy POD is an algorithmic process that is employed to further exploit the dataset created by first two methodology. LBM section describes the application of methodology for testing functional surfaces within channel flow setting. Flow characteristics within control valve trim are computed using CFD methodology. The chapter ends with describing Gappy POD algorithm and its integration into inverse design process.

3.1. Numerical simulations by Lattice Boltzmann method

Surface feature influence on flow characteristics was investigated by Lattice Boltzmann method. This mesoscopic approach is based on Boltzmann equation velocity space discretisation where velocities are represented by microscopic velocities. The approach has an advantage of bypassing conventional discretisation methodology of solving Navier-Stokes partial differential equations. This expedites computational process. Furthermore, the approach has an added advantage of parallelisation and is easy to programme with a capability of further integration into wider framework. Additionally, Navier-Stokes equations can be computed from Lattice Boltzmann equation using multiscale analysis [103].

Ludwig Boltzmann is credited with one of the founders of statistical mechanics and on developing kinetic theory of gases. Statistical approach predicts gas behaviour on macroscopic scale by using microscopic particle properties. Particle probabilities rather than statistical analysis of all particles are considered to formulate Boltzmann equation as:

$$\left(\frac{\delta f}{\delta t}\right) = \frac{\delta f}{\delta t}\Big|_{\text{collision}} + \frac{\delta f}{\delta t}\Big|_{\text{force}} + \frac{\delta f}{\delta t}\Big|_{\text{diffusion}} \quad (3.1)$$

Here, $f = f(\vec{x}, \vec{v}, t)$ is particle density function that depends on position \vec{x} , velocity \vec{v} and time t . Collision term accounts for internal particle-particle interaction while force term represents external forces. Diffusion term can further be evaluated as:

$$\left(\frac{\delta f}{\delta t}\right) = \frac{\delta f}{\delta t}\Big|_{\text{collision}} + \frac{\delta f}{\delta t}\Big|_{\text{force}} + \xi \cdot \left(\frac{\delta f}{\delta \vec{x}}\right) \quad (3.2)$$

ξ is the macroscopic (average) particle velocity. While defining ξ and neglecting external forces, the equation can be rearranged as follows:

$$\left(\frac{\delta f}{\delta t}\right) + \xi \cdot \left(\frac{\delta f}{\delta \vec{x}}\right) = \frac{\delta f}{\delta t}\Big|_{\text{collision}} \quad (3.3)$$

Collision term is a nonlinear integral differential equation. An approximation was published in 1954 as an approximation for small Mach number [103], introducing single relaxation time τ and equilibrium distribution function $f^{(0)}$:

$$\left(\frac{\delta f}{\delta t}\right) + \xi \cdot \left(\frac{\delta f}{\delta \vec{x}}\right) = -\frac{1}{\tau} [f - f^{(0)}] \quad (3.4)$$

The flow dynamics evolves as particle density f across lattice changes following two steps process of relaxation and streaming. Relaxation is towards local Maxwellian equilibrium distribution that captures molecular collision effect. Streaming is the process in which particle density values move along associated microscopic velocities to the neighbouring node. Equation 3.4 is discretised over velocity space and time into a finite number of velocities \vec{e}_i :

$$\left(\frac{\delta f_i}{\delta t}\right) + \xi \cdot \left(\frac{\delta f_i}{\delta \vec{x}}\right) = -\frac{1}{\tau} [f_i - f_i^{(0)}] \quad (3.5)$$

Term on the right side of above equation denotes Bhatnagar-Gross-Krook (BGK) collision operator, with a relaxation towards local equilibrium while left side describes streaming operator. Local Maxwellian equilibrium function approximation can be computed by using Taylor series expansion and choosing proper lattice model [104] as:

$$f_i^{(0)} = \rho \cdot w_i \cdot \left[1 + 3 \cdot (\vec{e}_i \cdot \vec{u}) + \frac{9}{2} \cdot (\vec{e}_i \cdot \vec{u})^2 - \frac{3}{2} \cdot u^2\right] \quad (3.6)$$

Macroscopic mass density ρ is computed by summing particle distributions f_i . Similarly, macroscopic velocity \vec{u} is computed by summing all particle densities going in specific direction and subtracting particle densities going in opposite direction. The results are further normalised using mass density. The following equations show density and momentum computation from particle densities:

$$\rho = \sum_{i=0}^{18} f_i \quad \text{and} \quad \rho \vec{u} = \sum_{i=0}^{18} f_i \vec{e}_i \quad (3.7)$$

It should be noted that collision and streaming operations can be implemented independently specifically for solid boundaries [105]. The weighting factor w_i depends on choosing lattice model and velocity direction i .

Lattice Boltzmann models are denoted by $D_m Q_n$, in which m denotes number of dimensions and n denotes number of discrete velocities. As an example, for two and three-dimensional, figure 3.1 shows the models. Circles denotes directional probability densities f_i . Every structure represents single lattice cell with centre point marked as zero. Lattice Boltzmann algorithm can be implemented with lattice specific values such as discrete velocities e_i (as shown in equations 3.8 and 3.10) and weight w_i (as shown in equations 3.9 and 3.11). Discrete velocities are given in lattice units and defined by vector of size m for each n velocities, Weights are computed from the momentums [104]. The lattice chosen for this study is D3Q9.

Figure 3.2 shows the flow domain that was used for functional surface fluid flow computation. Flow enters flow domain from inlet along positive X direction while exit flow domain from outlet. Top and bottom side of the domain is considered wall where no-slip boundary condition is imposed. No-slip boundary condition is implemented using bounce-back boundary condition. Discontinuous geometry structures can also be seen on the bottom wall with imposed no-slip boundary condition. Periodic boundary conditions are imposed in X and Z direction. Flow is 100 times gravity driven along X axis over discontinuous geometry structures.

No-slip boundary condition is implemented using bounce-back boundary condition. For this boundary condition, domain leaving microscopic particle densities are reflected back unchanged. The boundary nodes are not considered fluid domain part as boundary is considered to be located halfway between neighbouring fluid node and boundary nodes. Zou and He [107][108] implemented bounce-back boundary conditions and solved for unknown particle densities. Zou and He boundary condition are considered simplistic to implement even for complex geometries.

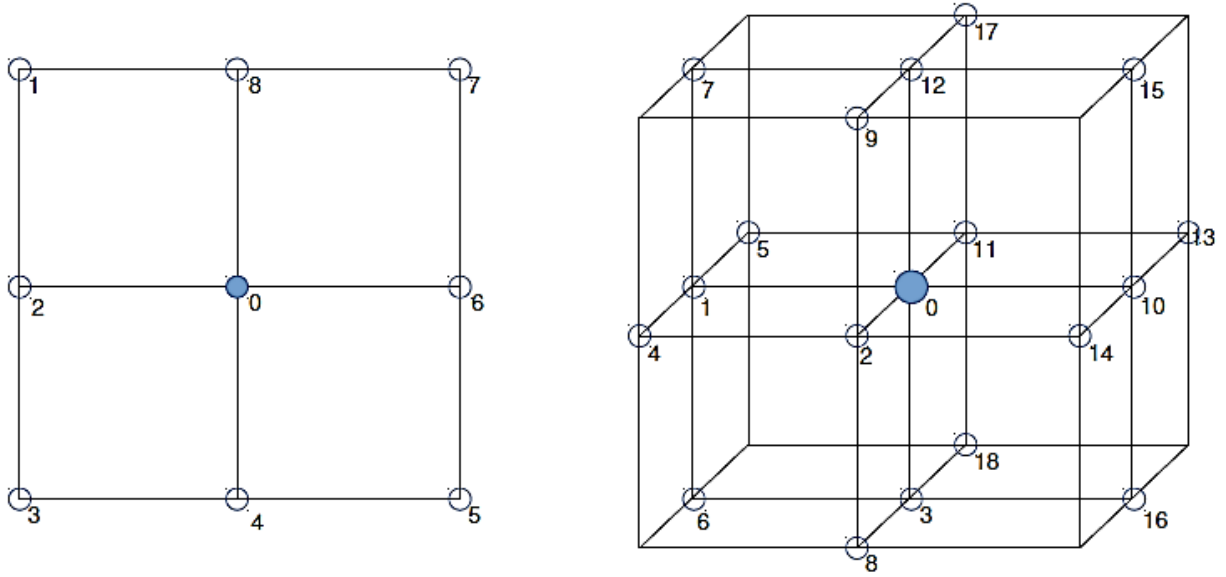


Figure 3.1: D2Q9 and D3Q19 models

The solutions for discrete velocities for D2Q9 and D3Q19 are shows below:

$$e_{i,D2Q9} = \begin{cases} (0,0), & i = 0 \\ (\pm 1,0), & i = 2,6, \\ (0,\pm 1), & i = 4,8, \\ (\pm 1,\pm 1), & i = 1,3,5,7 \end{cases} \quad (3.8)$$

$$w_{i,D2Q9} = \begin{cases} \frac{4}{9}, & i = 0 \\ \frac{1}{9}, & i = 2,4,6,8 \\ \frac{1}{36}, & i = 1,3,5,7 \end{cases} \quad (3.9)$$

$$e_{i,D3Q19} = \begin{cases} (0,0,0) & i = 0, \\ (\pm 1,0,0) & i = 1,10, \\ (0,\pm 1,0) & i = 2,11, \\ (0,0,\pm 1) & i = 3,12, \\ (\pm 1,\pm 1,0) & i = 4,5,13,14, \\ (\pm 1,0,\pm 1) & i = 6,7,15,16, \\ (0,\pm 1,\pm 1) & i = 8,9,17,18 \end{cases} \quad (3.10)$$

$$w_{i,D3Q19} = \begin{cases} \frac{1}{3}, & i = 0 \\ \frac{1}{18}, & i = 1 \dots 3,10 \dots 12, \\ \frac{1}{36}, & i = 4 \dots 9,13 \dots 18 \end{cases} \quad (3.11)$$

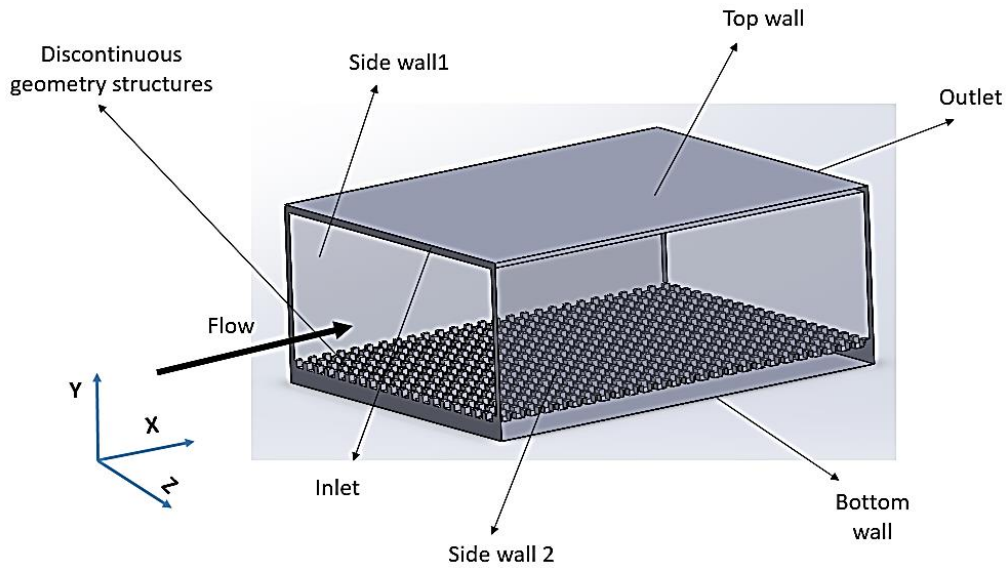


Figure 3.2: Flow domain

Dimensionless relaxation time used for simulations is $\tau = 0.500546$. The lattice spacing $dx = 1 \times 10^{-5} \text{m}$ and time step as $dt = 3 \times 10^{-9} \text{s}$ produced conditions for airflow simulations over discontinuous geometry elements. Numerical simulation was validated using standard Poiseuille flow velocity profile computed in plane channel flow as shown in Figure 3.3.

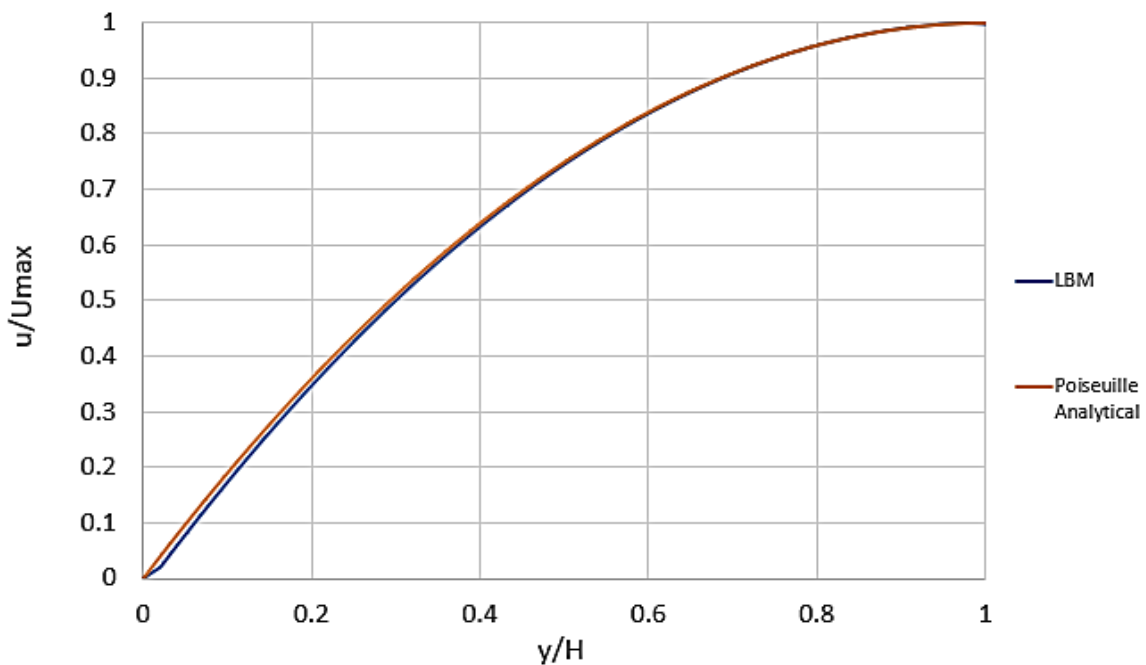


Figure 3.3: Plane channel flow velocity profile

Figure 3.3 shows velocity profile comparison between LBM computed and analytical Poiseuille equation. Poiseuille flow analytical equation for plane channel flow is given as follows [109]:

$$\frac{u}{U_{\max}} = 1 - \left\{ \left(1 - \frac{y}{H} \right) \times \left(1 - \frac{y}{H} \right) \right\} \quad (3.12)$$

H is the channel half height and U_{\max} is channel centreline velocity. The wall normal distance is measured from channel wall towards the centreline. The profile for LBM is measured at channel centre. A good agreement can be seen between two profiles. However, a small deviation can be noted in the velocities recorded near the wall. This is due to bounce back boundary condition implementation being of first order while LBM scheme being of second order.

3.2. Computational Fluid Dynamics (CFD) Model for Severe Service Control Valve Trim

Multistage continuous resistance trim is considered for this study as shown in Figure 1.6. This trim consists of 11 discs, with individual disc consisting 5 rows of cylinders. Fluid flows from outmost cylinder rows to innermost cylinder rows. Cylinder diameter in particular row is constant. However, as fluid travels towards innermost cylinder row, cylinder diameter decreases. This offers flow area expansion.

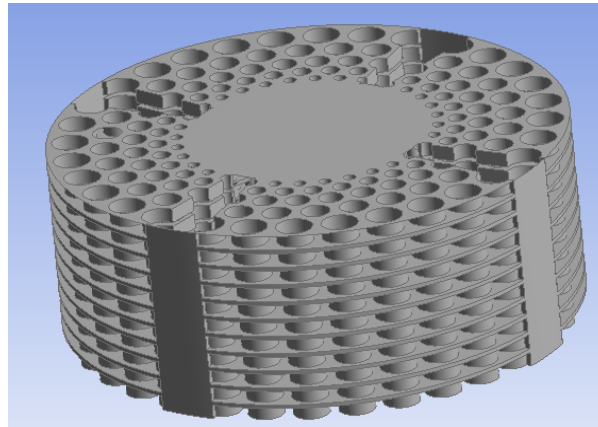


Figure 3.4: Multistage continuous resistance trim

Figure 3.4 shows three-dimensional CAD model of considered multistage continuous resistance trim. Figure 3.5(a) shows the mesh in main control valve body and figure 3.5(b) shows mesh in trim section. The fluid used for control valve numerical simulation is water. The density

specified for the simulation is 998.2 kg/m^3 while the viscosity specified is $0.001003 \text{ kg/m-sec}$. Valve and trim have been meshed with tetrahedral elements. Inlet outlet pipe sections have been meshed with hexahedral elements.

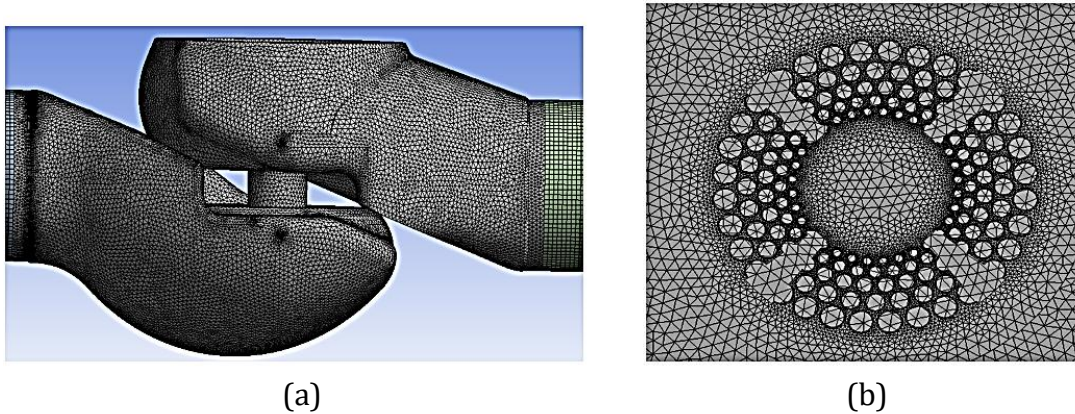


Figure 3.5: Meshing (a) Control valve (b) trim

The mesh is adopted from the study carried out by Asim *et al.* [110]. The minimum mesh size used in this study is 0.35 mm while maximum size used is 3 mm . As a result, 5.3 million mesh elements were formed within control valve and the trim. Tetrahedral elements are adopted for complex flow paths within trim geometry while hexahedral mesh is used for relatively simplified regions of outer and inner pipes. These mesh choices were further influenced by the fact that hexahedral mesh is commonly adopted for symmetric flows while tetrahedral elements for highly complex flows [111]. Near-wall region is equipped with additional hexahedral elements, specifically around the flow paths between the trim cylinders. Mesh independence testing is carried out on control valve using 3.4, 4.3 and 6.5 million mesh elements. Inlet pressure was monitored for these mesh elements. The inlet pressure trend was observed to be same for all mesh elements. Based on Grid Convergence Index (GCI) values, it was concluded that 5.3 million mesh elements were considered for flow prediction capabilities. For further information on mesh and mesh independence study refer to Asim *et al.* [110].

Inlet boundary condition specified for this simulation is 12.51 kg/s . In this study only one mass flow condition is considered. Trim flow capacity is found to be independent of passing flow rate. The Reynolds number obtained due to high flow rate is $1.5\text{E}05$. This indicated the flow in turbulent region. Asim *et al.* [110] chose the flow rate based on the recommendations stated in BS EN 60534-2. Furthermore, the chosen mass flow rate was used for experimental validation.

Pressure outlet boundary condition was used at the outlet of the control valve with a value of atmospheric pressure. A 5% turbulent intensity was added both to inlet and outlet of the valve. No-slip boundary condition was specified on the wall. Following Table 3.1 summarizes the boundary conditions used by Asim *et al.* [110] for simulation.

Table 3.1: Boundary conditions

Boundary	Type	Value
Inlet	Mass flow rate	12.51 kg/s
Outlet	Pressure	Atmospheric pressure (gauge=0 kPa)
Walls	Stationary Walls	No-slip

Solver setting and turbulence modelling it taken from the study conducted by Asim *et al.* [110]. Three-dimensional momentum and continuity equations are iteratively solved for water flow within the valve. Trim has complex flow path structure and experiences severe velocity gradients. This narrows down the choice of turbulence model to two equations shear stress transport (SST) k-w turbulent model. SST k-w not only include near wall blending function but also has modified turbulent viscosity modified to accommodate turbulent shear stress transport. Additional details on SST k-w can be found in literature[112]. In addition to Reynolds Average Navier-Stokes equations (RANS), the SST k-w model equation is also solved. A steady state solution was computed for control valve flow by discretising RANS equations. Semi Implicit Method for Pressure Linked Equations (SIMPLE) algorithm was employed for pressure-velocity coupling. Green gauss node based spatial gradient discretisation was employed. Momentum and turbulent gradients were evaluated using 2nd order upwind scheme. Inlet static pressure convergence was monitored during iterative process. Based on inlet pressure variations, 2500 iterations were established for computing final solutions. For further detail refer to Asim *et al.* [110].

The flow inside control valve, specifically within trim, is an interplay between pressure differential and wall shear stress. To effectively capture this process, the near-wall boundary layer is equipped with more mesh layers as mentioned earlier. The model has been validated with laboratory readings, details of which can be found Asim *et al.* [110]. Laboratory

experiment ranged from 375kPa at 10% VOP to 341.3kPa at 100% VOP. A no-slip boundary conditions has been applied on all the walls.

3.3. Proper Orthogonal Decomposition (POD)

This section describes the basic POD procedure. Optimum POD modes are chosen to maximize the cost [113]:

$$\max_{\Psi} \frac{\langle |(\mathbf{g}, \Psi)^2| \rangle}{(\Psi, \Psi)} = \frac{\langle |(\mathbf{g}, \Phi)^2| \rangle}{(\Phi, \Phi)} \quad (3.13)$$

(\mathbf{g}, Φ) is the inner product between eigenfunction Φ and the field $\mathbf{g}(\mathbf{x}, \mathbf{t})$, \mathbf{x} represents spatial coordinates, \mathbf{t} is the time. POD modes can be seen to be eigenfunctions of the kernel \mathbf{K} :

$$\mathbf{K}(\mathbf{x}, \mathbf{x}') = \langle \mathbf{g}(\mathbf{x}, \mathbf{t}), \mathbf{g}^*(\mathbf{x}', \mathbf{t}) \rangle \quad (3.14)$$

Here \mathbf{g}^* is the Hermitian of \mathbf{g} . Sirovich [114] introduced a method of snapshots as a way for determining eigenfunctions Φ without computing the kernel \mathbf{K} . It can be shown that for an ensemble of instantaneous field snapshots, eigenfunctions of \mathbf{K} can be linear combination of snapshots as follows:

$$\Phi = \sum_{i=1}^m \beta_i \mathbf{g}^i \quad (3.15)$$

Here \mathbf{U}^i is the computed solution at each point within computational grid for different time instances. It can be shown that coefficient β_i satisfy eigenvalue problem:

$$\mathbf{R}\beta = \Lambda\beta \quad (3.16)$$

Here \mathbf{R} is the auto-correlation matrix and the elements are given as:

$$R_{ik} = \left(\frac{1}{m} \right) (\mathbf{g}^i, \mathbf{g}^k) \quad (3.17)$$

Eigenfunctions of \mathbf{R} determines the POD modes while eigenvalues of \mathbf{R} show the importance of modes. The relative energy capture by ith POD mode is hence given by:

$$\frac{\lambda_i}{\sum_{j=1}^m \lambda_j} \quad (3.18)$$

Approximated representation of field \mathbf{g} can then be computed as:

$$\tilde{\mathbf{g}} \approx \sum_{i=1}^p \alpha_i \Phi^i \quad (3.19)$$

Here p is chosen such that $p \ll m$ and captures the desired energy level, Φ^i is the i^{th} POD mode and α_i are the respective time dependant POD coefficients.

Minimising approximation error \mathbf{E} :

$$\mathbf{E} = \int [\mathbf{g} - \sum_{i=1}^p \alpha_i \Phi^i]^2 dx \quad (3.20)$$

As a result of above minimisation, elements of Hermitian matrix can be expressed as modal inner product:

$$(\Phi^i, \Phi^j) = \delta_{ij} \text{ for } i = j \quad (3.21)$$

$$(\Phi^i, \Phi^j) = 0 \text{ for } i \neq j \quad (3.22)$$

δ_{ij} is the Kroenecker delta function. The above modal inner product relationship is valid for orthogonal modes with all known elements within respective modes. It also indicates Hermitian as an identity matrix. Furthermore, minimizing error also yields additional vector whose elements are computed by taking inner product between the field and the mode:

$$(\mathbf{g}, \Phi^i) \quad (3.23)$$

Hermitian matrix and the additionally computed vector are further utilised to form linear system of equations for computing POD modal coefficients. In short, full state field \mathbf{g} can be projected on to the relevant modes for computing POD modal coefficients.

$$\mathbf{M}\mathbf{b} = \mathbf{f} \quad (3.24)$$

Where $M_{ij} = (\Phi^i, \Phi^j)$ are elements in Hermitian matrix and $f_i = (\mathbf{g}, \Phi^i)$. Solving this equation yields POD modal coefficients. The POD methodology outlined above considers time dependant flows for which series of flow solutions are computed at different time instants. Epureanu et al. [115] applied the methodology in parameter space i.e. obtaining parameter dependent flow solutions.

3.4. Gappy Proper Orthogonal Decomposition

In basic POD procedure, it should be recalled that snapshot field \mathbf{g} defined full system state at grid points. Everson and Sirovich [91] modified basic POD method and developed a novel approach to handle “gappy” data set. Gappy data set is defined as when full system state is unknown or only sparse system measurements are present. This creates a challenge to fill these gaps and construct full system state.

Mathematically, gappy data set change is reflected in error minimization formulation as:

$$\mathbf{E} = \int_{\mathbf{n}} \left[\mathbf{g} - \sum_{i=1}^p \alpha_i \Phi^i \right]^2 d\mathbf{x} \quad (3.25)$$

Since the system state is defined on sparse grid points, error is minimised over support space \mathbf{n} . Support space \mathbf{n} can hence be defined as the sparse region where value for system state is known. For example, if 40% data is missing in snapshot field \mathbf{g} , grid points over which remaining 60% data is present can be defined as the support space.

It should be noted that sparsity gives limited system information, while inner product computation requires full system state information as pointed out in basic POD methodology. In short, modal orthogonality should be considered over full system state rather than partially known system state. Modal orthogonality relation to construct Hermitian matrix thus changes to:

$$(\Phi^i, \Phi^j)_{\mathbf{n}} \neq \mathbf{1} \quad \text{for } i = j \quad (3.26)$$

$$(\Phi^i, \Phi^j)_{\mathbf{n}} \neq \mathbf{0} \quad \text{for } i \neq j \quad (3.27)$$

It can be noted that Hermitian computed from above relations does not yield identity matrix. On the contrary, it yields non-zero off-diagonal elements and non-unity elements in diagonal. This is a direct result of orthogonality loss within support space \mathbf{n} . Similarly, minimizing error yields additional vector whose elements are now computed by taking inner product between the field and the mode in support space:

$$(\mathbf{g}, \Phi^i)_{\mathbf{n}} \quad (3.28)$$

As mentioned earlier, POD modal coefficient can be computed using following equation:

$$\mathbf{M}\mathbf{b} = \mathbf{f} \quad (3.29)$$

Where $M_{ij} = (\Phi^i, \Phi^j)_n$ are elements in Hermitian matrix and $f_i = (\mathbf{g}, \Phi^i)_n$. Solving the equation yields POD modal coefficients. For gappy data, POD modal coefficients can be computed by projecting full state field \mathbf{g} on \mathbf{n} . It can be inferred that with decrease in sparsity, modes might align themselves to become orthogonal i.e. Hermitian tend towards identity matrix. Additionally, Gappy modal coefficients tend towards basic POD modal coefficients.

3.5. Gappy POD based Inverse Design

Wilcox et. al applied Gappy POD based airfoil inverse design. This section describes Gappy POD adoption for functional surface inverse design. Figure 3.6 shows the flow chart for the algorithm. In the beginning, damaged snapshot matrix and the corresponding mask matrix is prepared. Damaged snapshot matrix contains Gappy data. Elements within mask matrix is defined either 1 or 0 corresponding to if data is present or absent within damaged snapshot matrix. Furthermore, gappy data within damaged snapshot matrix is replaced with average value of that row. It should also be noted that snapshot matrix is augmented. For example, each column vector within snapshot matrix can be represented as follows:

$$\mathbf{g}^i = \begin{bmatrix} \mathbf{c}^i \\ \mathbf{p}^i \end{bmatrix} \quad (3.30)$$

Here, \mathbf{g}^i is the i^{th} augmented snapshot that not only contain pressure \mathbf{P}^i but also the corresponding coordinates on which pressure is measured. Further flow field information can also be included if desired within augmented snapshot set. Table 3.2 shows the structure of augmented snapshot matrix used in subsequent chapters. For chapter 4, velocity control point snapshot is augmented with corresponding geometrical design parameter. Similarly, frictional factor snapshot is augmented with corresponding geometrical design parameter. In chapter 5 local flow capacity snapshot is augmented with corresponding geometrical design parameter.

Equation 3.31 shows the matrix structure that is adopted in chapter 4 for functional surface inverse design. Individual columns in matrix consist of nine augmented snapshots. First two elements in augmented snapshot consists geometrical parameter while the rest of snapshot

elements consists flow characteristics 'm' distribution over 2300 grid points. Flow characteristics 'm' considered are velocity control point and friction factor distribution. Equation 3.32 shows the adopted matrix structure in chapter 5 for multistage continuous resistance trim inverse design. Individual columns in matrix consist of 100 augmented snapshots. First five elements in augmented snapshot consists geometrical parameters while the next five snapshot elements contain flow characteristics over five rows of cylinder. Flow characteristics considered are local flow capacity distribution within multistage continuous resistance trim top disc.

Figure 3.6 shows the Gappy POD algorithm. Algorithm starts by inputting damaged augmented snapshot matrix. Masking and averaging operations yield new snapshot matrix **h**. This newly defined matrix is then iterated and Gappy operations are performed. Loop starts by computing POD modes for **h**. The modes are deployed for Gappy operations and inner product evaluation. Computed values from Gappy operations are employed to evaluate modal coefficient vector **b**. Gappy data within **h** is replaced with the corresponding modal expansion. Loop is terminated based on maximum iterations achieved or eigenvalue spectrum convergence.

Table 3.2: Augmented vector

Chapter	Augmented Vector
4	$\begin{bmatrix} \frac{h}{sx} \\ \text{control points} \end{bmatrix}$
	$\begin{bmatrix} \frac{h}{sx} \\ \text{friction factor} \end{bmatrix}$
5	$\begin{bmatrix} R \\ D \\ Cv \end{bmatrix}$

$$[m] = \begin{bmatrix} 0.25 & 0.14 & 0.10 & 0.5 & 0.28 & 0.20 & 0.75 & 0.42 & 0.30 \\ 1 & 1 & 1 & 1 & 1 & 1 & 1 & 1 & 1 \\ m_{31} & m_{32} & m_{33} & m_{34} & m_{35} & m_{36} & m_{37} & m_{38} & m_{39} \\ & \vdots & & & \vdots & & & \vdots & \\ m_{22981} & m_{22982} & m_{22983} & & & & m_{22987} & m_{22988} & m_{22989} \\ m_{22991} & m_{22992} & m_{22993} & \dots\dots\dots & & & m_{22997} & m_{22998} & m_{22999} \\ m_{23001} & m_{23002} & m_{23003} & & & & m_{23007} & m_{23008} & m_{23009} \end{bmatrix} \quad (3.31)$$

$$[m] = \begin{bmatrix} \left(\frac{R_1}{D_1}\right)_{11} & & \left(\frac{R_1}{D_1}\right)_{1100} \\ \left(\frac{R_2}{D_2}\right)_{21} & & \left(\frac{R_2}{D_2}\right)_{2100} \\ \left(\frac{R_3}{D_3}\right)_{31} & \dots \dots \dots & \left(\frac{R_3}{D_3}\right)_{3100} \\ \left(\frac{R_4}{D_4}\right)_{41} & \dots \dots \dots & \left(\frac{R_4}{D_4}\right)_{4100} \\ \left(\frac{R_5}{D_5}\right)_{51} & \dots \dots \dots & \left(\frac{R_5}{D_5}\right)_{5100} \\ (Cv_1)_{61} & \dots \dots \dots & (Cv_1)_{6100} \\ (Cv_2)_{71} & \dots \dots \dots & (Cv_2)_{7100} \\ (Cv_3)_{81} & & (Cv_3)_{8100} \\ (Cv_4)_{91} & & (Cv_4)_{9100} \\ (Cv_5)_{101} & & (Cv_5)_{10100} \end{bmatrix} \quad (3.32)$$

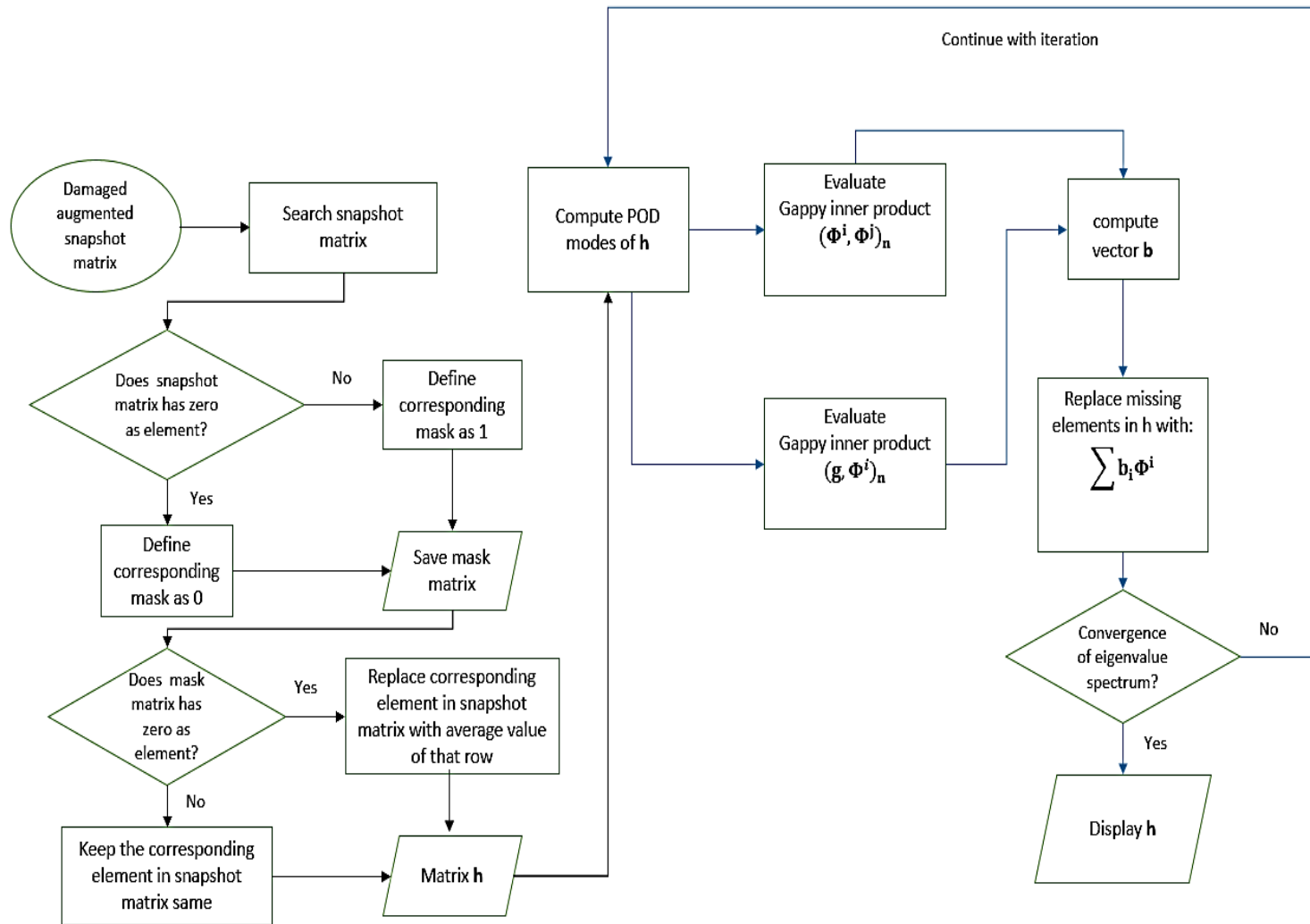


Figure 3.6: Gappy POD Algorithm

3.6. Summary

In summary, chapter described advanced numerical methods that were employed for analysis. The chapter explained the adopted molecular Lattice Boltzmann Method (LBM) that was used for computing high fidelity numerical solutions for simple flow characteristics. Mathematical formulation for LBM was described in detail along with boundary conditions. Chapter also described Computational Fluid Dynamics (CFD) model for severe service control valve. The CFD turbulent models along with model mesh was also described in detail. It further details the boundary conditions used for complex flow simulation within severe service control valve. Furthermore, chapter described Gappy POD methodology and along with its mathematical formulation. It also described in detail the data matrix adopted in subsequent chapters.

CHAPTER 4

INVERSE DESIGN OF FUNCTIONAL SURFACES CONTAINING SIMPLE DISCONTINUOUS GEOMETRY STRUCTURE FOR PRESCRIBED SIMPLE FLOW CHARACTERISTICS

Bio-inspired functional surfaces form major part of engineering solutions. Drag reduction, enhanced heat transfer, improved wettability etc. are some of the functions that are sought by engineering applications. Chapter 2 discussed functional surface flow characterisation literature and concluded that functional surface geometry structures significantly influenced flow characteristics. This chapter introduces inverse design methodology for functional surfaces. Two distinct flow characteristics are prescribed as target: velocity control points and local friction factor distribution. Velocity control points dictates velocity field that is developed over the functional surface. Local friction factor dictates local wall shear stress that effectively controls pressure drop within wall bounded flows. The methodology produced functional surface geometry parameters for prescribed flow characteristics. Chapter starts with qualitative and quantitative flow description based on spatial flow field modal distribution. Subsequently, investigation into inverse design sensitivity is carried out leading to choose flow characteristics prescription for inverse design. Furthermore, suitable functional surface geometry parameter range was identified for inverse design applicability. Subsequently, a software environment integrating low fidelity representation with optimization framework is proposed.

4.1. Introduction

Bio-inspired surfaces have been used to perform specific functions. In aerodynamics and hydrodynamics these functions could be specified as drag, heat or velocity characteristics. Chapter 2 discussed relevant literature outlining various bio-inspired surfaces producing drag and heat characteristics. This chapter discusses functional surface inverse design for prescribed velocity and surface drag behaviour. Inverse design strategy is formulated for subspace derived from arbitrary design space.

Velocity field computed for different design points in design space is given functional form. The velocity function control points are computed for respective design points. Subsequently, local wall shear stress and friction factor is obtained. An ensemble snapshot is constructed containing design point snapshots with individual snapshots having flowfield information augmented with its respective geometry parameter.

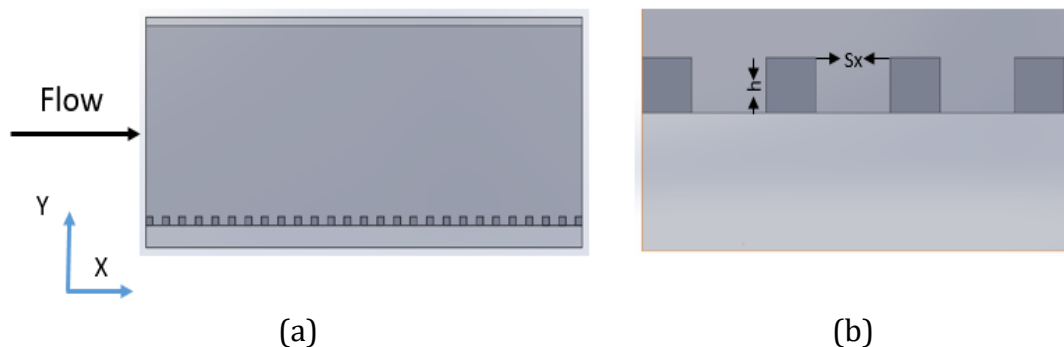


Figure 4.1: (a) Flow domain XY view (b) Discontinuous geometry structure parameters

Figure 4.1 shows the functional surface flow domain and discontinuous geometry structures. Figure 4.1(b) shows zoomed in view on discontinuous geometry structure highlighting its design parameters. A design space is computed by varying these parameters as shows in Table 4.1. The height (h) and spacing (s_x) between bumps are measured in lattice units (lu).

Table 4.1: Design points

Design point	Height h (lu)	Spacing sx (lu)	Geometrical parameter h/sx
1	1	4	0.25
2	1	7	0.14
3	1	10	0.10
4	2	4	0.50
5	2	7	0.28
6	2	10	0.20
7	3	4	0.75
8	3	7	0.42
9	3	10	0.30

Molecular LBM solver computes flow solution on the design points of table 4.1. The flow is directed along X (streamwise). Furthermore, the obtained velocity field is given function form as in equation 4.1:

$$\frac{\widehat{u}}{U_{\max}} = \mathbf{a} \times \left(\frac{y}{\delta}\right)^3 + \mathbf{b} \times \left(\frac{y}{\delta}\right)^2 + \mathbf{c} \times \left(\frac{y}{\delta}\right) \quad (4.1)$$

Here,

a, b & c = Velocity profile control points

y=Wall normal distance

δ= Half channel height

\bar{u} = Time averaged velocity

U_{\max} = Maximum velocity

Velocity functional form has three control points and are defined spatially in the channel. It can be seen that this functional form satisfies boundary conditions:

$$\left(\frac{\widehat{u}}{U_{\max}}\right)_{\left(\frac{y}{\delta}\right)=0} = 0 \quad (4.2)$$

$$\left(\frac{d^2\left(\frac{\widehat{u}}{U_{\max}}\right)}{dx^2}\right)_{\left(\frac{y}{\delta}\right)=0} = 0 \quad (4.3)$$

$$\left(\frac{\bar{u}}{U_{\max}}\right)_{\left(\frac{y}{\delta}\right)=1} = 1 \quad (4.4)$$

The last boundary condition yield following relation between control points:

$$\mathbf{a} + \mathbf{b} + \mathbf{c} = 1 \quad (4.5)$$

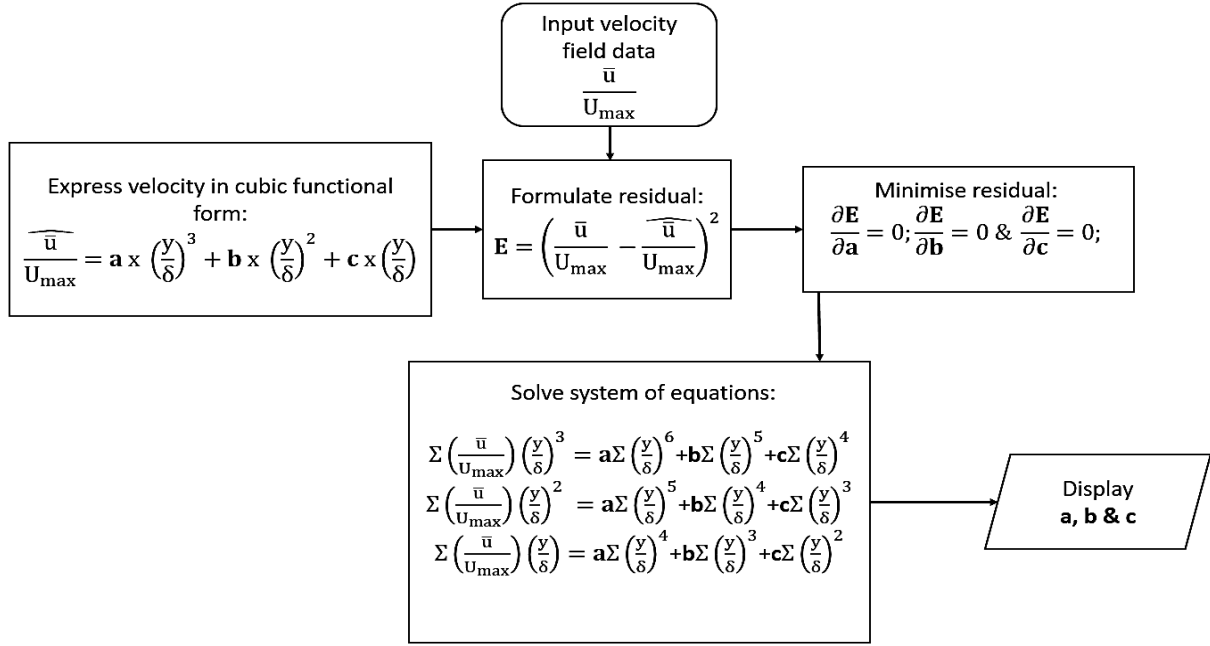
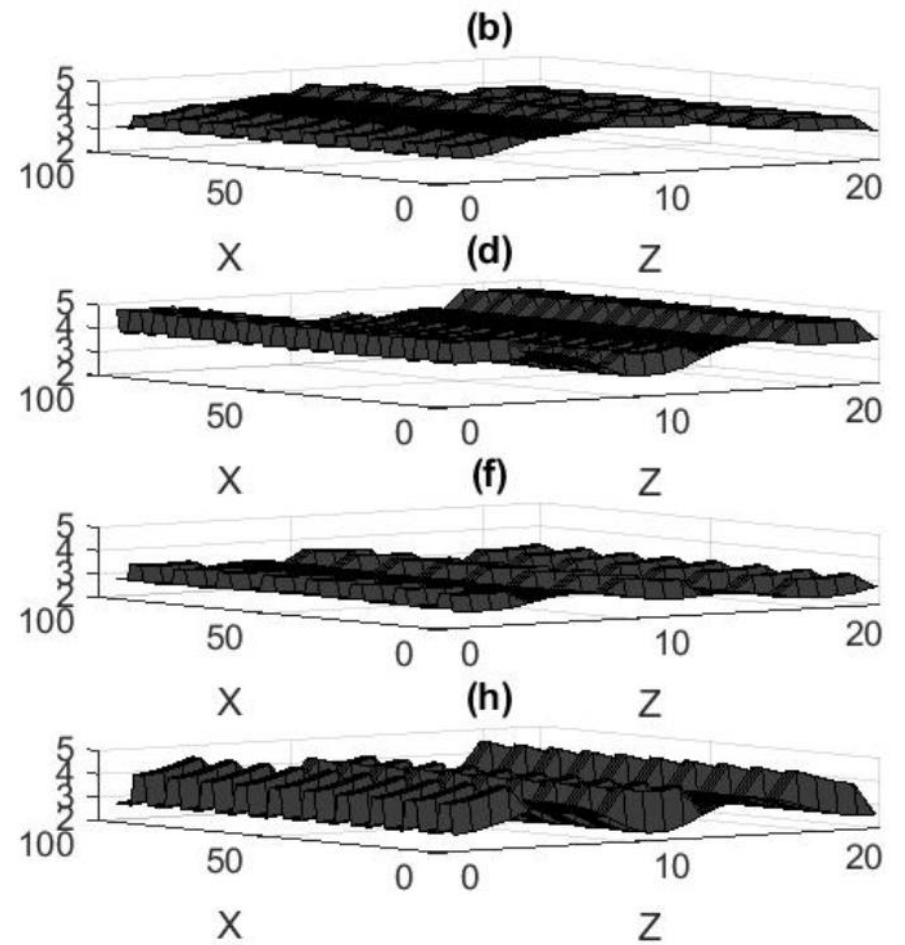
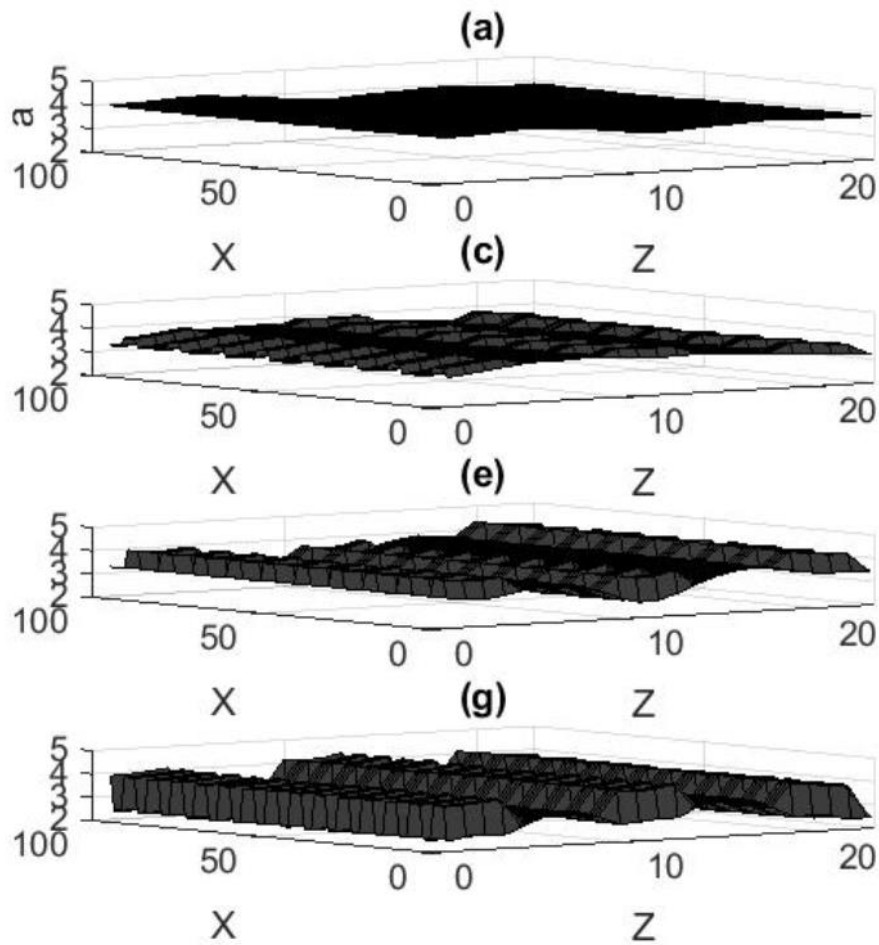


Figure 4.2: Control points computation flow chart

Figure 4.2 shows flow chart for computing velocity profile control points. The computation hinges on minimising residual between actual velocity points $\left(\frac{\bar{u}}{U_{\max}}\right)$ and functional form expressed velocity points $\left(\frac{\widehat{u}}{U_{\max}}\right)$. To minimise, the partial derivatives w.r.t individual control points are computed and set to zero. This consequently yields system of linear equations. Data summation (Σ) is carried out in wall normal (y) direction. Simultaneously solving this system of linear equation yields desired velocity profile control points.

As briefly mentioned, velocity profile control points are observed to be streamwise and cross-stream (Z) spatial function. Figure 4.3, 4.4 & 4.5 show control point variation at different design points



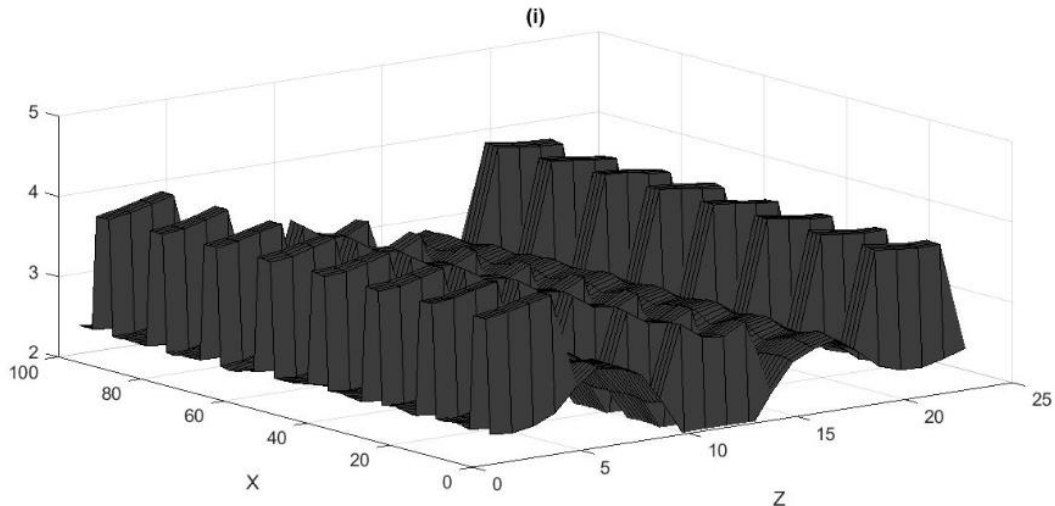
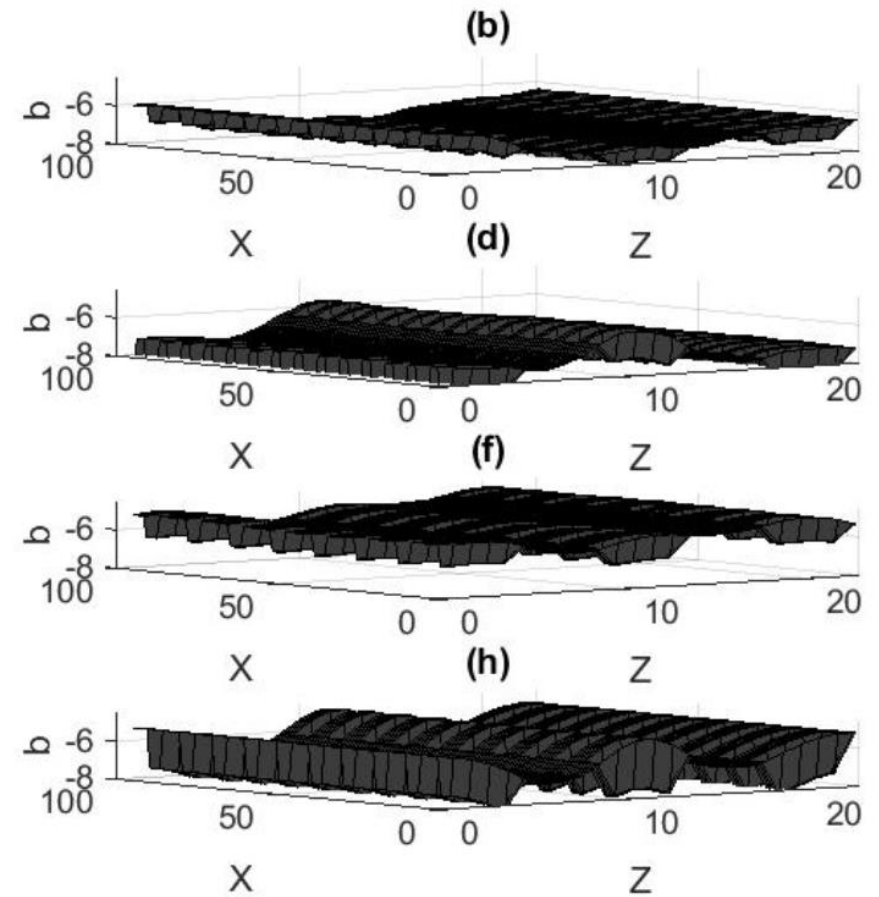
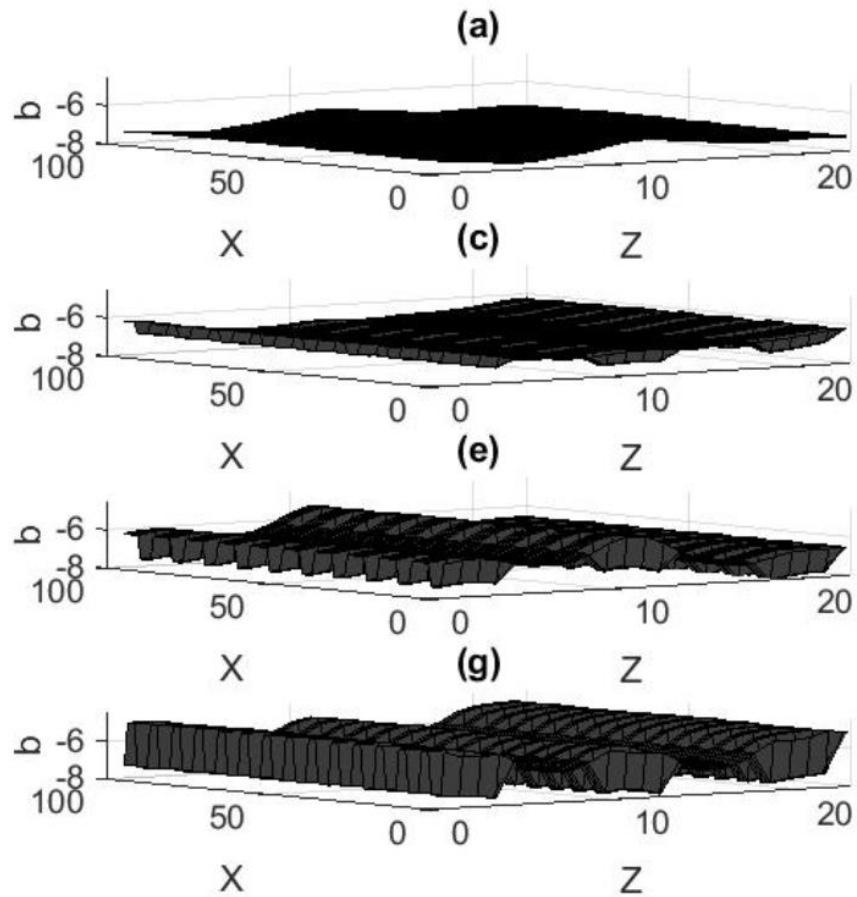


Figure 4.3: Control point **a** spatial distribution (a) $h=1$; $sx=4$ (b) $h=1$; $sx=7$ (c) $h=1$; $sx=10$ (d) $h=2$; $sx=4$ (e) $h=2$; $sx=7$ (f) $h=2$; $sx=10$ (g) $h=3$; $sx=4$ (h) $h=3$; $sx=7$ (i) $h=3$; $sx=10$

Figure 4.3 shows control point **a** variation. Homogenous variation of **a** can be observed in streamwise direction with non-homogeneity maintained in cross stream. Control point **a** observed maximum value of 3.693 within design space at a design point: $h=2$ and $sx=4$. Subsequent maximum value 4.466 was observed at a design point of $h=1$ and $sx=7$. Control point **a** observed minimum value was 1.63 within design space at design point: $h=3$ and $sx=10$. Subsequent minimum value was observed to be 2.295 at design of $h=3$ and $sx=7$. A range of **a** can be inferred from these values to be between 1.63 and 3.693. From figure 4.3, control point **a** distribution can also be inferred to be a waveform in cross stream direction. This waveform can visibly be noted for design points: $h=1$ & $sx=4$; $h=2$ & $sx=7$ and $h=3$ & $sx=10$.



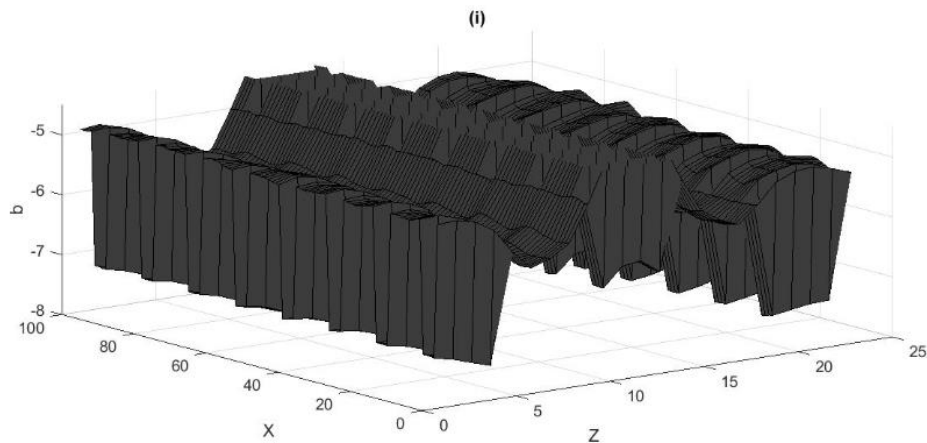
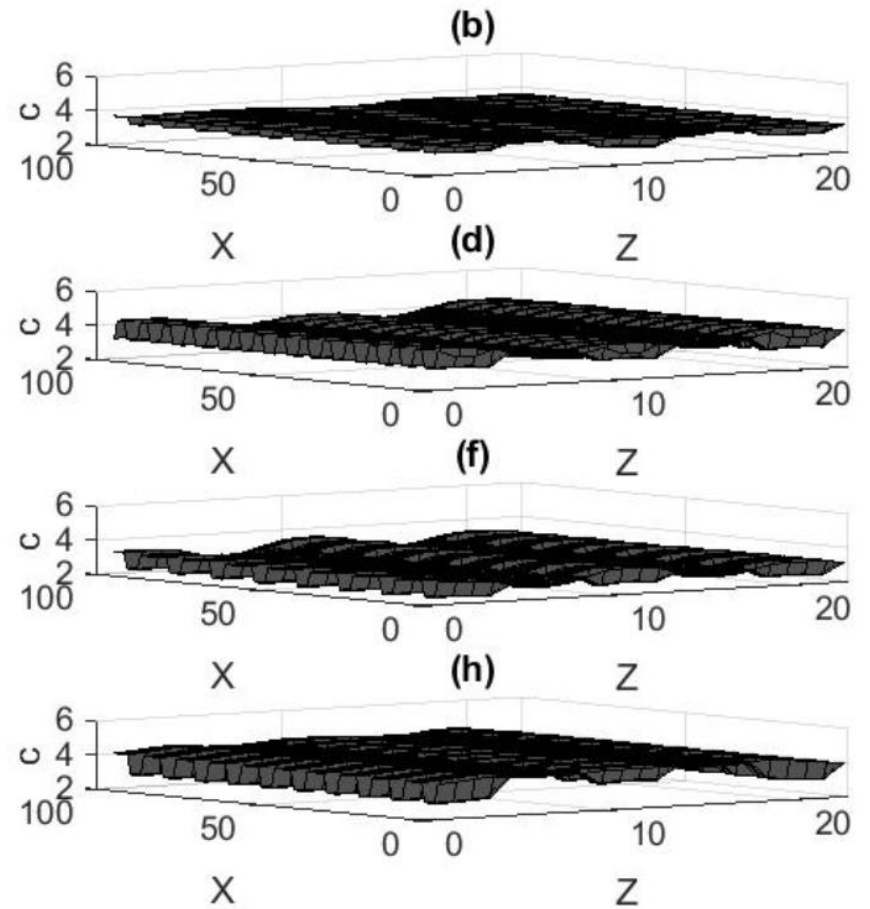
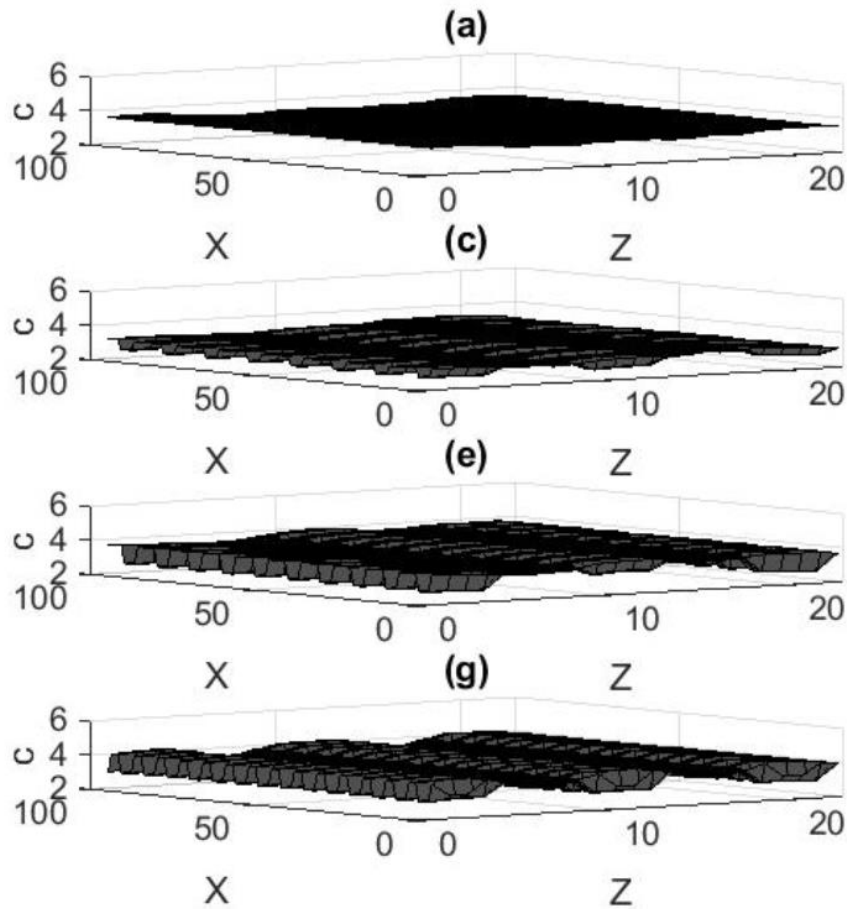


Figure 4.4: Control point **b** spatial distribution (a) $h=1$; $sx=4$ (b) $h=1$; $sx=7$ (c) $h=1$; $sx=10$ (d) $h=2$; $sx=4$ (e) $h=2$; $sx=7$ (f) $h=2$; $sx=10$ (g) $h=3$; $sx=4$ (h) $h=3$; $sx=7$ (i) $h=3$; $sx=10$

Figure 4.4 shows control point **b** variation. Homogenous variation of **b** can be observed within design space in streamwise direction with non-homogeneity maintained in cross stream. Control point **b** observed maximum value of -3.804 within design space at design point: $h=3$ and $sx=10$. Subsequent maximum value of -4.74 was observed at design point of $h=2$ and $sx=10$. The minimum **b** value was observed to be -8.728 at design point of $h=2$ and $sx=4$. Subsequent minimum value was observed to be -8.11 at design point: $h=2$ and $sx=7$. A range of **b** can be inferred from these values to be between -8.728 and -3.804. Control point **b** distribution can be inferred to be of waveform in cross stream direction. This waveform can again visibly be noted for design points: $h=1$ & $sx=4$; $h=2$ & $sx=7$ and $h=3$ & $sx=10$. Qualitatively, control point **a** and **b** spatial distribution can be seen to be mirror image to each other.



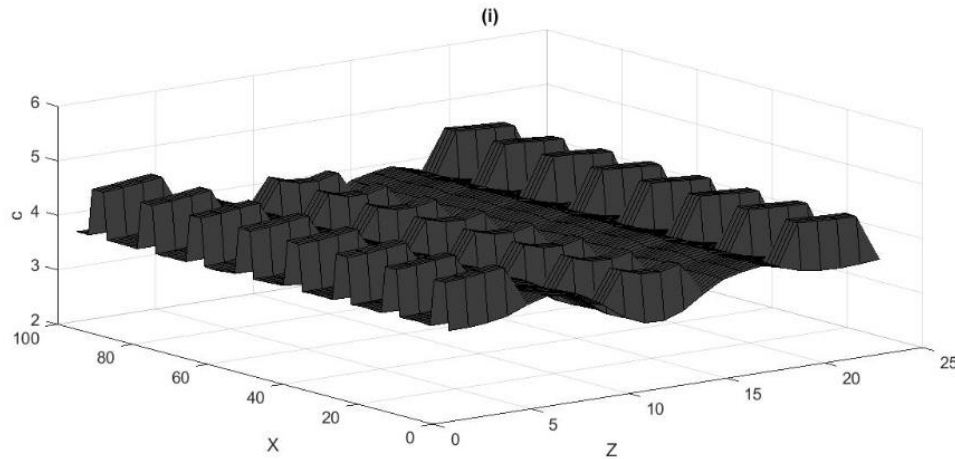
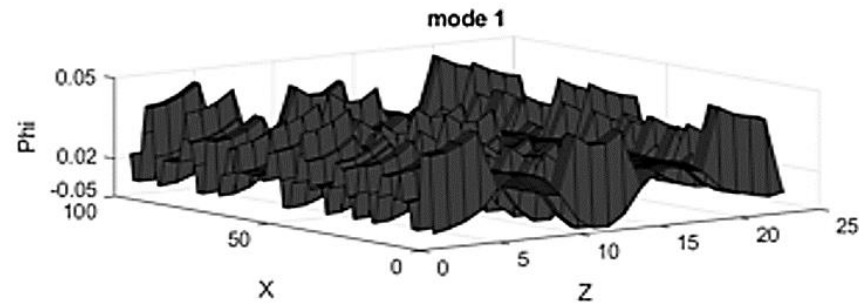


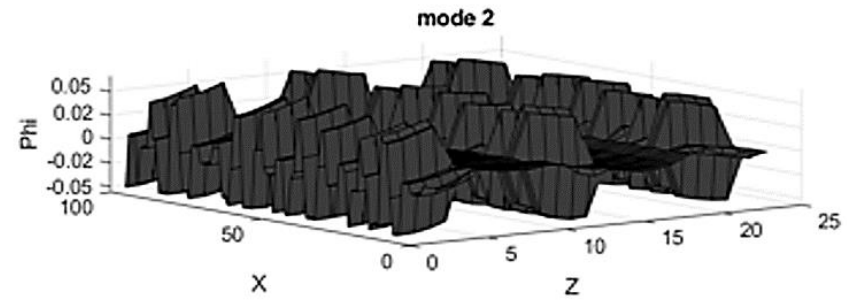
Figure 4.5: Control point c spatial distribution (a) $h=1$; $sx=4$ (b) $h=1$; $sx=7$ (c) $h=1$; $sx=10$ (d) $h=2$; $sx=4$ (e) $h=2$; $sx=7$ (f) $h=2$; $sx=10$ (g) $h=3$; $sx=4$ (h) $h=3$; $sx=7$ (i) $h=3$; $sx=10$

Figure 4.5 shows control point c variation. Homogenous variation of c can be observed in streamwise direction with non-homogeneity maintained in cross stream. Control point c observed maximum value of 5.060 within design space at design point: $h=2$ and $sx=4$. Subsequent maximum value of 4.80 was observed at design point of $h=3$ and $sx=7$. The minimum c value was observed to be 3.184 at a design point of $h=3$ and $sx=10$. Subsequent minimum value was observed to be 3.45 at a design point of $h=2$ and $sx=10$. A range of control point c can be determined from these values to be between 3.184 and 5.060. Control point c distribution can be inferred to be of waveform in cross stream direction. This waveform can again visibly be noted for design points: $h=1$ & $sx=4$; $h=2$ & $sx=7$ and $h=3$ & $sx=10$.

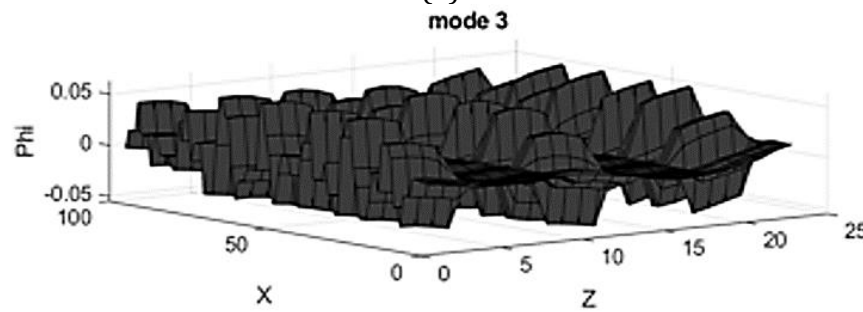
Modal analysis is carried out for velocity function control points. Analysis begins by computing design space modes with respective energy spectrums. Based on energy spectrum, dominant modes are identified that contain 99.99% energy. Based on modal maxima and minima locations, possible flow sensing positions are identified.



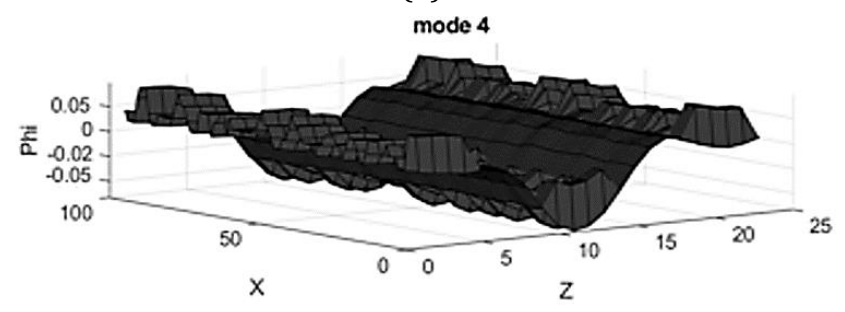
(a)



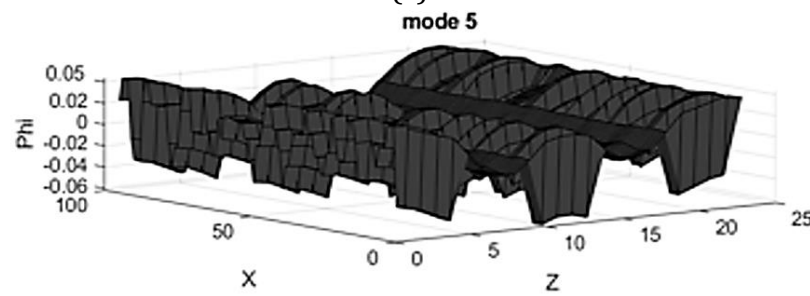
(b)



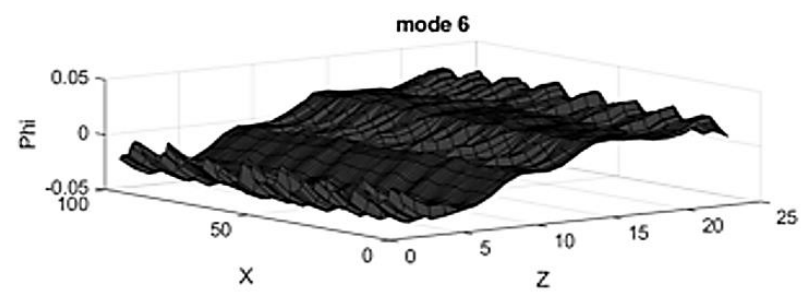
(c)



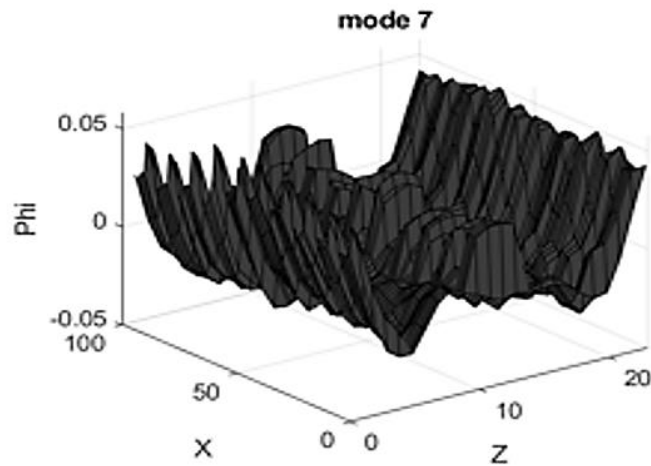
(d)



(e)



(f)



(g)

Figure 4.6: Modes for control point a (a) mode1, (b) mode 2, (c) mode 3, (d) mode 4, (e) mode 5, (f) mode 6 and (g) mode 7

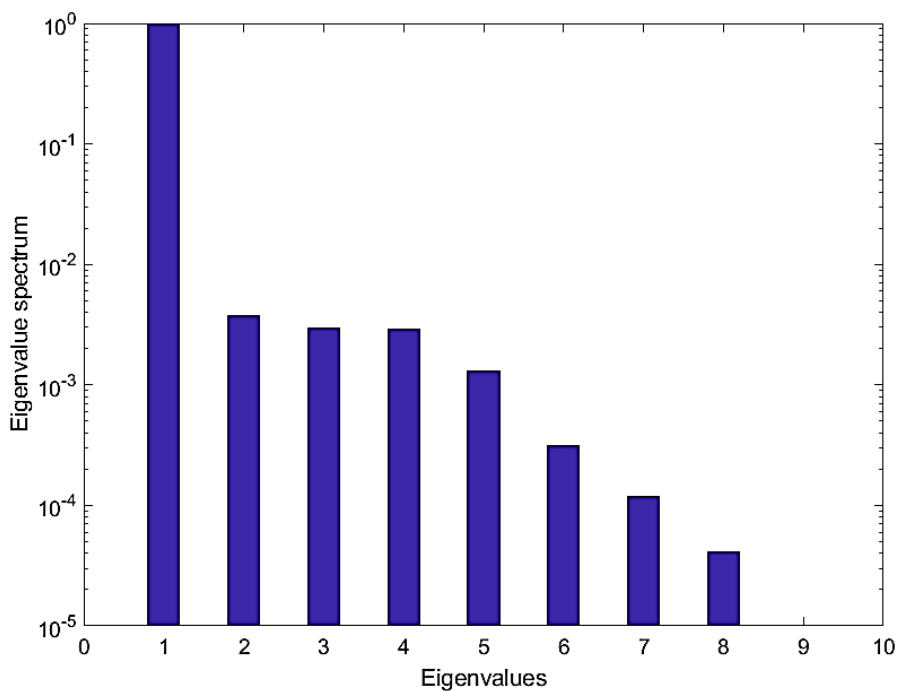


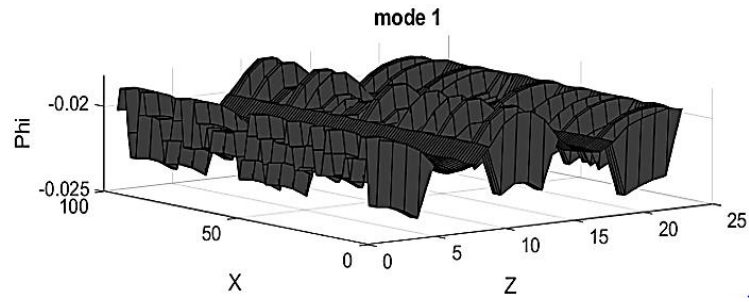
Figure 4.7: Eigenvalue spectrum for POD modes of control point a

Figure 4.6 shows control point a modal distribution. Homogenous modal distribution can be observed along streamwise direction with non-homogeneity maintained in cross stream. All together seven modes contain 99.99% of total energy. This can evidently be

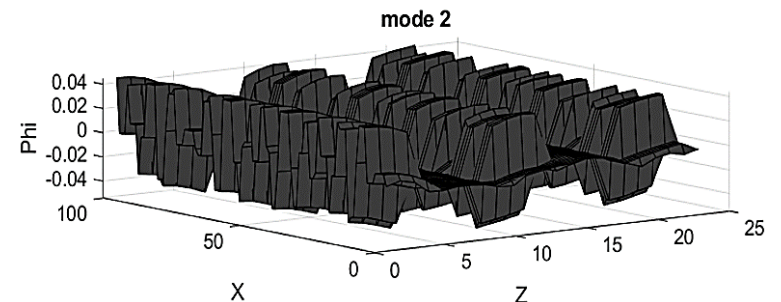
seen in eigenvalue spectrum in figure 4.7. First mode has 98.86% energy contain while subsequent modes decrease in energy. It can also be seen that first mode has highest convergence rate compared to higher subsequent modes. Table 4.2 shows the spatial location of modal maxima and minima for control point **a**. The location is measured in lattice units along streamwise and cross stream direction. Highest modal activity for most energetic mode can be observed to be concentrated at 95 lattice units in streamwise direction at 19 & lattice units in cross stream direction. Additionally, this activity can also be seen to be concentrated at a location 21 lattice units in streamwise direction and 12 lattice units in cross stream direction.

Table 4.2: Control point **a** modes maxima and minima

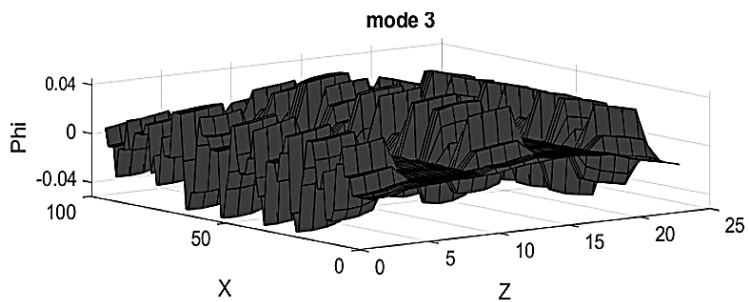
Mode	Maximum Value	Location		Minimum Value	Location	
		Streamwise (lu)	Cross stream (lu)		Streamwise (lu)	Cross stream (lu)
1	0.0246	95	19	0.0176	21	12
2	0.0528	15	10	-0.0451	86	12
3	0.0627	56	1	-0.0546	32	13
4	0.0391	54	19	-0.0531	8	11
5	0.0439	76	1	-0.0625	44	10
6	0.0368	56	22	-0.0454	38	3
7	0.0579	65	1	-0.0447	48	18



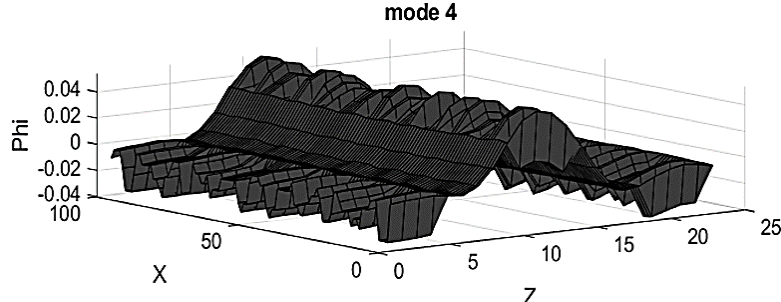
(a)



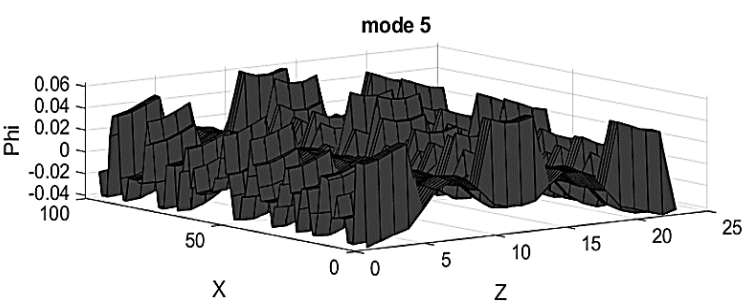
(b)



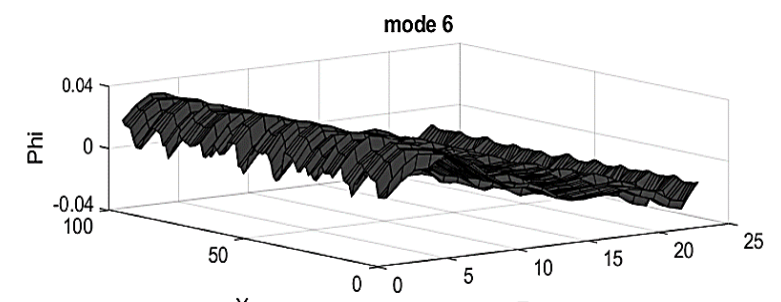
(c)



(d)



(e)



(f)

Figure 4.8: Modes for control point **b** (a) mode1, (b) mode 2, (c) mode 3, (d) mode 4, (e) mode 5 and (f) mode 6

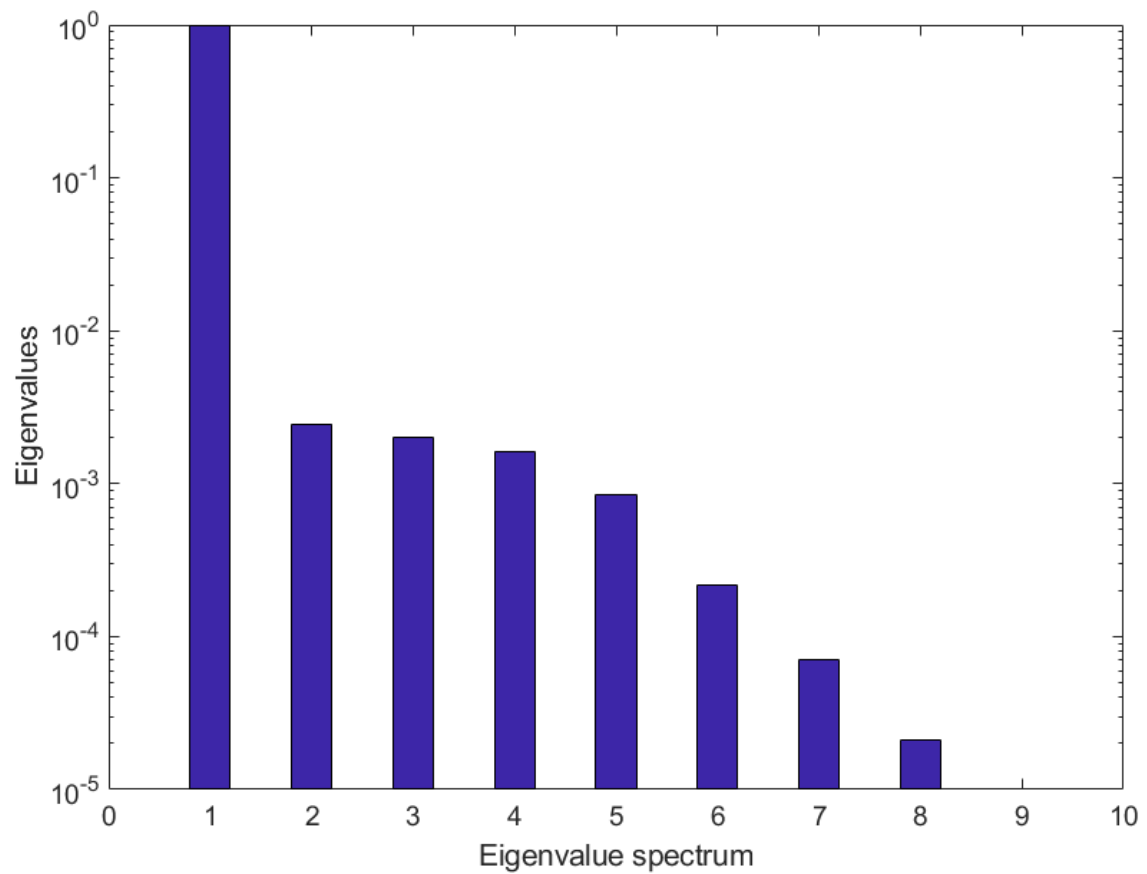
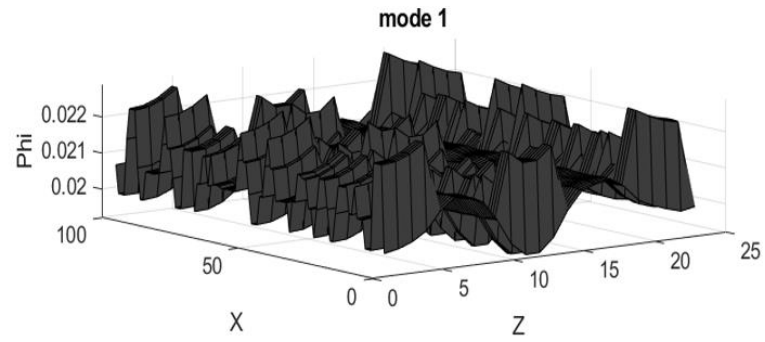


Figure 4.9: Eigenvalue spectrum for POD modes of control point **b**

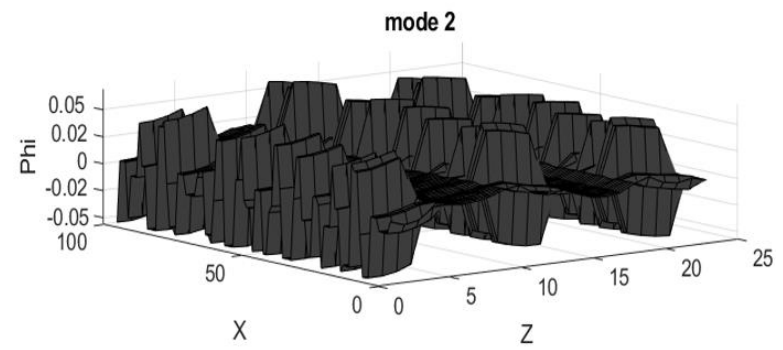
Figure 4.8 shows control point **b** modal distribution. Homogenous modal distribution can be observed along streamwise direction with non-homogeneity maintained in cross stream. All together six modes contain 99.99% of total energy. This can evidently be seen in eigenvalue spectrum in Figure 4.9. First mode has 99.27% energy contain while subsequent modes decrease in energy. Table 4.3 shows the spatial location of modal maxima and minima for control point **b**. The location is measured in lattice units along streamwise and cross stream direction. Highest modal activity for most energetic mode can be observed to be concentrated at 21 lattice units in streamwise direction and 12 lattice unit in cross stream direction. Additionally, this activity can also be seen to be concentrated at a location 95 lattice units in streamwise direction and 19 lattice units in cross stream direction.

Table 4.3: Control point **b** modes maxima and minima

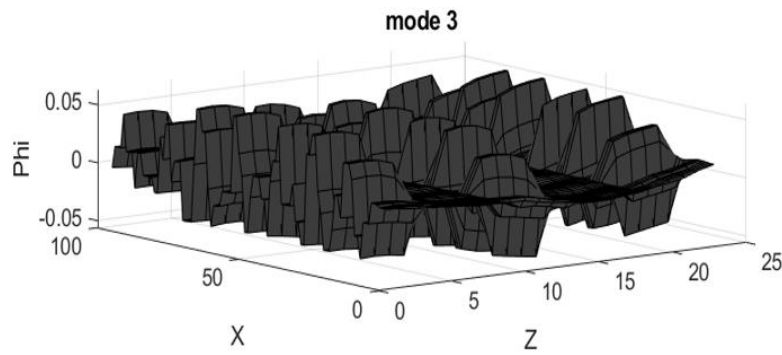
Mode	Maximum Value	Location		Minimum Value	Location	
		Streamwise (lu)	Cross stream (lu)		Streamwise (lu)	Cross stream (lu)
1	-0.0182	21	12	-0.0241	95	19
2	0.0444	11	1	-0.0542	15	10
3	0.0561	32	13	-0.0652	56	2
4	0.0538	8	11	-0.0402	54	19
5	0.0630	44	10	-0.0432	20	21
6	0.0433	38	3	-0.0407	55	22



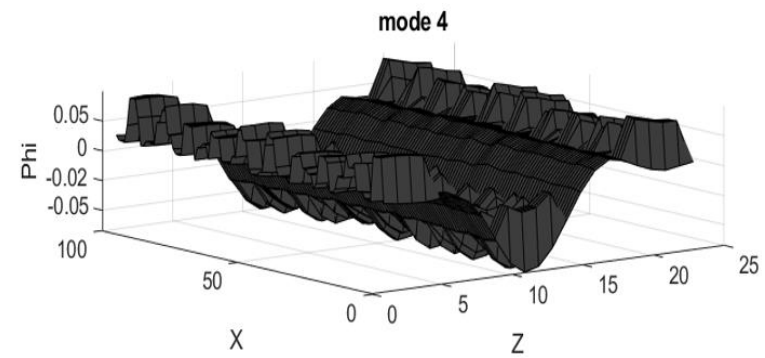
(a)



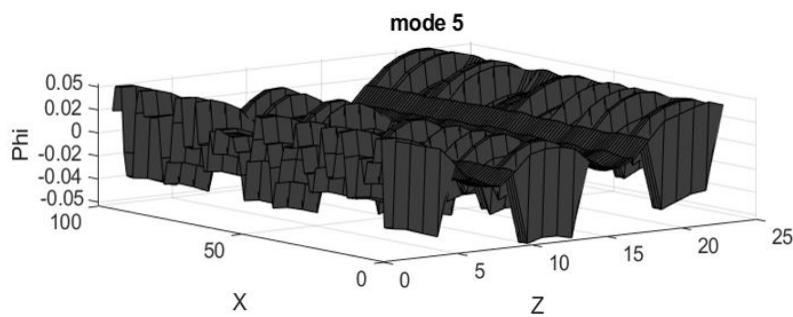
(b)



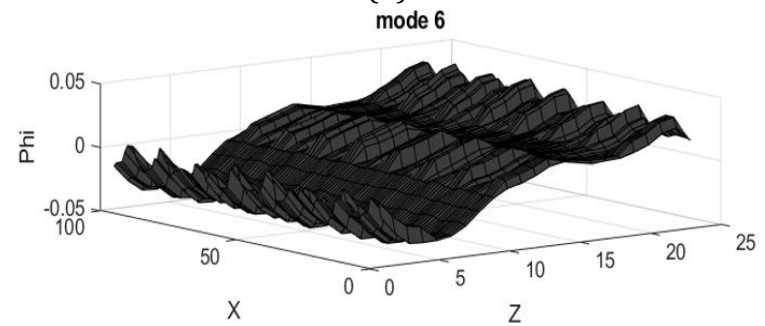
(c)



(d)



(e)



(f)

Figure 4.10: Modes for control point **c** (a) mode1, (b) mode 2, (c) mode 3, (d) mode 4,
(e) mode 5 and (f) mode 6

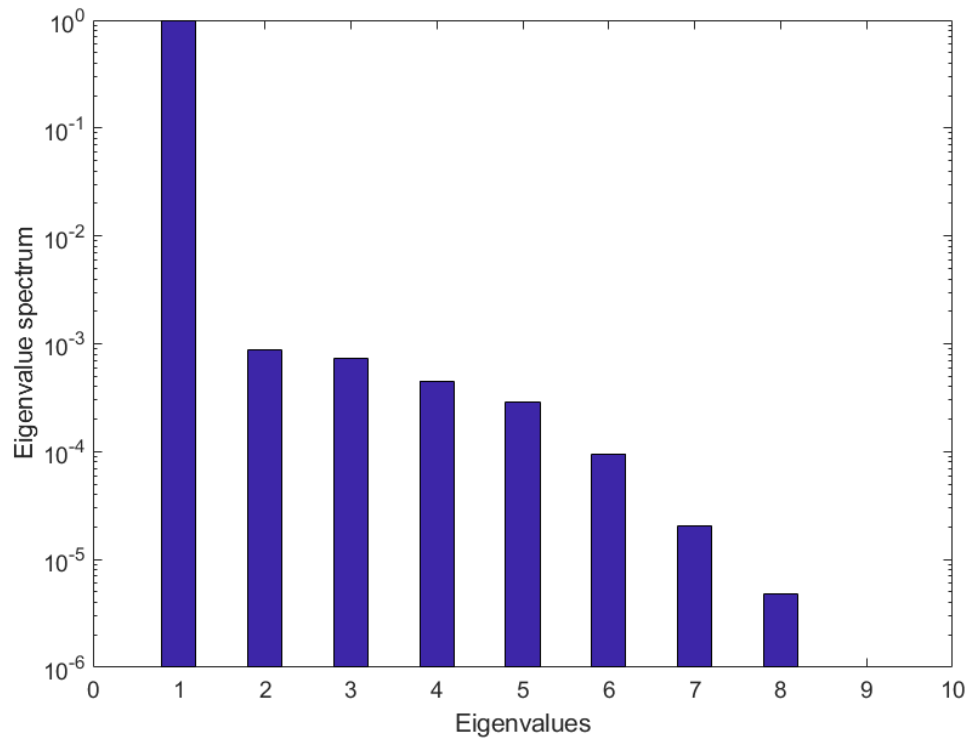


Figure 4.11: Eigenvalue spectrum for POD modes of control point **c**

Figure 4.10 shows control point **c** modal distribution. Homogenous modal distribution can be observed along streamwise direction with non-homogeneity maintained in cross stream. All together six modes contain 99.99% of total energy. This can evidently be seen in eigenvalue spectrum in Figure 4.11. First mode has 99.75% energy contain while subsequent modes decrease in energy. Table 4.4 shows the spatial location of modal maxima and minima for control point **c**. The location is measured in lattice units along streamwise and cross stream direction. Highest modal activity for most energetic mode can be observed to be concentrated at 95 lattice units in streamwise direction and 19 lattice unit in cross stream direction. Additionally, this activity can also be seen to be concentrated at a location 21 lattice units in streamwise direction and 11 lattice units in cross stream direction.

Table 4.4: Control point **c** modes maxima and minima

Mode	Maximum Value	Location		Minimum Value	Location	
		Streamwise (lu)	Cross stream (lu)		Streamwise (lu)	Cross stream (lu)
1	0.0229	95	19	0.0192	21	11
2	0.0551	15	10	-0.0452	11	2
3	0.0629	56	2	-0.0560	32	13
4	0.0399	54	19	-0.0536	1	11
5	0.0425	20	21	-0.0638	44	10
6	0.0434	55	22	-0.0395	19	4

Modal analysis revealed control point dominant modes. Dominance was identified based on respective energy spectrums and it was seen that control points respective first modes energy content exceeded 99%. Seven, six and six modes were identified as dominant modes respectively for control points **a**, **b** and **c**. Furthermore, analysis identified energetic modes local maxima and minima locations.

For control point **a**, first mode maxima were identified at 95 & 19 lattice units (lu) along streamwise and cross-stream directions while first mode minima were identified at 21 & 12 lu along streamwise and cross-stream directions. For control point **b**, first mode maxima were identified at 21 & 12 lattice units (lu) along streamwise and cross-stream directions while first mode minima were identified at 95 & 19 lu along streamwise and

cross-stream directions. For control point **c**, first mode maxima were identified at 95 & 19 lattice units (lu) along streamwise and cross-stream directions while first mode minima were identified at 21 & 11 lu along streamwise and cross-stream directions.

For control point **a**, second mode maxima were identified at 15 & 10 lattice units (lu) along streamwise and cross-stream directions while second mode minima were identified at 86 & 12 lu along streamwise and cross-stream directions. For control point **b**, second mode maxima were identified at 11 & 1 lattice units (lu) along streamwise and cross-stream directions while second mode minima were identified at 15 & 10 lu along streamwise and cross-stream directions. For control point **c**, second mode maxima were identified at 15 & 10 lattice units (lu) along streamwise and cross-stream directions while second mode minima were identified at 11 & 2 lu along streamwise and cross-stream directions.

Since first mode contains highest energy (variance), its local modal maxima and minima can potentially be flow sensing positions. The same is true for second dominant mode locations. Based on first mode, 95 lattice unit along streamwise and 19 lattice unit cross-stream can be seen as common modal activity location among all the control points, making it as possible flow sensing position. Based on first mode another common modal activity location among all the control points is 21 and 11 lattice unit along streamwise and cross-stream respectively, making it as another possible flow sensing position. Based on second mode, 15 and 10 lattice unit along streamwise and cross-stream respectively identified as common modal activity location among all control points, making it another potential flow sensing positions. Altogether, modal analysis revealed three potential flow sensing positions. Further sensing positions can be added based on higher mode local maxima and minima. However, sensing effectiveness gets constant with subsequent higher mode inclusion on account of lower cumulative energy content.

4.2. Inverse Design

Previous section established qualitative and quantitative control point distribution for nine design points. Computed respective modes revealed governing flow structures. This section exploits flow structures to inverse design functional surface for prescribed control points and friction factor distribution.

Prescribing velocity control points gives velocity field as target while prescribing friction factor gives surface shear as target. Velocity field heavily dictates heat transfer characteristics through momentum exchange while surface shear dictates pressure drops within wall bounded flows. Investigation is carried out into inverse design sensitivity to velocity control points. The investigation is useful to identify least sensitive velocity control points to be prescribed for inverse design process. Additionally, sensitivity investigation identifies snapshots sharing common flow structures. Furthermore, surface shear based inverse design results would be discussed. Subsequently, velocity and surface shear based functional surface inverse design framework is established. This framework is useful for designing a surface for a desired velocity field or surface shear.

4.2.1. Inverse design sensitivity

Sensitivity of Gappy POD based inverse design process is investigated to identify least sensitive target control points and common flow structure sharing snapshots. The scope of this investigation is limited to functional surface inverse design for given velocity function control points and surface shear stress distribution. For this investigation, eight high fidelity flow field snapshots are used with missing elements in ninth snapshot as mentioned in chapter 3. Altogether, control points are computed on 2300 surface spatial locations at different design points in Table 4.1. The goal is to compute non-dimensional geometrical parameter with a specified control point distribution.

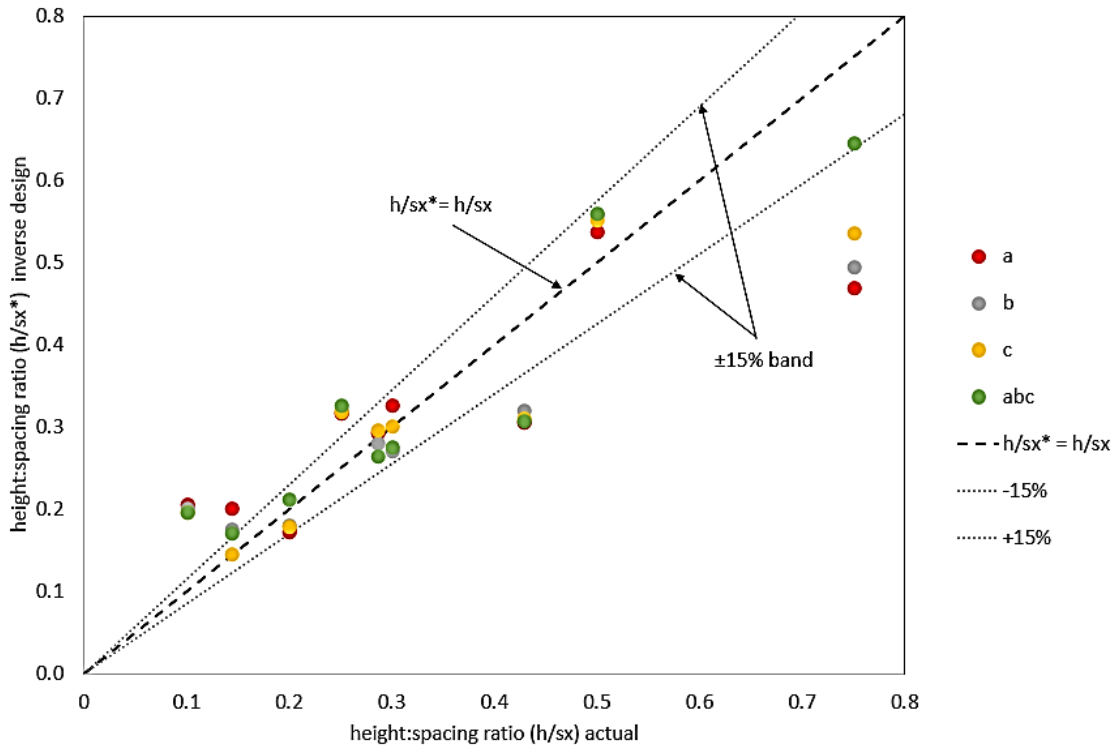


Figure 4.12: Geometrical parameter correlation at different control points

Surface is represented by non-dimensional geometrical parameter: h/sx . Figure 4.12 shows correlation between h/sx for specified control point surface distribution. Altogether, 36 points based on nine snapshot ensemble for individual and combined prescribed control point distribution are shown in the graph. A detailed explanation is provided in chapter 3 for inverse design computation. It can be seen that around half of the points are within 15% band. Points that are outside, are less scattered away from 15% band. Four points can be seen within 15% band on prescribing only control point **a** as target distribution. The farthest point obtained while prescribing only control point **a** distribution is when geometrical parameter has inverse design computed value of 0.46 while actual value being 1.6 times the computed. Four points can be seen within 15% band on prescribing only control point **b** as target distribution. The farthest point obtained while prescribing only control point **b** distribution is when geometrical parameter has inverse design computed value of 0.49 while actual value deviating by around 32%.

Five points can be seen within 15% band on prescribing only control point **c** as target distribution. The farthest point obtained while prescribing only control point **c** distribution is when geometrical parameter has actual value of 0.75 while computed inverse design value being deviated by around 30% from the actual value. Five points can be seen within 15% band on prescribing all control point values as target distribution. The farthest point obtained while prescribing all control point values is when geometrical parameter has inverse design computed value of 0.19 while actual value deviating by around 50%.

The investigation concludes that inverse design is least sensitive for prescribed control point **c** or all control points distribution. This least sensitivity further indicates common flow structures existence among snapshot ensemble.

4.2.2. Control points based inverse design

This section describes velocity profile control points based functional surface inverse design. Implicitly, velocity field within domain would be prescribed, subsequently carrying surface parameter computation using inverse design process described in chapter 3.

INVERSE DESIGN OF FUNCTIONAL SURFACES CONTAINING SIMPLE DISCONTINUOUS GEOMETRY
STRUCTURE FOR PRESCRIBED SIMPLE FLOW CHARACTERISTICS

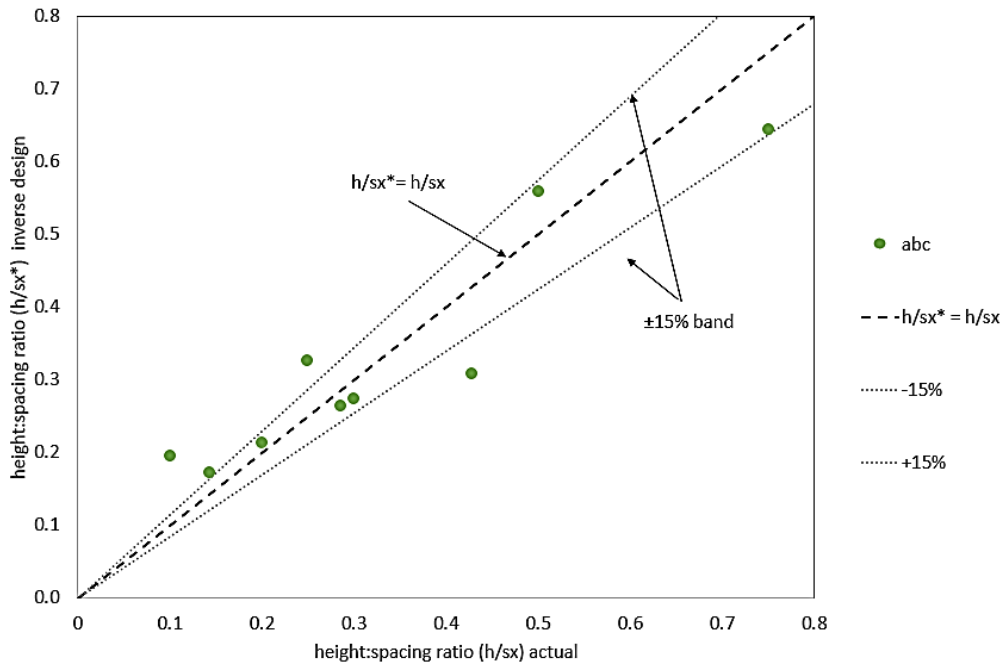


Figure 4.13: Geometrical parameter correlation for control points distribution

Figure 4.13 shows correlation obtained while prescribing all velocity control points. As described in sensitivity analysis, only five design points are within stipulated band while one design point on the margin. Three design points can also be observed to outside this band. Significant deviation from band indicates that some of the geometries are not contained within the subspace spanned by snapshot ensemble.

Table 4.5: Computation modes

No of modes	Computed h/sx	Actual h/sx	Deviation %
1	0.3	0.42	40
	0.27	0.3	11
2	0.55	0.5	-9
3	0.26	0.28	8
	0.21	0.2	-5
4	0.33	0.25	-24
6	0.17	0.14	-18
	0.19	0.1	-47
8	0.64	0.75	17

Table 4.5 shows computed modes vs actual geometrical parameter values. The table also shows subsequent number of computational modes required to reach minimum deviation between computed and actual values. It can be seen that inverse design of point $\mathbf{h}/\mathbf{sx}=0.75$ required highest number of modes while $\mathbf{h}/\mathbf{sx}=0.42$ and 0.3 required lowest number of modes. It can be noted that mode 1 and 6 records highest absolute deviation of computed value from actual value. This indicates $\mathbf{h}/\mathbf{sx}=0.42$ and 0.1 is not contained within the subspace spanned by their respective number of modes mentioned in Table 4.5.

As discussed in chapter 3, Gappy inner product computation over support space used respective modes and augmented snapshot vector(\mathbf{g}), leading to matrix \mathbf{M} and vector \mathbf{f} . The modal expansion coefficients are further computed by multiplying inverse \mathbf{M} with \mathbf{f} . Gappy inner product evaluation reveals orthogonality relationship between modes over support space. Evaluating orthogonality becomes computationally important as \mathbf{M} and its inverse goes towards identity matrix for orthogonal modes. This mitigates computational expense during inverse design process.

Modal expansion coefficients can be seen as a direct result of Gappy inner products. While modes are spatial functions, the coefficients are design variable functions. Modes contain dominant flow structure information while the corresponding design-dependant coefficient hints at the extent of modal dominance. Gappy inner products $((\Phi^i, \Phi^j)_n$ & $(\mathbf{g}, \Phi^i)_n$) and modal expansion coefficient evolution for Table 4.5 designs are further discussed.

INVERSE DESIGN OF FUNCTIONAL SURFACES CONTAINING SIMPLE DISCONTINUOUS GEOMETRY
STRUCTURE FOR PRESCRIBED SIMPLE FLOW CHARACTERISTICS

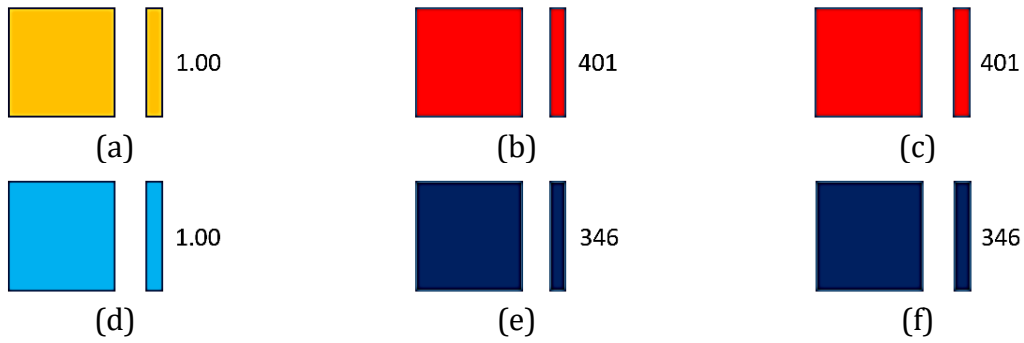


Figure 4.14: (a) Gappy inner product $(\Phi^i, \Phi^j)_n$ (b) Gappy inner product $(\mathbf{g}, \Phi^i)_n$ (c) Modal Coefficient for $\mathbf{h}/\mathbf{sx}=0.42$; (d) Gappy inner product $(\Phi^i, \Phi^j)_n$ (e) Gappy inner product $(\mathbf{g}, \Phi^i)_n$ (f) Modal Coefficients for $\mathbf{h}/\mathbf{sx}=0.3$

Figure 4.14 shows modal Gappy inner product evolution over support space \mathbf{n} and subsequently computed modal coefficients for inverse design of $\mathbf{h}/\mathbf{sx}=0.42$ and $\mathbf{h}/\mathbf{sx}=0.3$. It can be noted from Table 4.5 that only one mode was used in inverse design process, indicating subspace reduction. Consequently, only one value can be noted for Gappy inner products $(\Phi^i, \Phi^j)_n$ and $(\mathbf{g}, \Phi^i)_n$. As a result, only one modal expansion coefficient was used to compute inverse design value. This significantly reduces incurred inverse design computation expense.

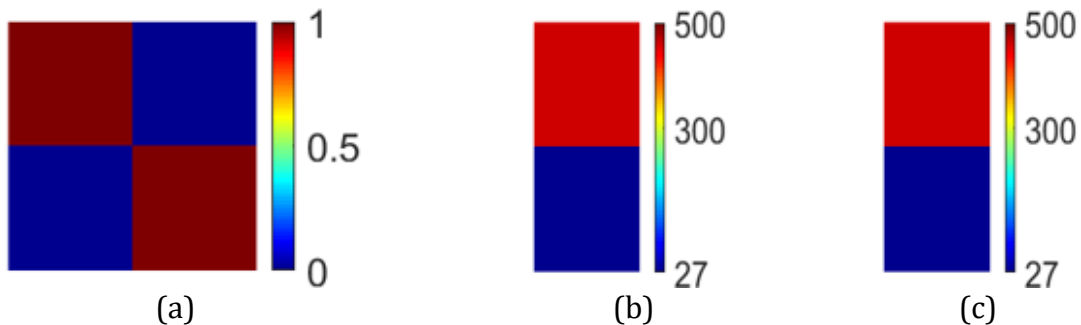


Figure 4.15: (a) Gappy inner product $(\Phi^i, \Phi^j)_n$ (b) Gappy inner product $(\mathbf{g}, \Phi^i)_n$ (c) Modal Coefficient for $\mathbf{h}/\mathbf{sx}=0.5$;

Change can be noted for $\mathbf{h}/\mathbf{sx} = 0.5$ in Figure 4.15 as subspace can now be represented by two modes. Gappy inner product $(\Phi^i, \Phi^j)_n$ can be seen to be symmetric about diagonal. Additionally, it can be seen that inner product between first two modes produced zero as off-diagonal values indicating orthogonality between first two modes. As a result, the computed two modal expansion coefficients are same as Gappy inner product $(\mathbf{g}, \Phi^i)_n$.

INVERSE DESIGN OF FUNCTIONAL SURFACES CONTAINING SIMPLE DISCONTINUOUS GEOMETRY
STRUCTURE FOR PRESCRIBED SIMPLE FLOW CHARACTERISTICS

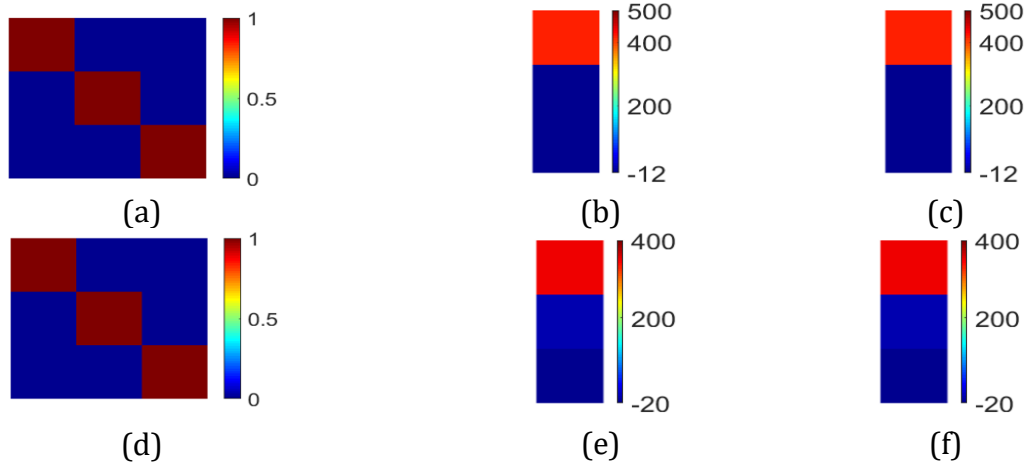


Figure 4.16: (a) Gappy inner product $(\Phi^i, \Phi^j)_n$ (b) Gappy inner product $(\mathbf{g}, \Phi^i)_n$ (c) Modal Coefficient for $\mathbf{h}/\mathbf{sx}=0.28$; (d) Gappy inner product $(\Phi^i, \Phi^j)_n$ (e) Gappy inner product $(\mathbf{g}, \Phi^i)_n$ (f) Modal Coefficients for $\mathbf{h}/\mathbf{sx}=0.2$

Figure 4.16 shows modal Gappy inner product evolution over support space \mathbf{n} and subsequently computed modal coefficients for inverse design of $\mathbf{h}/\mathbf{sx}=0.28$ and 0.2 . It can be seen that three modes dominate inverse design computation. It can also be noted that three modes-maintained orthogonality, resulting in identity matrix. Three values can be noted for Gappy inner product $(\mathbf{g}, \Phi^i)_n$ and modal expansion coefficients. The coefficients signify individual mode extent of dominance. For example, $\mathbf{h}/\mathbf{sx}=0.28$ and 0.2 first modal coefficient has highest value, signifying greater first mode dominance.

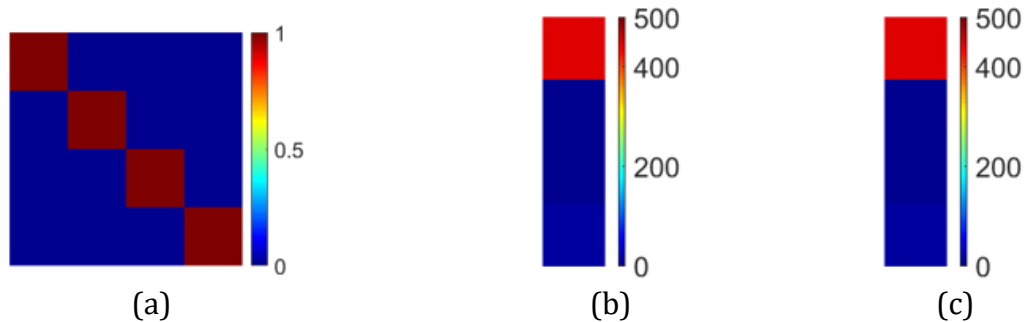


Figure 4.17: (a) Gappy inner product $(\Phi^i, \Phi^j)_n$ (b) Gappy inner product $(\mathbf{g}, \Phi^i)_n$ (c) Modal Coefficient for $\mathbf{h}/\mathbf{sx}=0.25$

Figure 4.17 shows modal Gappy inner product evolution over support space \mathbf{n} and subsequently computed modal coefficients for inverse design of $\mathbf{h}/\mathbf{sx}=0.25$. Subspace can be seen to expand over four modes. Furthermore, all the four modes can be seen to be orthogonal to each other as evidenced in Gappy inner product $(\Phi^i, \Phi^j)_n$. As a result, four modal expansion coefficients and Gappy inner product $(\mathbf{g}, \Phi^i)_n$ have same value.

Figure 4.18 shows modal Gappy inner product evolution over support space \mathbf{n} and subsequently computed modal coefficients for inverse design of $\mathbf{h}/\mathbf{sx}=0.14$ and 0.1 . Subspace can be seen to be expanded over six modes. Furthermore, all the six modes can be seen to be orthogonal to each other as evidenced in Gappy inner product $(\Phi^i, \Phi^j)_n$. As a result, six modal expansion coefficients and Gappy inner product $(\mathbf{g}, \Phi^i)_n$ have same value.

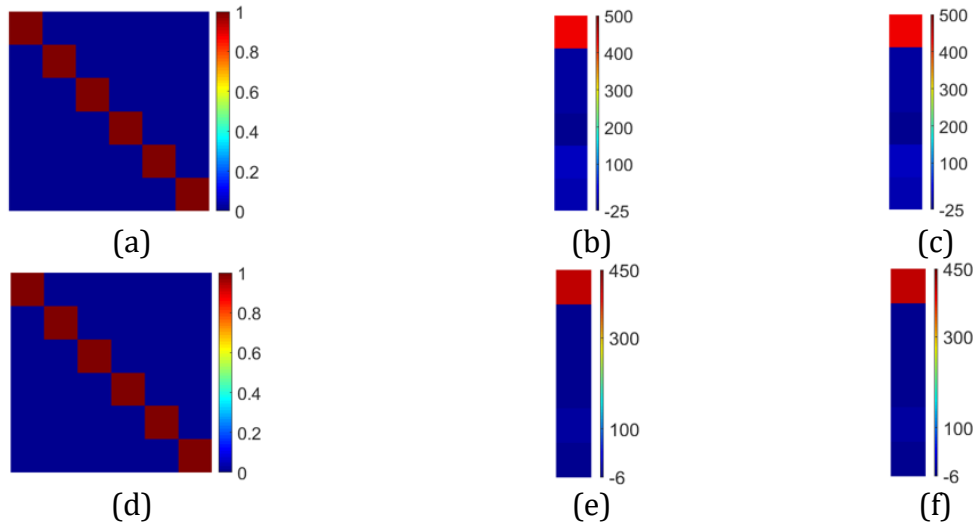


Figure 4.18: (a) Gappy inner product $(\Phi^i, \Phi^j)_n$ (b) Gappy inner product $(\mathbf{g}, \Phi^i)_n$ (c) Modal Coefficient for $\mathbf{h}/\mathbf{sx}=0.14$; (d) Gappy inner product $(\Phi^i, \Phi^j)_n$ (e) Gappy inner product $(\mathbf{g}, \Phi^i)_n$ (f) Modal Coefficient for $\mathbf{h}/\mathbf{sx}=0.1$

Figure 4.19 shows modal Gappy inner product evolution over support space \mathbf{n} and subsequently computed modal coefficients for inverse design of $\mathbf{h}/\mathbf{sx}=0.75$. Subspace can be seen to be expanded over eight modes. Furthermore, all the eight modes can be seen to be orthogonal to each other as evidenced in Gappy inner product $(\Phi^i, \Phi^j)_n$. As a result, eight modal expansion coefficients and Gappy inner product $(\mathbf{g}, \Phi^i)_n$ have same value.

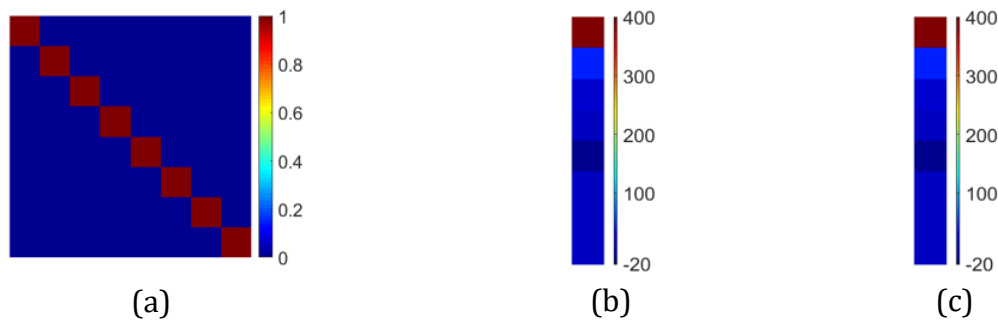


Figure 4.19: (a) Gappy inner product $(\Phi^i, \Phi^j)_n$ (b) Gappy inner product $(\mathbf{g}, \Phi^i)_n$ (c) Modal Coefficient for $\mathbf{h}/\mathbf{sx}=0.75$

A suitable h/sx range with stipulated number of modes can be identified for control point based inverse design process. Table 4.6 shows modal design variations based on original nine snapshot ensemble. Closest computed values to design points are shown in yellow. As noted in figure 4.13, Table 4.6 again shows maximum deviation for three design points $h/sx = 0.1, 0.25$ and 0.42 . Furthermore, no proper consensus can be seen to have developed between computed inverse design values and number of computational modes used. This deters from defining a range over which particular mode can be seen to be active.

A new snapshot ensemble can be created by discarding snapshots for design points $h/sx = 0.1, 0.25$ and 0.42 , which were outside (outliers) stipulated error band as shown in figure 4.13, from original ensemble. This further illustrates that the outliers and inliers (points within error band) might not be sharing same dominating flow structures. Table 4.7 shows modal design variations based on new snapshot ensemble.

Table 4.6: Original ensemble based modal variations

h/sx	Modes	1	2	3	4	5	6	7	8	9
0.25		0.38	0.36	0.36	0.33	0.06	0.07	0.04	0.04	0.04
0.14		0.38	0.31	0.35	0.19	0.22	0.17	0.17	0.05	0.05
0.10		0.37	0.34	0.33	0.24	0.19	0.20	0.21	0.17	0.17
0.50		0.34	0.56	0.57	0.82	0.63	0.67	0.69	0.31	0.31
0.29		0.34	0.24	0.26	0.40	0.33	0.18	0.15	0.48	0.48
0.20		0.29	0.25	0.21	0.08	0.15	0.18	-0.01	0.20	0.20
0.75		0.27	0.34	0.35	0.29	0.51	0.47	0.44	0.64	0.64
0.42		0.31	0.00	-0.04	0.06	0.31	1.01	1.41	1.45	1.45
0.30		0.27	0.23	-0.15	0.04	0.35	0.25	0.05	0.06	0.06

Three modes based consensus can be observed to be developed in red colour based on new ensemble snapshots, dominating design space between $0.14 \leq h/sx \leq 0.29$. 38% can be seen as an absolute maximum percentage deviation within this range with an average absolute deviation of around 19%. These three modes can be used for inverse computations of functional surface in design space $0.14 \leq h/sx \leq 0.29$.

Table 4.7: New ensemble based modal variations

h/sx	Modes	1	2	3	4	5	6	Value Taken	Deviation %
0.14		0.46	0.47	0.23	0.30	0.26	0.26	0.23	-37.89
0.50		0.39	0.51	0.79	0.77	0.87	0.87	0.51	-1.96
0.29		0.40	0.37	0.28	0.02	0.13	0.13	0.28	2.04
0.20		0.34	0.23	0.17	0.25	0.09	0.09	0.17	17.65
0.75		0.29	0.32	0.44	0.40	0.25	0.25	0.44	70.45
0.30		0.32	-0.15	0.13	0.19	0.49	0.49	0.32	-6.25

Nine snapshot velocity control points based functional surface inverse design was explored. The process was found least sensitive while prescribing only c or all control points. Gappy inner products and modal coefficients for nine snapshot designs were investigated. Orthogonality was observed among involved computational modes. Furthermore, investigation established extent of mode one dominance based on modal coefficient. A particular range was identified for functional surface inverse design process. It was found that new ensemble based three modes can be used for this process.

4.2.3. Surface shear based inverse design

Local surface wall shear stress is defined as follows:

$$\tau_w = \mu \left. \frac{\partial \bar{u}}{\partial y} \right|_{y=0} \quad (4.6)$$

Derivative can then be computed from the functional form of velocity profile, yielding following form:

$$\tau_w = \mu \frac{cU_{\max}}{\delta} \quad (4.7)$$

Local wall shear stress can be seen directly proportional to control point c , indicating identical spatial distribution.

Local friction factor is hence defined as:

$$f = \frac{\tau_w}{\frac{1}{2}\rho u^2} \quad (4.8)$$

τ_w = Local wall shear stress

$\frac{1}{2}\rho u^2$ = Local kinetic energy density

Here, local kinetic energy density is calculated from local bulk velocity. Figure 4.20 shows obtained geometrical parameter correlation for prescribed local friction factor distribution. Similar to velocity control points, nine high fidelity snapshots depicting local friction factor distribution are used for this investigation. Altogether, nine points are present on the graph. It can be seen that two points are within 15% band while seven points are outside. Farthest point obtained while prescribing local friction factor distribution is when geometrical parameter has an actual value of 0.75 while computed inverse design value deviated by around -165%. The second farthest point has an inverse design value with absolute deviation of 60% from actual value. Two points can also be seen bordering the band indicating deviation close to 15%.

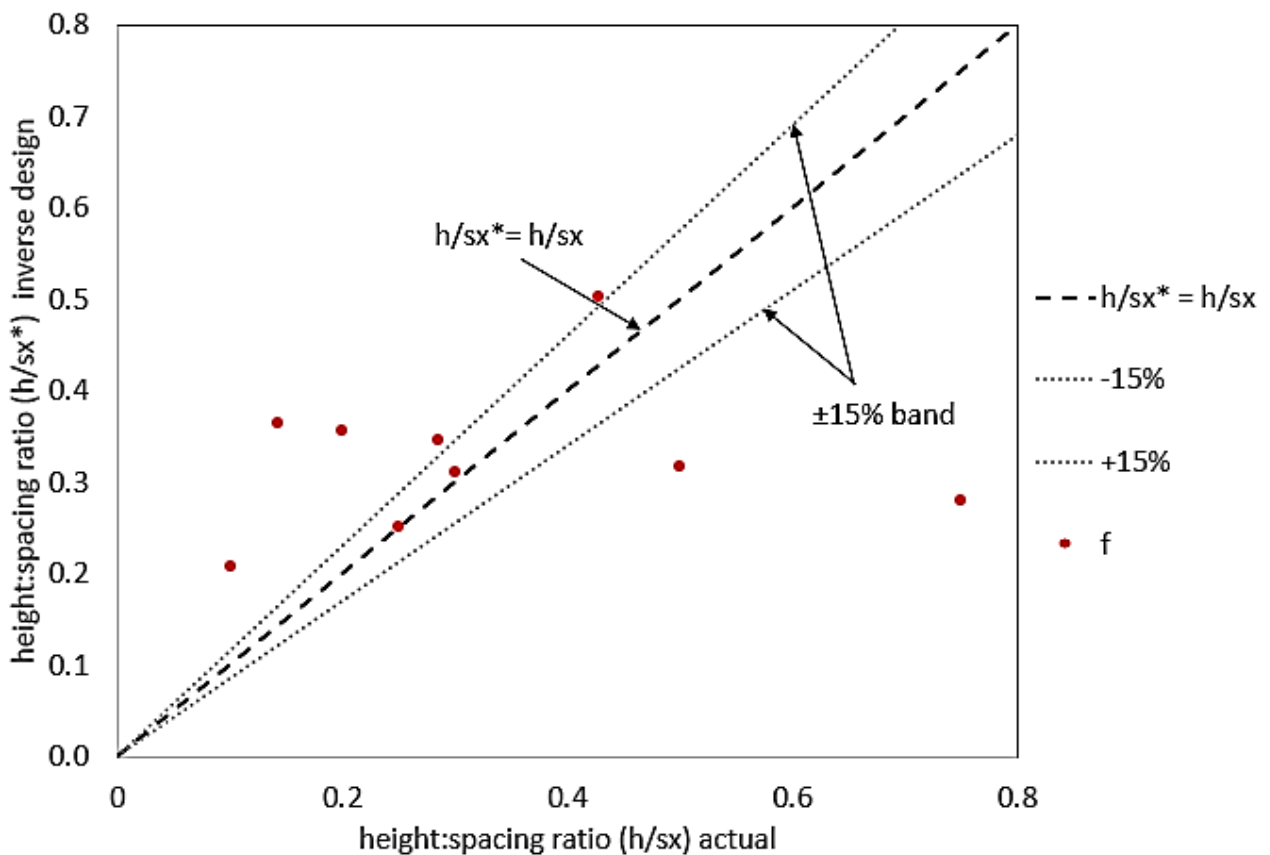


Figure 4.20: Geometrical parameter correlation for friction factor distribution

Table 4.8: Computational modes

No of modes	Computed h/sx	Actual h/sx	Deviation %
1	0.36	0.42	16.67
	0.32	0.50	56.25
	0.35	0.28	-20.00
	0.36	0.20	-44.44
	0.28	0.75	167.86
4	0.25	0.25	0.00
	0.31	0.30	-3.23
6	0.50	0.42	-16.00
8	0.21	0.10	-52.38

Table 4.8 shows computed vs actual geometrical parameter values. The table also shows subsequent number of computational modes required to reach minimum deviation between computed and actual values. It can be seen that inverse design of point $h/sx=0.1$ required highest number of modes while $h/sx=0.42, 0.5, 0.28, 0.2$ and 0.75 required lowest number of modes. It can be noted that mode 1 and 8 records highest absolute deviation of computed value from actual value. This indicates $h/sx=0.1$ and 0.75 is not contained within the subspace spanned by their respective number of modes mentioned in Table 4.8.

As discussed in chapter 3, Gappy inner product computation over support space used respective modes and augmented snapshot vector(\mathbf{g}), leading to matrix \mathbf{M} and vector \mathbf{f} . The modal expansion coefficients are further computed by multiplying inverse \mathbf{M} with \mathbf{f} . Gappy inner product evaluation reveals orthogonality relationship between modes over support space. Evaluating orthogonality becomes computationally important as \mathbf{M} and its inverse goes towards identity matrix for orthogonal modes. This mitigates computational expense for inverse design process.

Modal expansion coefficients can be seen as a direct result of Gappy inner products. While modes are spatial functions, the coefficients are design variable functions. Modes contain dominant flow structure information while the corresponding design-dependant coefficient hints at the extent of modal and associated flow structure dominance. Gappy inner products $((\Phi^i, \Phi^j)_n)$ & $(\mathbf{g}, \Phi^i)_n$ and modal expansion coefficient evolution for Table 4.8 designs are further discussed.

Figure 4.21 show modal Gappy inner product evolution over support space \mathbf{n} and subsequently computed modal coefficients for inverse design of $\mathbf{h}/\mathbf{s}\mathbf{x}=0.42$ and $\mathbf{h}/\mathbf{s}\mathbf{x}=0.5$. It can be noted from Table 4.8 that only one mode was used to inverse design these design points indicating reduction in subspace. Consequently, only one value can be noted for Gappy inner products $(\Phi^i, \Phi^j)_{\mathbf{n}}$ and $(\mathbf{g}, \Phi^i)_{\mathbf{n}}$. As a result, only one modal expansion coefficient was used to compute inverse design value. This significantly reduces incurred inverse design computation expense.

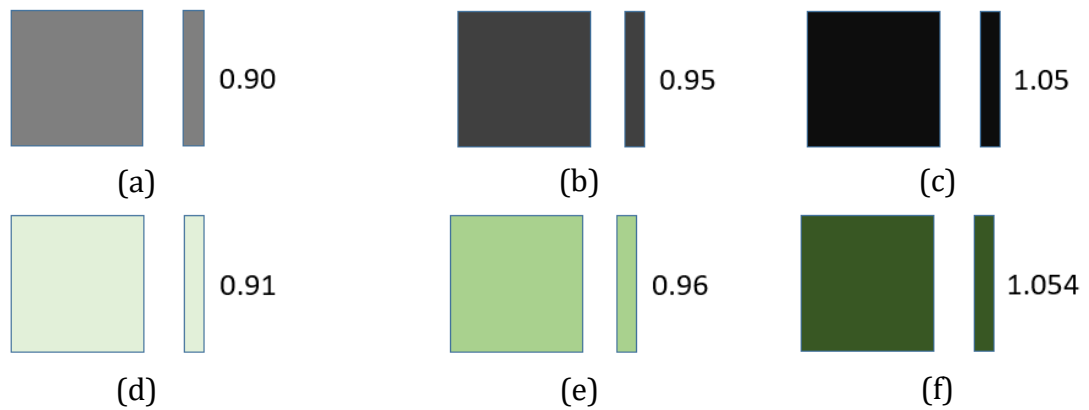


Figure 4.21: (a) Gappy inner product $(\Phi^i, \Phi^j)_{\mathbf{n}}$ (b) Gappy inner product $(\mathbf{g}, \Phi^i)_{\mathbf{n}}$ (c) Modal Coefficient for $\mathbf{h}/\mathbf{s}\mathbf{x}=0.42$; (d) Gappy inner product $(\Phi^i, \Phi^j)_{\mathbf{n}}$ (e) Gappy inner product $(\mathbf{g}, \Phi^i)_{\mathbf{n}}$ (f) Modal Coefficients for $\mathbf{h}/\mathbf{s}\mathbf{x}=0.50$

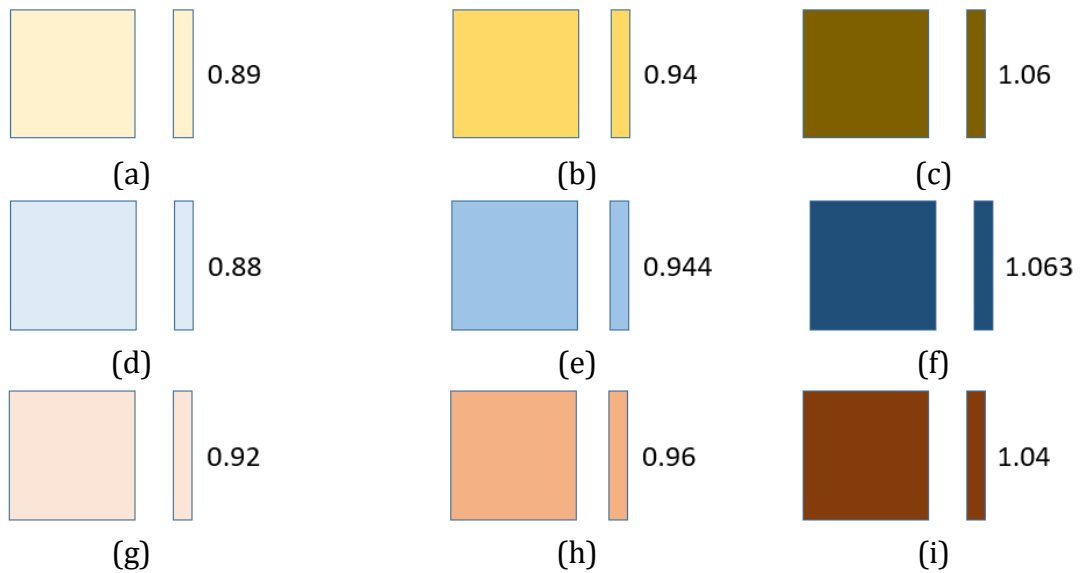


Figure 4.22: (a) Gappy inner product $(\Phi^i, \Phi^j)_{\mathbf{n}}$ (b) Gappy inner product $(\mathbf{g}, \Phi^i)_{\mathbf{n}}$ (c) Modal Coefficient for $\mathbf{h}/\mathbf{s}\mathbf{x}=0.28$; (d) Gappy inner product $(\Phi^i, \Phi^j)_{\mathbf{n}}$ (e) Gappy inner product $(\mathbf{g}, \Phi^i)_{\mathbf{n}}$ (f) Modal Coefficients for $\mathbf{h}/\mathbf{s}\mathbf{x}=0.20$; (g) Gappy inner product $(\Phi^i, \Phi^j)_{\mathbf{n}}$ (h) Gappy inner product $(\mathbf{g}, \Phi^i)_{\mathbf{n}}$ (i) Modal Coefficient for $\mathbf{h}/\mathbf{s}\mathbf{x}=0.75$

Figure 4.22 shows Gappy inner products over support space \mathbf{n} and corresponding modal coefficients for inverse design of $\mathbf{h}/\mathbf{sx}=0.20, 0.28$ and 0.75 . It can be noted from the figure that subspace has been reduced to one, as only one mode is used for computation. It can be noted from Table 4.8 that only one mode was used to inverse design these design points indicating reduction in subspace. Consequently, only one value can be noted for Gappy inner products $(\Phi^i, \Phi^j)_n$ and $(\mathbf{g}, \Phi^i)_n$. As a result, only one modal expansion coefficient was used to compute inverse design value. This significantly reduces incurred inverse design computation expense.

Figure 4.23 shows Gappy inner products over support space \mathbf{n} and corresponding modal coefficients for inverse design of $\mathbf{h}/\mathbf{sx}=0.25$ and 0.30 . It can be noted from the figure that subspace has been reduced to four, as only four modes are used for computation. Furthermore, orthogonality can be seen to be maintained by third and fourth mode. In both cases, Gappy inner product $(\Phi^i, \Phi^j)_n$ can be seen to be non-identical symmetric matrix, while modal coefficients maintained non-negative values. This significantly imposes computational cost for computing inverse \mathbf{M} and further expand solution over four modes subspace.

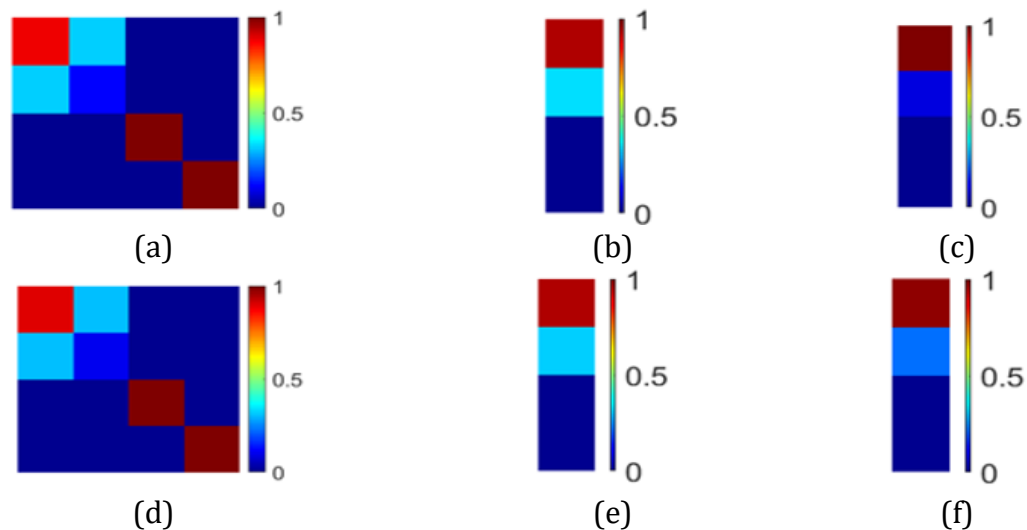


Figure 4.23: (a) Gappy inner product $(\Phi^i, \Phi^j)_n$ (b) Gappy inner product $(\mathbf{g}, \Phi^i)_n$ (c) Modal Coefficient for $\mathbf{h}/\mathbf{sx}=0.25$; (d) Gappy inner product $(\Phi^i, \Phi^j)_n$ (e) Gappy inner product $(\mathbf{g}, \Phi^i)_n$ (f) Modal Coefficients for $\mathbf{h}/\mathbf{sx}=0.30$

INVERSE DESIGN OF FUNCTIONAL SURFACES CONTAINING SIMPLE DISCONTINUOUS GEOMETRY
 STRUCTURE FOR PRESCRIBED SIMPLE FLOW CHARACTERISTICS

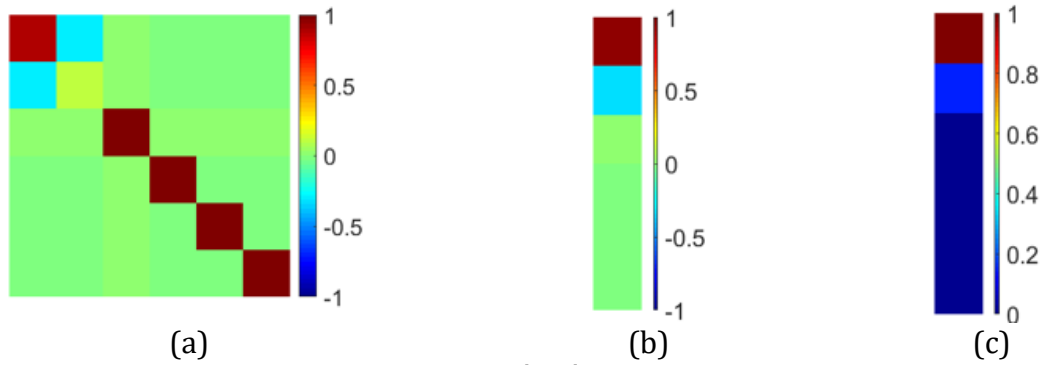


Figure 4.24: (a) Gappy inner product $(\Phi^i, \Phi^j)_n$ (b) Gappy inner product $(g, \Phi^i)_n$
 (c) Modal Coefficient for $h/sx=0.42$

Figure 4.24 shows Gappy inner products over support space n and corresponding modal coefficients for inverse design of $h/sx=0.42$. It can be noted that subspace have been reduced to six modes. Overall observation can be made that orthogonality have propagated beyond first two modes and hence most of the subspace contains orthogonal modes. Gappy inner product $(\Phi^i, \Phi^j)_n$ can now be seen to be almost identical symmetric matrix. Modal coefficients maintain non-negative values with largest value being for first modal coefficient indicating extent of first mode dominance. However, non-orthogonal modal presence and solution expansion over six modes increases computation expense.

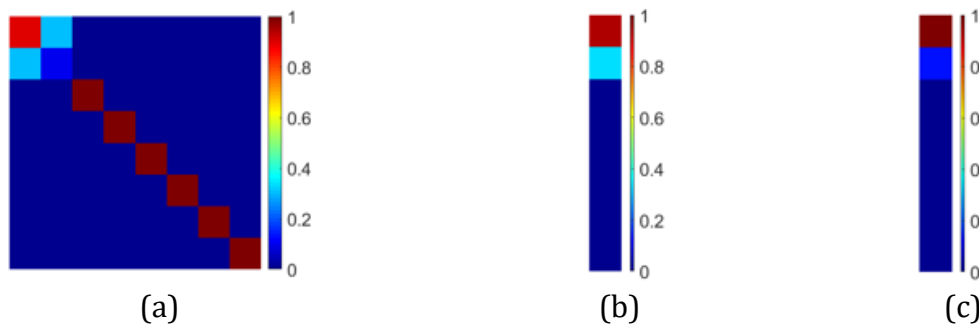


Figure 4.25: (a) Gappy inner product $(\Phi^i, \Phi^j)_n$ (b) Gappy inner product $(g, \Phi^i)_n$
 (c) Modal Coefficient for $h/sx=0.1$

Figure 4.25 shows Gappy inner products over support space n and corresponding modal coefficients for inverse design of $h/sx=0.1$. It can be noted that subspace have been reduced to eight modes. Overall observation can be made that orthogonality have propagated beyond first two modes and hence most of the subspace contains orthogonal modes. Gappy inner product $(\Phi^i, \Phi^j)_n$ can now be seen to be almost identical symmetric matrix. Modal coefficients maintain non-negative values with largest value being for first modal coefficient indicating extent of first mode dominance.

A suitable h/sx range with stipulated number of modes can be identified for surface shear based inverse design process. Table 4.9 shows modal design variations based on original nine snapshot ensemble. Closest computed values to design points are shown in yellow. As noted in figure 4.20, table 4.9 shows maximum deviation for five design points $h/sx = 0.1, 0.14, 0.2, 0.5$ and 0.75 . Furthermore, no proper consensus can be seen to have developed between computed inverse design values and number of computational modes used. This deters from defining a range over which particular mode can be seen to be active.

A new snapshot ensemble can be created by discarding snapshots for design points $h/sx = 0.1, 0.14, 0.2, 0.5$ and 0.75 , which were outside (outliers) stipulated error band as shown in figure 4.20, from original ensemble. This further illustrates that the outliers and inliers (points within error band) might not be sharing same dominating flow structures. Table 4.10 shows modal design variations based on new snapshot ensemble.

Table 4.9: Original ensemble based modal variations

h/sx	Modes	1	2	3	4	5	6	7	8	9
0.25		0.35	0.28	0.30	0.25	0.26	0.18	0.20	0.16	0.16
0.14		0.36	2.20	9.96	34.59	58.66	54.57	56.87	58.62	58.62
0.10		0.37	0.27	0.27	0.30	0.30	0.23	0.23	0.21	0.21
0.50		0.32	-2.42	-2.94	-1.38	-0.19	0.96	0.93	0.89	0.89
0.29		0.35	1.28	0.61	0.50	0.47	0.12	0.12	0.59	0.59
0.20		0.36	7.06	30.92	65.13	108.19	100.05	98.36	96.05	96.05
0.75		0.28	0.05	0.05	0.05	-0.52	-0.83	-0.99	-0.88	-0.88
0.43		0.33	-3.58	-4.23	-1.58	0.02	0.50	1.05	1.28	1.28
0.30		0.34	6.63	1.61	0.31	0.28	0.43	-0.21	-0.27	-0.27

Table 4.10: New ensemble based modal variations

h/sx	Modes				Value Taken	Deviation %
	1	2	3	4		
0.25	0.34	0.30	0.17	0.17	0.34	-26.33
0.29	0.33	0.44	0.34	0.34	0.33	-12.88
0.43	0.28	0.21	-1.13	-1.13	0.28	53.77
0.30	0.32	-0.21	-1.69	-1.69	0.32	-7.14

Closest computed value to actual h/sx is highlighted in yellow and red. One mode based consensus can be observed to be developed in red colour based on new ensemble snapshots, dominating design space between $0.25 \leq h/sx \leq 0.30$. Around 26% can be seen

as an absolute maximum percentage deviation within this range with an average absolute deviation of around 15%. One mode based on new snapshot ensemble can be used for inverse computations of functional surface in design space $0.25 \leq \mathbf{h}/\mathbf{sx} \leq 0.30$.

Nine snapshot friction factor based functional surface inverse design was explored. Sensitivity investigation showed only four design snapshots sharing common dominant modes. Gappy inner products and modal coefficients for nine snapshot designs were investigated. Non-orthogonality was observed among first two computational modes. Furthermore, investigation established extent of mode one dominance based on modal coefficient for all design points. A particular range was identified for friction factor based functional surface inverse design process. It was found that new ensemble based one mode can be used for this process.

4.3. Innovative Low Fidelity based Functional Surface Inverse Design Environment (LFF-SIDE)

Following above investigation, it was established that for a prescribed velocity control point distribution, functional surface inverse design required three modes based on new snapshot ensemble as in Table 4.7. Similar investigation led to a conclusion that for prescribed friction factor distribution, functional surface inverse design required one mode, computed based on new snapshot ensemble as in Table 4.10. Error level decreased for new ensemble snapshot of velocity control points and friction factor. Furthermore, a range was established over which functional surface inverse design computation might work for respective prescription criterion. This section establishes inverse design environment for functional surface applicable for identified range.

Environment consist of following major components:

- High fidelity module
- Snapshot Ensemble
- Optimizer
- Low fidelity module/Geometry Generator

Figure 4.26 shows proposed LFF-SIDE novel architecture. The architecture capitalises on low fidelity POD approach for designing functional surface. The optimizer computes the required POD coefficients based on Gappy data provided. A new geometry is generated in each iteration, along with its flow field characteristics (control point or friction factor distribution). The newly generated geometry and corresponding flow field characteristic are checked against user-specified design bounds. The cycle continues until optimiser achieves an optimum geometry. Each component of the environment is further discussed as follows.

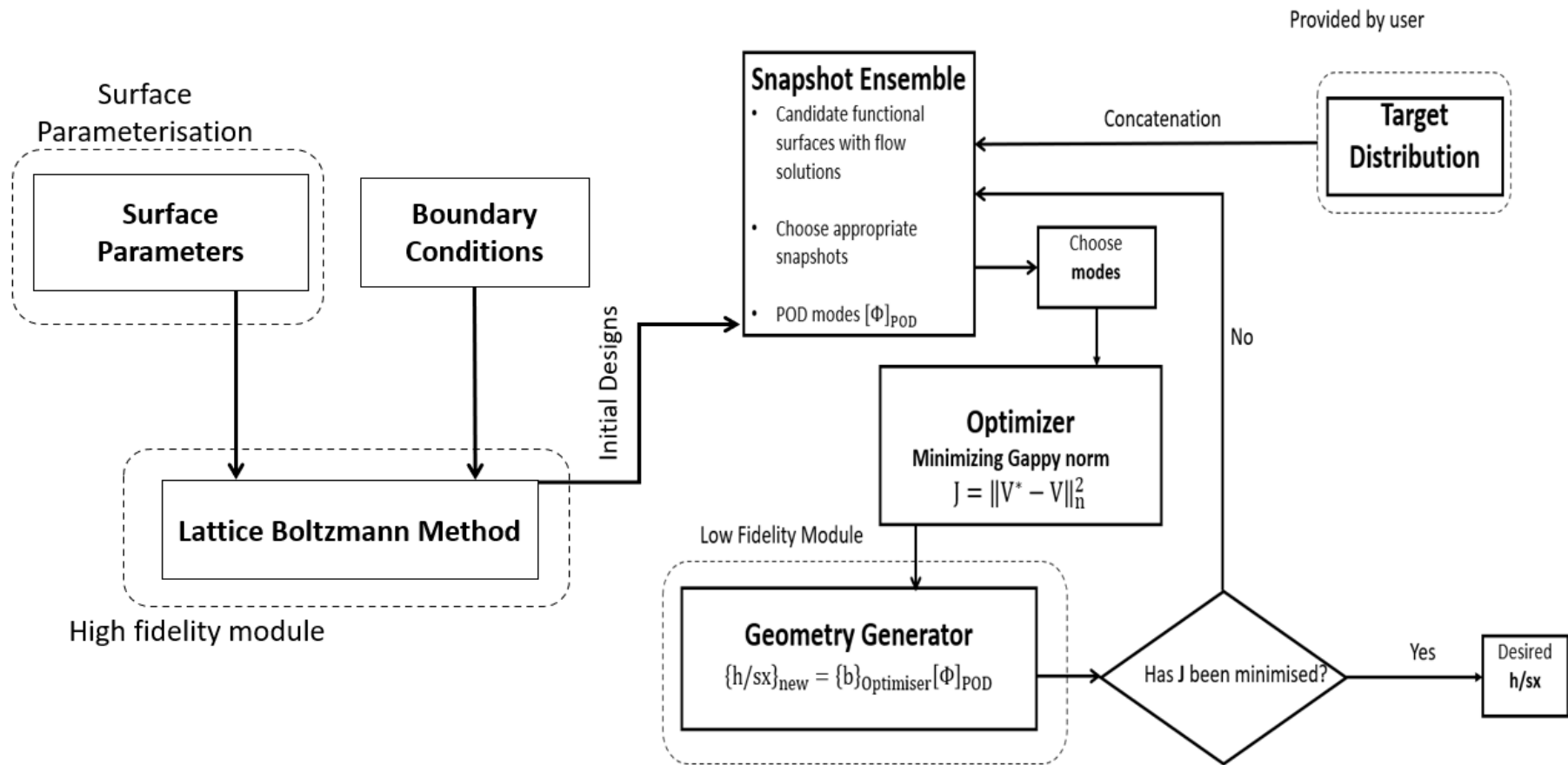


Figure 4.26: LFF-SIDE Architecture

4.3.1. High fidelity module

High fidelity module forms one of the key elements of LFF-SIDE architecture. It contains Lattice Boltzmann solver that computes flow solution to different functional surfaces. The solver is written in C and unlike other Navier-Stokes solvers, lattice Boltzmann is relatively easy to programme with a capability of further integration to other available platforms. The module produces flow snapshots for snapshot ensemble.

Surface parameters and boundary conditions forms an input to high fidelity module. By parametrising, different functional surfaces are obtained with varying height and spacing within the bumps. This builds functional surface design space from family of candidate configurations. As a result, design space is built for exploration. Flow field for these functional surfaces are computed with each computation taking ~15 days CPU time on Intel i6 @3 GHz processor. Similar boundary conditions are taken for flow field calculation of these surfaces to extract design change flow field variation. The following modules are written in MATLAB script with a CPU runtime of less than 0.5 seconds on Intel i7 @3.4 GHz processor.

4.3.2. Snapshot Ensemble

The computed flow fields for respective functional surfaces is collectively passed down as initial designs to snapshot ensemble. Ensemble augments these snapshots with their respective functional surface geometry parameters. Thus, each column of the resultant snapshot matrix starts with geometry parameters followed by corresponding flow characteristics.

The two flow characteristics that are considered for prescription are: velocity control points and friction factor. Distribution of either can be specified as target to be achieved for inverse design process. As established, velocity control points prescription requires only three augmented snapshots while friction factor prescription requires one. These respective number of snapshots are used to compute orthogonal modes within iterative process. Thus, choice of appropriate snapshots is reflected in target to be achieved. Once target flow characteristics is decided followed by appropriate snapshot choice, number of orthogonal modes required for inverse design process is chosen. For velocity control point distribution, it was established that three modes can be utilized while for friction factor distribution one mode can be utilized.

Target distribution is concatenated as an additional column to constructed snapshot ensemble with first two rows containing surface information. Given the absence of surface information,

the particular element is initially filled as zero. This element is replenished in subsequent optimization run.

4.3.3. Optimizer

The optimizer aids in actual task of computing missing functional surface geometry parameter. This is achieved by minimising Gappy cost function (J) between target distribution (V^*) and achieved distribution (V) at each iteration. Optimizer produces modal coefficients as a result of this minimisation. Optimisation can further be relaxed in an attempt to improve on convergence.

4.3.4. Low fidelity module/Geometry Generator

Computed modal coefficients within optimizer are further passed down to low fidelity module. The coefficients are combined with respective orthogonal modes to compute missing functional surface parameter. Based on set convergence criterion, missing element within snapshot ensemble is replenished with newly computed value.

4.3.5. Advantages of LFF-SIDE

The environment established in the previous section derives its robustness from using low fidelity representation of a high-fidelity system. This preserves the essential features that dictates dynamic system. Some of the advantages of this environment are listed below:

1. A better control on optimisation can be achieved by building relevant snapshot ensemble. The ensemble can reflect 'designer's experience' that injects prior designing knowledge into optimisation process.
2. A faster flow field evaluation is achieved for intermediate functional surfaces that are generated within optimisation iteration. These intermediate functional surfaces and corresponding flow field can be further included to expand design space based on Gappy cost function.
3. Reduced computation time to derive functional surface.

4.3.6. Limitations of LFF-SIDE

Although functional surface design environment offers major benefits for effective and faster optimization process, there are certain limitations, as listed below:

1. The current environment is applicable for inverse design of functional surface for geometrical parameter falling in below range:

$0.2 \leq \mathbf{h}/\mathbf{sx} \leq 0.3$ for **control points** prescription

$0.29 \leq \mathbf{h}/\mathbf{sx} \leq 0.75$ for **friction factor** prescription.

2. The prescribed target (control points or friction factor distribution) is assumed to be contained within the subspace spanned by relevant modes.

4.4. Summary

In summary, study found computed functional form for high fidelity velocity data. Using least square fit, control points were computed along with its local spatial distribution. Modal analysis revealed governing flow structures and corresponding flow sensing positions. The identified flow structures were further exploited for control point and friction factor based functional surface inverse design. Sensitivity analysis revealed control point prescription. Further investigation focused on Gappy inner product and modal orthogonality. Extent of modal structure dominance was established. Based on new snapshot ensemble, a subspace was identified along with particular number of modes in operation for prescribed control point and friction factor distribution. Furthermore, a novel functional surface design environment for identified subspace was established for prescribed control points and friction factor distribution.

CHAPTER 5

INVERSE DESIGN OF FUNCTIONAL SURFACES CONTAINING SIMPLE DISCONTINUOUS GEOMETRY STRUCTURE FOR PRESCRIBED COMPLEX FLOW CHARACTERISTICS

Bio-inspired functional surface application within flow handling systems is sought after. This application potentially can reduce drag and improve on to flow handling system pumping efficiency. Controlled pressure drop can be another added advantage to avoid cavitation, vibration, acoustic noise etc. Chapter 2 discussed relevant control valve literature that highlighted these problems. It also discussed control valve trim-based flow control. The following chapter introduces inverse design methodology for a control valve trim for a prescribed complex flow characteristic. Specifically, inverse design trim cylinder elements to achieve targeted local flow capacity distribution. Local flow capacity was found to be influenced by pressure drop across each cylinder along with flow rate. Changes in cylinder radii brought in design variations within parameter space. Utilising computed design space, a relationship was developed between geometrical parameters and local flow capacity. This relationship was exploited to expand design space. Gappy POD inverse design methodology exploited the expanded design space to obtain geometrical parameters corresponding to the targeted local flow capacities. A framework is proposed for this inverse design.

5.1. Introduction

Globe type control valve forms an integral part within flow handling systems in power plants, oil and gas and nuclear industry. Trim is an essential control valve component that regulates flow. In thesis introduction, flow capacity was introduced as a valve global performance evaluator and was seen to embed global flow information. It was introduced that conventional control valve design methodology uses sizing equations in conjunction with global flow capacity multi-stage control valve design. However, the conventional design methodology fails to undertake into account local flow behaviour responsible for cavitation, vibration, noise etc. Furthermore, Chapter 2 discussed relevant literature establishing flow three dimensionality within control valve. Chapter also described previous work carried out on local geometrical feature influence over local flow behaviour.

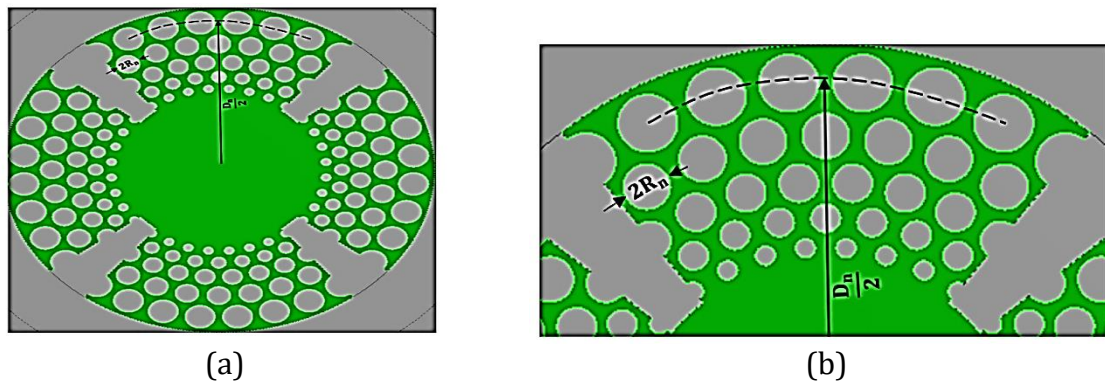


Figure 5.1: (a) Trim disc (b) Quarter disc with dimensions

Conventional control valve design methodology follows top-down approach of prescribing global performance indicator and deriving corresponding local geometrical features. This chapter introduces bottom-up design methodology of deriving local geometrical features for prescribed multi-stage trim local performance indicators. The discussions and results are limited to globe type control valve. Figure 5.1 shows multi-stage continuous resistance trim top disc along with cylinder element dimensions. Top

disc choice is justified as it has been reported in previous investigations outlined in chapter 2. It can be seen that single trim disc have five rows with each row cylindrical elements radius as R_n while $\frac{D_n}{2}$ is the radial cylindrical elements row position from trim disc centre determining trim size. Here n represents row number. The flow is radially inwards with cylinder radius decreasing from trim out to inside. Individual discs are stacked to form trim as shown in figure 5.2.

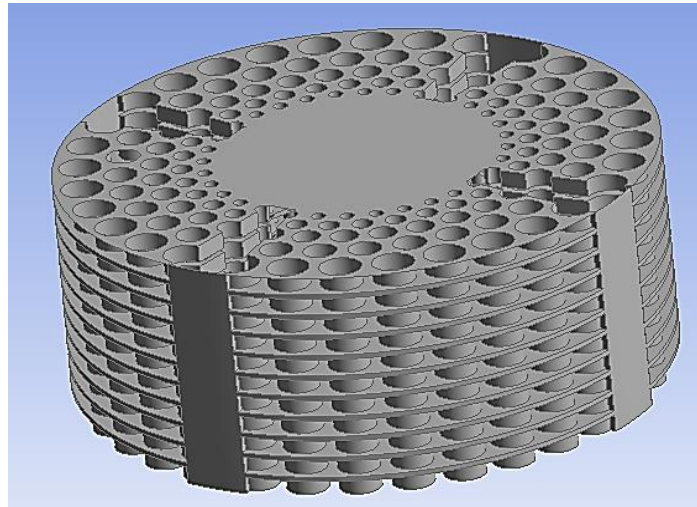


Figure 5.2: Stacked trim discs

Asim *et al.* [110] studied relationship between local hydrodynamic characteristic and local geometrical features within globe type control valve trim. Study involved performing design of experiments for perturbed cylinder diameters for row 1 to 5. Row cylinder dimensions varied as $R_1:0.003\text{m}-0.0024\text{m}$; $R_2:0.002375\text{m}-0.0019\text{m}$; $R_3:0.002\text{m}-0.0016\text{m}$; $R_4:0.0015\text{m}-0.0012\text{m}$ and $R_5:0.001\text{m}-0.0008\text{m}$ with trim size determined by $D_1:0.038\text{m}$; $D_2:0.033$; $D_3:0.028\text{m}$; $D_4:0.024\text{m}$ and $D_5:0.021\text{m}$. Trim and cylinder dimensions were selected based on associated manufacturing feasibility and cost limitations. Total 25 geometrical combinations (designs) were identified subsequently computing corresponding flow solutions. Computed pressure and mass flow rate value for individual design were further utilised to calculate individual row local flow capacity.

As mentioned, Chapter 2 provided relevant literature that established local geometrical feature influence over local flow behaviour within control valve trim. This chapter starts by introducing regression analysis for design space spanned by 25 designs of Asim *et al.* [110]. The analysis is carried out to show cumulative quantitative and quantitative local row cylinder dimensional change influence on local row flow capacity. Local geometrical changes precipitates in the form of local flow area expansion or contraction. Pressure drop decreases with flow area expansion and vice versa. This subsequently increases or decreases trim flow capacity. However, this observation is limited to certain critical limit as discussed by Asim *et al.* [70]. In regression analysis, local row cylinder radius is scaled with radial cylinder row diameter to form non-dimensional parameter. This is to maintain equation homogeneity. The non-dimensional parameter is further integrated within regression equation formulation to expand design space.

Following equation shows numerical simulations-based regression model for local row cylinder:

$$Cv_n = 10^{P_1} \times \left(\frac{R_1}{D_1}\right)^{P_2} \times \left(\frac{R_2}{D_2}\right)^{P_3} \times \left(\frac{R_3}{D_3}\right)^{P_4} \times \left(\frac{R_4}{D_4}\right)^{P_5} \times \left(\frac{R_5}{D_5}\right)^{P_6} \quad (5.1)$$

Here,

Cv_n = nth row flow capacity

$\frac{R_n}{D_n} = \frac{\text{Radius of nth row cylinders}}{\text{nth row centre line diameter}}$

P_i = ith power coefficient of design parameter

As mentioned, R_n and D_n are design parameters dictates nth row cylinder radii and centre line diameter respectively while corresponding local flow capacity Cv_n measures nth row flow capacity. Equation relates non-dimensional trim design parameters to local row flow capacity. It is a multivariable equation derived by maintaining dimensional homogeneity and shows cumulative influence of design parameters on local row flow capacity. Table 5.1 lists important regression statistics. It shows computed R Square value along with power coefficients for different local row flow capacities. The power coefficient values determine non-dimensional design parameters individual extent of influence on

respective local flow capacity. As an example, table 5.1 shows considerable $\frac{R_1}{D_1}$ influence as its absolute power coefficient value is relatively highest.

Table 5.1: Power coefficients for respective local flow capacity

R Square=0.96					
	P2	P3	P4	P5	P6
Cv1	-2.44	0.05	0.08	0.05	0.13
Cv2	1.02	-2.00	-0.33	-0.06	0.02
Cv3	0.11	0.43	-2.05	-0.16	-0.05
Cv4	-0.06	0.13	0.54	-1.26	0.19
Cv5	0.06	0.10	0.46	0.13	-1.02

Figure 5.3 plots between regression computed and actual local flow capacities. It can be seen that regression computed flow capacities have excellent correlation with actual flow capacities demonstrating regression computed data accuracy obtained for 25 designs. However, a single point outlier can be noticed for second row flow coefficient.

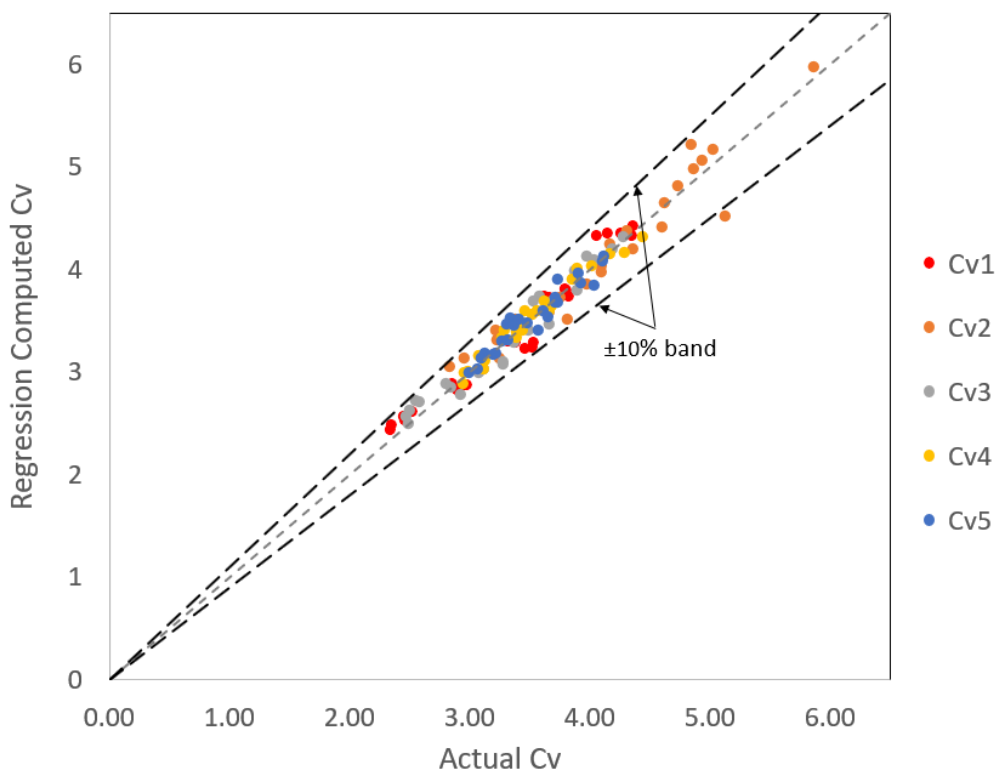


Figure 5.3: Regression vs actual local flow capacities correlation

5.2. Qualitative and quantitative description

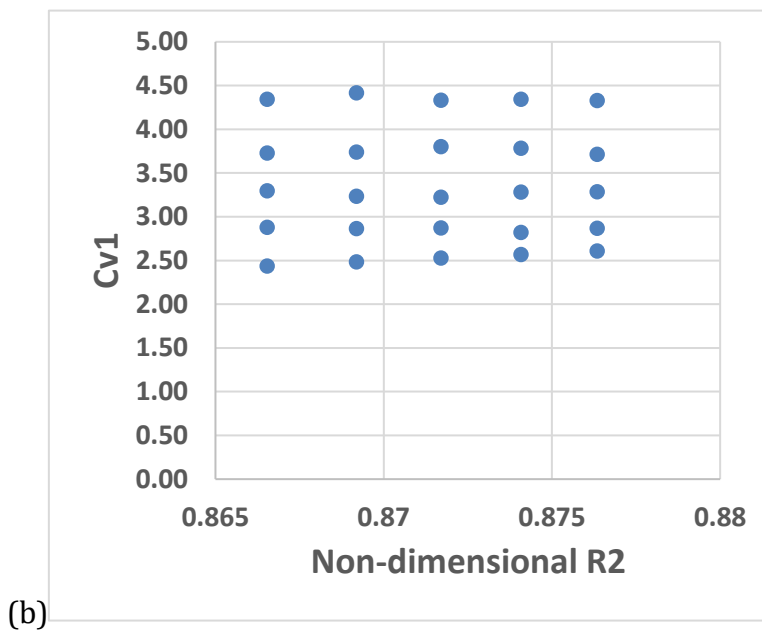
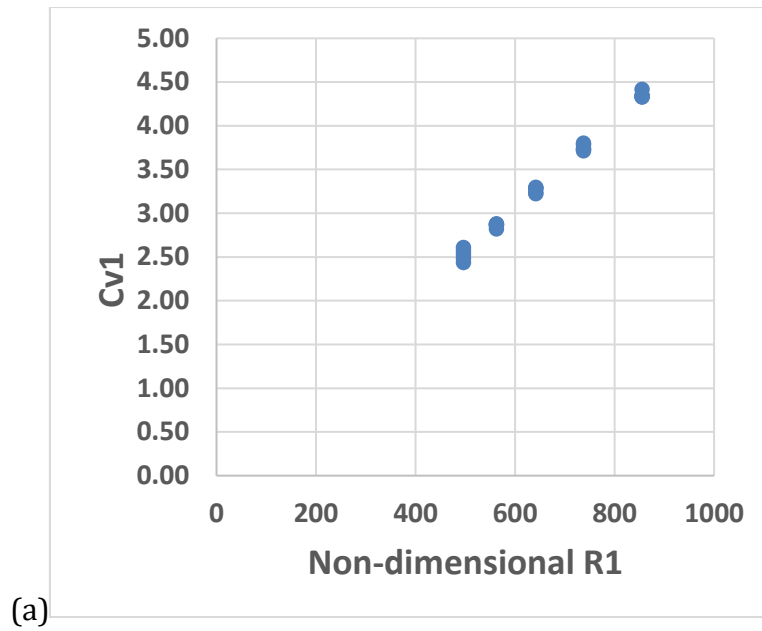
This section describes individual design parameters qualitative and quantitative influence on local flow capacities. The graphs shown in this section plots individual row flow capacity on y-axis against non-dimensional design parameter $\left(\frac{R_i}{D_i}\right)^{P_{i+1}}$ on x-axis. Here R_i , D_i and P_{i+1} are i th row cylinder radius, chord radius and coefficient respectively. R_i and D_i are trim design parameters and are non-dimensional w.r.t each other for design generalisation.

5.2.1. Influence on Cv1

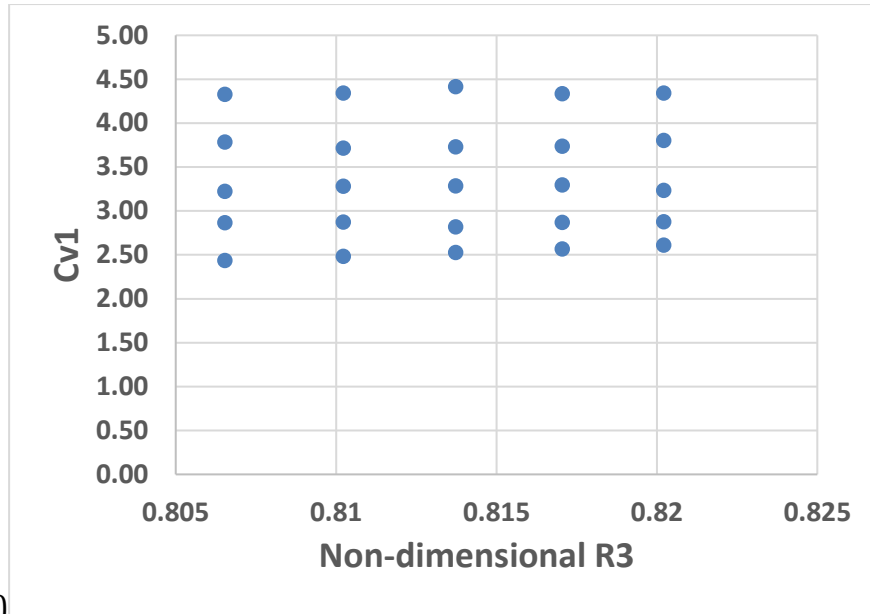
Figure 5.4 shows the influence of design perturbation on row one flow capacity. Overall observation of R1 being the influential parameter among the radii can be made. The possible reason might be increased pressure drop across first row cylinder due to decrease in flow area. It can also be seen that R3 and R4 does not have significant effect on row one flow capacity. This shows insignificant effect of cumulative flow area change in row three and four. A monotonously linear decrease of flow capacity with non-dimensional R1 can be seen.

This is due to flow area decrease with subsequent pressure drop increase across individual cylinders. The rate of this decrease is observed to be around 0.005. Maximum variation in non-dimensional R1 was observed to be around 13%. Relatively much less variation is observed for flow capacity with other non-dimensional design parameters indicating lesser influence. The maximum variations in other respective non-dimensional design parameters are around 1%, 2%, 1%, 3% and 15% respectively. Although a significant variation can be noted for non-dimensional R5, this change was observed not to play key role in the cumulative effect to change row one flow capacity. This is due to no significant flow area change with non-dimensional R5. The only notable change with non-dimensional R5 in flow capacity was observed from around 4.2 to 5.

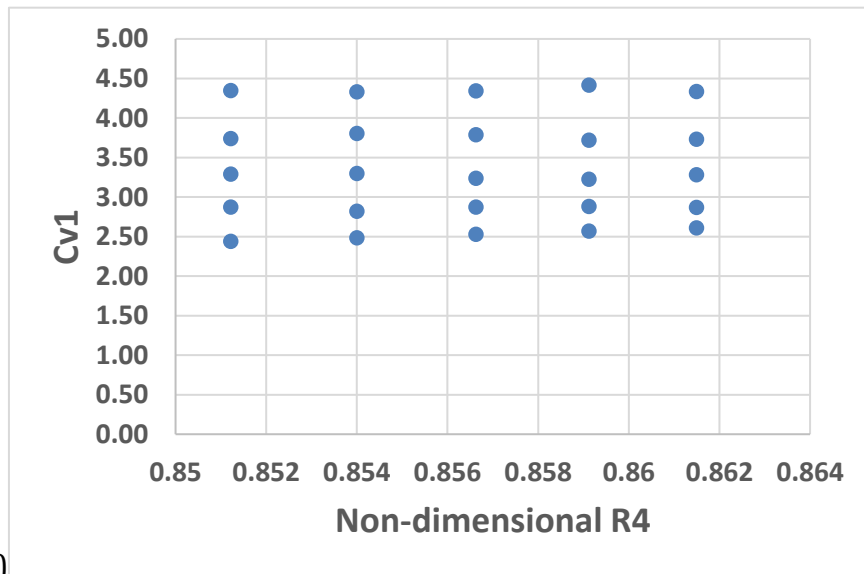
INVERSE DESIGN OF FUNCTIONAL SURFACES CONTAINING SIMPLE DISCONTINUOUS GEOMETRY
 STRUCTURE FOR PRESCRIBED COMPLEX FLOW CHARACTERISTICS



INVERSE DESIGN OF FUNCTIONAL SURFACES CONTAINING SIMPLE DISCONTINUOUS GEOMETRY
 STRUCTURE FOR PRESCRIBED COMPLEX FLOW CHARACTERISTICS



(c)



(d)

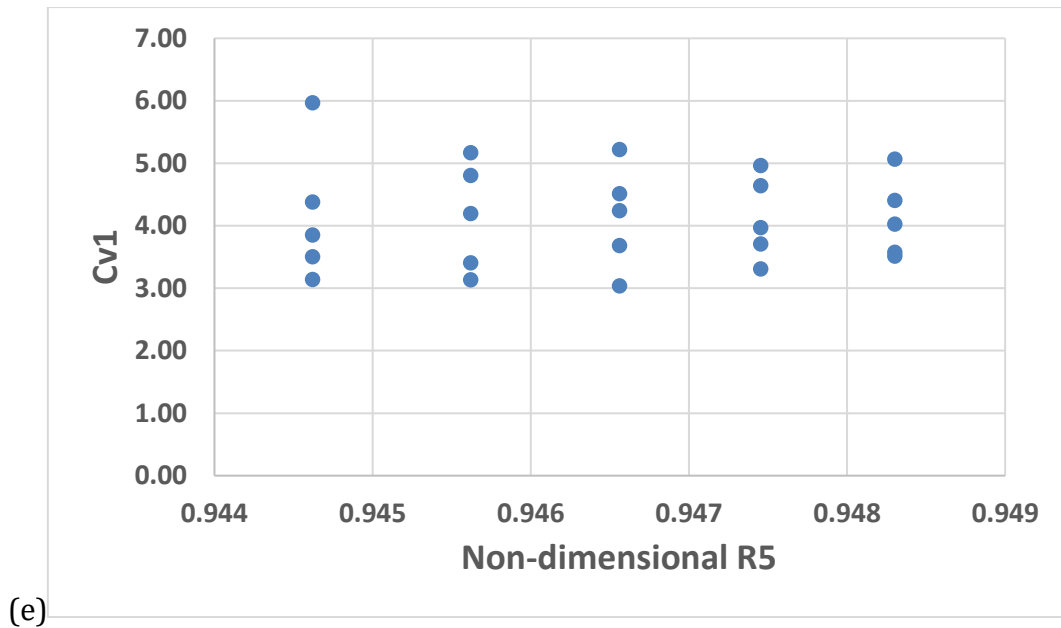


Figure 5.4 (a)-(e): Row one flow capacity variation with design points

As previously mentioned, the influence of individual terms in the regression equation on respective local flow capacities are determined by the power coefficient of that term. It can be noted from table 5.1, power P1 is highest when calculating row one flow capacity indicating greater influence of non-dimensional R1. The other coefficients have relatively lower values indicating lesser influence. Although lesser influence, other non-dimensional design parameters do play a part in cumulative effect. Observed change of 2% in the graph of non-dimensional R1 is the cumulative effect brought in by other design parameters at constant non-dimensional R1. On the contrary, graphs of other design parameters show increase in local flow capacity at constant non-dimensional design parameter. This can be attributed to the fact that non-dimensional R1 has greater amount of influence than other design parameters.

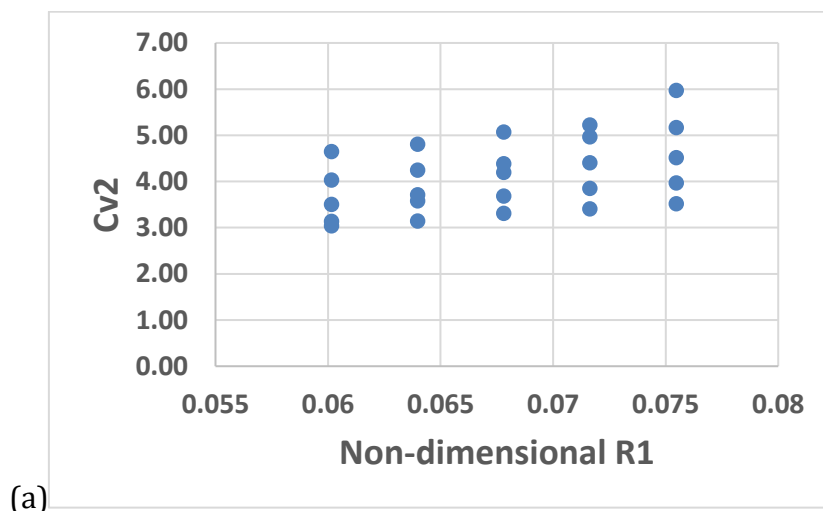
Cumulative effect of radii perturbation on respective local flow capacities is observed since the flow system is continuum. It can be seen that for row 1 flow capacity this effect might only be dominated by R1 due row 1 local flow area reduction with an increase in R1. This decreases mass flow rate and increases pressure drop across row 1 cylinders, consequently decreasing row 1 flow capacity. On the contrary, row 1 flow capacity can be

seen to be almost unaltered by R2, R3, R4 and R5 change. This can be attributed to local flow area contraction and expansion due local geometrical changes (Asim 2019).

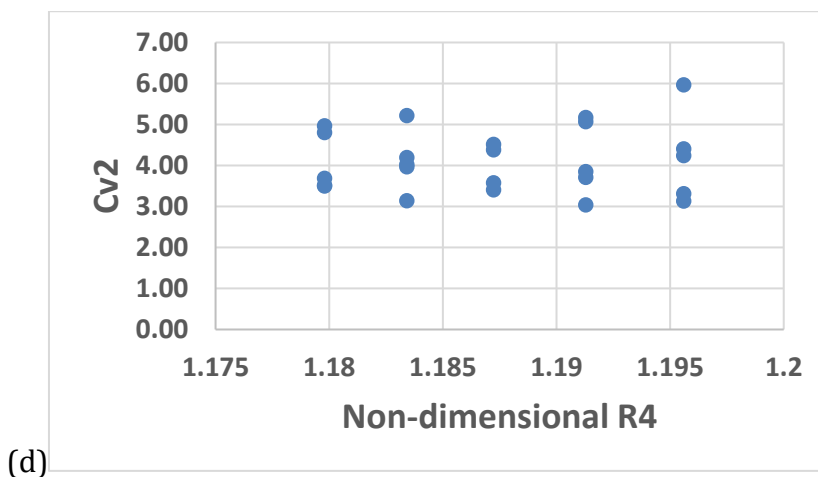
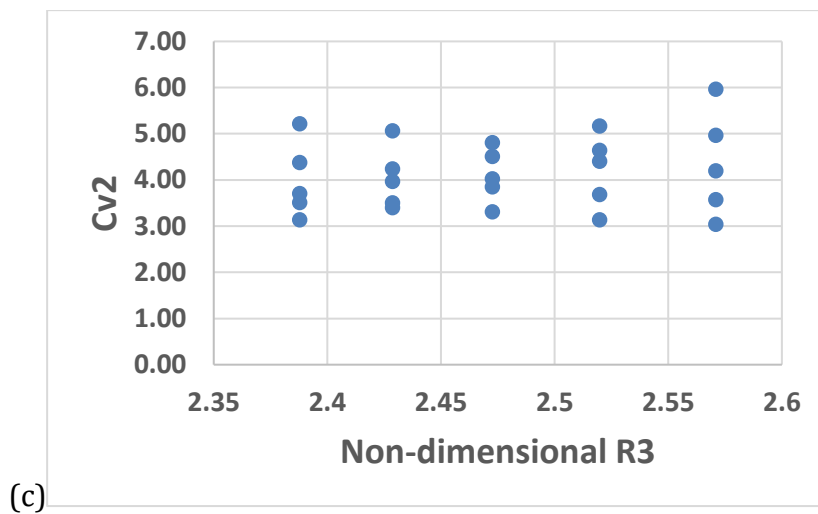
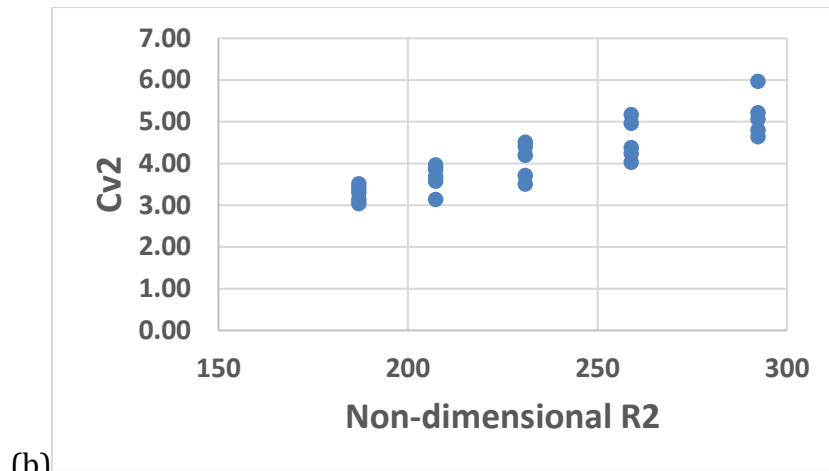
5.2.2. Influence on Cv2

Figure 5.5 shows flow capacity change with design point variation. It can be observed that design parameters R1 and R2 both affect the row two flow capacity. R2 has steepest slope while R1 has relatively less steep slope. This observation can be attributed to relative flow area change in row one and two. R1 change affects downstream pressure, implicitly affecting pressure drop across row two cylinders while R2 change affects the immediate flow area and pressure drop across row two cylinders. Compared to figure 5.4, it can be seen that both R1 and R2 affect the row two flow capacity. A maximum geometrical variation of around 56% can be seen for R2. Such variation affects the row two flow capacity almost by 75%. A non-significant change is observed in flow capacity with a change in other design parameters.

Complex interaction between first and second row flow area change resulted in cumulative effect on row two flow coefficient. This complex interaction is mostly in the form of mass flow and pressure drop change across row two cylinders. These flowfield changes are further reflected in row two flow capacity.



INVERSE DESIGN OF FUNCTIONAL SURFACES CONTAINING SIMPLE DISCONTINUOUS GEOMETRY
 STRUCTURE FOR PRESCRIBED COMPLEX FLOW CHARACTERISTICS



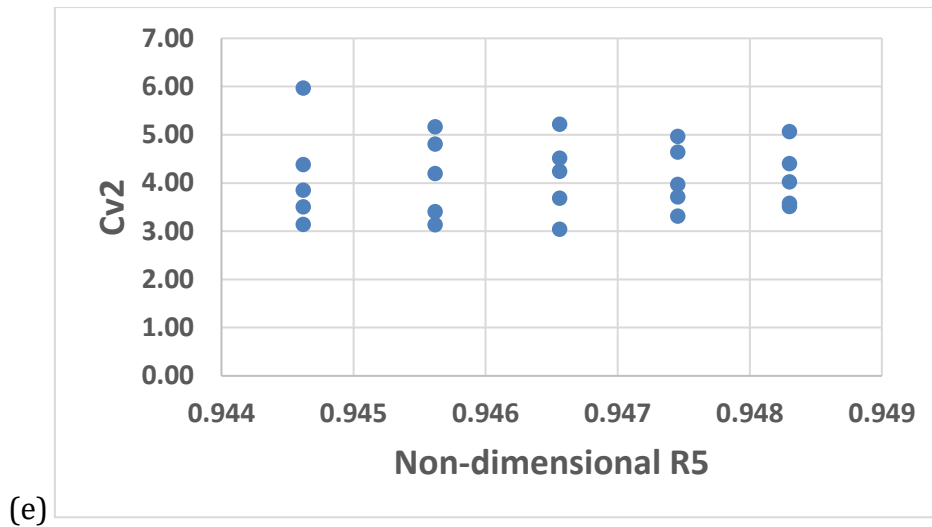


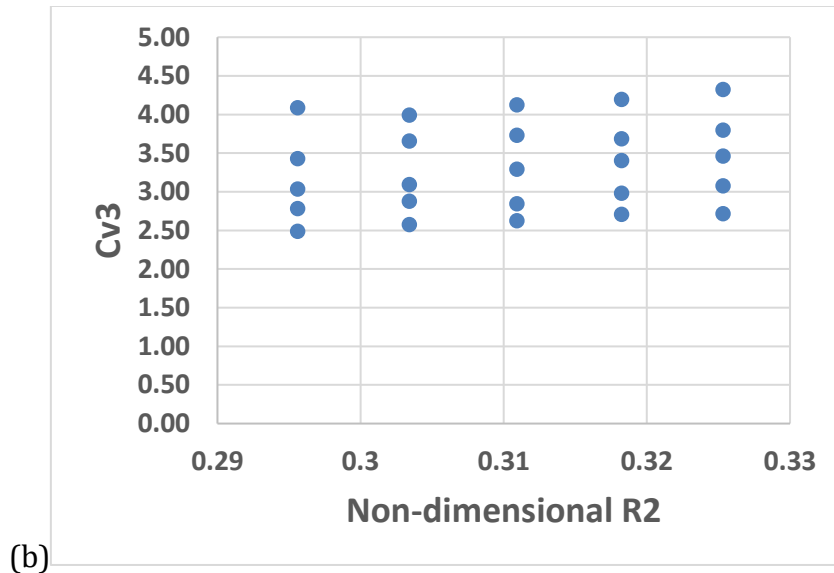
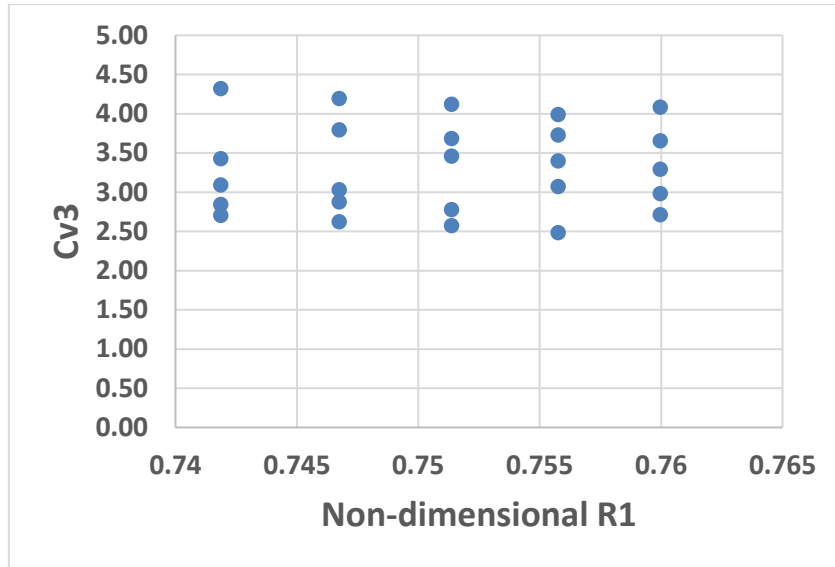
Figure 5.5 (a)-(e): Row two flow capacity variation with design points

5.2.3. Influence on Cv3

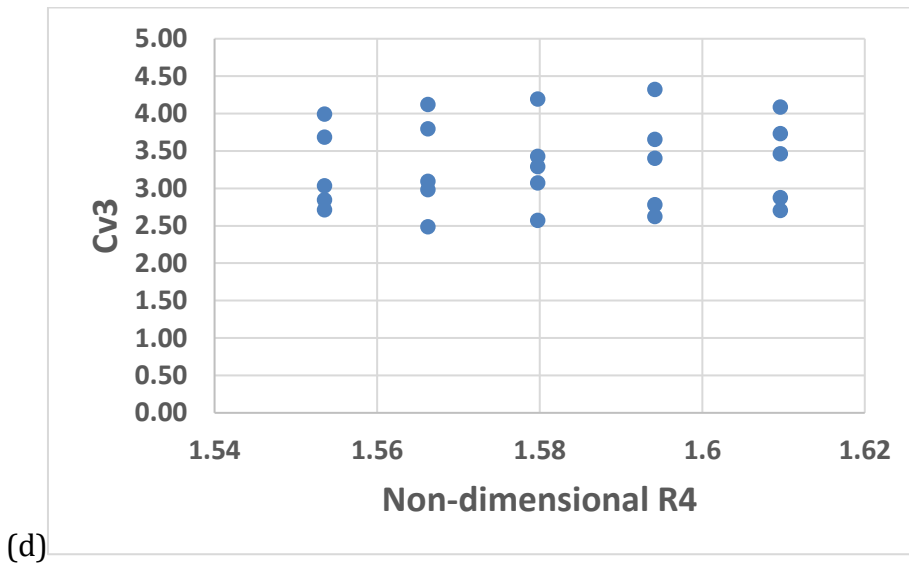
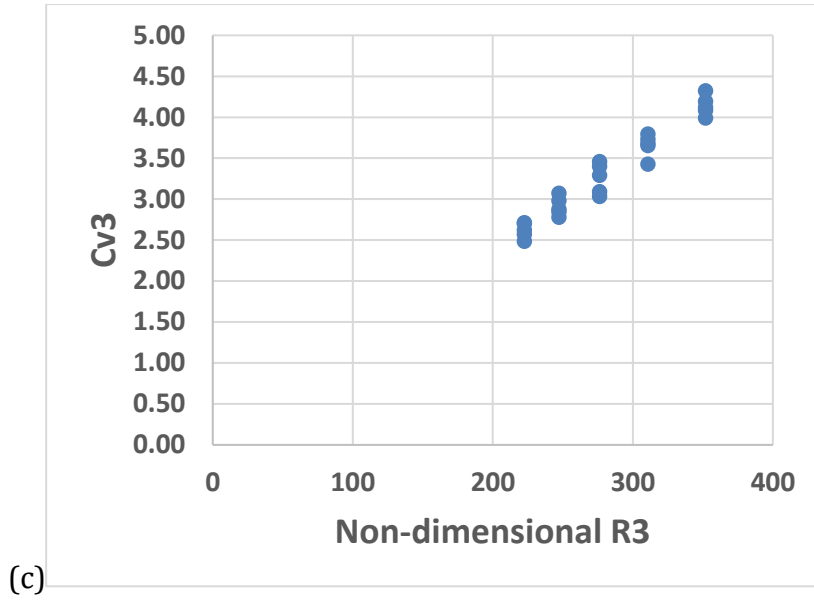
Compared to previous figures, figure 5.6 shows that row three flow capacity is relatively less affected by upstream row cylinders. Among upstream contributions, row one cylinders still have significant influence on row three flow capacity. Cumulative flow area change affects local flow capacity. Design changes in row two have relatively lesser impact on row three flow capacity.

A significant contribution can be noted from design changes in row three cylinder. A change of around 45% is noted with the design change of row three cylinder. Compare to figure 5.5, the trend followed by flow capacity is steep with row three-cylinder design change and is comparable to figure 5.4.

INVERSE DESIGN OF FUNCTIONAL SURFACES CONTAINING SIMPLE DISCONTINUOUS GEOMETRY
 STRUCTURE FOR PRESCRIBED COMPLEX FLOW CHARACTERISTICS



INVERSE DESIGN OF FUNCTIONAL SURFACES CONTAINING SIMPLE DISCONTINUOUS GEOMETRY
STRUCTURE FOR PRESCRIBED COMPLEX FLOW CHARACTERISTICS



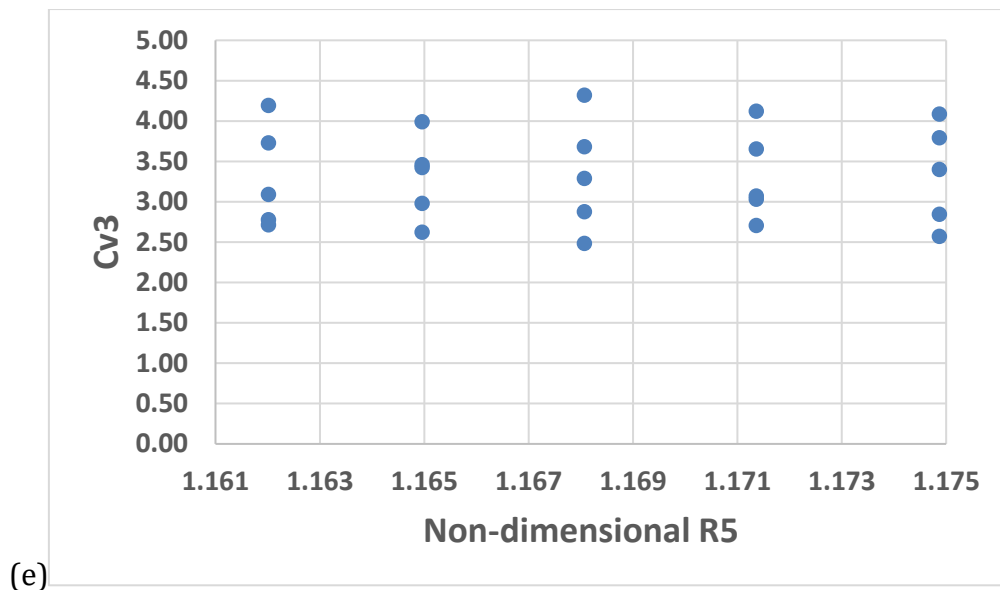
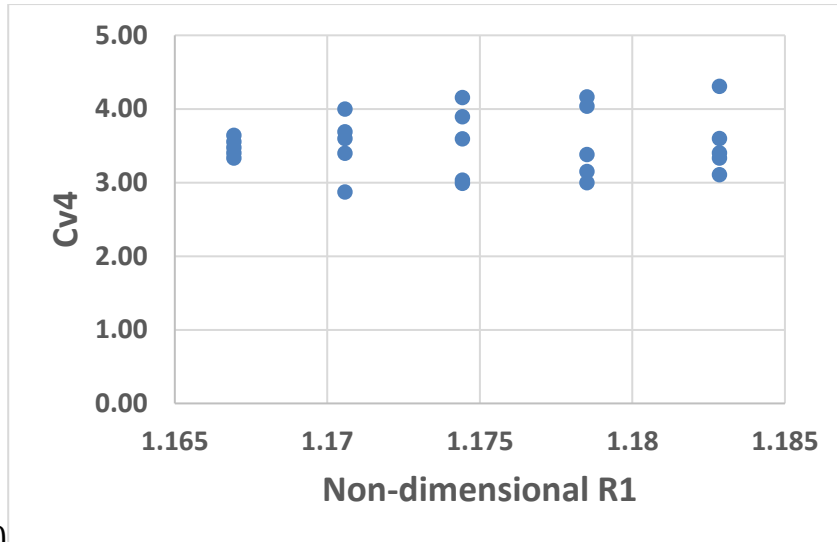


Figure 5.6 (a)-(e): Row three flow capacity variation with design points

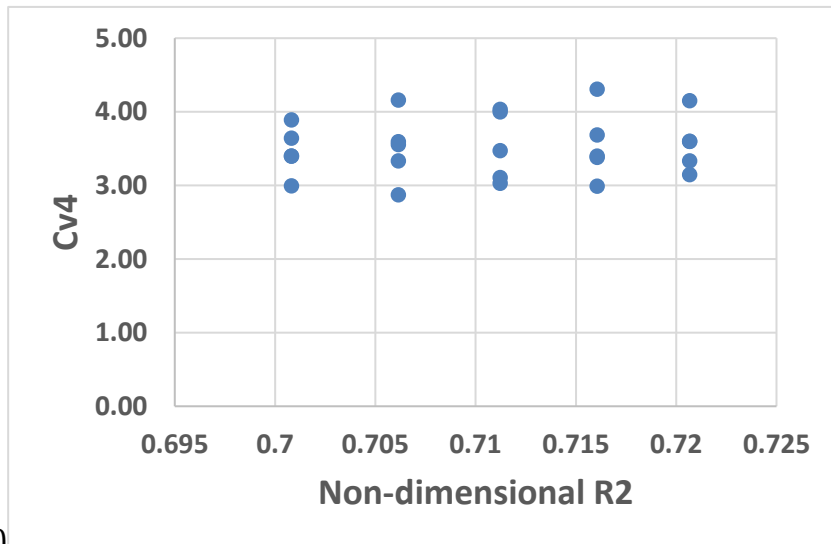
5.2.4. Influence on Cv4

It can be seen from figure 5.7 that row four flow capacity is significantly affected by the design modifications of row four cylinders. This noticeable change is visible as a steep graph of row four flow capacity. Flow capacity is observed to increase and then become constant for row three cylinders. This similar trend can be observed for row one, two and four cylinders. Although, it should be noted that flow capacity starts to decrease after attaining maxima as can be seen in R5 graph. Row one flow capacity can be seen to change around 12%.

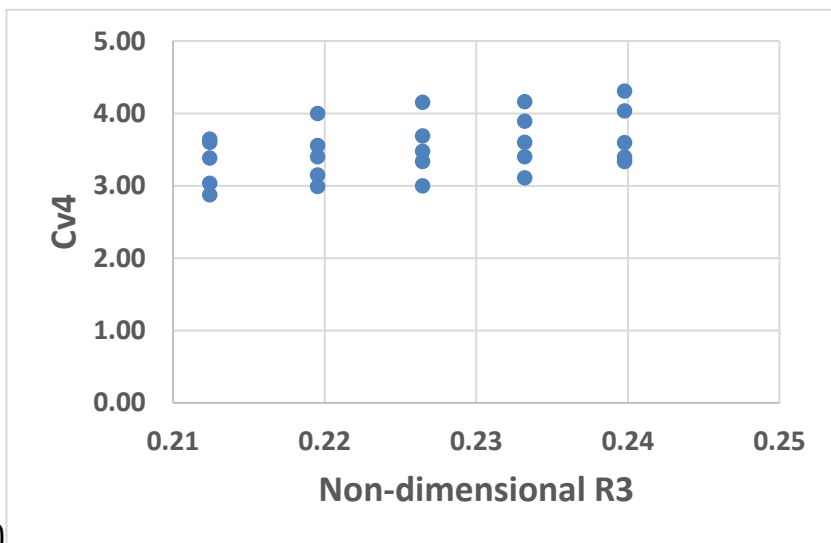
INVERSE DESIGN OF FUNCTIONAL SURFACES CONTAINING SIMPLE DISCONTINUOUS GEOMETRY
 STRUCTURE FOR PRESCRIBED COMPLEX FLOW CHARACTERISTICS



(a)



(b)



(c)

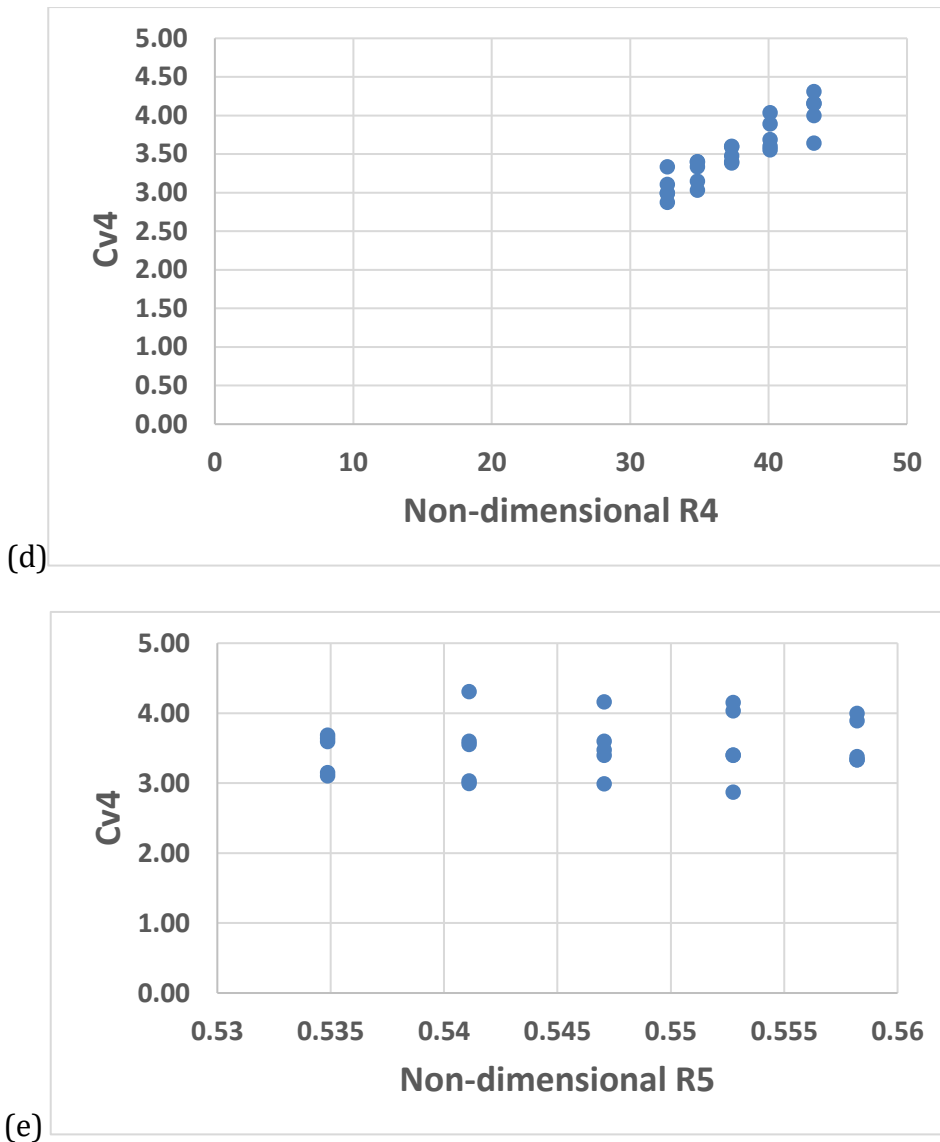
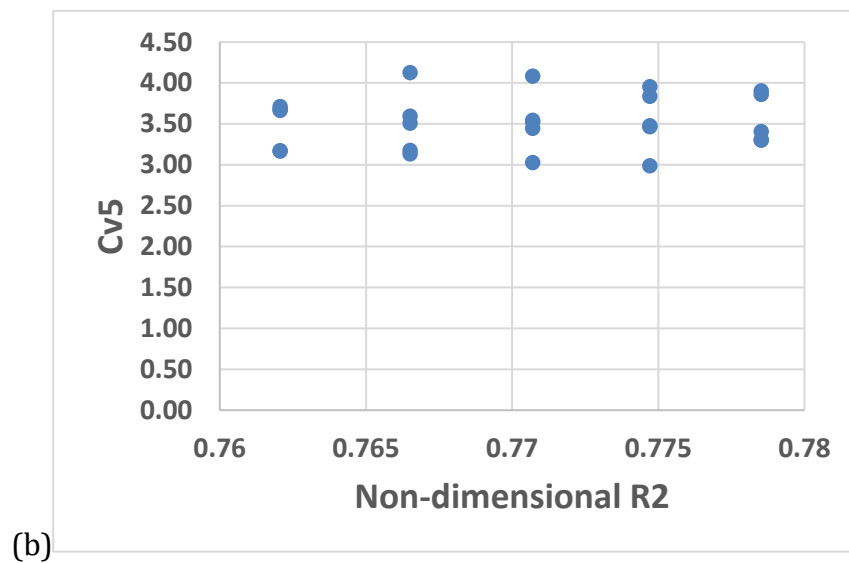
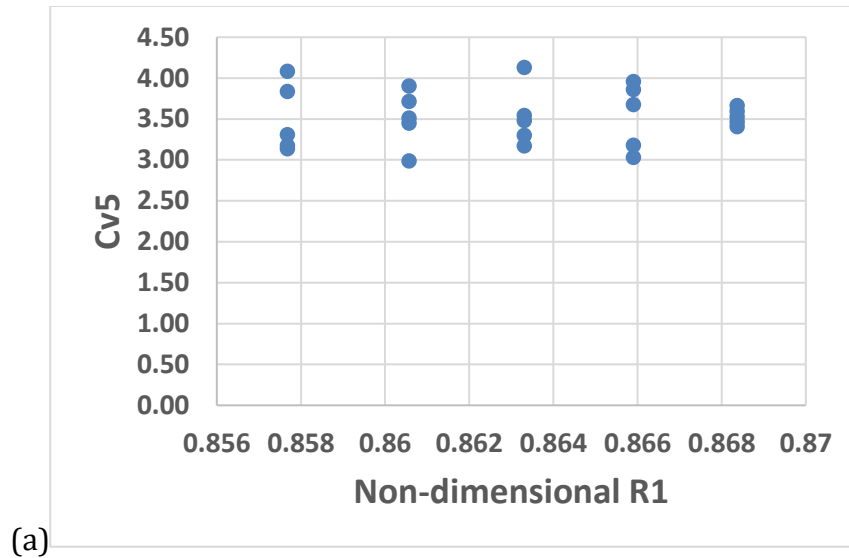


Figure 5.7 (a)-(e): Row four flow capacity variation with design points

It can be seen that changes in row one cylinder brings noticeable change to row four flow capacity. Possible reason can be flow area contraction with increase in row one-cylinder dimension. A consistency can be noted with row three changes. An increase in downstream flow area can possibly balance changes in pressure distribution leading to slower change in flow capacity. This slower change is noticeable in the graphs of R1, R2 R3 and R5.

5.2.5. Influence on Cv5



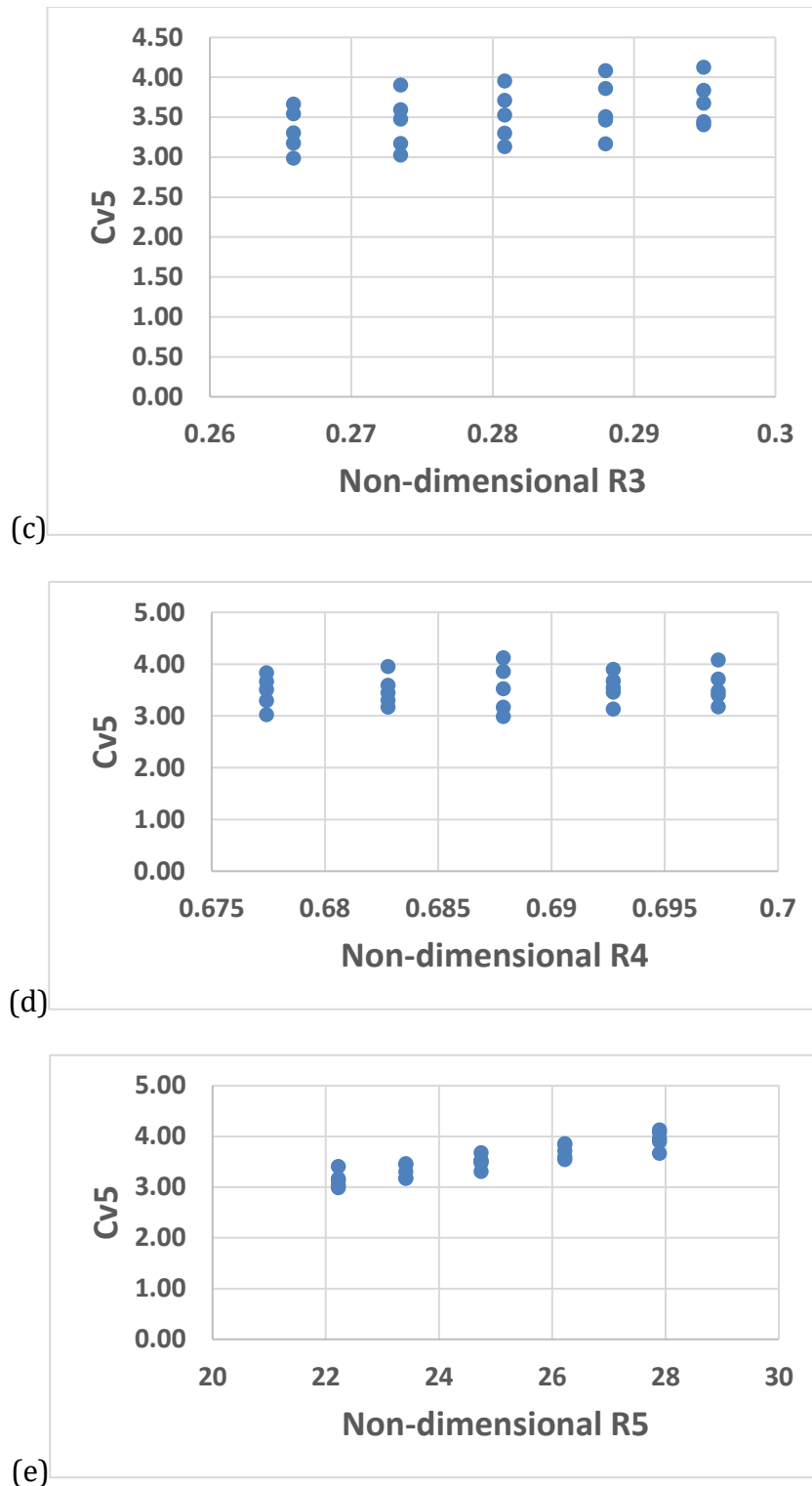


Figure 5.8 (a)-(e): Row five flow capacity variation with design points

Figure 5.8 shows design parameters' influence on row five flow capacity. Significant impact can be noticed for row five design change. A relatively slower flow capacity change with design can be noticed in the graph of R3. Almost constant flow capacity can be noted

for R1, R2 and R4 design changes. Row five flow capacity can further be seen to be affected by row three cylinders. This is possibly due to expanded flow area that further decreased pressure drop.

The investigation showed cumulative geometrical change influence over individual row flow capacity. Local row flow capacities were found to be significantly affected by particular row cylinder dimensional changes. This evidently can be seen in individual row flow capacity graphs and power coefficient values in Table 5.1. Next section utilizes the developed regression equation to expand design space. In addition to existing 25 trim design, 75 more were added using regression equation creating an ensemble of 100 augmented snapshots. Individual row flow capacities were computed using row cylinder dimensions. The dimensions varied were $R_1:0.003\text{m}-0.0024\text{m}$ at $6\text{E}-06\text{m}$ step; $R_2:0.002375\text{m}-0.0019\text{m}$ at $4.8\text{E}-06\text{m}$; $R_3:0.002\text{m}-0.0016\text{m}$ at $4\text{E}-06\text{m}$; $R_4:0.0015\text{m}-0.0012\text{m}$ at $3\text{E}-06\text{m}$ and $R_5:0.001\text{m}-0.0008\text{m}$ at $2\text{E}-06\text{m}$. By expanding design space, further trim designs with corresponding local flow capacities are added. This expanded design space is exploited for globe type valve trim hydraulic design.

5.3. Modal analysis and sparsity investigation

Chapter 1 introduced globe type valve trim and its global performance evaluator equation. It briefly mentioned top-down control valve design approach along with its limitations. Chapter 2 identified relevant literature for globe type control valve. Literature revolved around preliminary and advanced flowfield investigations that have been carried out. It was identified that current globe type control valve research lacked established inverse design framework computing local geometrical features for prescribed flow characteristics.

This section establishes inverse design framework for globe type control valve trim. The process computes trim local geometrical features for prescribed local flow capacities. The framework is unique in its design approach as it takes three-dimensional local flow characteristics into consideration. Specifically, framework utilizes governing local flow structures to derive local geometrical features.

Modal analysis is carried out to establish dominant local flow capacity and trim design modes. As mentioned before, subjected to manufacturing and cost limitations, various trim designs are obtained based on local row cylinder dimensional variations as R_1 :0.003m-0.0024m at 6E-06m step; R_2 :0.002375m-0.0019m at 4.8E-06m step; R_3 :0.002m-0.0016m at 4E-06m step; R_4 :0.0015m-0.0012m at 3E-06m step and R_5 :0.001m-0.0008m at 2E-06m step. Regression equation is applied to compute corresponding trim local flow coefficients. Energy spectrum based dominant modes containing 99.99% energy are identified for snapshot ensemble containing local flow coefficients and trim geometrical designs. This is further extended to identify augmented snapshot ensemble dominant modes. Dominant modes identify major governing flow and design structures. Flow sensing position based on local flow modal extrema are identified. Furthermore, the flow and design structures are integrated within low fidelity model based Gappy POD methodology discussed in Chapter 3. The low fidelity approach achieves faster computation while preserving major flow features. The Gappy POD methodology is tested on 100 incomplete snapshots ensemble for convergence characterisation. Finally, original multi-stage continuous resistance trim design is carried out as a problem of incomplete snapshot leading to inverse design framework.

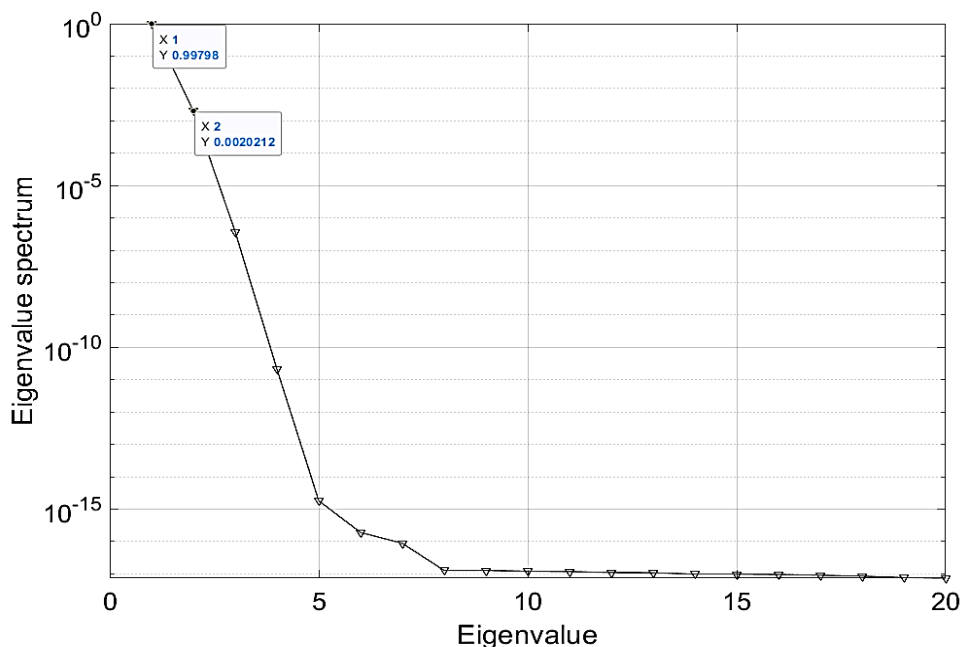


Figure 5.9: Local flow capacity eigenvalue spectrum

Local flow coefficient modes are computed. Figure 5.9 shows the eigenvalue spectrum for snapshot matrix containing local flow capacities computed from steady state flow for

various design points. 99.99% of energy can be observed to be contained within the first two modes. It can be seen that spectrum magnitude decreases for subsequent higher modes. Given that first two modes contain 99.99% of energy, the subspace can now be spanned only by two modes. Figure 5.10 shows first two relevant local flow coefficients modes. In figure 5.10, row 1 and 2 are mode one and two respectively while column represents trim flow coefficient location. Highest modal activity can be seen to be concentrated at mode one 2nd column and mode two 1st column as shown in figure 5.10. Higher modal activity indicates greater design change influence over row one and two local flow capacities. This possibly can be due to significant trim row 1 and 2 flow area change. Lowest modal activity can be seen at mode one 1st and 3rd column while for mode two at last column as shown in figure 5.10. Furthermore, based on modal extrema, three flow sensing positions within trim top disc can be at: row one, two and five.

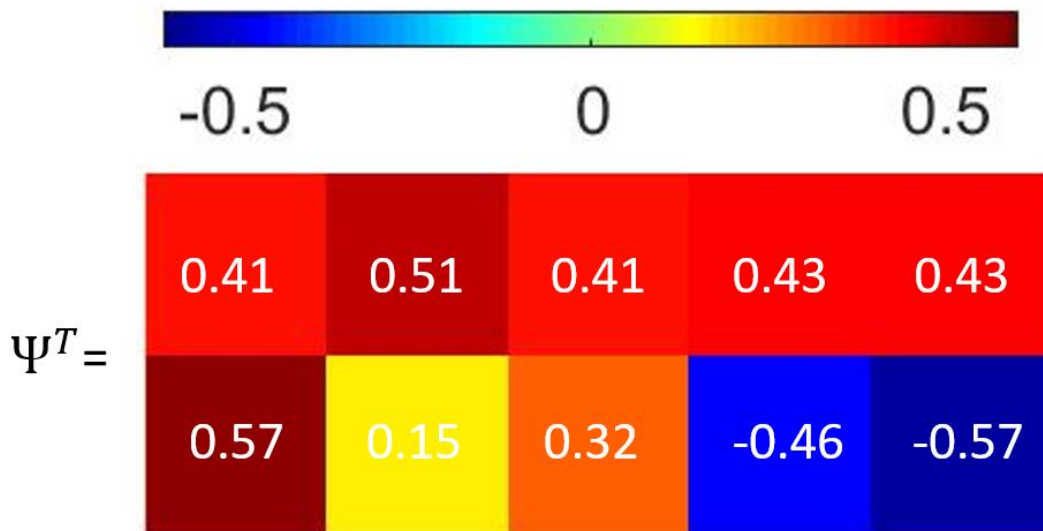


Figure 5.10: Local flow capacity modes

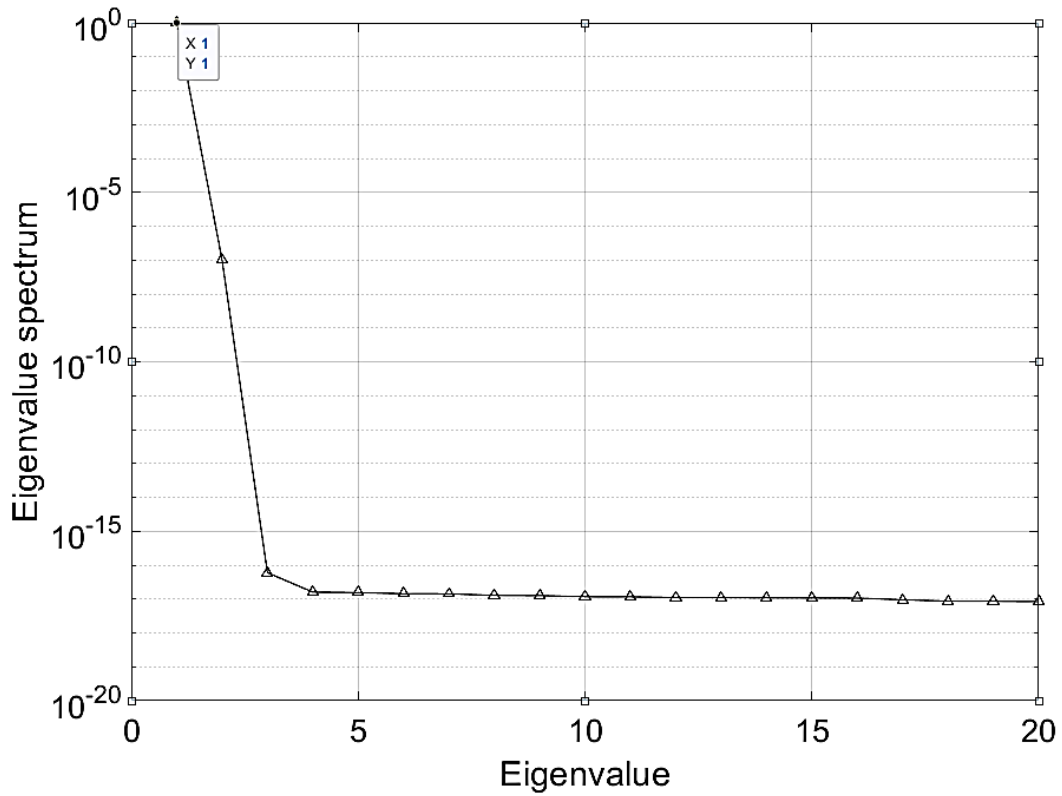


Figure 5.11: Eigenvalue spectrum of design parameters at design points

Figure 5.11 shows the eigenvalue spectrum for the snapshot matrix containing design parameters for trim cylinder dimensional changes previously discussed. 99.99% of energy can be observed to contain within first mode. It can be seen that spectrum magnitude decreases for subsequent higher modes. Given that the first mode contains 99.99% of energy, the reduced subspace can now be represented by only one mode. Figure 5.12 shows relevant one design mode. Column represents trim flow coefficient location. Highest design modal activity can be seen to concentrate at trim row one cylinders. This higher modal activity indicates dominance of row one cylinder dimensional change. Lowest modal activity can be seen at trim row five cylinders indicating relatively lesser influence of last row cylinders dimensional change.



Figure 5.12: Design mode

Figure 10 shows the eigenvalue spectrum for the augmented snapshot matrix containing design parameters and corresponding local flow capacities for trim cylinder dimensional changes previously discussed. 99.99% of energy can be observed to contain within first two modes. It can be seen that spectrum magnitude decreases for subsequent higher modes. Subspace can be spanned by two modes given that it contains 99.99% of energy. Figure 5.13 shows relevant modes for augmented snapshot ensemble. In figure 5.14, row 1 and 2 are mode one and two respectively. The first five columns in figure 5.14 represents trim row flow coefficient locations and last five columns represents trim row cylinder dimensions. Points of highest and lowest modal activity can be seen to correlate to that of individual flow capacity and design parameter modes.

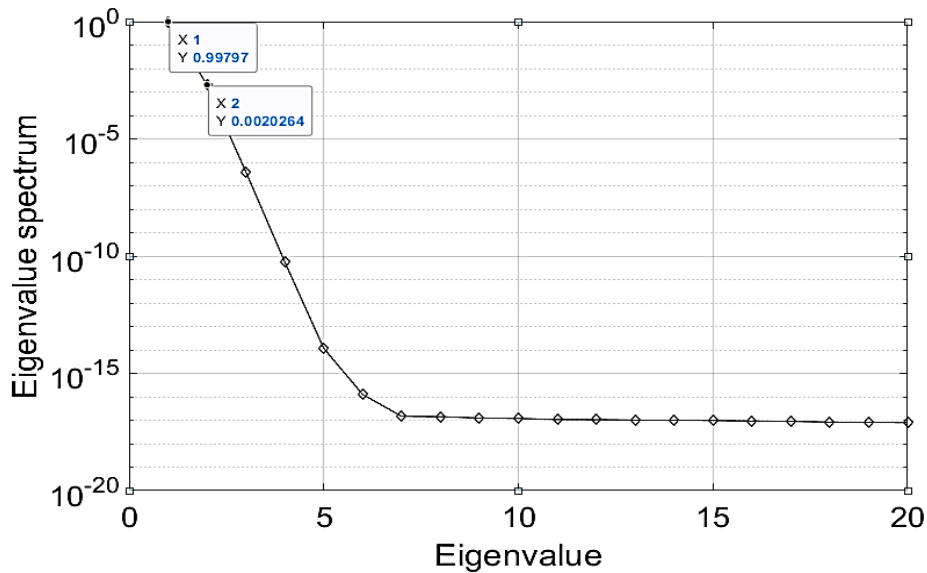


Figure 5.13: Eigenvalue spectrum of augmented snapshots

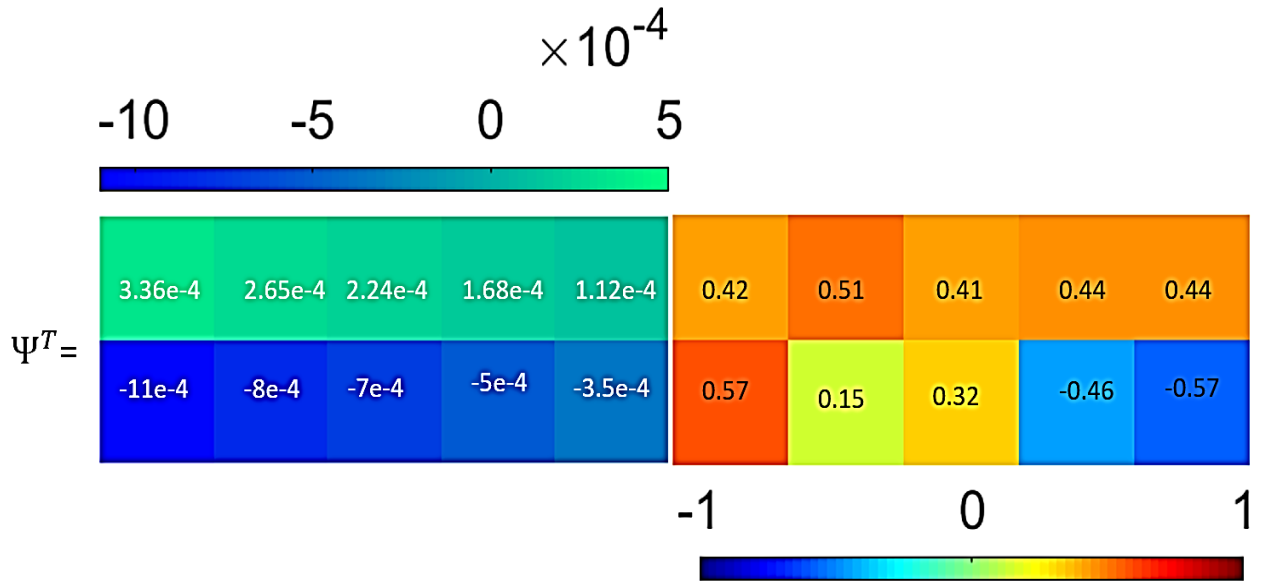


Figure 5.14: Augmented snapshot modes

5.3.1. Sparse Trim Ensemble

This section investigates POD mode computation for incomplete (sparse) snapshot set. In particular, computed modes repaired incomplete augmented snapshot set at each iteration. Wilcox *et al.* [83] concluded snapshot rebuilding process convergence as a function of individual snapshot structure and amount of its missing data. Wilcox *et al.* [83] considered snapshot ensemble containing airfoil coordinates augmented with corresponding pressure values. The snapshot ensemble considered for this study consists of trim geometrical designs augmented with corresponding local flow coefficients. This ensemble varies considerably than that was previously considered by any study for Gappy POD. Furthermore, this section establishes convergence characteristics in rebuilding damaged or missing element augmented snapshot set by randomly discarding 40%, 50% and 60% augmented snapshot data. Investigation is unique to the augmented snapshot ensemble considered and explores Gappy POD process sensitivity to ensemble sparsity.

Chapter 3 discussed Gappy POD process. In this investigation, flow solutions resulting in different local flow capacities at various trim designs discussed previously are combined to form snapshot ensemble. However, individual snapshots are augmented with corresponding trim design parameters. A 100-member augmented snapshot is formed. Chapter 3 discussed process for repairing damaged or missing element snapshots. A brief

overview of the process goes as follows: Compute new snapshot ensemble by replacing missing elements with the average over available data at that point. Compute first approximation of POD modes. Furthermore, compute new ensemble by repairing and replacing only missing elements with first approximated POD modes. Compute second POD modes approximation for new ensemble. Continue the process to follow convergence criteria.

Figure 5.15 shows the locations for missing data points. The first five locations represent design parameters for each row cylinders while subsequent locations are for corresponding local flow capacities. For figure 5.15(a) data presence can be noted at 1st, 2nd, 5th, 6th, 9th and 10th location resulting in only 40% data loss. For figure 5.15(b) data presence can be noted at 1st, 5th, 6th and 10th location. This results in 60% data loss in an individual augmented snapshot. For figure 5.15(c) data presence can be noted at 1st and 6th location resulting in 80% data loss.

Figure 5.16 shows the modal inner product over support space \mathbf{n} after reaching convergence. The fact that missing data exists within individual snapshots, inner product is carried out over support space rather than full space. Consequently, non-diagonal elements are non-zero while diagonal elements are not equal to unity. A snapshot set with completely known elements can produce inner product of identity matrix. Increase in the value of non-diagonal elements correlates with percentage increase in snapshot missing elements. It can also be seen that for 40% and 60% missing data, diagonal elements tend towards unity. This demonstrates that with decrease in missing data, inner product tends to produce unity for diagonal element and zero for non-diagonal. Additionally, it also suggests improvement in orthogonality of POD modes over support space \mathbf{n} . Figure 5.16 can also be seen to have symmetric inner products and the size of each depends on the number of POD modes used to repair snapshots. From the figure it can be inferred that two POD modes were used.

Figure 5.17 shows the eigenvalue spectrum convergence for 60% missing data. The exact spectrum represents that of complete data set. It can be seen that first two modes with combined spectrum energy of 99.99% are converged within 10 iterations. However, subsequent higher modes required further iterations to converge. For example, modes 3-6 are not converged even after 30 iterations. The rate of convergence for POD modes can

be observed from the figure. It can be seen that first two relevant modes have higher rate of convergence. Spectrum energy for first two modes matches with that of exact spectrum curve within 10 iterations indicating faster convergence rate. However, spectrum energy for higher modes between 3-6 still show significant energy deviation from that of actual spectrum. At least 30 iterations are required to obtain third mode energy close to that of exact energy spectrum. Fifth mode can be seen to converge after 45 iterations.

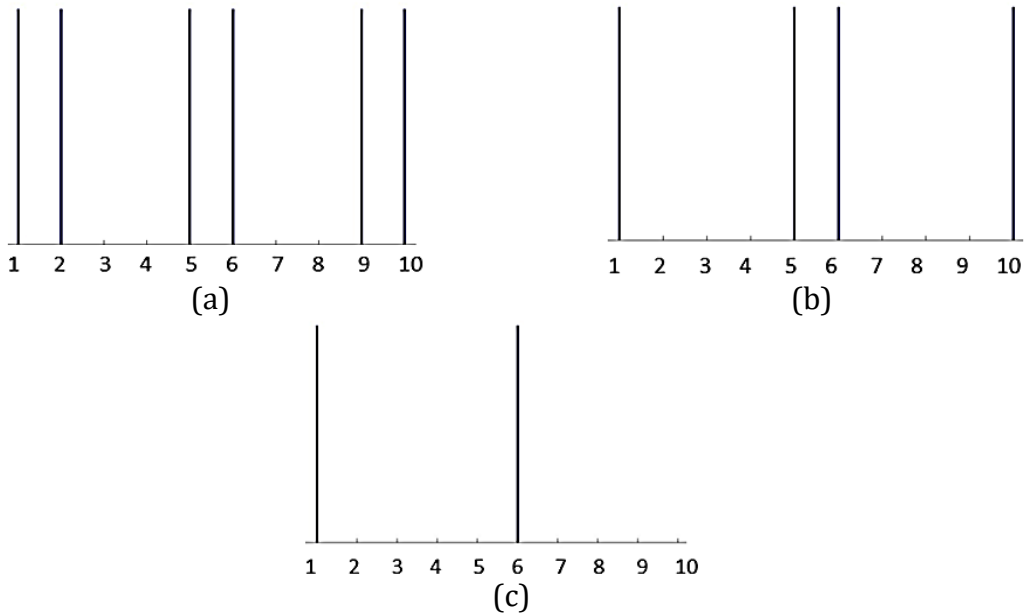


Figure 5.15: Data location for (a) 40% missing data (b) 60% missing data (c) 80% missing data in individual snapshot

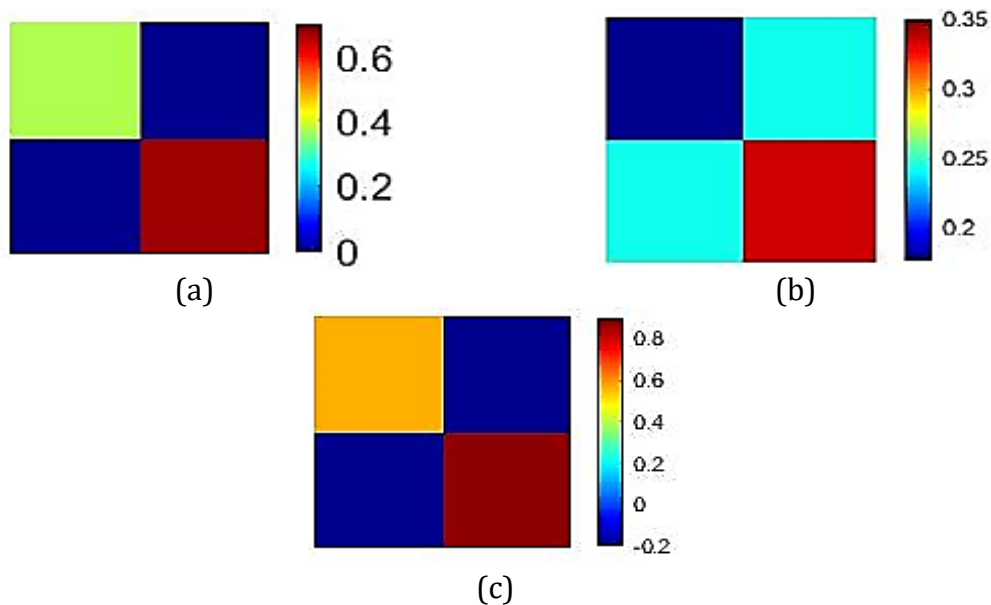


Figure 5.16: Gappy inner product $(\Phi^i, \Phi^j)_n$ for (a) 60% missing data (b) 80% missing data (c) 40% missing data in an individual snapshot

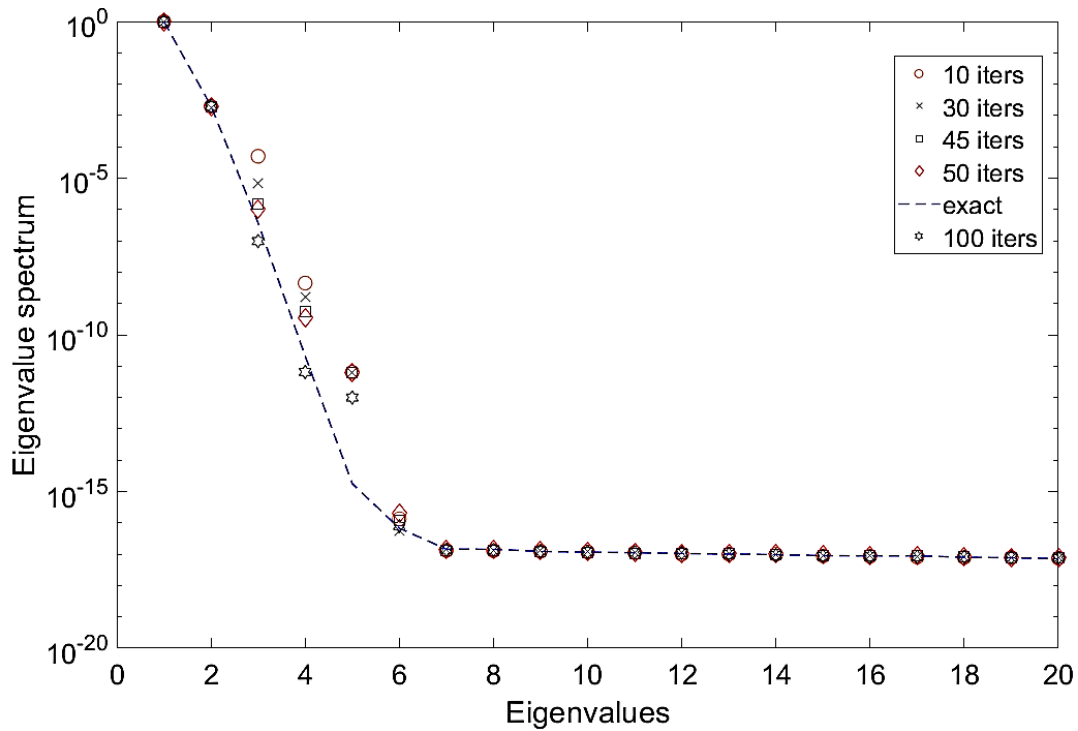


Figure 5.17: Spectrum convergence process for 60% incomplete snapshot

Figure 5.18 shows the eigenvalue spectrum convergence for 80% missing data. The exact spectrum represents that of complete data set. It can be seen that first two modes with combined spectrum energy of 99.99% are converged after 1st iteration. However, subsequent higher modes required further iterations to converge. For example, modes 3-6 are not converged even after 100 iterations. The rate of convergence for POD modes can be observed from the figure. It can be seen that first two relevant modes have higher convergence rate. Spectrum energy for first two modes matches with that of exact spectrum curve at 1st iteration indicating faster convergence rate. However, spectrum energy for higher modes still shows significant energy deviation from that of the actual spectrum. At least 50 iterations are required to obtain third mode's energy close to that of exact energy spectrum. Spectrum for fourth mode converges at 1st iteration but then deviates from actual spectrum curve. Same observation can be noted for fifth mode where deviation is maximum for 100th iteration.

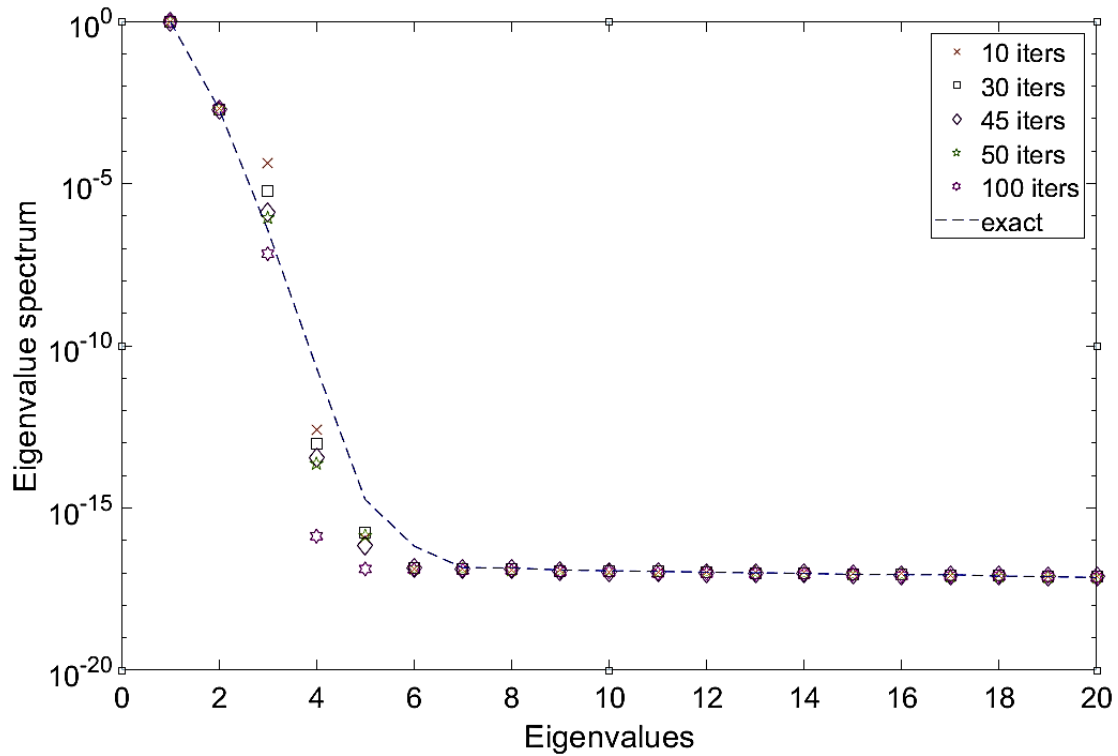


Figure 5.18: Spectrum convergence process for 80% incomplete snapshot

Figure 5.19 shows the eigenvalue spectrum convergence for 40% missing data. The exact spectrum represents that of complete data set. It can be seen that first two modes with combined spectrum energy of 99.99% are converged after 1st iteration. However, subsequent higher modes required further iterations to converge. For example, no significant spectrum energy change with iterations can be noted for fourth mode. The rate of convergence for POD modes can be observed from the figure. It can be seen that first two relevant modes have higher rate of convergence as spectrum energy for first two modes matches with that of exact spectrum curve at 1st iteration. However, spectrum energy for higher modes still shows significant energy deviation from that of actual spectrum. At least 50 iterations are required to obtain third mode energy close to that of exact energy spectrum. Fifth mode spectrum can be observed not to converge even after 100 iterations. Sixth mode spectrum converged at 1st iteration but started to deviate for subsequent iterations.

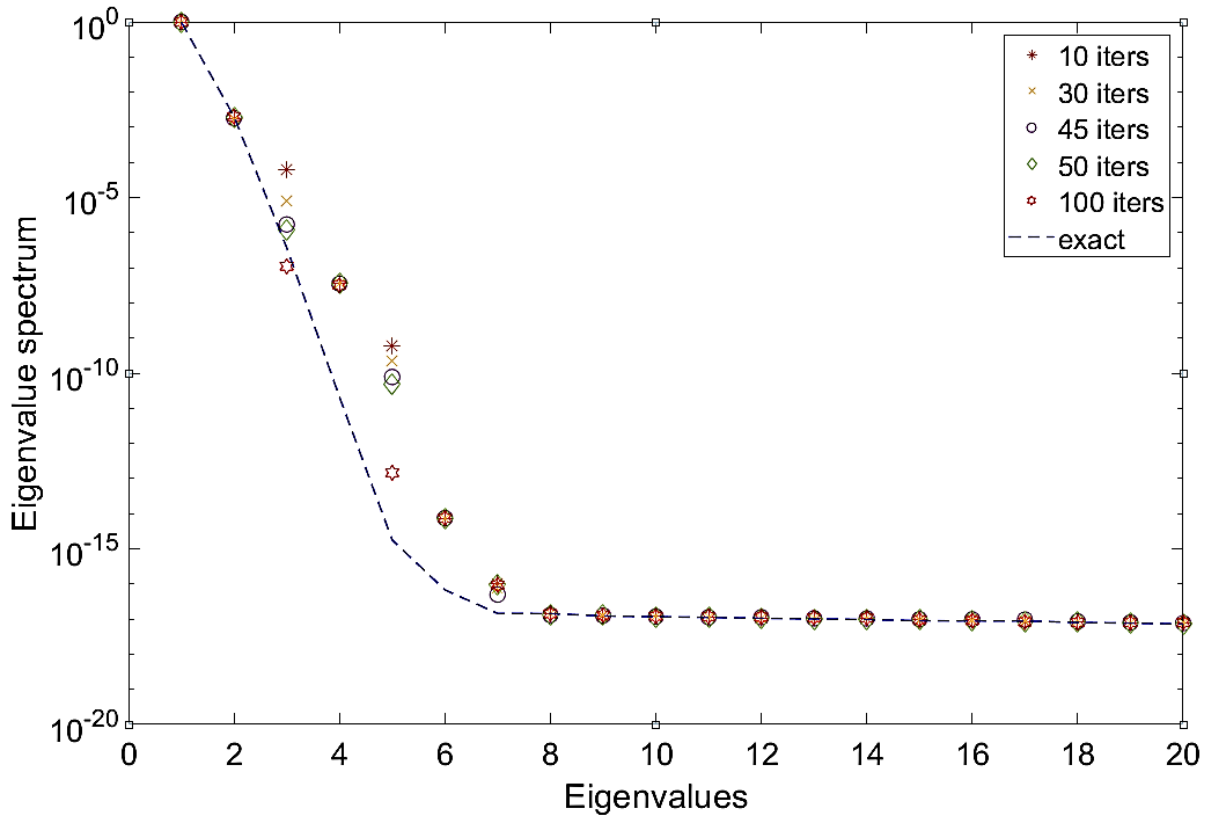


Figure 5.19: Spectrum convergence process for 40% incomplete snapshot

Common observations can be drawn from the above spectral graphs. A point of inflection can be seen to exist around fifth eigenvalue for the exact curve. It can be noted that 1st and 2nd eigenvalues converge faster at 1st iteration. The same can be observed for the eigenvalues eight and higher indicating higher convergence rate. The behaviour of graphs changes around inflection point. It can be seen that for all missing data spectral graphs, fifth eigenvalue did not converge even after 100 iterations while third converges around 50 iterations. It can be seen that computed spectral values at each iteration finds it difficult to follow exact curve around inflection point. Additionally, majority of iterative points are on the upper side of exact curve for 60% missing data. On the contrary, majority iterative points are observed to be on the bottom side of exact curve. However, iterative points can be relatively observed to be close to exact curve for 40% missing data. It can be concluded from these observations that spectral convergence depends on detail of particular snapshot ensemble. Particularly, it depends on the amount of missing data within an individual snapshot as concluded by Wilcox *et al.* [83].

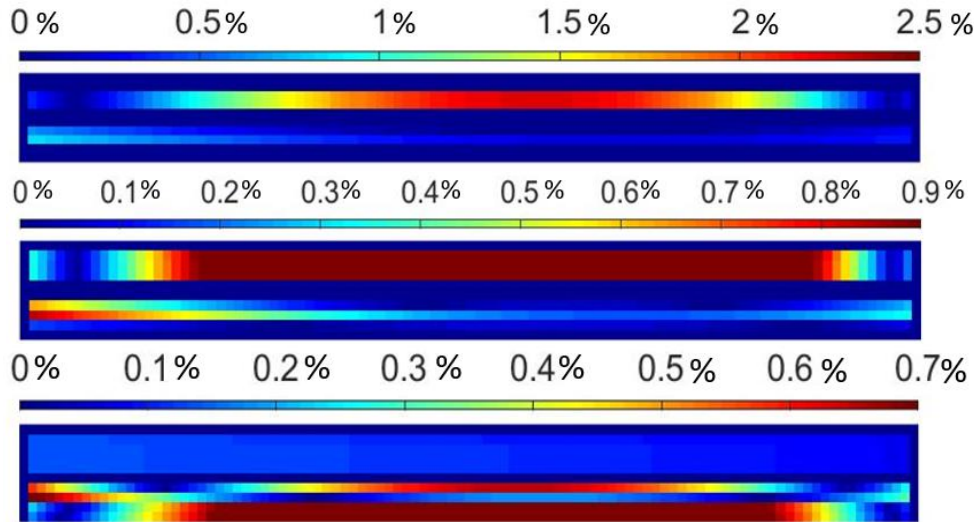


Figure 5.20: Pointwise percentage error for (a) 40% missing data ensemble (b) 60% missing data ensemble (c) 80% missing data ensemble

To convey the absolute quality of snapshot repair, pointwise error for snapshot ensemble can be defined as follows:

$$\hat{e} = \frac{|s_i - \tilde{s}_i|}{|s_i|} \times 100 \quad (5.2)$$

Here s_i is the actual snapshot element \tilde{s}_i is corresponding repaired element. Figure 5.20 shows the pointwise percentage error for missing snapshot ensembles. A maximum error of 0.9%, 0.7% and 2.5% can be noted for 60%, 80% and 40% missing data respectively. Average pointwise error can be observed to be around same in all the missing snapshot ensembles.

A correlation can be drawn between existing data sparsity and required number of iterations to reach stipulated convergence. The correlation can provide added advantage of roughly predicting required number of iterations for available data quality. At first, term 'relative energy' is defined as follows:

$$|E_i - E_0| \quad (5.3)$$

E_i = ith iteration energy

E_0 = Exact energy

E_i is energy spectrum computed at i th iteration during ensemble repair process while E_0 is the 'true' or exact snapshot ensemble energy. Relative energy is the i th computed spectrum energy with respect to exact snapshot ensemble energy. Further to computing relative energy, cumulative relative energy is defined as follows:

$$\sum_{k=0}^m |E_i - E_0|_k \quad (5.4)$$

The expression 5.4 defines cumulative relative energy as summation of all k th modal relative energy computed at i th iteration. Figure 5.21 shows cumulative relative energy computed for 40%, 60% and 80% missing data quality. The energies can be seen to increase and decrease to converge at certain value. Furthermore, convergence rate can be seen higher for 80% missing data sparsity in contrast to 40%. As an example, for convergence criteria set at $5E-05$ cumulative relative energy, 80% missing data sparsity converges at 87 iterations while 40% at 100. However, this observation is limited to convergence criteria set below $1E-04$. It is intuitive to conclude that smaller the amount of missing data faster should be convergence rate. However, figure 5.21 shows opposite. Wilcox *et al.* [83] concluded that higher iteration numbers are required to compute spatially high frequency flow structures. This can be observed in figure 5.18 and 5.19 where higher convergence rate can be seen for spatially low frequency structures (1-2 eigenvalues) and low convergence rate for spatially high frequency structures corresponding to 3-6 eigenvalues. Higher iterations are required to rebuilt spatially high frequency structures from sparse data. Furthermore, number of iterations depends not only on data sparsity but also on sparsity distribution within snapshots. This can be seen in figure 5.15 where maximum data presence within 40% missing data sparsity and have lower convergence rate. This concludes data location relevance within snapshot for computing spatially high frequency flow structures.

It can be concluded that for convergence criteria set below $1E-04$ cumulative relative energy, a qualitative correlation can be drawn between data sparsity and required number of iterations for repairing. It can be seen that for data sparsity ranging from 40-80%, the number of iterations can range from 100-87. This is assuming sparse data presence in the locations reported in this investigation.

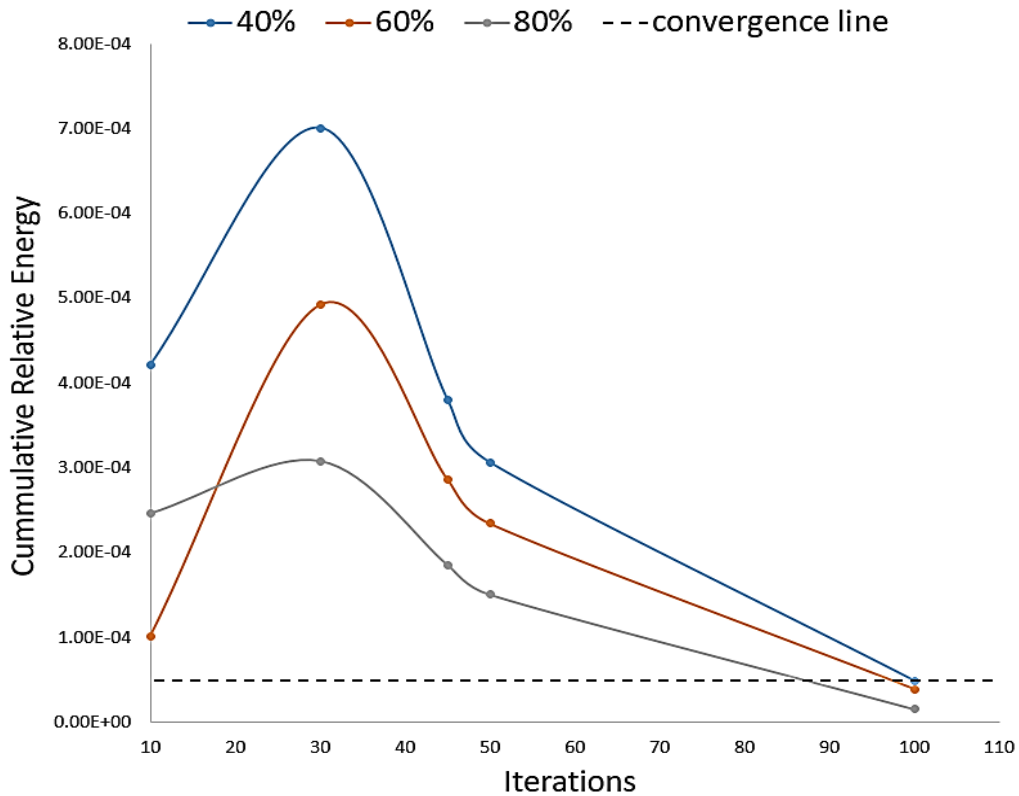


Figure 5.21: Cumulative Relative Energy

This section established convergence characteristics for trim augmented snapshot ensemble sparsity. Investigation utilized Gappy POD methodology to repair sparse trim ensemble. In doing so, Gappy POD efficacy to solve sparse trim ensemble problem is investigation. Investigation revealed Gappy POD high effectiveness in repairing trim ensemble of varying sparsity. Next section treats trim inverse design problem as trim sparsity.

5.4. Original trim inverse design investigation

This section demonstrates the application of Gappy POD methodology as applied to inverse design of control valve trim. The methodology uses collected snapshot ensemble that are augmented as previously described. CFD results were used to generate flow results against design modification for snapshot generation. The goal is to use Gappy POD methodology for computing trim design parameters for stipulated trim local flow capacity distribution.

As mentioned in chapter 3, inverse design problem can be treated as a problem of missing data within snapshots. Figure 5.22 shows the inverse design results tested against high

fidelity simulation results. The local flow capacity variations tested were Cv_1 :2.661-2.743 at 1.175E-02 step; Cv_2 :3.558-3.650 at 1.03E-02 step; Cv_3 :2.755-2.824 at 9.95E-03 step; Cv_4 :3.347-3.369 at 3.13E-03 step and Cv_5 :3.414-3.427 at 1.90E-03m step. The corresponding non-dimensional design parameters $\left(\frac{R_n}{D_n}\right)$ varied as $\frac{R_1}{D_1}=0.078-0.077$ at 1.53E-04; $\frac{R_2}{D_2}=0.071-0.072$ at 1.41E-04; $\frac{R_3}{D_3}=0.070-0.069$ at 1.38E-04; $\frac{R_4}{D_4}=0.0619-0.0610$ at 1.22E-04; $\frac{R_5}{D_5}=0.047-0.046$ at 9.28E-05. The test local flow capacities are chosen that are not contained in the snapshot ensemble. Altogether, eight designs were tested and a good correlation can be seen with the results contained within $\pm 10\%$ band. Row four flow capacity can be observed to be closer to the upper limit of $\pm 10\%$ band. Row one and three flow capacity falls on 45-degree line indicating insignificant deviation of inverse design results from high fidelity simulations.

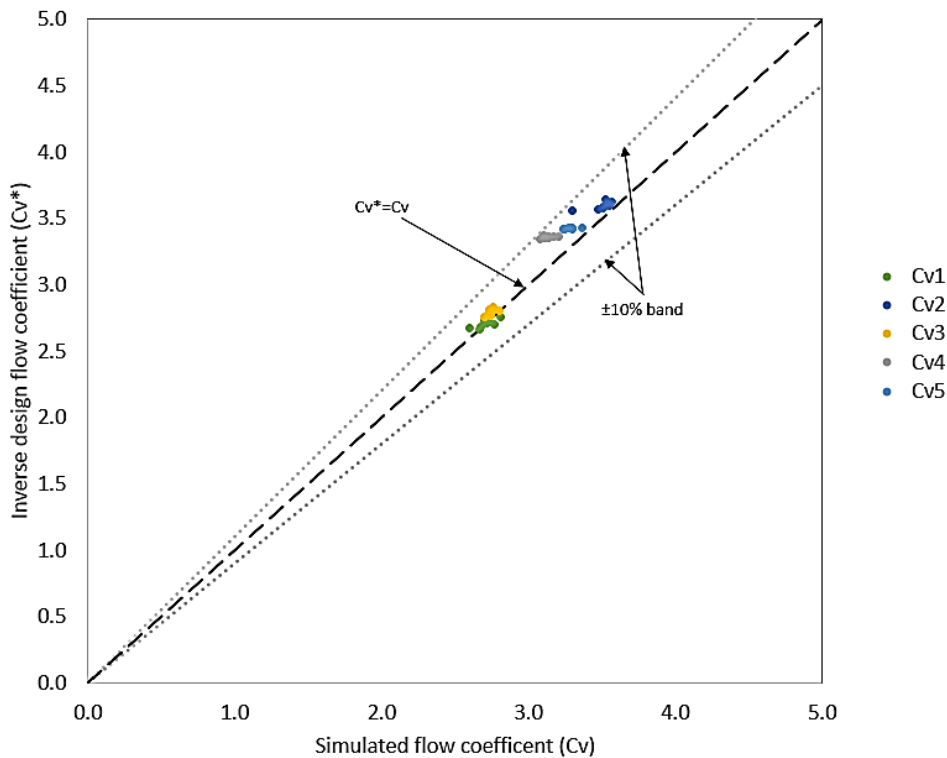


Figure 5.22: Correlation of Local flow capacity

Table 5.2 shows comparison of inverse design methodology on upper and lower limits of snapshot ensemble. The comparison is carried out to establish possible inverse design errors on the ensemble limits. An insignificant deviation can be noted on upper and lower

design limits. However, 2% deviation can be noted on the lower limit. Corresponding local flow capacity deviation can also be seen to be negligible.

Table 5.2: Inverse design comparison on upper and lower limits of design space

	Inverse design upper limit	Simulated upper limit	Deviation	Inverse design lower limit	Simulated lower limit	Deviation
R1	3.00E-03	3.00E-03	0%	2.35E-03	2.40E-03	2%
R2	2.37E-03	2.38E-03	0%	1.86E-03	1.90E-03	2%
R3	2.00E-03	2.00E-03	0%	1.57E-03	1.60E-03	2%
R4	1.50E-03	1.50E-03	0%	1.18E-03	1.20E-03	2%
R5	1.00E-03	1.00E-03	0%	7.85E-04	8.00E-04	2%
Cv1	2.61E+00	2.61E+00	0%	4.20E+00	4.20E+00	0%
Cv2	3.51E+00	3.51E+00	0%	4.78E+00	4.78E+00	0%
Cv3	2.71E+00	2.71E+00	0%	3.98E+00	3.98E+00	0%
Cv4	3.33E+00	3.33E+00	0%	3.69E+00	3.69E+00	0%
Cv5	3.41E+00	3.41E+00	0%	3.62E+00	3.62E+00	0%

Figure 5.23 shows the application of inverse design methodology to the original trim top disc. The actual trim top disc cylinder dimensions are R1: 3E-03; R2: 2.37E-03; R3: 2.00E-03; R4: 1.5E-03 and R5: 1.00E-03. It can be noted that with an increase in number of modes, the predicted values for trim design parameters agree more closely to the exact solution. However, this observation is only limited to three modes. Numerous other observations can be made about the figure. It can be seen that minimum of two modes are required to converge to original trim design parameters. To further enhance the convergence, higher modes can be used for prediction. Although, for modes greater than three, predicted values start to diverge from original trim design parameters.

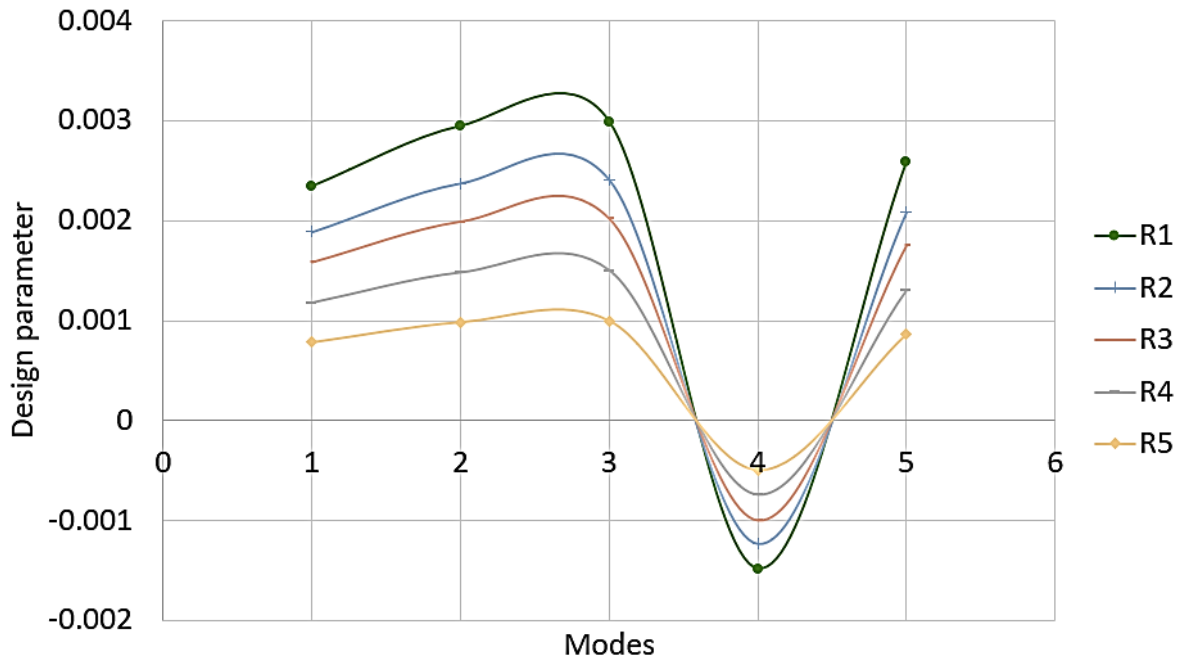


Figure 5.23: Original trim top disc dimension evolution with computation modes

As mentioned earlier, inverse design snapshot contains target local flow capacities with design parameters as missing elements. This snapshot is further concatenated with snapshot ensemble containing no missing elements. Figure 5.24 shows the evolution of modal inner product over support space \mathbf{n} for original trim inverse design. It can be seen that Gappy inner product produces identity matrix when two, three and four modes are used in inverse design process. Consequently, diagonal elements are unity while non-diagonal elements are close to zero. This further demonstrates complete orthogonality of POD modes over support space \mathbf{n} . Loss in the orthogonality can be noted with an inclusion of fifth mode in inverse design process. In particular, Gappy inner product between fifth and fourth mode produced greatest absolute loss of orthogonality. This loss correlates with deviation from actual trim dimensions in figure 5.23. Gappy inner product can also be seen not to be diagonal in its characteristics. However, orthogonality preservation can be noted for Gappy inner product between first, second and third mode.

INVERSE DESIGN OF FUNCTIONAL SURFACES CONTAINING SIMPLE DISCONTINUOUS GEOMETRY
 STRUCTURE FOR PRESCRIBED COMPLEX FLOW CHARACTERISTICS

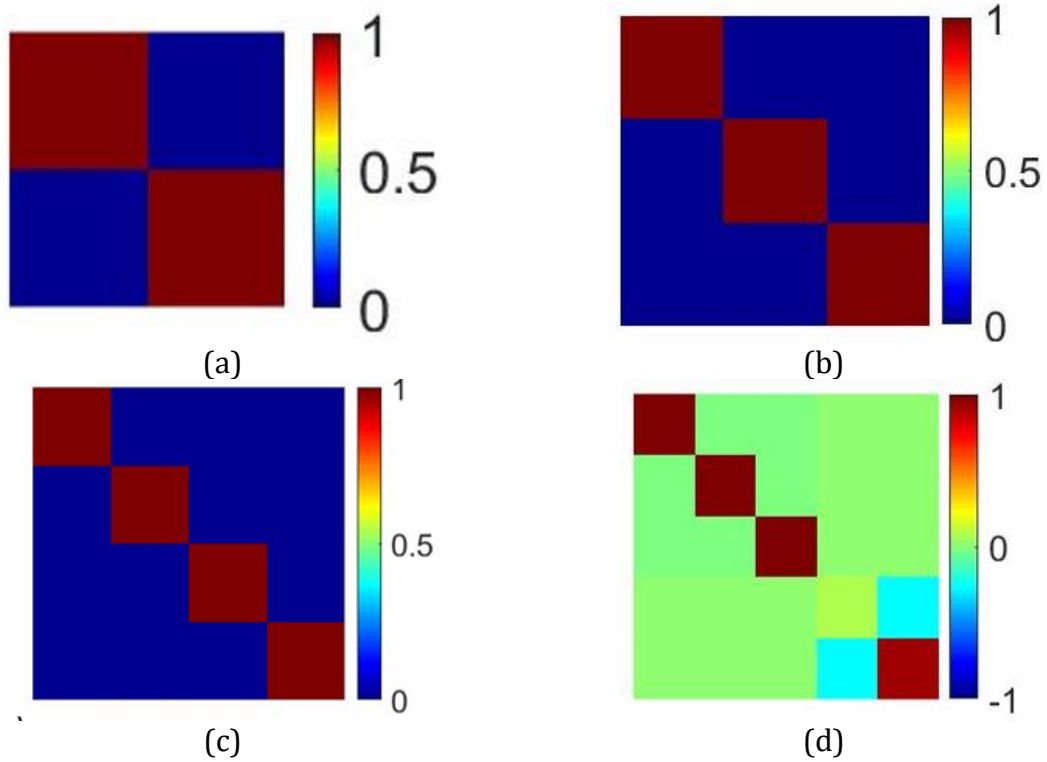


Figure 5.24: Gappy inner product $(\Phi^i, \Phi^j)_n$ for number of modes (a) $m=2$ (b) $m=3$ (c) $m=4$ (d) $m=5$ used for original trim inverse design

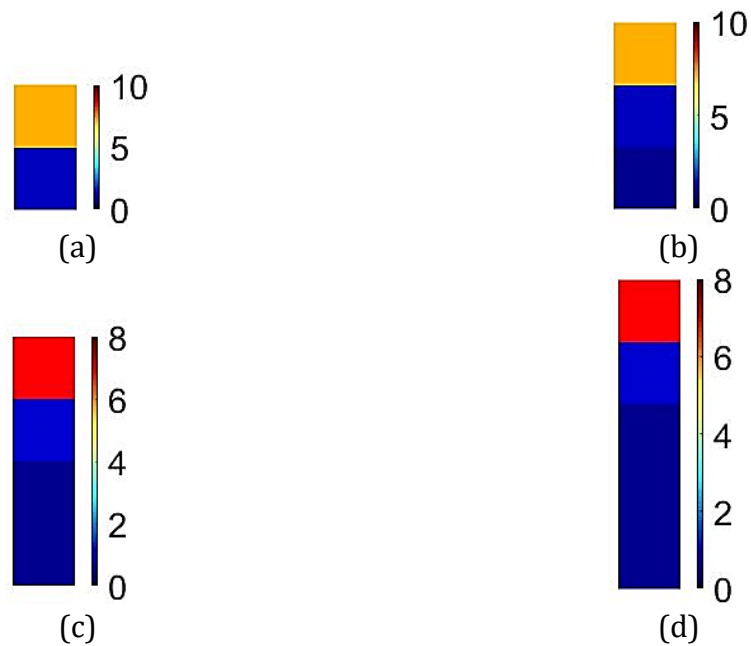


Figure 5.25: Gappy inner product $(g, \Phi^i)_n$ for number of modes (a) $m=2$ (b) $m=3$ (c) $m=4$ (d) $m=5$ used for original trim inverse design

Figure 5.25 shows Gappy inner product evolution with number of modes used in inverse design process. Figure 5.25 (a)-(c) shows inner products $(\mathbf{g}, \Phi^i)_n$ as the corresponding inner products $(\Phi^i, \Phi^j)_n$ have identity matrices. Consequently, the computed modal expansion coefficients are same as inner product $(\mathbf{g}, \Phi^i)_n$. However, the Gappy product $(\Phi^i, \Phi^j)_n$ for figure 5.25(d) does not have identity matrix. As a result, the computed modal expansion coefficients deviate from the inner product $(\mathbf{g}, \Phi^i)_n$. This deviation can be significant at last two elements of figure 5.25(d) due to loss of modal orthogonality as previously discussed in reference to figure 5.25(d). Hence, it can also be inferred that first three elements of modal expansion coefficient would be same as first three elements in figure 5.25(d). Table 5.3 further illustrates above points.

Table 5.3: Modal coefficient comparison

Modes							
2		3		4		5	
$(\mathbf{g}, \Phi^i)_n$	Modal Coefficients	$(\mathbf{g}, \Phi^i)_n$	Modal Coefficients	$(\mathbf{g}, \Phi^i)_n$	Modal Coefficients	$(\mathbf{g}, \Phi^i)_n$	Modal Coefficients
6.99	6.99	6.99	6.99	6.99	6.99	6.99	6.99
0.56	0.56	0.56	0.56	0.56	0.56	0.56	0.56
		0.01	0.01	0.01	0.01	0.01	0.01
				0.0001	-0.0001	0.004	0.0005
						0.001	0.0005

It can be seen that using two or three as number of modes produced correct result for original trim top disc inverse design. Furthermore, higher mode admittance into computation produced considerably diverged results. Higher modal admittance produced non-orthogonality as reflected in Gappy inner product $(\Phi^i, \Phi^j)_n$ in figure 5.24. This is particularly visible for five mode admittance into computational process. A linkage can be developed between the number of computational modes used and computed Gappy inner product $(\Phi^i, \Phi^j)_n$ quality. Condition number can be computed for Gappy inner products indicating “modal orthogonality loss”. Modal orthogonality loss can be defined for Gappy inner product $(\Phi^i, \Phi^j)_n$ deviation from identity matrix. This happens

due to non-orthogonal modal presence. Condition number defines the ratio of largest to smallest singular value of the matrix. The logarithm of condition number estimates the precision loss due to non-orthogonal modes.

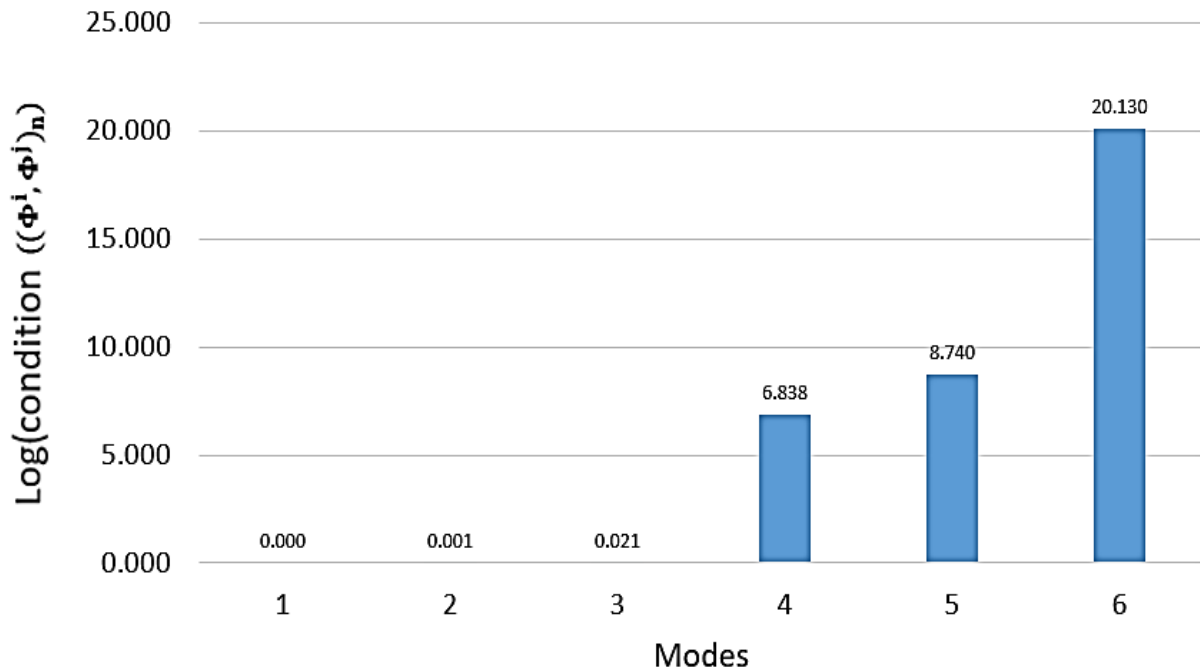


Figure 5.26: Original trim top disc condition number evolution with computational modes

Figure 5.26 shows log of computed condition number for original trim top disc Gappy inner product $(\Phi^i, \Phi^j)_n$. The Gappy product is computed for number of modes admitted within inverse design process of top disc. Minimum condition number can be noted for number of modes to be one, two and three. Condition number starts exponentially increasing for further number of modal admittances within inverse design process. This exponential increase can be associated with modal orthogonality loss and consequent inverse design deviation from the actual trim disc dimensions. This establishes minimum condition number requirement as one of the criteria to determine optimum inverse design computation modes for original trim disc.

Figure 5.13 previously showed augmented snapshot ensemble eigenvalue spectrum. It was established that first two modes contained 99.99% energy. The same augmented ensemble was utilised to derive relevant inverse design computational modes for original trim inverse design. It can be inferred from figure 5.13 and figure 5.26 that number of modes cannot be one as it does not contain 99.99% energy and hence can be seen in figure

5.23 not to compute accurate cylinder dimensions. Therefore, it can be inferred from these figures that number of modes to be used within inverse design process of original trim disc can be two or three modes. However, admitting three modes within inverse design process can be computationally expensive due to solution projection on three modes. This limit optimal number of modes to be used in trim top disc inverse design process to two modes.

Figure 5.27(a) shows the application of inverse design methodology to the upper limit in parameter space shown in Table 5.2. The actual trim top disc cylinder dimensions are R1: 2.35E-03; R2: 1.86E-03; R3: 1.57E-03; R4: 1.18E-03 and R5: 7.85E-04. It can be noted in figure 5.27 (a) that with an increase in number of modes, the predicted values for trim design parameters agree more closely to the exact solution. However, this observation is only limited to three modes. Numerous other observations can be made about the figure. It can be seen that minimum of two modes are required to converge to actual dimensions. To further enhance the convergence, higher modes can be used for prediction. Although, for modes greater than three, predicted values start to diverge from actual dimensions.

Figure 5.27 (b) shows log of computed condition number for corresponding Gappy inner product $(\Phi^i, \Phi^j)_n$ to figure 5.27 (a) computation. The Gappy product is computed for number of modes admitted within inverse design process. Minimum condition number can be noted for number of modes to be one, two and three. Condition number starts exponentially increasing for further number of modal admittances within inverse design process. This exponential increase can be associated with modal orthogonality loss and consequent inverse design deviation from the actual dimensions. This establishes minimum condition number requirement as one of the criteria to determine optimum inverse design computation modes similar to original trim top disc.

Figure 5.13 previously showed augmented snapshot ensemble eigenvalue spectrum. It was established that first two modes contained 99.99% energy. The same augmented ensemble was utilised to derive relevant inverse design computational modes for figure 25 (a). It can be inferred from figure 5.13 and figure 5.27 (b) that number of modes cannot be one as it does not contain 99.99% energy and hence can be seen in figure 5.27 (a) not to compute accurate cylinder dimensions.

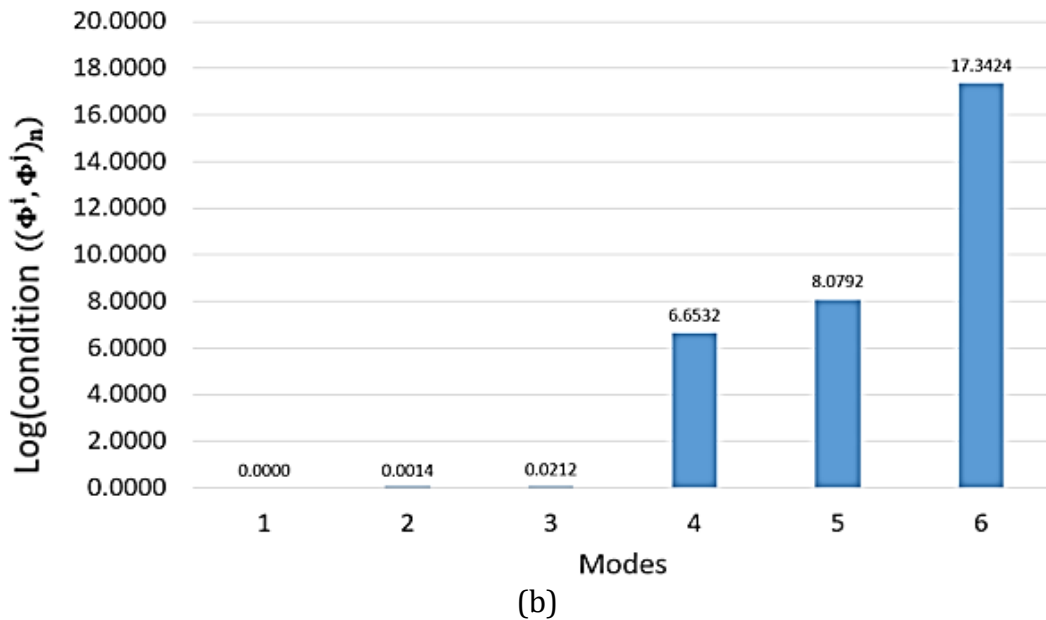
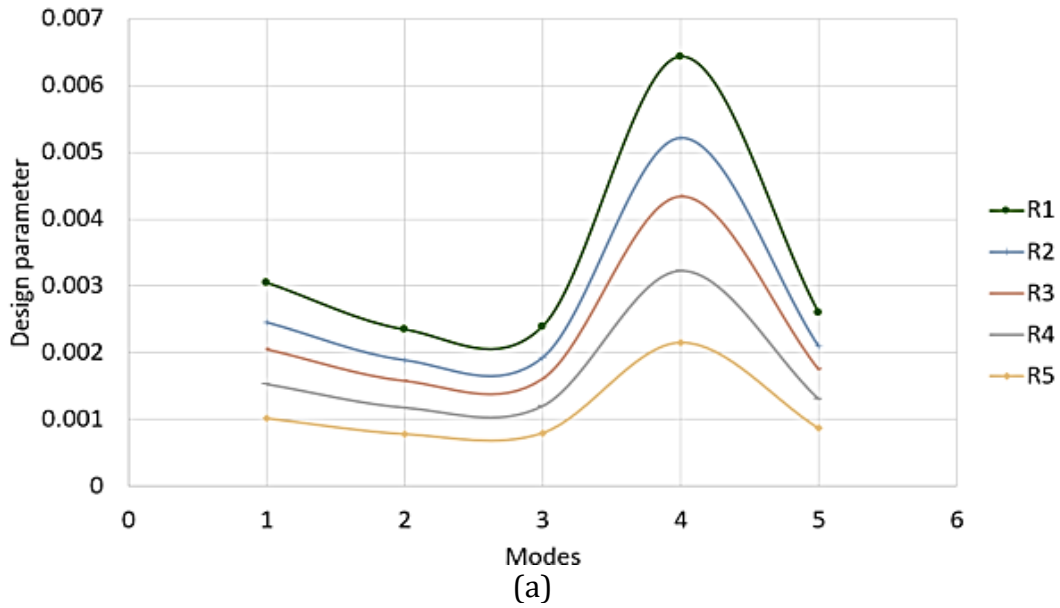


Figure 5.27: (a) Upper limit design trim top disc dimension evolution with computation modes (b) Upper limit design trim top disc condition number evolution with computational modes

Therefore, it can be inferred from these figures that number of modes to be used within inverse design process can be two or three modes. However, admitting three modes within inverse design process can be computationally expensive. Similar to original trim top disc design, this again limit optimal number of modes to be used to two modes.

Condition number in conjunction with augmented snapshot ensemble energy spectrum can be seen to decide optimum computational modes for trim top disc inverse design. A general framework can be issued for multistage continuous resistance trim inverse

design for prescribed local flow coefficient distribution based on the observed modal criteria. It can be recalled that multistage continuous resistance trim consists of various discs stacked together. Total number of disc present are 11 with each individual disc containing cylindrical resistance elements to control pressure drop. In chapter 3, relevant trim literature identified lack of multistage continuous resistance trim design framework. In particular, it was highlighted that current trim designing practices does not take local flow three dimensionality into consideration. Next section addresses this shortcoming and introduces novel design framework for multistage continuous resistance trim.

5.5. Novel Low Fidelity based Trim Design Framework (LF-TDF)

Multistage continuous resistance trim consists of 11 discs. Each disc can further be divided into four quarters. Individual quarters consist of five-cylinder rows. Figure 5.1 and 5.2 show individual disc and trim arrangement respectively. It can be seen that within trim, discs are arranged in parallel as flow enters each disc simultaneously. Furthermore, within individual discs flow enters from all directions simultaneously, indicating parallel arrangement of discs quarters. However, within individual quarters flow enters each row consequentially, indicating series arrangement of rows.

Asim *et al.* [70] investigated trim flow and formulated numerous expressions that relate trim flow capacities to individual trim disc row flow capacities for top disc. A parallel expression was formulated relating trim flow capacity to individual discs and series expression was formulated relating individual row flow capacity to disc flow capacity. The formulated expressions are as follows:

$$C_{V_{Disc}} = \frac{1}{\sqrt{\sum_1^j \left(\frac{1}{C_{V_{Row j}}^2} \right)}} \quad (5.5)$$

$$C_{V_{Trim}} = \sum_1^i C_{V_{Disc i}} \quad (5.6)$$

Here j represents number of rows while i represents number of discs within trim. The case considered here has $j=5$ and $i=11$. The above equations can be embedded within LF-TDF. It should be recalled that Asim *et al.* [65] also observed small variations within

individual discs quarter flow capacities. Such observation simplifies trim design as inverse design computation is only needed to be carried out for individual discs quarters.

Framework consist of following major components:

- High fidelity module
- Snapshot Ensemble
- Modal optimisation
- Optimizer
- Low fidelity module/Geometry Generator

Figure 5.28 shows proposed LT-TDF architecture. The architecture capitalises on low fidelity POD approach for trim design. Trim flow capacity is prescribed as target. Local quarter row flow capacity ($C_{V_{Row}}$) for individual disc is selected to compute disc and trim flow capacity using $C_{V_{Disc}}$ and $C_{V_{Trim}}$ equations (5.5 & 5.6 respectively). The computed trim flow capacity is compared to the prescribed trim flow capacity and if matched, the selected $C_{V_{Row}}$ is further concatenated within snapshot ensemble. $C_{V_{Row}}$ selection can be made based on experience or current snapshot ensemble knowledge. The optimizer computes required POD coefficients based on Gappy data provided. A new trim geometry is generated in each iteration, along with its flow field characteristics (local flow capacity distribution). The newly generated trim geometry and corresponding flow field characteristic are checked against user-specified design bounds. The cycle continues until optimiser achieves an optimum geometry. Each component is further discussed as follows:

5.5.1. High fidelity module

High fidelity module forms one of the key elements of LF-TDF architecture. It contains Navier Stokes solver that computes flow solution for different trim designs. Commercial software package FLUENT is used to simulate flow solution for trim. The module produces flow snapshots for snapshot ensemble.

Trim design parameters and boundary conditions forms an input to high fidelity module. By parametrising, different trim designs are obtained with varying cylindrical resistance element dimensions. This builds trim design space from family of candidate configurations. Flow field for these trim designs are computed with each

trim steady-state computation taking ~ 2 hours CPU time on Intel i6 @3 GHz processor.

The following modules are written in MATLAB script with a CPU runtime of less than 0.5 seconds on Intel i7 @3.4 GHz processor.

5.5.2. Snapshot Ensemble

The computed flow fields for respective trim designs is collectively pass down as initial designs to snapshot ensemble. Ensemble augments these snapshots with their respective trim geometry parameters. Thus, each column of the resultant snapshot matrix starts with geometry parameters followed by corresponding flow characteristics.

The flow characteristics that is considered for prescription is individual disc quarter local row flow capacity. The distribution is specified as target to be achieved for inverse design process. The required number of modes for individual disc quarter inverse design is computed in modal optimisation module. These number of modes are further utilized within iterative process. Thus, choice of appropriate snapshots is reflected in target to be achieved. Once target flow characteristics is decided followed by appropriate snapshot choice, number of orthogonal modes required for inverse design process is chosen. Target distribution is concatenated as an additional column to constructed snapshot ensemble with first five rows containing trim geometry information. Given the absence of trim geometry information, particular missing elements are initially filled as zero. These elements are replenished in subsequent optimization run.

5.5.3. Modal Optimisation

Modal optimisation module computes number of modes required for individual trim disc inverse design. Optimised number of modes are computed to maintain: computational quality and computational efficiency.

Figure 5.29 shows the module in detail. The computed modes in snapshot ensemble forms input to modal optimisation module. First five modes are chosen and Gappy inner product $(\Phi^i, \Phi^j)_n$ is computed among $\Phi^1\Phi^1, \Phi^1\Phi^2, \Phi^1\Phi^2\Phi^3, \Phi^1\Phi^2\Phi^3\Phi^4$ &

$\Phi^1 \Phi^2 \Phi^3 \Phi^4 \Phi^5$. Condition number is computed for Gappy inner products and are further compared to set condition number criterion. Gappy inner product $(\Phi^i, \Phi^j)_n$ with orthogonal modes yields identity matrix with condition number one. However, non-orthogonal modes yield non-unity condition number indicating orthogonality loss. The extent of orthogonality loss is quantified in condition number. As was observed in original trim top disc inverse design, the computed dimension values remained near to actual trim dimensions for minimised condition number of 1, 1.003 and 1.05 for one, two and three modes respectively. These condition numbers were well below two and preserved modal orthogonality. However, higher modal inclusion distorted orthogonality with exponential increase in condition number well beyond two. This was further reflected in computed dimension divergence from actual dimension. If no modes are observed satisfying set condition number criteria, 10 modes from snapshot ensemble are searched. The modes satisfying condition number criteria are further chosen. Corresponding modal energies are identified. A summation of modal energies is computed by including individual modal energies at a time. The summation terminates once set criteria of 99.99% is achieved. The obtained modes thus not satisfy minimum condition number and sum modal energy criterion.

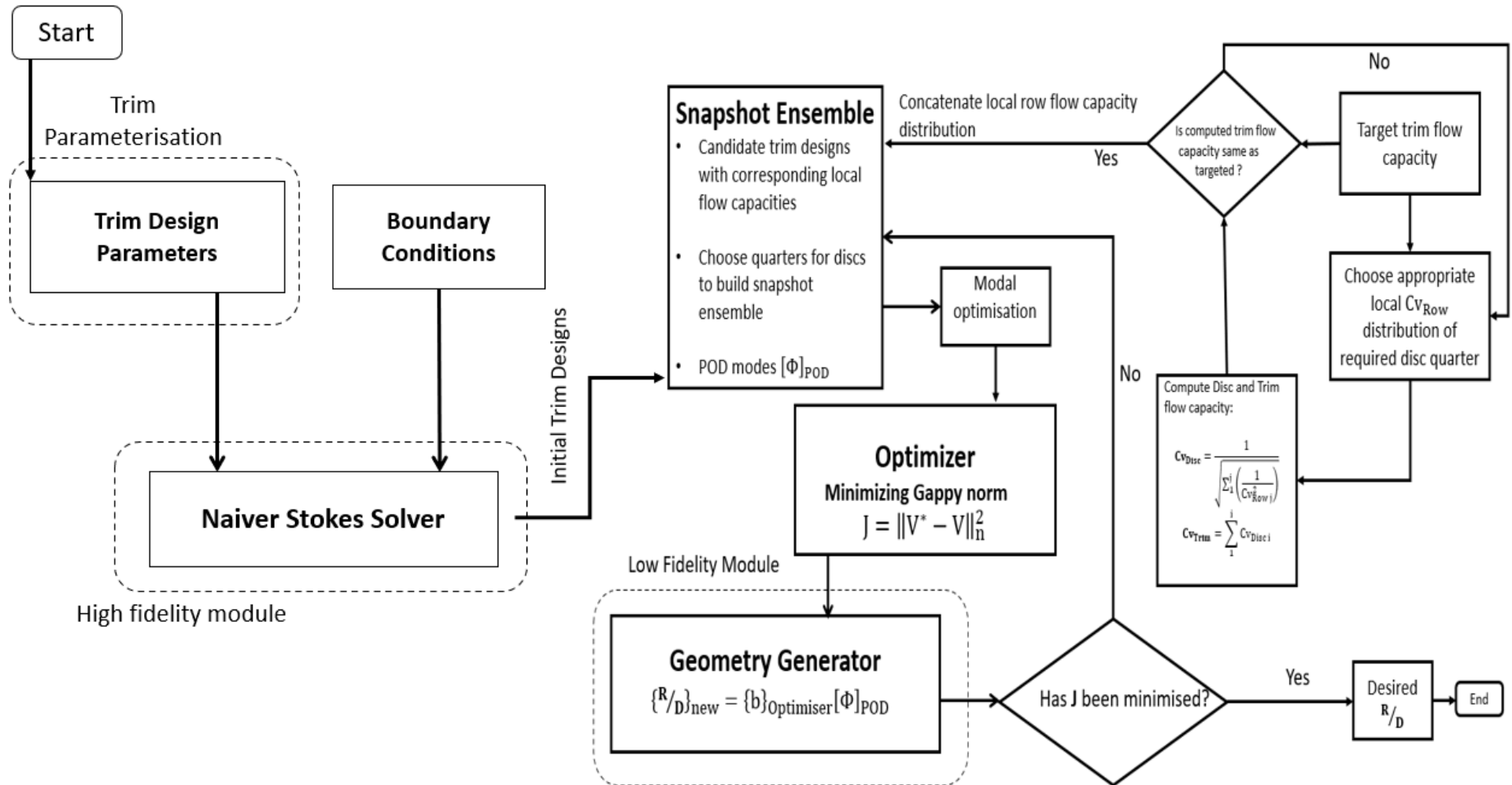


Figure 5.28: LF-TDF Architecture

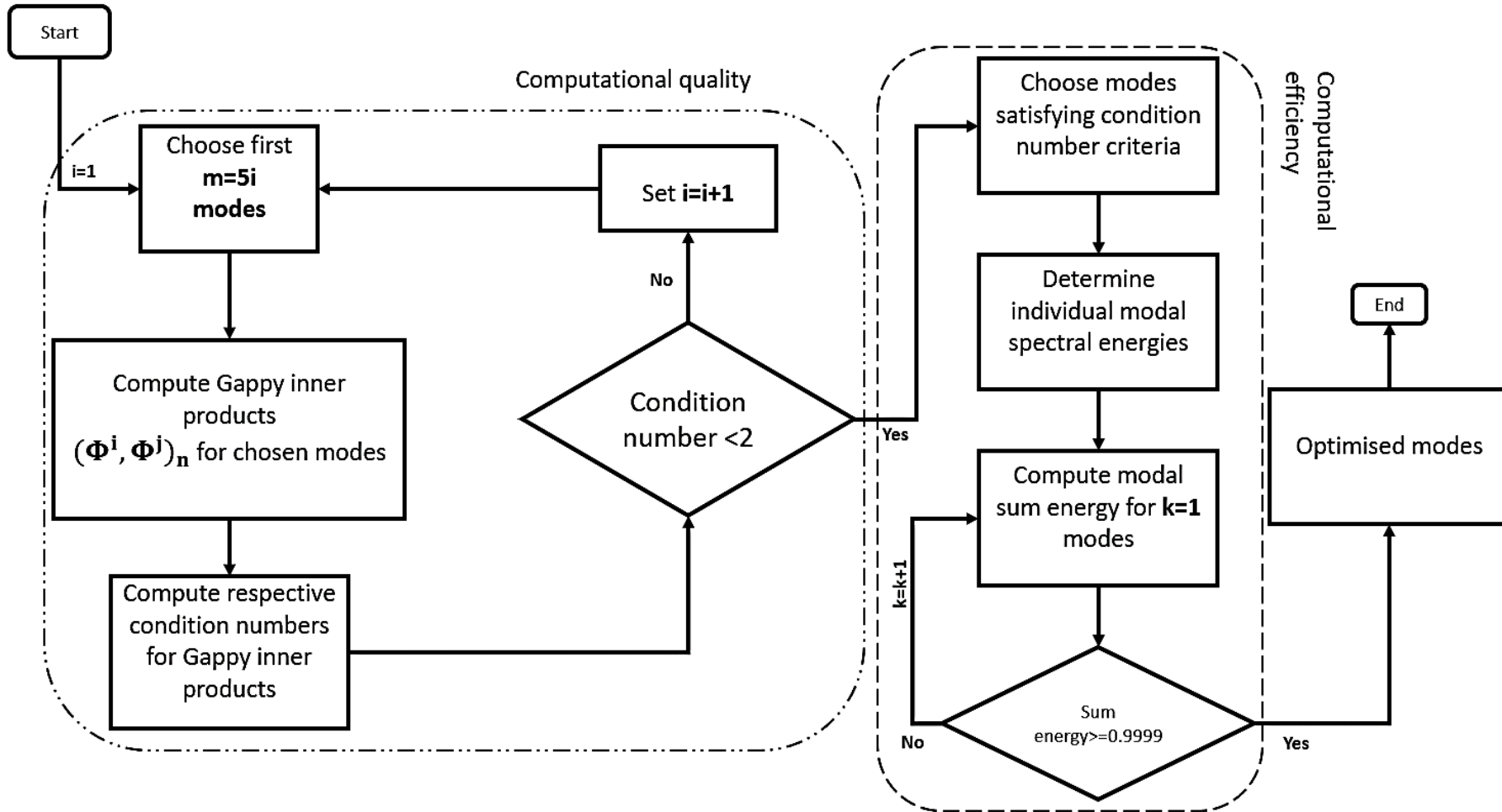


Figure 5.29: Modal Optimisation

It can be seen that condition number maintains computational quality while sum modal energy criterion maintains computational efficiency for inverse design process. Computational quality considers the modal orthogonality loss and corresponding inverse design data quality. However, computational efficiency considers number of computational resources used during inverse design process.

5.5.4. Optimizer

The optimizer aids in actual task of computing missing trim geometry parameters. This is achieved by minimising Gappy cost function (J) between target distribution (\mathbf{V}^*) and achieved distribution (\mathbf{V}) at each iteration. Optimizer produces modal coefficients as a result of this minimisation. Optimiser intakes optimised number of modes from modal optimisation module and computes Gappy inner products required for modal coefficient.

5.5.5. Low fidelity module/Geometry Generator

Computed modal coefficients within optimizer are further passed down to low fidelity module. The coefficients are combined with respective optimised orthogonal modes to compute missing trim geometry parameters. Based on set convergence criterion, missing elements within snapshot ensemble is replenished with newly computed value.

5.5.6. LF-TDF Advantages

The framework established in the previous section derives its robustness from using low fidelity representation of a high-fidelity system. This preserves the essential features that dictates dynamic system while maintaining computational efficiency. Some of the advantages of the framework are listed below:

1. A better control on optimisation can be achieved by building relevant snapshot ensemble. The ensemble can reflect 'designer's experience' that injects prior designing knowledge into optimisation process.
2. A better design control over local flow condition leading to global flow behaviour change such as cavitation, noise, vibration etc. can be seen incorporated within designing procedure. Trim designs avoiding these global flow behaviour changes can now be computed.
3. A faster flow field evaluation is achieved for intermediate trim designs that are generated within optimisation iteration. These intermediate trim designs and

corresponding flow field can be further included to expand design space based on Gappy cost function J .

4. Low fidelity model based reduced computation time to derive trim designs.

5.5.7. LF-TDF Limitations

Although trim design framework offers major benefits for effective and faster optimization process, there are certain limitations, as listed below:

1. The current framework is applicable only to design multistage continuous resistance trim.
2. The prescribed target (trim local row flow capacity) is assumed to be contained within the subspace spanned by relevant mode.

5.6. Summary

In summary, study introduced novel regression model linking cumulative local geometry change effect on the local flow capacity. The model was further used for design space expansion and creating trim augmented snapshot ensemble. Modal analysis for expanded design space revealed governing flow structures. Based on flow structure extrema, flow sensing positions were determined. Investigation into multistage continuous resistance trim sparse augmented snapshot ensemble established convergence characteristics. A qualitative correlation was established relating available trim ensemble data quality to the required number of iterations for stipulated convergence. Furthermore, a novel modal optimisation criterion was established maintaining computational efficiency and computational quality. Moreover, a novel framework for continuous resistance trim inverse design was established employing the modal optimisation criterion. The framework intakes trim local flow capacities and generates local geometrical features based on low fidelity approach.

CHAPTER 6

CONCLUSIONS

Detailed conclusions are drawn in this chapter based on the work carried out in previous chapters on functional surface and multistage continuous resistance trim design. Major achievements are summarised along with novel contributions to existing knowledge base. In doing so, initial aims and objectives of this study are possibly referred. Finally, current work is reviewed and recommendations on future work is developed.

6.1. Research Problem Synopsis

Bio-inspired surfaces can be one of the most efficient strategies that can be employed within industrial asset design for optimum performance. These surfaces have key industrial employment advantage in geometrical simplicity and yet bringing major efficiency disruption in asset performance. The disruption is brought in by either encouraging or discouraging certain local phenomenon in the immediate vicinity of bio-inspired surface. It thus become imperative to have a framework for designing surfaces to engineer required local phenomenon. Importantly, framework should lay principled approach to compute surface geometrical parameters as a function of local phenomenon. Such bio-inspired surfaces can now be called functional surfaces. Aerodynamic drag reducing functional surface can be a typical example. Inspired from shark skin geometry, the functional surface can produce optimum or targeted surface drag distribution.

Control valve forms major part of industrial flow handling systems. The globe type control valve considered in this study consists of multistage continuous resistance trim. Individual trim disc consists cylindrical resistance elements for controlled pressure drop. Consequently, the disc acts as functional surface responsible for pressure drop characteristics. Current trim design practice follows top down approach of prescribing trim flow capacity and deriving geometry. However, as pointed out in chapter 2, the approach fails to take design consideration of local flow effects leading to unwanted phenomenon of cavitation, noise, vibration etc.

Comprehensive literature review in chapter 2 revealed major gaps in functional surface and multistage continuous resistance trim design. It was established that current literature lacks in any established functional surface framework to derive surface geometry parameters for prescribed flow characteristics. Furthermore, literature identified existence of flow three-dimensionality before entering multistage continuous resistance trim. Consequently, individually stacked disc flow capacity varied. However, it was identified that traditional top-down trim design approach does not take flow three-dimensionality into consideration. Consequently, a requirement of bottom-up trim design framework was identified that derived local geometrical features based on prescribed local flow characteristics distribution. Primary aims and objectives summary is provided in following sections along with major contributions and achievements. For reference, Chapter 2 notes detailed objectives within individual aims.

6.2. Research Aims and Major Achievements

Thesis main aims and corresponding achievements are defined as follows:

Research Aim 1: Establishing novel inverse design software environment for functional surface containing simple discontinuous geometry structures for prescribed simple flow characteristics.

Achievement 1: This study introduced inverse design methodology for functional surfaces. Two distinct flow characteristics were prescribed as target: velocity control points and local friction factor distribution. Velocity control points dictated developed velocity field and hence associated heat transfer characteristics over the functional surface. Local friction factor dictated local wall shear stress that effectively controls pressure drop within wall bounded flows. Control points for individual nine designs were derived using least square fit of high-fidelity velocity data, thus yielding local velocity functional form. Spatial control point distribution over 2300 points revealed qualitatively and quantitative velocity field variation with change in surface parameter values. Control point based modal analysis revealed governing flow structures. Flow sensing positions were identified based on dominant flow structure extrema. Furthermore, dominant flow structures were exploited for control point or friction factor based inverse design.

Nine snapshot velocity control points based functional surface inverse design was explored. Sensitivity investigation revealed Gappy POD based inverse design being least sensitive to control point \mathbf{c} or all control point prescription. Sensitivity investigation further indicated common flow structure existence among snapshots of \mathbf{c} and \mathbf{abc} . A further investigation into Gappy inner products $(\Phi^i, \Phi^j)_n$ & $(\mathbf{g}, \Phi^i)_n$ of individual design points explored modal orthogonality relationship over support space \mathbf{n} and its impact on computational efficiency. The resultant modal expansion coefficients revealed extent of modal dominance. Discarding outliers, new snapshots ensemble was computed. New ensemble based three mode consensus was observed to be developed for identified subspace of $0.14 \leq \mathbf{h}/\mathbf{sx} \leq 0.29$. Nine snapshot friction factor based functional surface inverse design was explored. Sensitivity investigation showed only four design snapshots sharing common dominant modes. Gappy inner products and modal coefficients for nine snapshot designs were investigated. Non-orthogonality was

CONCLUSIONS

observed among first two computational modes. Furthermore, investigation established extent of mode one dominance based on modal coefficient for all design points. Discarding outliers, new snapshots ensemble was computed. New ensemble based one mode consensus was observed to be developed for identified subspace of $0.25 \leq \mathbf{h}/\mathbf{sx} \leq 0.30$. A novel Low Fidelity based Functional Surface Inverse Design Environment (LFF-SIDE) combining high fidelity and low fidelity approach for identified range was proposed. Based on target prescription, the LFF-SIDE chooses appropriate snapshot ensemble from original nine snapshot sets and computes required modes. For designing functional surface in the range $0.14 \leq \mathbf{h}/\mathbf{sx} \leq 0.29$ based on local velocity control point prescription, LFF-SIDE selected six snapshots and computed three modes. For designing functional surface in the range $0.25 \leq \mathbf{h}/\mathbf{sx} \leq 0.30$ based on local friction factor prescription, LFF-SIDE selected four snapshots and computed one mode.

Research Aim 2: Establishing novel inverse design framework for functional surfaces containing simple discontinuous geometry structure for prescribed complex flow characteristics.

Achievement 2: This study introduced multistage continuous resistance trim inverse design methodology. Local flow capacities were prescribed as the target. Prescribing local flow capacities provide bottom-up design control over local flow conditions leading to cavitation, vibration, acoustic noise etc. A regression model was developed linking local row cylinder dimensions to local flow capacities. Qualitative and quantitative influence of change in local row cylinder dimensions on individual local flow capacities was estimated. Furthermore, design space was expanded to add more trim geometries and corresponding local flow capacities to the snapshot ensemble. Newly computed snapshot ensemble modal analysis revealed governing flow and design structures. Flow sensing positions were identified based on dominant flow structure extrema. Furthermore, dominant flow structures were exploited for local flow capacity based inverse design.

This section established convergence characteristics for sparse multistage continuous resistance trim augmented snapshot ensemble. Investigation utilized Gappy POD methodology to repair sparse trim ensemble. In doing so, Gappy POD efficacy to solve sparse trim ensemble problem is investigation. Investigation revealed Gappy POD high effectiveness in repairing trim

CONCLUSIONS

ensemble of varying sparsity. Sparsity characteristics for intricate geometrical features and corresponding complex flow features snapshot ensemble was investigated. Eigenvalue spectrum convergence characteristics was established for 40%, 60% and 80% missing data. It was concluded that spectral convergence depends on detail of particular snapshot ensemble. Particularly, it depends on the amount of missing data within an individual snapshot. To roughly predict required number of iterations for given data quality, a correlation was drawn between existing data sparsity and required number of iterations to reach stipulated convergence. Based on cumulative relative energy, 87 to 100 number of iterations were predicted for rebuilding sparse multistage continuous resistance trim snapshot ensemble.

Further to establishing Gappy POD efficacy for rebuilding sparse trim snapshot ensemble, the method was applied for multistage continuous resistance trim inverse design. Modal orthogonality loss was established and further explored for its application to modal optimisation. The extent of orthogonality loss is quantified in condition number Optimised number of modes are computed to maintain: computational quality and computational efficiency. Condition number maintained computational quality while sum modal energy criterion maintained computational efficiency for inverse design process. Computational quality considered modal orthogonality loss and corresponding inverse design data quality while computational efficiency considers number of computational resources used during inverse design process.

A novel Low Fidelity based Trim Design Framework (LF-TDF) combining high fidelity and low fidelity approach for trim design is proposed. Based on target prescription, the LF-TDF employs condition number and sum modal energy criteria to compute optimised modes. The modes are further combined with the modal coefficients to compute low fidelity representation.

6.3. Thesis Conclusions

Supporting the existing literature, a comprehensive study has been carried out regarding designing of functional surface and multistage continuous resistance trim. Novelty has been added to the designing process of functional surfaces and multistage continuous resistance trim.

Research Objective 1: Developing functional form of velocity field with qualitative and quantitative control points spatial description for various design changes.

Conclusion 1: From the investigations regarding effect of discontinuous geometry features on simple flow behaviour carried out in this study, it can be concluded that three velocity control points can be used for describing LBM computed high fidelity velocity field. The velocity information is thus embedded within control points. Furthermore, from the qualitative investigation of control points spatial distributions it can be concluded that control point **a** and **c** follow similar spatial distribution trend while control point **b** spatial distribution being the mirror image.

Research Objective 2: Identifying governing flow structures and flow sensing positions for functional surface.

Conclusion 2: From the modal analysis regarding effect of discontinuous geometry features on simple flow behaviour carried out in this study, it can be concluded that control points respective first mode energy content exceeded 99%. Seven, six and six modes were identified as dominant modes for control points **a**, **b** and **c** respectively. Dominance was determined based on respective energy spectrums. Furthermore, analysis identified energetic modes local maxima and minima locations. Modal extrema can be flow sensing positions. Altogether, modal analysis revealed three potential flow sensing positions. Furthermore, it was also concluded that sensing positions can be added based on higher mode local maxima and minima. However, sensing effectiveness gets constant with subsequent higher mode inclusion on account of lower cumulative energy content.

Research Objective 3: Investigating Gappy POD sensitivity for prescribed control point or friction factor distribution and identifying particular number of modes operated functional surface design subspace.

Conclusion 3: From sensitivity analysis regarding effect of discontinuous geometry features on simple flow behaviour carried out in this study, it can be concluded that functional surface

CONCLUSIONS

inverse design was found least sensitive to prescribed velocity control point distribution of \mathbf{c} or all control points. Moreover, Gappy inner product $(\Phi^i, \Phi^j)_n$ over support space \mathbf{n} observed modal orthogonality, indicating computationally efficient control point based inverse design process. It can also be concluded that outlier and inlier velocity control points-based design points might not be sharing similar dominating flow structures. Further exploration identified velocity control point based design subspace with three operating modes computed from new snapshot ensemble. Furthermore, Gappy inner product $(\Phi^i, \Phi^j)_n$ over support space \mathbf{n} observed modal non-orthogonality, indicating relative computational inefficiency for friction factor based inverse design process. Moreover, it can also be concluded that outlier and inlier friction factor-based design points might not be sharing similar dominating flow structures. Further exploration identified friction point based design subspace with one operating mode computed from new snapshot ensemble.

Research Objective 4: Developing regression-based model relating local flow capacity with local geometrical discontinuous features for qualitative and quantitative description.

Conclusion 4: From the investigations regarding cumulative effect of discontinuous geometrical features on complex flow behaviour carried out in this study, it can be concluded that local row cylinder dimension change has significant effect on considered row cylinder local flow capacities. This can be seen in local flow capacity graphs and power coefficient values. Moreover, it can also be concluded that this complex geometrical interaction brought in by flow area change majorly affects mass flow rate and pressure drop across the cylinders.

Research Objective 5: Identifying governing flow structures and flow sensing positions for multistage continuous resistance trim.

Conclusion 5: From the modal analysis regarding effect of discontinuous geometry features on complex flow behaviour carried out in this study, it can be concluded that local flow capacity and design change first mode energy content exceeded 99%. Two and one modes were identified as dominant modes for local flow capacity and design change respectively.

CONCLUSIONS

Dominance was determined based on respective energy spectrums. Furthermore, analysis identified local flow capacity energetic modes local maxima and minima locations. Modal extrema can be flow sensing positions. Altogether, modal analysis revealed three potential flow sensing positions within trim top disc at 1st, 2nd and 5th row cylinders. Furthermore, two modes were identified as dominant modes for augmented snapshot ensemble computed by combining trim top disc geometrical and flow information. It was identified that two modes of augmented snapshot ensemble contained 99.99% of flow energy. It was concluded that augmented snapshot modal extrema can be seen to correlate to that of individual flow capacity and design parameter modal extrema.

Research Objective 6: Investigating trim ensemble sparsity and developing novel optimised modal selection criterion.

Conclusion 6: From the sparsity investigation of trim ensemble consisting discontinuous geometry features effect on complex flow behaviour carried out in this study, it can be concluded that for 40%, 60% and 80% sparsity, first two modes have higher convergence rate. The same can be concluded for higher modes greater than seven. Moreover, investigation concluded rate of eigenvalue spectrum convergence as a function of snapshot ensemble sparsity. This was particularly observed to be true for convergence rate of modes between 3-8. Furthermore, a correlation was drawn between existing data sparsity and required number of iterations to reach stipulated convergence using cumulative relative energy. For the investigated sparse data locations, it was concluded that 100-87 iterations can be required for data sparsity ranging from 40%-80% for convergence criterion set below 1E-04 cumulative relative energy. Further to considering inverse design problem as sparsity problem, it can be concluded that Gappy inner product $(\Phi^i, \Phi^j)_n$ has significant effect over deriving the dimensions of trim geometrical features. Particularly, modal orthogonality over support space n was identified as major contributing factor. Therefore, it can be concluded that monitoring condition number of Gappy inner product $(\Phi^i, \Phi^j)_n$ can quantitatively diagnose modal orthogonality loss. Furthermore, it can be concluded that a novel optimised modal selection criterion can be formulated by combining modal spectral energy criterion (number of modes containing 99.99% energy) with condition number criterion (diagnosing orthogonality loss). Consequently, it can be concluded that condition number criterion maintains computational

quality while modal spectral energy criterion maintains computational efficiency to deliver optimised number of modes for inverse design computation.

6.4. Thesis Contribution

Novelties are described in this section summarising major thesis contributions:

Contribution 1

One of the major contributions of this investigation is establishing novel inverse design software environment of functional surface containing discontinuous geometry structure for identified design subspace. The established environment enables functional surface inverse design, contained within identified design subspace, against the prescribed simple flow characteristics. Available literature cites flow investigations over bio-inspired functional surfaces. These studies primarily focused on geometrical effect on flow features, however, lacked in linking generated flow features to geometry parameters. High fidelity Lattice Boltzmann flow simulation capability enabled the author to compute flow structures for arbitrarily selected design space. The flow structures are principally utilised to compute low fidelity representation for inverse designing discontinuous geometry structure on functional surface within identified design subspace. Specific number of modes to be used for inverse design computation were identified for velocity control points and friction factor-based prescription. Furthermore, flow sensing positions were selected in principle manner. Moreover, velocity functional form was computed, subsequently obtaining velocity control point distribution.

Contribution 2

Another major contribution of this study is function surface inverse design to regulate flow within multistage continuous resistance trim. Literature identified current top down trim design methodologies. Furthermore, it was also identified lack of three-dimensional flow information implementation within top down trim design approach. Additionally, current design practices fail to undertake local flow effects into design consideration. Design based on the local flow effects can mitigate or eliminate unwanted flow phenomenon of cavitation, noise, vibration etc. Based on these shortcomings, a novel framework is established to inverse design continuous resistance trim for prescribed local flow capacity distribution. High fidelity

CONCLUSIONS

computational fluid dynamics simulation capability enabled the author to compute flow structures for trim design space. The flow structures are principally utilised to compute low fidelity representation for inverse designing discontinuous geometry structure on trim disc surface. Study also investigated modal orthogonality over support space and its implementation within design framework. The investigation established a novel criterion to compute optimised modes for inverse design process. The criterion computes number of modes by maintaining inverse design computational quality and efficiency. Furthermore, flow sensing positions within trim top disc were selected in principle manner. Moreover, a regression equation linking cumulative local geometrical change effect on local flow capacity is developed.

6.5. Recommendations for Future Work

Functional surface inverse design and its application for flow control within multistage continuous resistance trim have been explored. This is primarily done by bridging the identified gaps within the literature. Concluding remarks, as presented in the above section, unlocks further potential research in the area of functional surface, multistage continuous resistance trim and inverse design. Some of the identified future work is described as follows:

Recommendation 1

One of the primary future works that can be carried out is to identify inverse design subspace derived from design space for complex flow phenomenon using mesoscopic approach of Lattice Boltzmann Method (LBM). Developing LBM for complex phenomenon such as turbulent flow can be intellectually and computationally challenging. However, this development can capture relevant turbulent flow structures and further advance the scope of inverse design to complex turbulent flows. Moreover, current work focused on inverse design of functional surface containing rectangular shape discontinuous geometry structures. Further explorations can be carried out to inverse design functional surface containing discontinuous geometry structure shape computed out of multiple discontinuous geometry structure shapes. To carry this out, an effective framework might be necessary that combines flow structure information from multiple discontinuous geometry structure shapes to compute geometry for prescribed flow characteristics. Moreover, further study can be conducted on the effect of functional surface discontinuous geometry features on simple to complex flow transition. The work can further be extended to form effective control strategy for desired flow transition characteristics.

Recommendation 2

Current study focused on multistage continuous resistance trim inverse design using Gappy POD. Future exploration can also look into deriving a general trim design framework that is independent of trim type. Furthermore, the current study also identified prime flow sensing positions based on modal extrema. Identified sensing positions coupled with Gappy POD can further be explored to design adaptive flow control schemes for efficient flow within the trim and avoid unwanted flow effects. Bio-inspired functional surfaces and their inverse design can further be explored as better and diverse flow control options.

Recommendation 3

Current study focused on the designing aspects of functional surface containing discontinuous geometry structures for prescribed simple and complex flows. Furthermore, current study was limited on the designing functional surfaces containing simple discontinuous geometry structures. Future explorations can focus on fabricating functional surfaces by using 3D printer technology. One of the primary advantages of using this technology is the fabrication of intricate geometrical structures. The technology can allow to manufacture bespoke functional surfaces containing complex geometrical structures that are combination of simple geometrical structures. The technology further allows combining materials of varied mechanical strength to be fabricated together for applications demanding properties of flexibility and rigidity within functional surfaces. 3D printed functional surfaces offer a better flow control option as it allows meticulous control over geometrical features and shapes.

Recommendation 4

Current study focused on optimising single objective function to obtain geometrical parameter. However, artificial intelligence fuelled tools can further be studied to be deployed for multi-objective optimisation. One such tool to be investigated can be Artificial Neural Network (ANN). ANN can be used to build computationally efficient surrogate models that can be deployed for rapid design evaluation. This artificial intelligence approach can not only map linear functional relations but also non-linear functional relations. Artificial intelligence approach or specifically ANN's can be a handy tool to solve multi-objective optimisation problems with an ability to be integrated into a wider designing framework.

Recommendation 5

Another future area for focus could be that of digital twin. Digital twin is defined as the virtual replica of the product or system that mirrors the actual physical product or system. Digital twin changes its status based on the information provided by the sensors installed on the physical product or system. Future research can focus on creating digital twin for multi-stage continuous resistance trim. The trim digital twin can utilize sensory information from the sensors placed at the trim positions derived in this thesis. Based on this sensor information, the trim digital twin can change its state to accurately reflect the physical trim. The trim digital twin can then be employed to prevent failures due to cavitation by continuous process monitoring within multi-stage continuous resistance trim.

REFERENCES

- [1] Rosen, M., Cornford, N. Fluid Friction of Fish Slimes. *Nature* 234, 49–51 (1971)
doi:10.1038/234049a0.
- [2] Blake, R.W.; Chan, K.H.S. Models of the turning and fast-start swimming dynamics of aquatic vertebrates. *J. Fish Biol.* 2006, 69, 1824–1836.
- [3] Bannasch, R.; Wilson, R.P.; Culik, B. Hydrodynamic aspects of design and attachment of a back-mounted device in penguins. *J. Exp. Biol.* 1994, 194, 83–96.
- [4] Reif, W.E. Squamation and ecology of sharks. *Courier Forschungsinstitut Senckenberg* 1985, 78, 1–255.
- [5] Bechert, D.W.; Bruse, M.; Hage, W. Experiments with three-dimensional riblets as an idealized model of shark skin. *Exp. Fluids* 2000, 28, 403–412.
- [6] Luo, Y.H.; Yuan, L.; Li, J.H.; Wang, J.S. Boundary layer drag reduction research hypotheses derived from bio-inspired surface and recent advanced applications. *Micron* 2015, 79, 59–73.
- [7] Tong, J.; Lu, T.B.; Ma, Y.H.; Wang, H.K.; Ren, L.Q.; Arnell, R.D. Two-body abrasive wear of the surfaces of pangolin scales. *J. Bionic Eng.* 2007, 4, 77–84.
- [8] Abdel-Aal, H.A.; El Mansori, M. Tribological analysis of the ventral scale structure in a python regius in relation to laser textured surfaces. *Surf. Topogr. Metrol. Prop.* 2013, 1.
- [9] Klein, M.C.G.; Gorb, S.N. Epidermis architecture and material properties of the skin of four snake species. *J. R. Soc. Interface* 2012, 9, 3140–3155.
- [10] Hazel, J.; Stone, M.; Grace, M.S.; Tsukruk, V.V. Nanoscale design of snake skin for reptilian locomotion via friction anisotropy. *J. Biomech.* 1999, 32, 477–484.
- [11] Stavenga, D.G.; Foletti, S.; Palasantzas, G.; Arikawa, K. Light on the moth-eye corneal nipple array of butterflies. *Proc. R. Soc. B* 2006, 273, 661–667.

REFERENCES

- [12] Wilson, S.J.; Hutley, M.C. The optical-properties of moth eye antireflection surfaces. *Opt. Acta* 1982, 29, 993–1009.
- [13] Siddique, R.H.; Gomard, G.; Holscher, H. The role of random nanostructures for the omnidirectional anti-reflection properties of the glasswing butterfly. *Nat. Commun.* 2015, 6.
- [14] Prum, R.O.; Quinn, T.; Torres, R.H. Anatomically diverse butterfly scales all produce structural colours by coherent scattering. *J. Exp. Biol.* 2006, 209, 748–765.
- [15] Vukusic, P.; Sambles, J.R.; Ghiradella, H. Optical classification of microstructure in butterfly wing-scales. *Photon. Sci. News* 2000, 6, 61–66.
- [16] Galusha, J.W.; Richey, L.R.; Gardner, J.S.; Cha, J.N.; Bartl, M.H. Discovery of a diamond-based photonic crystal structure in beetle scales. *Phys. Rev. E* 2008, 77.
- [17] Kunz .C, Muller. F. & Graf. S. Bio-inspired functional surfaces based on laser-induced periodic surface structures *Materials* 2016, 9, 476.
- [18] Trillium flow technologies, https://www.trilliumflow.com/wp-content/uploads/2019/11/TFTUK_201909-X-Stream-Brochure-PW.pdf, accessed on 06/12/2019 at 1530 hrs.
- [19] Industrial process control valves, Part 2-4: flow capacity – test procedures. British Standards BSI; 2003. BS EN 60534-2-4.
- [20] Industrial process control valves, Part 2-5: flow capacity – test procedures. British Standards BSI; 2003. BS EN 60534-2-5.
- [21] Lewis F. Moody, “Friction Factors for Pipe Flow”, *Transactions of the A.S.M.E.*, pp. 671 -684 November 1944
- [22] C. F. Colebrook, “Turbulent Flow in Pipes With Particular Reference to the Transition Region between the Smooth and Rough Pipe Laws”, *Journal of the*

REFERENCES

- Institution of Civil Engineers (London, England), vol. 11, 1938-1939, pp. 133-156.
- [23] Bechert, D., Bruse, M., Hage, W., Van Der Hoeven, J. G., Hoppe, G., 1997. Experiments on drag-reducing surfaces and their optimisation with an adjustable geometry. *J. Fluid Mech.* 338, 59–87.
- [24] Lee, S. J., Lee, S. H., 2001. Flow field analysis of a turbulent boundary layer over a riblet surface. *Phys. Fluids.* 30, 153–166.
- [25] Choi, H., Moin, P., Kim, J., 1993. Direct numerical simulation of turbulent flow over riblets. *J. Fluid Mech.* 255, 503–539.
- [26] Goldstein, D., Handler, R., Sirovich, L., 1995. Direct numerical simulation of turbulent flow over a modelled riblet covered surface. *J. Fluid Mech.* 302, 333–376.
- [27] Bandyopadhyay .P. & Hellum .A., 2014 Modeling how shark and dolphin skin patterns control transitional wall-turbulence vorticity patterns using spatiotemporal phase reset mechanisms, *Scientific Reports*.
- [28] Wen. L., Weaver. J, Lauder G., Biomimetic shark skin: design, fabrication and hydrodynamic function, *Journal of Experimental Biology* 2014 217: 1656-1666; doi: 10.1242/jeb.097097
- [29] Oeffner, J. and Lauder, G. V. (2012). The hydrodynamic function of shark skin and two biomimetic applications. *J. Exp. Biol.* 215, 785-795.
- [30] Wen, Li & Weaver, James & Thornycroft, Patrick & Lauder, George. (2015). Hydrodynamic function of biomimetic shark skin: Effect of denticle pattern and spacing. *Bio inspiration & biomimetics.* 10. 066010. 10.1088/1748-3190/10/6/066010.
- [31] Schwarz van Manen AD (1992) Coherent structures over grooved surfaces. PhD thesis, Department of Electrical Engineering, Technische Universiteit Eindhoven, The Netherlands.

REFERENCES

- [32] Schneider M, Dinkelacker A (1993) Drag reduction by means of surface riblets on an inclined body of revolution. In: Speziale CG, Launder BE (eds) Near-wall turbulent flows. Elsevier, Amsterdam, pp 771–780.
- [33] Hage W, Bechert DW, Bruse M (1999) Cross-flow effects on optimized riblets. In: Cha'ra Z, Pollert J (eds) Proceedings of the 11th European drag reduction working meeting, 15–17 September 1999, Prague, Czech Republic, p 66.
- [34] Hage W, Bechert DW, Bruse M (2000) Yaw angle effects on optimized riblets. Notes Numer Fluid Mech 76:278–285.
- [35] Dinkelacker A, Nitschke-Kowsky P, Reif W-E (1988) On the possibility of drag reduction with the help of longitudinal ridges in the walls. In: Liepmann HW, Narasimha R (eds) Turbulence management and re-laminarization, IUTAM Symposium, Bangalore, India, 1987. Springer, Berlin Heidelberg New York, pp 109–120.
- [36] Koeltzsch K.; Dinkelacker A. & Grundmann R. Flow over convergent and divergent wall riblets, Experiments in Fluids 33 (2002) 346-350.
- [37] Schoppa, W., Hussain, F., 1998. A large-scale control strategy for drag reduction in turbulent boundary layers. Phys. Fluids 10, 5, 1049–1051.
- [38] Schoppa, W., Hussain, F., 2002. Coherent structure generation in near-wall turbulence. J. Fluid Mech. 453, 57–108.
- [39] Monty J.P, Hutchins N.& Nugroho B., Large scale spanwise periodicity in a turbulent boundary layer induced by highly ordered and directional surface roughness, International Journal of Heat and Fluid Flow 41 (2013) 90-102.
- [40] Harun, Zambri & Abbas, Ashraf Amer & Dheyaa, R & Ghazali, Mohamad Izhar. (2016). Ordered roughness effects on NACA 0026 airfoil.
- [41] Herbert T. Secondary instability of plane channel flow to subharmonic three-dimensional disturbances, The Physics of Fluids 26, 871 (1983).

REFERENCES

- [42] Cossu, C & Brandt, L, Stabilization of Tollmien-Schlichting waves by finite amplitude optimal streaks in the Blasius boundary layer, *Physics of Fluids* (2002) Volume 14, Number 8.
- [43] Fransson, J. H. M., Talamelli, A., Brandt, L., Cossu, C., 2004. Experimental and theoretical investigation of the nonmodal growth of steady streaks in a flat plate boundary layer. *Phys. Fluids*. 16, 3627.
- [44] Fransson, J. H. M., Talamelli, A., Brandt, L., Cossu, C., 2006. Delaying transition to turbulence by a passive mechanism. *Phys. Rev. Lett.* 96, 064501.
- [45] Fransson, J. H. M., Talamelli, A., Cossu, C., 2005. Experimental study of the stabilization of Tollmien-Schlichting waves by finite amplitude streaks. *Phys. Fluids*. 17, 054110.
- [46] Fransson, J. H. M., Talamelli, A., 2012. On the generation of steady streamwise streaks in flat-plate boundary layers. *J. Fluid Mech.* 698, 211–234.
- [47] Elyyan., Heat transfer augmentation surfaces using modified dimple/protrusions, Doctor of Philosophy thesis (2008).
- [48] Rohsenow, W., Hartnett, J. & Cho, Y. *Handbook of Heat Transfer* (McGrawHill Professional, 1998).
- [49] Carey, V. P. *Liquid Vapor Phase Change Phenomena: An Introduction to the Thermophysics of Vaporization and Condensation Processes in Heat Transfer Equipment* 2nd edn (CRC Press, 2007).
- [50] Dhir, V. K. Boiling heat transfer. *Annu. Rev. Fluid Mech.* 30, 365–401 (1998).
- [51] Kim, S. J., Bang, I. C., Buongiorno, J. & Hu, L. W. Effects of nanoparticle deposition on surface wettability influencing boiling heat transfer in nanofluids. *Appl. Phys. Lett.* 89, 153107 (2006).
- [52] Feng, B., Weaver, K. & Peterson, G. P. Enhancement of critical heat flux in pool boiling using atomic layer deposition of alumina. *Appl. Phys. Lett.* 100, 053120 (2012).

REFERENCES

- [53] Min, D. H. et al. 2-D and 3-D modulated porous coatings for enhanced pool boiling. *Int. J. Heat Mass Transf* 52, 2607–2613 (2009).
- [54] Park, S. D. et al. Effects of nanofluids containing graphene/graphene-oxide nanosheets on critical heat flux. *Appl. Phys. Lett.* 97, 023103 (2010).
- [55] Nikolayev, V. S., Chatain, D., Garrabos, Y. & Beysens, D. Experimental evidence of the vapor recoil mechanism in the boiling crisis. *Phys. Rev. Lett.* 97, 184503 (2006).
- [56] Chu, K.-H., Enright, R. & Wang, E. N. Structured surfaces for enhanced pool boiling heat transfer. *Appl. Phys. Lett.* 100, 241603 (2012).
- [57] Chu, K.-H., Joung, Y. S., Enright, R., Buie, C. R. & Wang, E. N. Hierarchically structured surfaces for boiling critical heat flux enhancement. *Appl. Phys. Lett.* 102, 151602 (2013).
- [58] Haramura, Y. & Katto, Y. A new hydrodynamic model of critical heat flux, applicable widely to both pool and forced convection boiling on submerged bodies in saturated liquids. *Int. J. Heat Mass Transf.* 26, 389–399 (1983).
- [59] Zuber, N. *Hydrodynamic Aspects of Boiling Heat Transfer* (Research Laboratory, Los Angeles and Ramo-Woolridge Corporation, Univ. California, 1959).
- [60] Ahn, H. S., Jo, H. J., Kang, S. H. & Kim, M. H. Effect of liquid spreading due to nano/microstructures on the critical heat flux during pool boiling. *Appl. Phys. Lett.* 98, 071908 (2011).
- [61] Zhang, B. J. & Kim, K. J. Effect of liquid uptake on critical heat flux utilizing a three-dimensional, interconnected alumina nano porous surfaces. *Appl. Phys. Lett.* 101, 054104 (2012).
- [62] O’Hanley, H. et al. Separate effects of surface roughness, wettability, and porosity on the boiling critical heat flux. *Appl. Phys. Lett.* 103, 024102 (2013).

REFERENCES

- [63] Varanasi. K, Buongiorno. J & Dhillon. N, Critical heat flux maxima during boiling crisis on textured surfaces, *Nature Communications* (2015).
- [64] Rothstein. J & Ou. J, Direct velocity measurements of the flow past drag-reducing ultrahydrophobic surfaces, *Physics of Fluids* (2005).
- [65] Krogstad, P.A., Antonia, R.A, 1999, Surface roughness effects within turbulent boundary layer, *Exp. Fluids* 27, 450-460.
- [66] Technie, M.F., Bergstrom, D.J. Balachandar, R., 2003. Roughness effects in the low Re open-channel turbulent boundary layers. *Exp. Fluids* 33, 338-346.
- [67] Bakken, O.M., Krogstad, P.A. Ashrafian, A. Andersonn, H.I 2005. Reynolds number effects in the outer layer of the turbulent flow in channel with rough walls. *Phys. Fluids* 17.
- [68] Shah, M.K, Agelinchaab, M., Tachie, M.F., 2008. Influence of PIV interrogation area on turbulent statistics up to 4th order moments in smooth and rough wall turbulent flows, *Exp. Therm. Fluid Sci.* 32.
- [69] Volino, R.J., Schultz., M.P., Flack, K.A., 2011 Turbulence structure in a boundary layer over periodic two- and three-dimensional roughness *J. Fluid Mech.* 676, 172-190.
- [70] Asim, T., Mishra, R., Oliveira, A., & Charlton, M. (2019). Effects of the geometrical features of flow paths on the flow capacity of a control valve trim. *Journal of Petroleum Science and Engineering*, 172, 124-138. <https://doi.org/10.1016/j.petrol.2018.09.050>
- [71] Green .J, Mishra R, Charlton M, Owen R. Validation of CFD predictions using process data obtained from flow through an industrial control valve. *J Phys Conf Ser* 2012; 364.
- [72] Green J, Mishra R, Charlton M, Owen R, Local analysis of flow conditions within a geometrically complex control valve trim using CFD. *J Phys Conf Ser* 2012; 364.

REFERENCES

- [73] Klas R, Haban V, Rudolf P, Study of the nozzle check valve with respect to its operating characteristics. EPJ Web Conf 2018.
- [74] Asim T, Charlton M, Mishra R, CFD based investigations for the design of control valves used in energy systems. Energy Convers Manag 2017;153:288-303.
- [75] Asim T, Mishra R, Charlton M, Olivera C, Capacity testing and local flow analysis if a geometrically complex trim installed within a commercial control valve, international conference on jets, wakes and separated flows, 16-18 June, Stockholm, Sweden 2015.
- [76] Olivera A, Capacity testing of X-Stream valves for single component single phase flows. Technical report submitted to Weir Valves and Controls Ltd; 2017.
- [77] Wang P., Ma H, Quay B, Santavicca DA, Liu Y. Computational fluid dynamics of stream flow in a turbine control valve with a bell-shaped spindle. Appl Therm Eng 2018.
- [78] Qui T, Dai H, Lei Y, Liu Y. Effect of valve needle speed on flow characteristics in control valve for unity pump fuel system Ad Mech Eng 2018.
- [79] Asim T. Capacity testing of X-Stream valves for single component single phase flows. Technical report submitted to Weir Valves and Controls Ltd. 2013.
- [80] Lisowski E, Filo G. CFD analysis of the characteristics of a proportional flow control valve with an innovative opening shape. Energy Convers Manag 2016.
- [81] Kong L. Wei W, Yan Q. Application of flow field decomposition and reconstruction in studying and modelling the characteristics of a cartridge valve. Eng Appl Comput Fluid Mech 2018.
- [82] J.A. Chada, D.E. Hobson, A. Marshall, D.H. Wilkinson, Acoustic source properties of governor valves, 1980 ASME PVP Conference, San Francisco, USA August 12–15, 41 (1980) 125–138.

REFERENCES

- [83] F.G. Hammitt, *Cavitation and Multiphase Flow Phenomena*, McGraw-Hill Inc.,USA, 1980.
- [84] R. Petkovsek, G. Mocnik, J. Mozina, Measurements of the high pressureultrasonic wave and the cavitation bubble by optodynamic method, *FluidPhase Equilibria* 256 (2007) 158–162
- [85] Valve Magazine, *Flashing and Cavitation*, Summer 2015
- [86] Lighthill, M., *A New Method of Two-Dimensional Aerodynamic Design*, Aeronautical Research Council, London, 1945.
- [87] McFadden, G., *An Artificial Viscosity Method for the Design of Supercritical Airfoil*, New York Univ., Rept. C00-3077-158, New York, 1979.
- [88] Hicks, R., and Henne, P., *Wing Design by Numerical Optimization*, *Journal of Aircraft*, Vol. 15, 1978, pp. 407–412.
- [89] Jameson, A., *Aerodynamic Design via Control Theory*, *Journal of Scientific Computing*, Vol. 2, 1988, pp. 233–260.
- [90] LeGresley, P., and Alonso, J., *Investigation of Non-Linear Projection for POD Based Reduced Order Models for Aerodynamics*, AIAA Paper 2001-0926, Jan. 2001.
- [91] Everson, R., and Sirovich, L., *The Karhunen–Loeve Procedure for Gappy Data*, *Journal of the Optical Society of American*, Vol. 12, 1995, pp. 1657–1664.
- [92] Bui-Thanh T., Damodaran M. & Willcox K. *Aerodynamics data reconstruction and inverse design using proper orthogonal decomposition*, *AIAA Journal* Vol.42, No. 8, August 2004.
- [93] Renhui, Zhang & Guo, Rong & Yang, Jun-Hu & Luo, Jiaqi. (2017). *Inverse Method of Centrifugal Pump Impeller Based on Proper Orthogonal Decomposition (POD) Method*. *Chinese Journal of Mechanical Engineering*. 30. 1025-1031. 10.1007/s10033-017-0137-x.

REFERENCES

- [94] Murry N. & Ukeiley L., An application of Gappy POD for subsonic cavity flow PIV data. *Exp. Fluids* (2007) 42:79-91.
- [95] Xu Q. & Tsering-xiao B. Gappy POD based reconstruction of the temperature field in Tibet. *Theoretical and Applied Climatology* (2019).
- [96] Carlberg K. & Stephan R. Gappy data reconstruction and applications in archaeology. *Computer applications and quantitative methods in Archaeology* (2010).
- [97] Willcox K, Unsteady flow sensing and estimation via the gappy proper orthogonal decomposition, *Computers & Fluids* 35 (2006) 208-226.
- [98] Raben, Samuel & Charonko, John & Vlachos, Pavlos. (2012). Adaptive gappy proper orthogonal decomposition for particle image velocimetry data reconstruction. *Measurement Science and Technology*. 23. 025303. 10.1088/0957-0233/23/2/025303.
- [99] Saini P., Steinberg M. & Arndt C., Development and evaluation of Gappy POD for noisy PIV measurements in gas turbine combustors. 54TH AIAA Aerospace Sciences Meeting (2016).
- [100] Lyu Z, Kenway GWK, Martins JRR. Aerodynamic shape optimization investigations of the common research model wing benchmark. *AIAA J* 2015;53(4):968–85. doi: 10.2514/1.J053318 .
- [101] Imiela M. High-fidelity optimization framework for helicopter rotors. *Aerosp Sci Technol* 2012;23:2–16. doi: 10.1016/j.ast.2011.12.011.
- [102] Hicken JE, Zingg DW. Aerodynamic optimization algorithm with integrated geometry parameterization and mesh movement. *AIAA J* 2010;48(2):400–13. doi: 10.2514/1.44033.
- [103] D.A. Wolf-Gladrow, *Lattice-gas cellular automata and lattice Boltzmann models: an introduction*, Springer, Berlin (2000).

REFERENCES

- [104] Alexander Dreweke. Implementation and Optimization of the Lattice Boltzmann Method for the Jackal DSM System. Bachelor thesis, Friedrich-Alexander-Universität, Erlangen-Nürnberg, 2005.
- [105] R. Mei, W. Shyy, D. Yu, and L.-S. Luo. Lattice Boltzmann method for 3-D flows with curved boundary. *Journal of Computational Physics*, 161(2):680–699, 2000.
- [106] M. Sukop. Lattice Boltzmann modelling an introduction for geoscientists and engineers. Springer, Berlin New York, 2006.
- [107] X. He and Q. Zou. Analysis and boundary condition of the lattice Boltzmann BGK model with two velocity components. arXiv preprint comp-gas/9507002, 1995.
- [108] Q. Zou and X. He. On pressure and velocity boundary conditions for the lattice Boltzmann BGK model. *Physics of Fluids (1994-present)*, 9(6):1591–1598, 1997.
- [109] An internet book on fluid dynamics <http://brennen.caltech.edu/fluidbook/basicfluidynamics/Navierstokesexactolutions/poiseuilleflow.pdf> accessed on 06/10/2019 at 1530 hrs.
- [110] Asim T., Oliveira A., Charlton M. & Mishra R., Improved design of a multistage continuous resistance trim for minimum energy loss in control valves, *Energy* 174 (2019).
- [111] Pozrikidis C. Fluid dynamics theory, computation and numerical simulation. USA: Kluwer Academic Publishers; 2001.
- [112] Ansys Inc. *Shear-Stress transport (SST) k-w Model* [Online] Release 12.0 2009-01-23 Accessed on 07-07-2020 <https://www.afs.enea.it/project/neptunius/docs/fluent/html/th/node67.htm>

REFERENCES

- [113] Holmes, P., Lumley, J., and Berkooz, G., *Turbulence, Coherent Structures, Dynamical Systems and Symmetry*, Cambridge Univ. Press, Cambridge, England, U.K., 1996.
- [114] Sirovich, L., *Turbulence and the Dynamics of Coherent Structures. Part 1: Coherent Structures*, *Quarterly of Applied Mathematics*, Vol. 45, No. 3, 1987, pp. 561–571.
- [115] Epureanu, B. I., Dowell, E. H., and Hall, K., *Mach Number Influence on Reduced-Order Models of Inviscid Potential Flows in Turbomachinery*, *Journal of Fluids Engineering*, Vol. 124, No. 4, 2002, pp. 977–987

APPENDICES

A-1. Lattice Boltzmann Code

```
#include <stdio.h>
#include <stdlib.h>
#include <math.h>
#include <omp.h>
/*
// Lattice structure D3Q19

//simulation parameters 6-8-35
int  nx  = 200;           //lattice size
int  ny  = 150;
int  nz  = 24;
int  d   = 8.0;          //tube diameter
int  time = 2e8;
double u0 = 0.04;
int  save = 500;         //write to disk every # steps

int  h    = 0.9768;
int  sw   = 3.0;
int  w    = 3.0;
int  a    = 20;

int  offx = 1;
int  offz = 1;

int  dx   = 8.3982;
int  dz   = 7.5;

double tau = 3.3;        //mu=0.000182 //relaxation time
```

APPENDICES

```
double gx    = 1.0e-07;           //body force (gravity) in x direction
double gy    = 0.0;              //body force (gravity) in y direction
double gz    = 0.0;
FILE *errorfile;

int  bbot = 0;                    //bottom wall 0=periodic, 1=half way
bounce back
int  btop = 0;                    //top    wall 0=periodic, 1=half way
bounce back
int  blef = 0;                    //left  wall 0=periodic, 1=inlet
int  brig = 0;                   //right wall 0=periodic, 1=outlet
int  bfro = 0;                    //front wall 0=periodic, 1=half way
bounce back
int  bbac = 0;                    //back  wall 0=periodic, 1=half way
bounce back
//global variables
int t,x,y,z,k,n,m,err,np, offx, offz;
double ***solid;
double ***rho, ***ux, ***uy, ***uz;           //macroscopic variables
arrays
double ****fp, ****fn, ****f_tmp; //distribution functions arrays
double feq[19],feq1[19], colision_tmp[19], b[19]; //equilibrium
function arrays
double vel, vel1, vel2, vel3;

double wi[19]= {1.0/3.0, 1.0/18.0, 1.0/36.0, 1.0/18.0, 1.0/36.0,
1.0/18.0, 1.0/36.0, 1.0/18.0, 1.0/36.0, 1.0/36.0, 1.0/18.0,
1.0/36.0, 1.0/36.0, 1.0/18.0, 1.0/36.0, 1.0/36.0, 1.0/36.0,
1.0/36.0, 1.0/36.0};
```

APPENDICES

```
double ex[19]= {0.0, 1.0, 1.0, 0.0,-1.0,-1.0,-1.0, 0.0, 1.0, 0.0,
0.0, 0.0, 0.0, 0.0, 0.0, 1.0,-1.0,-1.0, 1.0};
double ey[19]= {0.0, 0.0, 1.0, 1.0, 1.0, 0.0,-1.0,-1.0,-1.0, 1.0,
0.0,-1.0,-1.0, 0.0, 1.0, 0.0, 0.0, 0.0, 0.0};
double ez[19]= {0.0, 0.0, 0.0, 0.0, 0.0, 0.0, 0.0, 0.0, 0.0, 1.0,
1.0, 1.0,-1.0,-1.0,-1.0, 1.0, 1.0,-1.0,-1.0};

double cx[7]= {0.0, 1.0, 0.0, -1.0, 0.0, 0.0, 0.0};
double cy[7]= {0.0, 0.0, 1.0, 0.0, -1.0, 0.0, 0.0};
double cz[7]= {0.0, 0.0, 0.0, 0.0, 0.0, 1.0, -1.0};
//functions
void initialize();
void calculate_density();

void calculate_velocities();
void calculate_equilibrium(int x, int y, int z);
void calculate_equilibrium1(int x, int y, int z);
void calculate_colision();
void streaming(int x, int y, int z);
void update_boundary();

void save_data();
double*** allocate_three_dimensional_array_double(int nx, int ny,
int nz);
double**** allocate_four_dimensional_array_double(int nx, int ny,
int nz, int k);

int main(int argc, char *argv[])
{
    printf("LBM Single Phase BGK code\n");
    printf("K.J.Kubiak & Shrawasti Sahare 2020\n");
```

APPENDICES

```
//step1 - Initialize fp and fn to feq
initialize();

for (t=0; t<time+1; t++)
{

    //update macroscopic quantities

    calculate_density();
    calculate_velocities();

    //calculate collision step (equilibrium, collision,
streaming)
    calculate_colision();

    //bounce back distribution function on solid nodes
    update_boundary();

    //write data to disk

    if (t%save==0)
    {
        save_data();
        printf("t=%d\n",t);
    }

    if (err==1)
    {
        printf("Unstability at t=%d \n",t);
    }
}
```

APPENDICES

```
        return 1;
    }
    //swap pointers to distribution functions arrays
    f_tmp = fp;
    fp = fn;
    fn = f_tmp;
}

//finalize and free allocated memory
free(rho);
free(ux);
free(uy);
free(uz);
free(solid);
free(fp);
free(fn);

return 0;
}

void initialize()
{
    err = 0;
    //allocate memory
    rho = allocate_three_dimentional_array_double(nx,ny,nz);
    ux = allocate_three_dimentional_array_double(nx,ny,nz);
    uy = allocate_three_dimentional_array_double(nx,ny,nz);
    uz = allocate_three_dimentional_array_double(nx,ny,nz);
    solid = allocate_three_dimentional_array_double(nx,ny,nz);
    fp = allocate_four_dimentional_array_double(nx,ny,nz,19);
    fn = allocate_four_dimentional_array_double(nx,ny,nz,19);
```

APPENDICES

```
for (z=0; z<nz; z++)
{
    for (y=0; y<ny; y++)
    {
        for (x=0; x<nx; x++)
        {
            ux[x][y][z] =0.009;
            uy[x][y][z] =0.0;
            uz[x][y][z] =0.0;
        }
    }
}

for (z=0; z<nz; z++)
{
    for (y=0; y<ny; y++)
    {
        for (x=0; x<nx; x++)
        {
            //initialize density
            rho[x][y][z] = 1.0;

            //initialize boundary condition
            solid[x][y][z] = 0.0;
```

APPENDICES

```
if ((bbot==1) && (y==0))
{
    solid[x][y][z] = 1.0;    //bottom wall
}
if ((btop==1) && (y==ny-1))
{
    solid[x][y][z] = 1.0;    //top wall
}
if ((blef==1) && (x==0))
{
    solid[x][y][z] = 2.0;    // inlet
}
if ((brig==1) && (x==nx-1))
{
    solid[x][y][z] = 3.0;    //outlet 3
}
if ((bfro==1) && (z==nz-1))
{
    solid[x][y][z] = 1.0;    //front wall
}
if ((bbac==1) && (z==0))
{
    solid[x][y][z] = 1.0;    //back wall
}

//cube

for (n=1; n<31; n++)
{
    for (m=1; m<4; m++)
    {
```

APPENDICES

```
        if      ((x>=(offx+(n-1)*(w+dx))))      &&
(x<=(offx+((n*w+(n-1)*dx))) && y<=h && z>=0 && z>=(offz+(3*m-3)*sw)
&& z<=(offz+(3*m-2)*sw))
        {
            solid[x][y][z] = 1.0;
        }
    }
}
```

```
//calculate local equilibrium for x,y,z location
calculate_equilibrium(x, y, z);
```

```
for (k=0; k<19; k++)
{
    //calculate collision step
    fp[x][y][z][k] = feq[k];
    fn[x][y][z][k] = feq[k];
}
}
}
```

```
void calculate_density()
{
    for (x=0; x<nx; x++)
    {
        for (y=0; y<ny; y++)
```

APPENDICES

```
{
    for (z=0; z<nz; z++)
    {

        if (solid[x][y][z]==0)
        {
            rho[x][y][z] = 0.0;

            for (k=0; k<19; k++)
            {

                rho[x][y][z] = rho[x][y][z] + fp[x][y][z][k];
            }

        }
    }
}
```

```
void calculate_velocities()
{
    //calculate rho, ux and uy, uz

    for (x=0; x<nx; x++)
    {
        for (y=0; y<ny; y++)
        {
            for(z=0; z<nz; z++)
            {
```

APPENDICES

```

ux[x][y][z] = 0.0;
uy[x][y][z] = 0.0;
uz[x][y][z] = 0.0;

for (k=0; k<19; k++)
{
    //calculate velocities
    ux[x][y][z] = ux[x][y][z] +
ex[k]*fp[x][y][z][k]/rho[x][y][z];
    uy[x][y][z] = uy[x][y][z] +
ey[k]*fp[x][y][z][k]/rho[x][y][z];
    uz[x][y][z] = uz[x][y][z] +
ez[k]*fp[x][y][z][k]/rho[x][y][z];

}

ux[x][y][z] = ux[x][y][z] +tau*gx/rho[x][y][z];
uy[x][y][z] = uy[x][y][z] +tau*gy/rho[x][y][z];
uz[x][y][z] = uz[x][y][z] +tau*gz/rho[x][y][z];
}

}
}
}

```

```

void calculate_colision()
{
    for (x=0; x<nx; x++)
    {
        for (y=0; y<ny; y++)
        {
            for (z=0; z<nz; z++)

```

APPENDICES

```

{

if (solid[x][y][z]==0)
{

    for (k=0; k<19; k++)
    {
        //calculate equilibrium function
        vel1 = (ex[k]*ux[x][y][z] + ey[k]*uy[x][y][z] +
ez[k]*uz[x][y][z]);
        vel2 = (vel1 * vel1);
        vel3      =      (ux[x][y][z]*ux[x][y][z]      +
uy[x][y][z]*uy[x][y][z] + uz[x][y][z]*uz[x][y][z]);

        feq[k] = wi[k]*rho[x][y][z]*(1.0 + 3.0*vel1 +
4.5*vel2 - 1.5*vel3);
        if (feq[k]!=feq[k])
        {
            err=1; //check for simulation instability
        }
    }

    for (k=0; k<19; k++)
    {
        //calculate collision step
        colision_tmp[k]      =      fp[x][y][z][k]      -
((fp[x][y][z][k] - feq[k])/tau); //+feq1[k]-feq[k];
    }

    //perform local streaming step for x,y location
    int bot, top, lef, rig, frt, bck;
    //for a given x,y the neighbour nodes are as follows

```

APPENDICES

//ny and ny is the domain size, this is assuming
periodic boundary condition

```
bot = (y+ny-1)%ny;  
top = (y+1)%ny;  
frt = (z+1)%nz;  
bck = (z+nz-1)%nz;  
lef = (x+nx-1)%nx;  
rig = (x+1)%nx;
```

```
fn[x][y][z][0] = colision_tmp[0];  
fn[rig][y][z][1] = colision_tmp[1];  
fn[rig][top][z][2] = colision_tmp[2];  
fn[x][top][z][3] = colision_tmp[3];  
fn[lef][top][z][4] = colision_tmp[4];  
fn[lef][y][z][5] = colision_tmp[5];  
fn[lef][bot][z][6] = colision_tmp[6];  
fn[x][bot][z][7] = colision_tmp[7];  
fn[rig][bot][z][8] = colision_tmp[8];
```

```
fn[x][top][frt][9] = colision_tmp[9];  
fn[x][y][frt][10] = colision_tmp[10];  
fn[x][bot][frt][11] = colision_tmp[11];  
fn[x][bot][bck][12] = colision_tmp[12];  
fn[x][y][bck][13] = colision_tmp[13];  
fn[x][top][bck][14] = colision_tmp[14];
```

```
fn[rig][y][frt][15] = colision_tmp[15];  
fn[lef][y][frt][16] = colision_tmp[16];  
fn[lef][y][bck][17] = colision_tmp[17];  
fn[rig][y][bck][18] = colision_tmp[18];
```

APPENDICES

```
        }
    }
}

void update_boundary()
{
    // Half-Way bounce back

    int bot, top, lef, rig, frt, bck;
    double tmp;

    for (x=0; x<nx; x++)
    {
        for (y=0; y<ny; y++)
        {
            for (z=0; z<nz; z++)
            {
                if (solid[x][y][z]==1.0)
                {
                    bot = (y+ny-1)%ny;
                    top = (y+1)%ny;
                    frt = (z+1)%nz;
                    bck = (z+nz-1)%nz;
                    lef = (x+nx-1)%nx;
                    rig = (x+1)%nx;

                    // Rotate vectors
                    tmp = fn[x][y][z][1];
                    fn[x][y][z][1] = fn[x][y][z][5];
```

APPENDICES

```
fn[x][y][z][5] = tmp;
```

```
tmp = fn[x][y][z][2];
```

```
fn[x][y][z][2] = fn[x][y][z][6];
```

```
fn[x][y][z][6] = tmp;
```

```
tmp = fn[x][y][z][3];
```

```
fn[x][y][z][3] = fn[x][y][z][7];
```

```
fn[x][y][z][7] = tmp;
```

```
tmp = fn[x][y][z][4];
```

```
fn[x][y][z][4] = fn[x][y][z][8];
```

```
fn[x][y][z][8] = tmp;
```

```
tmp = fn[x][y][z][11];
```

```
fn[x][y][z][11] = fn[x][y][z][14];
```

```
fn[x][y][z][14] = tmp;
```

```
tmp = fn[x][y][z][10];
```

```
fn[x][y][z][10] = fn[x][y][z][13];
```

```
fn[x][y][z][13] = tmp;
```

```
tmp = fn[x][y][z][9];
```

```
fn[x][y][z][9] = fn[x][y][z][12];
```

```
fn[x][y][z][12] = tmp;
```

```
tmp = fn[x][y][z][15];
```

```
fn[x][y][z][15] = fn[x][y][z][17];
```

```
fn[x][y][z][17] = tmp;
```

```
tmp = fn[x][y][z][16];
```

```
fn[x][y][z][16] = fn[x][y][z][18];
```

```
fn[x][y][z][18] = tmp;
```

APPENDICES

```
//send the vectors back to fluid nodes (streaming)

fn[x][y][z][0]      = fn[x][y][z][0];
fn[rig][y][z][1]    = fn[x][y][z][1];
fn[rig][top][z][2]  = fn[x][y][z][2];
fn[x][top][z][3]    = fn[x][y][z][3];
fn[lef][top][z][4]  = fn[x][y][z][4];
fn[lef][y][z][5]    = fn[x][y][z][5];
fn[lef][bot][z][6]  = fn[x][y][z][6];
fn[x][bot][z][7]    = fn[x][y][z][7];
fn[rig][bot][z][8]  = fn[x][y][z][8];

fn[x][top][frt][9]  = fn[x][y][z][9];
fn[x][y][frt][10]   = fn[x][y][z][10];
fn[x][bot][frt][11] = fn[x][y][z][11];
fn[x][bot][bck][12] = fn[x][y][z][12];
fn[x][y][bck][13]   = fn[x][y][z][13];
fn[x][top][bck][14] = fn[x][y][z][14];

fn[rig][y][frt][15] = fn[x][y][z][15];
fn[lef][y][frt][16] = fn[x][y][z][16];
fn[lef][y][bck][17] = fn[x][y][z][17];
fn[rig][y][bck][18] = fn[x][y][z][18];

}
if (solid[x][y][z]==2.0) //inlet
{
    bot = (y+ny-1)%ny;
    top = (y+1)%ny;
    frt = (z+1)%nz;
}
```

APPENDICES

```

bck = (z+nz-1)%nz;
lef = (x+nx-1)%nx;
rig = (x+1)%nx;

```

```

ux[x][y][z]=u0;
uy[x][y][z]=0.0;
uz[x][y][z]=0.0;

```

```

rho[x][y][z] = 1.0 ;

```

```

calculate_equilibrium(x,y,z);

```

```

fn[x][y][z][1] = feq[1]+fn[x][y][z][5]-feq[5];
fn[x][y][z][2] = feq[2]+fn[x][y][z][4]-feq[4];
fn[x][y][z][8] = feq[8]+fn[x][y][z][6]-feq[6];
fn[x][y][z][15] = feq[15]+fn[x][y][z][16]-
feq[16];
fn[x][y][z][18] = feq[18]+fn[x][y][z][17]-
feq[17];

```

```

fn[rig][y][z][1] = fn[x][y][z][1];
fn[rig][top][z][2] = fn[x][y][z][2];
fn[rig][bot][z][8] = fn[x][y][z][8];
fn[rig][y][frt][15] = fn[x][y][z][15];
fn[rig][y][bck][18] = fn[x][y][z][18];
}

```

```

if (solid[x][y][z]==3.0) // outlet
{
    bot = (y+ny-1)%ny;

```

APPENDICES

```

top = (y+1)%ny;
frt = (z+1)%nz;
bck = (z+nz-1)%nz;
lef = (x+nx-1)%nx;
rig = (x+1)%nx;

ux[nx-1][y][z] = (4*ux[nx-2][y][z]-ux[nx-
3][y][z])/3;
uy[nx-1][y][z] = (4*uy[nx-2][y][z]-uy[nx-
3][y][z])/3;
uz[nx-1][y][z] = (4*uz[nx-2][y][z]-uz[nx-
3][y][z])/3;

calculate_equilibrium(x, y, z);

// assign equilibrium values to all distribution
function vectors

fn[x][y][z][4] = feq[4];
fn[x][y][z][5] = feq[5];
fn[x][y][z][6] = feq[6];
fn[x][y][z][16] = feq[16];
fn[x][y][z][17] = feq[17];

fn[lef][top][z][4] = fn[x][y][z][4];
fn[lef][y][z][5] = fn[x][y][z][5];
fn[lef][bot][z][6] = fn[x][y][z][6];
fn[lef][y][frt][16] = fn[x][y][z][16];
fn[lef][y][bck][17] = fn[x][y][z][17];

}
}
}

```

APPENDICES

```
    }  
}  
  
void save_data()  
{  
  
    //vtk file format can be opened in open source software ParaView  
(www.paraview.org)  
    int x,y,z;  
    double u1,u2,u3,tmp,rh;  
    FILE *vtkfile;  
    char fname[255];  
    char vtkfilename[20] = "output";  
  
    //int check;  
    //char directory[20] = "output";  
    //check = mkdir(directory);  
    //if (check==-1) { }  
    //sprintf(fname,"%s/%s_%07d.vtk",directory,vtkfilename,t);  
  
    sprintf(fname,"%s_%07d.vtk",vtkfilename,t);  
    vtkfile = fopen(fname,"w");  
    fprintf(vtkfile, "# vtk DataFile Version 3.0\n");  
    fprintf(vtkfile, "K.J.Kubiak & Shrawasti Sahare LBM BGK  
code\n");  
    fprintf(vtkfile, "ASCII\n");  
    fprintf(vtkfile, "DATASET STRUCTURED_POINTS\n");  
    fprintf(vtkfile, "DIMENSIONS %d %d %d\n", nx, ny, nz);  
    fprintf(vtkfile, "SPACING 1 1 1\n");  
    fprintf(vtkfile, "ORIGIN 0 0 0\n");  
    fprintf(vtkfile, "POINT_DATA %d\n", nx*ny*nz);  
    fprintf(vtkfile, "FIELD FieldData 2\n");
```

APPENDICES

```
//write velocity
fprintf(vtkfile, "Velocity 3 %d double\n", nx*ny*nz);
for (z=0; z<nz; z++)
{
    for (y=0; y<ny; y++)
    {
        for (x=0; x<nx; x++)
        {
            u1 = ux[x][y][z];
            u2 = uy[x][y][z];
            u3 = uz[x][y][z];
            if (solid[x][y][z]==1)
            {
                u1=0.0;
                u2=0.0;
                u3=0.0;
            }
            fprintf(vtkfile, "%.4e ", u1);
            fprintf(vtkfile, "%.4e ", u2);
            fprintf(vtkfile, "%.4e ", u3);
        }
        fprintf(vtkfile, "\n");
    }
}
```

```
double**** allocate_four_dimensional_array_double(int nx, int ny,
int nz, int k)
{
    double ****p; /*declaration of p as: pointer-to-pointer-to-
pointer of int */
    int x, y, z;
```

APPENDICES

```
p = malloc( nx * sizeof(*p) ); /*Allocate pointers for the nx
*/
if (p != NULL)
{
    for (x = 0; x < nx; x++)
    {
        p[x] = malloc( ny * sizeof **p );/*Allocate pointers for
the ny */
        if (p[x] == NULL)
        {
            printf("Memory allocation failed. Exiting....");
            //return (1);
        }
        else
        {
            for (y = 0; y < ny; y++)
            {
                p[x][y] = malloc( nz * sizeof ***p ); /*Allocate
pointers for the nz */
                if (p[x][y] == NULL)
                {
                    printf("Memory allocation failed.
Exiting....");
                    //return (1);
                }
                else
                {
                    for (z = 0; z < nz; z++)
                    {
                        p[x][y][z] = malloc( k * sizeof ****p );
/*Allocate pointers for the nz */
                        if (p[x][y][z] == NULL)
                        {
```

APPENDICES

```

        printf("Memory allocation failed.
Exiting....");

        //return (1);
    }
}
}
}
}
}
}
}
}
else
{
    printf("Memory allocation failed. Exiting....");
}
return p;
}

```

```

double*** allocate_three_dimensional_array_double(int nx, int ny,
int nz)
{
    double ***p; /*declaration of p as: pointer-to-pointer-to-
pointer of int */
    int x, y;

    p = malloc( nx * sizeof(*p) ); /*Allocate pointers for the nx
*/
    if (p != NULL)
    {
        for (x = 0; x < nx; x++)
        {
            p[x] = malloc( ny * sizeof **p );/*Allocate pointers for
the ny */
            if (p[x] == NULL)

```

APPENDICES

```
{
    printf("Memory allocation failed. Exiting....");
    //return (1);
}
else
{
    for (y = 0; y < ny; y++)
    {
        p[x][y] = malloc( nz * sizeof ***p ); /*Allocate
pointers for the nz */
        if (p[x][y] == NULL)
        {
            printf("Memory allocation failed.
Exiting....");
            //return (1);
        }
    }
}
}
else
{
    printf("Memory allocation failed. Exiting....");
    //return (1);
}
return p;
}
```

A-2. Gappy Proper Orthogonal Decomposition Code

```

uk=1;%number of unknown

row=9202;
column=9;
add=0;

for i=1:row
    for j=1:(column+add)

        if (n(i,j)==1)

            h(i,j)= Uall(i,j);

        end

        if (n(i,j)==0)

            P=0;
            for k=1:(column+add)

                P= P + n(i,k);

            end

            gsum(i)=0;
            for k=1:(column+add)

                gsum(i)= gsum(i) + Uall(i,k);

            end

            h(i,j)= gsum(i)/P;    %replacing gappy data with row average

        end
    end
end

for l=1:100 %iterative loop

%basic POD start
R=h'*h;
[eV,D]=eig(R);
[L,I]=sort(diag(D));

for i=1:length(D)
eValue(length(D)+1-i)=L(i);
eVec(:,length(D)+1-i)=eV(:,I(i));
end;
eValue(length(eValue))=0;

```

APPENDICES

```
menergy=eValue/sum(eValue);

m=5;
for i=1:m
tmp=h*eVec(:,i);
phi(:,i)=tmp/norm(tmp);
end;

%basic POD end

for i=1:m

    for j=1:m

        A(i,j) = ((n(:,column).*phi(:,i))'*(n(:,column).*phi(:,j))));%gappy
operations

    end

    B(i,1) = (n(:,column).*h(:,column))'*(n(:,column).*phi(:,i)));

end

b=inv(A)*B; % obtaining coefficient vector b

for i=1:uk

    h(i,column)=0;

    for j=1:m

        h(i,column)= h(i,column) + phi(i,j)*b(j);%replacing with newly obtained
value

    end

end

iter(1)=1;

end
```

LIST OF PUBLICATIONS

1. **Sahare, S.**, Asim, T., Kubiak, K., Mishra, R., & Nsom, B. (2019). Inverse design of functional surfaces through low fidelity modelling.
2. Mishra, Rakesh, Albarzenji, Dhir, **Shrawasti, Sahare**, Sendanayake, Isuru and Pradhan, Suman (2015) Flow diagnostics. In: FLUVISU 2015, 16th - 20th November 2015, Pleumeur-Bodou/Lannion, France.